The initial mass function in early-type galaxies

Spiniello, Chiara

rijksuniversiteit
groningen

The Initial Mass Function in Early-Type Galaxies

Proefschrift

ter verkrijging van het doctoraat in de
Wiskunde en Natuurwetenschappen
aan de Rijksuniversiteit Groningen
op gezag van de
Rector Magnificus, dr. E. Sterken,
in het openbaar te verdedigen op
vrijdag 4 oktober 2013
om 14:30 uur

door

Chiara Spiniello

geboren op 11 november 1984
te Napels, Italië

Promotores:	Prof. dr. L.V.E. Koopmans Prof. dr. S.C. Trager
Beoordelingscommissie:	Prof. dr. R.L. Davies Prof. dr. A. Helmi Prof. dr. K.H. Kuijken

ISBN: 978-90-367-6386-8 Printed version
ISBN: 978-90-367-6387-5 Electronic version

Tutte le verità sono facili da capire
una volta che sono state rivelate.
Il difficile é scoprirle...

All truths are easy to understand
once they are discovered.
The point is to discover them...

Galileo Galilei

To my unique marvellously noisy family...

Alla mia meravigliosamente rumorosa unica famiglia...

Cover:
Design by: Chiara Spiniello
Image Credit: Sloan Lens ACS Survey (SLACS, Bolton et al. 2006)
Back: HST image of "The Cosmic Horseshoe",
pilot program of the XLENS Survey (Chapter 3)

Printed by: Ipskamp Drukkers BV

Contents

1 Introduction

'I checked it very thoroughly,' said the computer,
'and that quite definitely is the answer.
I think the problem, to be quite honest with you,
is that you've never actually known what the question is.
' 'But it was the Great Question!
The Ultimate Question of Life, the Universe and Everything!'
howled Loonquawl.
'Yes,' said Deep Thought with the air of one who suffers fools gladly,
'but what actually is it?'
A slow stupefied silence crept over the men
as they stared at the computer and then at each other.
'Well, you know, it's just Everything ... Everything ...' offered Phouchg weakly.
'Exactly!' said Deep Thought.
'So once you know what the question actually is, you'll know what the answer means.

Douglas Adams,
The Hitchhiker's Guide to the Galaxy

In this thesis I investigate the internal structure and the distribution of dark and luminous matter in galaxies. Specifically, I focus on the inner regions of massive early-type galaxies (ETGs) and their stellar Initial Mass Function (IMF), with particular emphasis on constraining its low-mass end slope and its lower cutoff-mass, using galaxy spectra. The IMF is the distribution of stellar masses that form in one star-formation event in a given volume of space. Hence, since the star's mass determines its subsequent evolutionary path, all the observable properties of stellar populations and galaxies (i.e., colour, magnitude and luminosity) are heavily influenced by their IMFs and star-formation histories (SFHs). Although often unappreciated, the IMF is a fundamental cornerstone in modern astrophysics and cosmology. Thus detecting variations in the IMF shape with galaxy properties could provide insight into the process through which stars form. A systematic trend of the IMF with galaxy mass, environment, metallicity, or cosmic look-back time, would likely indicate that all the inferred SFHs, stellar masses and hence stellar mass density estimates could be systematically in error. Consequently, this could change our understanding of the formation mechanisms as well as the chemical evolution of galaxies within the Λ Cold Dark Matter (ΛCDM) cosmological framework.

This introduction briefly describes the cosmological framework and places the research presented in this thesis in a broader scientific context.

1.1 The ΛCDM paradigm

It is well established in cosmology that the Universe started from a single originating event, the Big Bang "singularity", and expanded since then with a rate that depends on the state and the density of matter and energy that constitute in the Universe. Thanks to the most recent results from WMAP (Hinshaw et al. 2012; Bennett et al. 2012) and Planck (Planck Collaboration et al. 2013b,a) we are now able to precisely determine the contributions to the energy-density of the various constituents of the Universe. According to the ΛCDM model, only some 4.9% of the total mass density of the Universe comprises ordinary matter from which visible planets, stars and galaxies are made. The rest of the matter is dominated by non-baryonic, cold, non-interacting matter whose presence is known only through its gravitational force. It is known as "dark matter" and makes up 26.8% of the energy density of the Universe. About 68.3% of the energy density at the present is believed to be in the form of dark energy, a hypothetical form of energy proposed to explain observations indicating that the Universe is expanding at an accelerating

rate (values are taken from the latest published results of the Planck Collaboration, 2013a,b).

The ΛCDM model is currently the commonly accepted cosmological framework, remarkably successful in explaining the observed expansion of space, the existence and structure (and anisotropies) of the Cosmic Microwave Background (CMB) radiation, the large scale structure of the Universe, and the observed distribution of lighter elements (i.e. hydrogen, helium, lithium).

Despite great progress in explaining the Universe on large scales, the details of the formation and evolution of structure in the Universe, amongst which are the most massive galaxies (i.e. ETGs), still remain an open question in present-day extragalactic astrophysics and cosmology. Galaxies constitute the back-bone of the large-scale visible structure of the Universe. In the local Universe, they are the product of a complex cosmological evolutionary process and their properties are a consequence of their mass-assembly, environmental, star-formation, and metal-enrichment histories.

In the ΛCDM framework, the formation and evolution of galaxies take place in gravitational potential wells of dark-matter halos (Blumenthal et al. 1984), where the stars form after mergers and accretion of gas, finally resulting in visible galaxies (Tegmark et al. 1997; Gao et al. 2007). However, the details of the baryonic physics behind galaxy formation in the centers of dark-matter halos are still debated, especially concerning the contribution from different types of feedback processes (e.g. stellar, AGN, SN) in regulating the gaseous budget and the role that mergers and secular evolution processes play in configuring the diverse morphologies observed today in galaxies. All these processes play a major role in determining how galaxies evolve throughout cosmic time, building up their stellar mass and shaping their present-day structure (White & Rees 1978; Springel, Di Matteo & Hernquist 2005b; Gao et al. 2007). In the current galaxy formation paradigm (e.g. Springel, Di Matteo & Hernquist 2005a), the early Universe had a much smoother dark-matter distribution than it has today. Through gravitational instabilities, dark matter started to form clumps which provided the starting framework for structure formation. Within these structures, gas cooled and formed stars (White & Rees 1978). The physical mechanism that shapes the luminous content inside the dark-matter potential (i.e. the stars and galaxies that we observe), driven by hydrodynamics and chemistry of gas and complex radiative feedback processes, remains to a large extent one of the key unknowns of modern extragalactic astronomy.

Two general theories for ETGs formation have been proposed in the last fifty years: monolithic collapse (Eggen, Lynden-Bell & Sandage 1962; Larson 1975;

Bressan, Chiosi & Fagotto 1994) and the hierarchical formation model (White & Rees 1978; Blumenthal et al. 1984; Frenk et al. 1988; Frenk 1988; White & Frenk 1991; Barnes 1992; Cole & Lacey 1996; Cole et al. 2000). According to monolithic collapse, galaxies are formed in a single intense burst of star formation, relatively early in the lifetime of the Universe, from the gravitational collapse of a cloud of primordial gas and since then they have undergone little or no structural evolution. However, the widely varying observed ages of different components of a same galaxy, the predicted size-growth of ETGs (Loeb & Peebles 2003; Robertson et al. 2006; Khochfar & Silk 2006; Naab et al. 2007), as well as results of the WMAP satellite (Bennett et al. 2003, 2012; Hinshaw et al. 2012) and large-scale structure all suggest a "bottom-up" structure formation, where galaxies grow via a series of mergers. Nevertheless, observations are often limited to low redshifts where sometimes it is hard to distinguish between a hierarchical aggregation that occurs quickly at high redshift and monolithic collapse at high redshift (Peebles 2002).

The ΛCDM cosmological model favours a hierarchical structure formation (e.g. Frenk 1988; Barnes 1992; Blumenthal et al. 1984; Cole & Lacey 1996) where CDM haloes are formed due to gravitational instabilities and evolve hierarchically through mergers (e.g. White & Rees 1978; Frenk et al. 1988; White & Frenk 1991; Lacey & Cole 1993; Cole et al. 2000). Hierarchical formation models predict that small baryonic structures form first in the center of dark-matter haloes, and then merge forming more massive structures, drastically transforming their morphology, with the consequent evolution of their stellar population. Direct evidence in favor of the merger scenario has been presented in several recent works showing that massive quiescent galaxies ($M_\star \sim 10^{11}\,M_\odot$) were much more compact at intermediate redshift ($z \sim 2$), with effective radii 3-5 times smaller than for comparably massive ETGs in the local universe (Daddi et al. 2005; Trujillo et al. 2006; Buitrago et al. 2008; van Dokkum 2008; Newman et al. 2012; van de Sande et al. 2011, 2013). The fact that they grew significantly in size, but much less in stellar mass, would also argue in favor of inside-out growth through *minor* mergers. In fact, whereas major mergers, involving nearly equal-mass components, will lead to comparable growth in both size and mass, minor mergers involving lower-mass companions can result in more efficient size-only growth (Bezanson et al. 2009; Naab, Johansson & Ostriker 2009; Hopkins et al. 2010). The hierarchical scenario naively implies that the more massive galaxies (ETGs), the end product of mergers of smaller systems, should form later than less massive galaxies. This seems in stark contrast, however, with the fact that very massive ETGs are found to be already in place at redshift $z \sim 1-3$ (Cimatti et al. 2004;

McCarthy et al. 2004; Glazebrook et al. 2004; Daddi et al. 2005; Saracco et al. 2005; Pérez-González et al. 2008; Marchesini et al. 2009; Ferreras et al. 2009; Caputi et al. 2011). The latter point is also confirmed by the straightforward interpretation of the evolution with redshift of the color-magnitude, fundamental plane, and size-magnitude, as clearly pointed out by Peebles (2002).

A detailed knowledge of the internal structure, luminous and dark-matter distribution, as well as a reliable study of the stellar population of the class of massive ETGs, is therefore crucial in order to achieve a better understanding of the formation and evolution of these systems and fully comprehend the processes in the hierarchical galaxy formation scenario.

1.2 Early-Type Galaxies: a basic overview

This thesis focuses on early-type galaxies (ETGs), whose formation history is complex and heavily debated in present-day extragalactic astrophysics, but whose role in the ΛCDM cosmological model is fundamental because they count for more than half of the total stellar mass in the Universe (e.g. Bell et al. 2003; Gallazzi et al. 2008).

An elliptical galaxy has approximately an ellipsoidal shape and a smooth, nearly featureless brightness profile. Ellipticals have very little gas and dust, and contain primarily an old and red stellar population (e.g. Renzini 2006; Clemens et al. 2006, 2009). Generally, ETGs are more common in denser environments, such as galaxy clusters, which is known as the morphology-density relation (e.g. Dressler 1980).

The surface brightness of an elliptical galaxy falls off smoothly with radius, and can in most of the cases be described by a De Vaucouleurs (1948) profile, or more generally a Sérsic law (Sérsic 1963, 1968),

$$I(R) = I_{\rm eff}\, e^{-b(n)[(R/R_{\rm eff})^{1/n}-1]}. \tag{1.1}$$

In Eq. 1.1, $R_{\rm eff}$ is the effective radius, i.e. the radius of the isophote that contains half of the total luminosity and $I_{\rm eff} \equiv I(R_{\rm eff})$ denotes the intensity at that radius. The parameter b_n has been determined numerically and can be approximated as $b_n = 2.0n - 0.33$ (e.g. Ciotti & Bertin 1999); n is a free parameter, also known as the Sérsic index (for $n = 4$, the Sérsic profile reduces to a De Vaucouleurs profile).

Despite their apparent complex formation histories, elliptical galaxies obey several tight empirical scaling relations between their structural parameters. These

play a central role in the study of galaxy evolution since they connect photometric characteristics and chemical composition to kinematical and dynamical properties of the systems (e.g. the Faber-Jackson $L_{\rm tot}$–$\sigma_\star$ relation, Faber & Jackson 1976; the color-$\sigma_\star$ relation, Bower, Lucey & Ellis 1992; the Mg_2–$\sigma_\star$ relation, Terlevich et al. 1981; Dressler et al. 1987; Guzman et al. 1992; Bender, Burstein & Faber 1993; or the M_{BH}–σ_{star} relation, Ferrarese & Merritt 2000; Gebhardt et al. 2000; Gültekin et al. 2009).

One of the most intriguing and useful scaling relations is the Fundamental Plane (FP, e.g. Djorgovski & Davis 1987; Dressler et al. 1987), a strikingly tight relation between the value of $R_{\rm eff}$, the average surface brightness within the effective radius ($\langle I_{\rm eff}\rangle$), and the central velocity dispersion σ_c. Because velocity dispersion and surface brightness are distance-independent observables, whereas the size is not, it is common to write the FP equation in the form:

$$R_{\rm eff} \propto \sigma_c^a \times \langle I_{\rm eff}\rangle^b \tag{1.2}$$

and to find that pair of parameters (a, b) for which the scatter either in the $R_{\rm eff}$ direction or in the direction orthogonal to the Fundamental Plane is minimized (Jorgensen, Franx & Kjaergaard 1996).

The fact that elliptical galaxies occupy only a small portion of the three-dimensional parameter space defined by the above-mentioned parameters has been explained by assuming that they are in virial equilibrium (e.g. Faber et al. 1987; Djorgovski & Davis 1987; Bender, Burstein & Faber 1992). If elliptical galaxies are assumed to be stationary self-gravitating systems, one expects

$$\sigma^2 \propto \frac{GM_{\rm dyn}}{R}. \tag{1.3}$$

Using a relation between the luminosity, the mean surface brightness and the effective radius $L = 2\pi\langle I_{\rm eff}\rangle {R_{\rm eff}}^2$, we can define the mass-to-light ratio (Υ) as

$$\Upsilon = \frac{M_{\rm dyn}}{2\pi\langle I_{\rm eff}\rangle R_{\rm eff}^2} \tag{1.4}$$

so that $M_{\rm dyn} = 2\pi\,\langle I_{\rm eff}\rangle\, R_{\rm eff}^2\,\Upsilon$ which will give, using Eq.1.2

$$R_{\rm eff} \propto \sigma_c^2 \times \langle I_{\rm eff}\rangle^{-1}. \tag{1.5}$$

Thus the virial-equilibrium values for the parameters are: $a = 2$, and $b = -1$ (see Djorgovski & Davis 1987 for a complete description). However, it has been

extensively shown in the literature that the measured values of the FP relation differ from the virial scaling (e.g., $a = 1.4$ and $b = -0.85$ from Bender, Burstein & Faber 1992), and therefore the Fundamental Plane is often said to be *tilted* (Prugniel & Simien 1996; Ciotti, Lanzoni & Renzini 1996; Busarello et al. 1997; Scodeggio et al. 1998; Trujillo, Burkert & Bell 2004; Reda, Forbes & Hau 2005; Robertson et al. 2006; Graves 2009; Secco & Bindoni 2009; Allanson et al. 2009; Grillo & Gobat 2010; Humphrey & Buote 2010). Moreover, the Fundamental Plane also has an intrinsic scatter that cannot be explained purely by observational errors (Jorgensen, Franx & Kjaergaard 1996).

A significant amount of effort has been invested to understand what physical processes are responsible for the observed tilt and scatter. A number of studies (e.g. Gregg 1992; Guzman, Lucey & Bower 1993; Jorgensen, Franx & Kjaergaard 1996; Prugniel & Simien 1996; Forbes, Ponman & Brown 1998; Gargiulo et al. 2009; Fraix-Burnet et al. 2010; Magoulas et al. 2012; Springob et al. 2012; Cappellari et al. 2013) indicate that variations in stellar populations are responsible for most of the scatter. The tilt instead has been interpreted as evidence that the mass-to-light ratio ($\Upsilon_{\rm dyn}$) depends on some combination of the three observables (Prugniel & Simien 1996; Trujillo, Burkert & Bell 2004; Ciotti, Lanzoni & Renzini 1996; Trujillo, Burkert & Bell 2004; Graves & Faber 2010). In particular, one could divide the mass-to-light in different terms representing the multiple physical process that could contribute to the tilt. In this way, variation in the $\Upsilon_{\rm dyn}$ can be attributed to: (i) variation in the dynamical structure of the galaxies, (e.g. non-homology: $M_{\rm dyn}/M_{\rm tot} \neq$ constant), (ii) variations in the baryonic to dark matter ratio enclosed in the $R_{\rm eff}$, (iii) variations of the IMF that regulates the way with which the galaxies formed their stars, and/or (iv) variations in the galaxy's stellar population, or combinations thereof.

The combination of two-dimensional photometric and spectroscopic data has allowed astronomers to show that the dynamical mass is a robust tracer of the total mass. For instance, recent work based on strong gravitational lensing (i.e. SLACS, Bolton et al. 2008a) suggests that the quantity $R_{\rm eff}\sigma^2_{\rm eff}$ is linearly proportional to the projected total mass estimated from the gravitational lensing effect, further reinforcing the assumption that $M_{\rm dyn} \propto M_{\rm tot}$ and that galaxies are nearly homologous (see also e.g. Koopmans et al. 2009).

For a given IMF, the stellar mass-to-light ratio ($\Upsilon_\star$) depends on the age and metallicity of the stellar population as well as on wavelength (e.g. Worthey 1994). It is well established by now that correlations exist between velocity dispersion and metallicity at fixed age (e.g. Faber & Jackson 1976; Faber 1977; Dressler et al. 1987; Trager et al. 2000a; Thomas et al. 2005) and between velocity dispersion

and age (e.g. Bernardi et al. 2005). Hence, stellar population models predict that $\Upsilon_\star$ will depend on the total mass and luminosity, plausibly introducing a tilt in the FP, that could depend on the observed wavelength (Pahre, Djorgovski & de Carvalho 1998). However, this dependence is weak and it alone cannot explain the observed tilt in the FP (Bernardi et al. 2003). Of fundamental importance is to note that all these studies have assumed a *universal* Initial Mass Function[1].

The studies above have shown that the stellar population effects and the non-homology assumption are at most weak and the dominant contribution to the FP's tilt has to be due to the systematic variation of $M_\star/M_{\rm tot}$ with galaxy mass, which reflects variations of the relative contribution of stars and dark matter.

In order to fully understand the structure and formation of ETGs in the context of the hierarchical galaxy formation model, we therefore need to investigate and comprehend the strong relationship that exists between baryonic matter, which dominates astrophysical observables, and dark matter, which dominates most of the dynamics during galaxy formation (e.g. Blumenthal et al. 1984).

The Fundamental Plane relation holds for giant, luminous ellipticals. The situation nevertheless, appears less clear for the dwarf ellipticals (dE), whose velocity dispersions are more difficult to measure because of their low surface brightnesses (Bender & Nieto 1990; Peterson & Caldwell 1993). A number of analyses have suggested that dwarf ellipticals do not follow the normal elliptical scaling relations (Nieto et al. 1990; Bender, Burstein & Faber 1992; de Carvalho & Djorgovski 1992; Zaritsky, Gonzalez & Zabludoff 2006b,a). However the situation is rendered ambiguous by the large scatter in the dE measurements and observational bias toward high-surface-brightness galaxies. In particular, Bender, Burstein & Faber (1992) analysed a heterogeneous sample of dynamically hot galaxies (giants ellipticals, ellipticals of intermediate luminosity, bulges of S0 and Sa galaxies, compact ellipticals, bright dwarfs elliptical and dwarfs spheroidals), all of them having spatially-resolved kinematics available at that time. They found that while bright dwarf ellipticals seem to follow the same trend as normal luminous ellipticals and bulges (with a relatively small offset in the relation and more scatter due to the lower quality of data), low-luminosity dwarf spheroidals (only five systems), are substantially offset from the plane, having higher mass-to-light ratios (i.e. being dark matter dominated) and having surface brightness increase with mass. This result challenged the long-standing assumption that the distribution of mass is directly proportional to the distribution of light, so

[1] A compelling numbers of papers have shown in the last few years that the IMF slope (at the low-mass end) might change with the stellar velocity dispersion. In this thesis we have found the same result. We will give evidence supporting this point in the subsequent chapters.

that the Fundamental Plane in mass could be transformed into a plane in light. Bender, Burstein & Faber (1992) explained the different plane of spheroids, later named the "Fundamental Manifold" by Zaritsky, Gonzalez & Zabludoff (2006b), by invoking different formation mechanisms for the different FP-based families. In fact, dry (i.e. gas-poor) and non-dissipative mergers seem a suitable formation channel for the giants and normal ellipticals, as well as for the compact elliptical and bulges. On the other hand, the dwarfs spheroidals must be formed through significant wind-driven gas loss, although tidal effects can be important in removing luminous matter from the galaxy (Yoshii & Arimoto 1987; Chiosi & Carraro 2002; Kourkchi et al. 2012a,b). A similar scenario has also been suggested by (Graham & Guzmán, 2003) who performed HST photometry of dwarf elliptical galaxies in the Coma cluster. Current simulations of dwarf galaxy formation, while predicting substantial winds, nevertheless, suppress star formation much less effectively than is required (Sawala et al. 2010), thus a definitive model for the formation of dwarfs spheroidals still remains elusive today.

Bender, Burstein & Faber (1993) took an additional step forward by extending the previous study linking the distribution of the same sample of dynamically hot galaxies in the FP with the ages and metallicities of their stellar population. Surprisingly, they found that only the central velocity dispersion has a large influence in determining the stellar population, whereas sizes, surface brightness and masses have a remarkably small, although not negligible, contribution. To explain the tight relation they observed between velocity dispersion and stellar population, which holds for all dynamically hot galaxies despite their masses or brightness, the authors suggested a model in which the overall stellar population is determined by a combination of total mass, which sets constraints on the metals that can escape at the moment of the formation, and local density, which determines the basic parameters of star formation (i.e. cooling, collapse, time-scale).

Later, Zaritsky, Gonzalez & Zabludoff (2006b,a) showed that the differences between the fundamental planes, defined by different families of spheroids from dwarf ellipticals to galaxy clusters, is the result of a nonlinear relationship between $\log\sigma$ and $\log(M/L)$. They suggested that galaxies lie on a progression of star formation efficiencies and baryon concentrations within dark matter halos.

Hence, while the existence of the FP for elliptical galaxies provides important clues about the formation of these galaxies, the implications are currently understood only at a qualitative level.

Progress in understanding ETGs therefore requires on the one hand a full characterization of the luminous mass distribution, as well as the stellar kinematics and the stellar population. On the other hand, it is equally necessary to precisely determine the dark-matter density profiles, and to understand how all these structures depend upon properties such as mass and age of the stellar-assembly. In short, we must unambiguously disentangle stellar and dark matter, and hence constrain the normalization and shape of the IMF, in order the precisely determine the value of $\Upsilon_\star$ that turns observed light into stellar mass, breaking the degeneracy that exists between them in most galaxy mass models.

1.3 The Baryonic Content of Nearby ETGs

An important step to draw a comprehensive picture of galaxies formation and evolution is to study the intrinsic mass distribution, the internal structure and the kinematics of the stellar constituents that have formed inside the dark-matter potential. Observations at high redshift are certainly the most direct way to look at galaxies in formation. Unfortunately, despite the great technological and instrumental progress, high-z observations often lack the necessary spectral information to constrain the physical processes in action during luminous structure formation (Faber et al. 2007). High-redshift galaxies are often faint, and only some of their global properties can currently be directly measured. Conversely, nearby galaxies can be studied in far greater detail. Massive, evolved, local systems with relatively faint traces of star-formation contain the fossil record of the structure formation processes dominated by the dark matter (e.g. Springel, Di Matteo & Hernquist 2005a) and therefore provide an alternative view of galaxy formation and evolution that is fully complementary to that given by high-redshift observations.

1.3.1 Stellar Kinematics of Nearby Galaxies

Significant progress on how galaxies forms has been made thanks to the advent of large galaxy surveys. A major contribution has been made by the Sloan Digital Sky Survey (SDSS; York et al. 2000) which firmly established the color bimodality of local galaxies. The "blue cloud" consists of star-forming gas-rich spiral galaxies, while the "red sequence" mostly consists of non-star-forming, evolved ETGs (e.g. Strateva et al. 2001; Faber et al. 2007). The general belief is that red and dead galaxies have formed by "wet mergers" (Toomre & Toomre 1972) of gas-rich blue-cloud galaxies during which one or more mechanisms

suppressed somehow the star formation via ejection of the gas (e.g. supermassive black hole, supernovae winds, gravitational gas heating Springel, Di Matteo & Hernquist 2005a,b; Kereš et al. 2005; Di Matteo, Springel & Hernquist 2005; Faber et al. 2007; Naab et al. 2007; Johansson, Naab & Ostriker 2009). Furthermore, dissipationless "dry mergers" of gas-poor, red galaxies are also required to move galaxies along the red sequence increasing their mass (Khochfar & Burkert 2003; Naab, Khochfar & Burkert 2006; Hopkins et al. 2009; Khochfar & Silk 2009) to match those of very massive local ETGs we observe today.

Observationally, a clear way to probe the need for both dry and wet mergers is to look at the kinematic structure of the remnants in the nearby Universe. The end result of a major merger between blue gas-rich galaxies will produce a stellar system dominated by rotation, since the gas will tend to form a disk (Naab, Jesseit & Burkert 2006) while a major mergers between red gas-poor galaxies will result in a massive red galaxy dominated by random motions because dissipationless processes will dominate in this case (Barnes 1992; Hernquist 1992; Naab, Burkert & Hernquist 1999; Naab & Burkert 2003) The existence of two kinematically different families within the red sequence population found by the SAURON (Bacon et al. 2001; Emsellem et al. 2007) and the ATLAS^{3D} projects (Cappellari et al. 2011) further confirms this result.

Thanks to spatially-resolved kinematics obtained with integral-field spectroscopy in the internal region of 260 galaxies, the ATLAS^{3D} team pointed out that ETGs can be divided in accord to their kinematical structure into two families: slow rotators, which exhibit complex stellar velocity fields and often include kinematically distinct cores, and fast rotators, which have regular velocity fields (Emsellem et al. 2007, 2011). By classifying galaxies by their specific angular momentum, they showed that the vast majority (85%) of ETGs are fast rotators, and include disks and often bars. Only a small fraction (15%) are slow rotators. This family shows very homogeneous characteristics: they appear relatively round on the sky, have triaxial structures, dominate the high-mass end ($M_{\rm dyn} > 10^{11}\,M_{\odot}$), have slightly larger $\Upsilon_{\star}$, and often exhibit central kinematically decoupled cores. These massive slow rotators are thought to have formed differently from the less massive and more common ETGs. They could in fact represent the extreme cases within the red sequence of galaxies that might have suffered from significant dry, metal-poor merging, without being able to rebuild a quickly rotating component within one effective radius. We refer to Cappellari et al. (2013) for a detailed discussion of the main implications of the existence of these two different families of ETGs for galaxy formation scenarios.

This unique set of data has allowed for a huge step forward in the our understanding of ETG formation mechanisms, providing an exquisite view of the stellar kinematics and dynamics in the internal region of ETGs with different masses, physical characteristics and possibly star formation and assembly histories. A complementary way to gain further insights on the star assembly is to characterize the stellar population of this intriguing class of galaxies.

1.3.2 Unresolved Stellar Population Studies of ETGs

A galaxy spectrum encodes an enormous amount of information about its dynamical state, chemical composition and star formation history. Hence, the analysis of the spectral energy distribution (SED) of a galaxy allows us to trace back its formation process, relating the assembly mechanisms to its intrinsic properties – such as mass or size – or to the environment where it was born (i.e. field, group or cluster).

With the exception of very nearby galaxies where individual stars can be resolved and studied, for more distant galaxies one has to infer properties of the stellar population by looking at the integrated light from all of the stars that form the galaxy. The underlying assumption is that a galaxy can be broken down into one (or more) Single Stellar Populations (SSP), representing a generation of coeval stars originally chemically homogeneous. This SSP approach dates back to Beatrice Tinsley who observed that globular and open clusters could be represented by a single coeval stellar population (Tinsley 1968, 1972; Tinsley & Gunn 1976).

Tinsley also developed the evolutionary stellar population synthesis (SPS) approach, using stellar evolution theory to constrain all the phases of stellar evolution for a range of different stellar types at a given age and metallicity. The construction of a stellar population models is conceptually straightforward and based on only three main ingredients: an assumption for the IMF shape, one or more sets of isochrones for various ages and metallicities (Z), and stellar spectra spanning a range of effective temperature ($T_{\rm eff}$), bolometric luminosity ($L_{\rm bol}$), and values for Z. The real situation however is more complicated because of the incompleteness of the isochrone tables, the incomplete set of stellar parameters explored by empirical stellar libraries, or conversely the difficulty of modeling massive stars in theoretical libraries (Kudritzki, Pauldrach & Puls 1987). Moreover, certain evolutionary phases of stellar life have poorly calibrated and not completely understood physics (see Conroy 2013 for a complete review on

the SPS technique and an extensive discussion on what can be reliably measured from galaxy SEDs).

When stars are not resolved, one may use photometric or spectroscopic observations of integrated magnitudes, colors and spectra to investigate the stellar population. The photometric method consists of measuring broadband colors (optical or infrared) and comparing them with the colors of model populations, while the spectroscopic method relies on the measurement of absorption (or emission) line-strengths representing relevant spectral features or on the fitting of a whole spectrum. In the following we will mainly refer to the latter and in particular to absorption-line-index measurements, which is the main technique used in this thesis.

The monochromatic integrated flux from an SSP is the sum of the fluxes of all the individual stars along the line of sight,

$$F_\lambda(t, Z) = \int_{m_l}^{m_h(t)} F_\lambda(t, Z, m)\, \phi(m)\, dm, \tag{1.6}$$

where $F_\lambda(t, Z, m)$ is the flux emitted by a star of mass m, metallicity Z and age t at a given wavelength λ, $\phi(m)$ is the IMF[2], while m_l and m_h are the lower and upper limit to the mass of the stars respectively. The choice of the value of m_l, as long as it is sufficiently small, should not affect significantly the value of $F_\lambda(t, Z)$, however it is critical to determine $\Upsilon_\star$ (see Chapter 6). The value of $m_h(t)$ indicates the mass of the most massive star still alive at time t and therefore is a strong function of the age of the stellar population.

The idea behind the line-strength technique is to measure individual absorption features that are sensitive to one or more parameters of the underlying integrated stellar population (e.g. age, metallicity, abundance ratios, IMF slope). These measurements are performed on a small part of a spectrum where a narrow-band filter of a few Å wide is centered on a particular absorption line. For a narrow feature labelled as i, the index, expressed in Å, is usually defined as

$$I_{i,\text{Å}} = \int_{\lambda_1}^{\lambda_2} \left(1 - \frac{F_{I,\lambda}}{F_{C,\lambda}}\right) d\lambda, \tag{1.7}$$

where $F_{I,\lambda}$ is the measured flux over the feature in the wavelength range from λ_1 to λ_2, whereas $F_{C,\lambda}$ represents the straight line connecting the mid-points of the side-band pseudo-continuum fluxes (e.g. Worthey 1994). For a broad molecular

[2]Until few years ago the IMF was mostly assumed to be universal and equal to the one of our Milky Way.

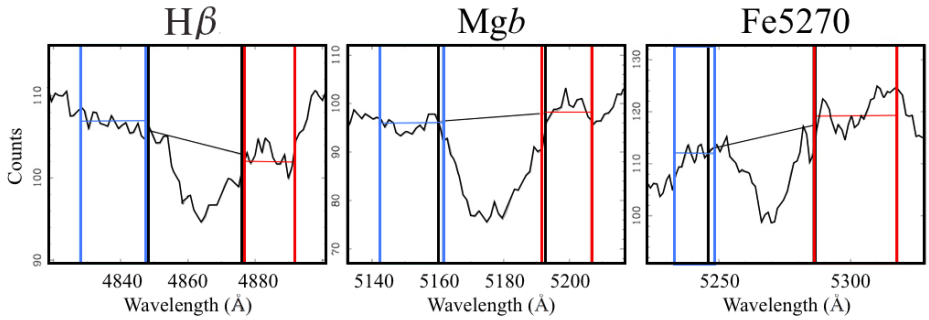

Figure 1.1: Example of line-index measurement in a galaxy spectra broadened to a final resolution of $\sigma = 300\,\mathrm{km\,s^{-1}}$. The three panels represent three classical Lick indices: Hβ, the most used age indicator in the optical and Mgb and Fe5270, often used to constrain metallicity. The black box and line represent the bandpass where the index is measured, red and blue boxes show the continuum side-band of the features. The figure has been realized with the code SPINDEX2 (Trager, Faber & Dressler 2008)

band, the index, measured in magnitude, is defined as

$$I_{i,\mathrm{mag}} = -2.5\log\left[\left(\frac{1}{\lambda_2-\lambda_1}\right)\int_{\lambda_1}^{\lambda_2}\frac{F_{I,\lambda}}{F_{C,\lambda}}d\lambda\right]. \tag{1.8}$$

Figure 1.1 shows an example of line-index measurement from a galaxy spectrum convolved to a final resolution of $300\mathrm{km\,s^{-1}}$.

In the 1980's a standard system of absorption indices, the Lick/IDS system (Burstein et al. 1984; Worthey 1994; Trager et al. 1998), was established. It defined a series of filters (indices) with their red and blue wavelength continuum intervals that are today still the standard indices to study the age and metallicity of the integrated stellar population in nearby galaxies. In fact, since Tinsley's work, it was soon understood that one could break the age-metallicity degeneracy[3] with proper choices of the indices and their continuum band-passes. Many of the indices such Mgb are sensitive to the metal content in cool stars, like RGB and AGB, and suffer comparably minor changes due to age. Others, such as the indices defined by the Balmer hydrogen lines (Hα, Hβ, Hδ), are mostly sensitive

[3]Galaxy colors become redder as the galaxy becomes older, because more stars move to the giant branch, and/or they becomes redder because of increasing metallicities, since the effective temperatures of most stars decrease because of the increase of opacity in the stellar photosphere. Worthey (1994) estimated that a factor of 3 increase in metallicity corresponds to a factor of 2 in age when using optical colors as age indicators.

to the temperature of Main-Sequence turn-off stars, hence to the age of the stellar population, and are largely unaffected by chemical abundances.

Over the last two decades a number a number of models and libraries of population synthesis models were (and are still being) developed (Bruzual & Charlot 1993; Worthey 1994; Bruzual & Charlot 2003; Maraston 2005; Schiavon 2007; Vazdekis et al. 2010; Conroy & van Dokkum 2012a). These models, in combination with the observed indices, allowed the measurement of age and metallicity of many galaxies in the local Universe (e.g. Trager et al. 2000a; Schiavon 2007; Graves et al. 2007; Tortora et al. 2010). However, thanks to the great improvements in the observations, mainly due to the exquisite quality of the Hubble Space Telescope (HST) data, stellar population modelling still lags behind observations when it comes to the interpretation of observations of galaxies at high redshifts.

A better handle on the uncertainties and the underlying assumptions of the models, as well as better calibrated data over a wider wavelength range (from the FUV to the FIR) will be required in the future to fully gain all the information that we, in principle, are able to extract from the analysis of galaxy SEDs. For instance, a very important assumption often hidden under the carpet in most stellar population models concerns the Initial Mass Function. In the early days of stellar population studies, it has been clear that the evolution in $\Upsilon_\star$ for a passively evolving stellar population is highly sensitive to and degenerate with the logarithmic slope of the IMF at the main sequence turn-off point (Tinsley 1980). Most of the integrated light of a galaxy comes from stars in a narrow mass interval around the turn-off (for a stellar population older than 3Gyr, $\sim 44\%$ of the light comes from the stars at the main-sequence turn-off, and about $\sim 53\%$from the RGB, see Worthey 1994; Trager et al. 2000a); conversely, a large fraction of the stellar mass comes in the form of low-mass stars. This implies that stellar masses derived from the fit of galaxy spectral lines or colors can have large systematic uncertainties, as a result of the assumed IMF.

1.3.3 The Initial Mass Function

The mass and chemical composition of a star are the dominant properties that determine its subsequent evolutionary path. The Initial Mass Function, the functional form that describes the probability distribution function of a population of stars at $t = 0$, therefore has critical implications in galaxy formation and evolution, setting the overall stellar mass-scale of galactic systems, controlling

the intensity of the stellar feedback processes and driving the chemical enrichment abundance patterns.

In his famous 1955 paper, Salpeter modelled the IMF with a single power-law of the form:

$$\Phi(\log M) = \frac{dN}{d\log M} \propto M^{-\Gamma} \tag{1.9}$$

where M is the mass of a single star and dN indicates the number of stars in the logarithmic mass range $\log M + d\log M$. If we can integrate this function and derive a proper normalization, we can calculate the number of stars within a logarithmic mass interval. Salpeter obtained his *canonical* integrated IMF for main-sequence stars in the solar neighbourhood in the form of a single power-law with $\Gamma = 1.35$ in the mass range $1 - 100\,M_{\odot}$. In this thesis, following his notation, we express the mass spectrum as:

$$\frac{dN}{dM} \propto M^{-x} \tag{1.10}$$

where $x = \Gamma + 1 = 2.35$. Successive authors extended the work below one solar mass suggesting that the IMF slope measured in the solar neighbourhood may deviate from the Salpeter and flatten at lower masses (i.e. Kroupa 2001; Chabrier 2003).

As pointed out in a recent review by Bastian, Covey & Meyer (2010), there is no compelling evidence for variation in the IMF for stars with masses $M > 1 - 2\,M_{\odot}$. Together with the fact that it is extremely difficult to measure the IMF normalization in extragalactic systems, this is the main reason why historically the stellar IMF has been assumed to be universal and equal to that measured in the solar neighbourhood in most research focussing on unresolved stellar population as well as on stellar dynamics.

However, over the last few years several works have suggested that the IMF might vary (Davé 2008; van Dokkum 2008) or depend on the stellar mass of the system (e.g. Treu et al. 2010; Graves & Faber 2010; Conroy & van Dokkum 2012a; Cappellari et al. 2012), as already indicated from early studies by Worthey (1992) and Trager et al. (2000b). In particular, in this thesis we show that more massive galaxies very likely have a large population of low-mass stars with $M < 0.2$–$0.3\,M_{\odot}$ (Chapter 4 and 5, Spiniello et al. 2012, 2013). Similar results have also been found in other published works, using different and independent techniques (van Dokkum & Conroy 2010; Auger et al. 2010a; Cappellari et al. 2012; La Barbera et al. 2013; Tortora, Romanowsky & Napolitano 2013).

According to Worthey (1994), between 60 and 80% of the stellar mass density

in the Universe is in the form of stars with masses $M < 0.5\,M_{\odot}$. These stars are very faint and give only a minimal contribution to the integrated light of an old population (for a single population of 13.5 Gyr, only few percent in the optical, see e.g. Conroy & van Dokkum 2012a). Obtaining a direct spectroscopic inference on the low-mass end of the IMF slope is therefore a challenging task. In this thesis we present one of the first successful efforts to directly probe the low-mass end of the IMF normalization and to investigate possible variation of its slope with galaxy properties such as stellar velocity dispersion or stellar mass. This result was made possible thanks to the combination of stellar population synthesis modeling, using spectra e.g. from SDSS and VLT X-Shooter, with stellar dynamics and gravitatonal lensing.

1.4 Strong gravitational lensing

One of the predictions of Einstein's Theory of General Relativity is the deflection of light rays in gravitational fields. Gravitational lensing studies this effect on the appearance of cosmic objects on different spatial scales. The strength of gravitational lensing is that the deflection of electromagnetic radiation is independent of the type of matter causing the gravitational field (i.e. both baryonic and non-baryonic) and hence it provides a powerful technique to detect dark matter even in the absence of baryons (e.g. Maoz & Rix 1993; Schneider 2006).

A full description of the gravitational lensing formalism goes beyond the scope of this thesis and we refer the reader to many excellent reviews on this topic (see Blandford & Narayan 1992; Schneider, Ehlers & Falco 1992; Narayan & Bartelmann 1996; Wambsganss 1998; Van Waerbeke & Mellier 2003; Kuijken 2003; Zakharov 2006; Kochanek 2006; Schneider 2006 for example).

Depending on the mass of the lens (i.e. deflector) and on the way gravitational lensing is manifested, we can divide the gravitational lensing into three main classes: (i) Strong lensing occurs when the lens is relatively massive (e.g. massive ETGs, clusters of galaxies). In this case the distortions are easily visible in the form of arcs or rings. In this lensing regime, nearby space-time is so warped that light can travel along multiple paths to the observer, producing multiple images of the background source. If a distant source is exactly aligned with a axisymmetric lens, the light can travel around any side of it, appearing as an complete ring (a so-called "Einstein ring"). The radius of the ring (the Einstein radius, $R_{\rm Ein}$) is proportional to the square root of the projected mass inside it. If the background source is sufficiently offset, or the lens has a complex shape, the source can still

appear in multiple locations, viewed from slightly different angles and brighter (magnified) or fainter (demagnified) than in reality, depending on the focussing of the light path. (ii) Weak lensing occurs when the distortions of background sources are much smaller and can only be detected statistically. The orientation and shapes of a very large numbers of distant galaxies can be averaged in any field to measure the shear. This, in turn, can be used to reconstruct the mass distribution in the area. Weak lensing effects can be used to study the cosmic microwave background, large scale structure, the structure of galaxies and clusters, and they provide a way to constrain the cosmological parameters and test the ΛCDM model (Schneider 2006). (iii) Microlensing occurs when no distortion in shape can be seen but the integrated light of all lensed images received from a background object changes in time. This type of lensing is generally associated with stars in the Milky Way as well as stars in distant galaxies (e.g. strong lenses).

In this thesis we use strong gravitational lensing to infer the total (luminous plus dark) mass of galaxies. Strong gravitational lensing is by far the most accurate (i.e. few percent precision, Kochanek 1991) mass-measurement technique available for the central regions of ETGs, providing a one-shot, purely gravity-dependent measurement of the total (L+D) projected mass enclosed by the lensed images (Maoz & Rix 1993; Rusin & Ma 2001; Koopmans & Treu 2002; Treu & Koopmans 2004; Rusin & Kochanek 2005; Dye & Warren 2005; Brewer & Lewis 2006, 2008). However, strong lensing does not allow us to unambiguously separate luminous from dark matter unless it is complemented with additional information about the stellar content. For instance, when gravitational lensing and stellar dynamics are applied in a self-consistent combined way (Barnabè & Koopmans 2007), they are particularly effective in the analysis of the internal structure of distant early-type galaxies (up to $z \sim 1$). In fact, they allow the robust determination of the mass profile of the lens galaxy (Koopmans & Treu 2002, 2003; Treu & Koopmans 2002, 2003, 2004; Jiang & Kochanek 2007; Barnabè & Koopmans 2007; Czoske et al. 2008; Barnabè et al. 2009a; Koopmans et al. 2009; Grillo et al. 2009; Treu 2010; Barnabè et al. 2011; Czoske et al. 2012), and the measurement of the fraction of dark matter enclosed within a certain aperture. When stellar population analysis is added, one can then unambiguously disentangle luminous from dark matter and completely characterize the internal structure and mass distribution of ETGs *beyond the local Universe*. When combined with a precise measurement of the galaxy's luminosity, gravitational lensing provides a measurement of the value of $\Upsilon_\star$, a strong function of the IMF slope, allowing the latter to be constrained (see Chapters 3, 4, 5 and 6 of this

thesis, published as Spiniello et al. 2011, 2012, 2013; Barnabè, Spiniello et al. 2013).

1.5 This Thesis

The shape of the low-mass end of the stellar initial mass function (IMF) in early-type galaxies (ETGs) and the internal distribution of their dark and luminous mass are still open issues in modern astrophysics, each of great importance to our understanding of galaxy formation. In the last few years, increasing evidence has emerged in favour of a non universal IMF that varies with galaxy mass (e.g. van Dokkum & Conroy 2010; Smith, Lucey & Carter 2012; Cappellari et al. 2012). In addition, strong gravitational lensing and dynamical models have shown that the internal fraction of dark matter in ETGs increases monotonically with the mass of the system (e.g. Zaritsky, Gonzalez & Zabludoff 2006b; Barnabè et al. 2009a; Auger et al. 2010a; Barnabè et al. 2011).

The conclusion of those studies is that the IMF (hence the stellar mass-to-light ratio) and the internal fraction of dark matter cannot both be universal, but it is very hard to break the degeneracy between the two effects. This motivated us to start a new survey: the X-Shooter Lens Survey (XLENS). With X-Shooter[4] long-slit spectra of massive ($\sigma_\star > 250\,\mathrm{km\,s^{-1}}$) lens galaxies selected from the Sloan Lens ACS Survey survey (SLACS, Bolton et al. 2006), and HST data already in hand, we set out to achieve the goal of constraining the shape and normalization of the low-mass end of the IMF through a joint lensing+dynamics+stellar population (SP) analysis. In addition, Barnabè et al. (2012, expanding the approach already presented in Barnabè & Koopmans 2007) have developed a fully self-consistent modelling of the stellar and dark matter component in lens galaxies that allows stellar masses to be measured directly from only lensing and dynamics without any assumption on the IMF. Having two independent constraints on the stellar mass, one from the fully self-consistent joint lensing+dynamics (L&D) analysis and the other from spectroscopy and SSP modelling, allows us to unambiguously disentangle IMF slope variations from variations in the dark-matter fraction and, for the first time, to infer its lower cutoff mass[5] (see Chapter 6). To make these two independent IMF measurements, we make use of the state-of-the-art joint lensing

[4]X-Shooter is a powerful, 3-armed, medium-resolution spectrograph on the VLT (D'Odorico et al. 2006; Vernet et al. 2011) with a broad wavelength coverage from the UV to the NIR (3000–25000 Å)

[5]The the lower cutoff mass represents a mass below which stars do not significantly change the stellar $\Upsilon_\star$

and kinematic code (Barnabè et al. 2012) and new SSP models (Conroy & van Dokkum 2012a)[6], the latter having been constructed specifically for the purpose of measuring the IMF slope down to $0.1\,M_{\odot}$ for old, metal-rich stellar populations.

The ultimate goal of the XLENS Survey, presented in this thesis, is the detailed study of the distribution of luminous and dark matter in the internal region of massive ETGs with redshift between $0.1 < z < 1$ that lie beyond the knee of the luminosity function (i.e. $\sigma_{ETG} > 250\,\mathrm{km\,s^{-1}}$) to gain a better understanding of the role that these massive systems play in the ΛCDM cosmological framework.

1.5.1 Outline of the thesis

Chapter 2, (Spiniello et al., in prep.), presents an overview of the Survey: we highlight the XLENS science goals and present the current sample, focusing on data selection, reduction and analysis. We also present spatially resolved kinematics up to $\sim 1 R_{\rm eff}$ of ten massive ETG lenses.

In Chapter 3, based on Spiniello et al. (2011), we present an XLENS pilot program. We demonstrate the robustness and validity of the scientific approach with an analysis of the extremely massive early-type galaxy SDSS J1148+1930 at redshift $z = 0.444$. We combine the extended kinematic profile of the lens with strong gravitational lensing and multi-color information derived from Sloan Digital Sky Survey (SDSS) images. The X-shooter spectra (3/10 of the requested OBs were done as GTO target, but due to bad weather the program could not be completed) did not reach the required signal-to-noise (S/N) for line-indices based stellar population studies.

The first index-based results are presented in Chapters 4 and 5 (Spiniello et al. 2012, 2013). In these chapters, we focus on constraining the low-mass end of the stellar IMF by comparing galaxy spectra with single stellar population models. In Chapter 4, we complement the X-Shooter spectrum of a very massive lens ETG with spectra of SDSS luminous red galaxies to build a statistically relevant sample of ETGs with different velocity dispersion in order to search for possible correlations between the IMF slope and the mass or the velocity dispersion of the galaxies. In Chapter 5, we present a new set of IMF-sensitive features in the optical. These new indicators, bluer than previously used ones, are particularly useful given the uncertainties of SSP models in the NIR and the difficulty of obtaining high S/N spectra of galaxies at redder wavelengths.

[6] We motivate the use of these models over others in Chapter 7

In Chapter 6, published as Barnabè, Spiniello et al. (2013), we obtain the stellar masses of the most and the least massive ETG of the current XLENS sample (SDSS J0936+0913 with $\sigma_\star \simeq 250\,\mathrm{km\,s^{-1}}$ and SDSS J0912+0029 with $\sigma_\star \simeq 330\,\mathrm{km\,s^{-1}}$) from spectroscopy and SSP modelling. We then obtain a second independent measure of the stellar masses for the same systems using the joint lensing and kinematic code of Barnabè et al. (2012), which allows stellar masses to be measured from only lensing and dynamics without any assumption on the IMF or knowledge of the stellar population. Comparing these two independent constraints on the stellar mass allows us to measure the IMF slope and, for the first time, to set a lower-mass limit (or turn-over) to the stellar IMF obtained from spectroscopy. The fact that both methods agree on the inferred mass for the IMF slope inferred from SSP modeling is a strong confirmation of the robustness of the method and a solid test of the absence of major hidden systematics.

In Chapter 7, we present a direct comparison between two published state-of-the-art of single stellar population models (Conroy & van Dokkum 2012a and Vazdekis et al. 2012) built with the purpose of studying the stellar populations of old, passive systems. We show that the variation of the IMF slope is a robust, model-independent result. Nevertheless, we highlight that these two SSP models sometimes give different predictions (expecially for some indicators, i.e. sodium), and thus a careful study of the single element abundance pattern is important to constrain the IMF accurately (Spiniello et al., in prep.). It is likely that massive ellipticals have a non-solar abundance pattern since they have undergone a different star formation history than the Solar neighbourhood and have already been shown to be overabundant in α-elements relative to the Sun (Peterson 1976; Peletier 1989; Worthey 1992).

Finally, in Chapter 8, we summarize our most significant results, we draw the conclusions and we outline few possible future projects based on the research carried out in this thesis.

2 XLENS: The X-Shooter Lens Survey

In research, great difficulties are felt at first and these cannot
be overcome except by starting from experiments ...
and then by conceiving certain hypotheses ...
But even so, very much hard work remains to be done and
one needs not only great perspicacity but often a degree of good fortune.

Christiaan Huygens

Based on:
C. Spiniello, L.V.E. Koopmans, S.C. Trager, in prep.

The goal of the X-Shooter Lens Survey (XLENS) is to disentangle the stellar and dark-matter content of massive early-type galaxies (ETGs), through combined strong gravitational lensing, dynamical and *spectroscopic* stellar population studies. We aim at the same time to constrain the normalization, shape and cutoff-mass ($M_{\rm low}$) of the low-mass end of the stellar initial mass function (IMF) in ETGs.

With multi-band, high-quality HST images in hand, we have obtained spectra of a sample of lens ETGs mainly from the Sloan Lens ACS Survey (SLACS, Bolton et al. 2006) with X-Shooter, the powerful broad-band (3000–25000 Å), 3-armed, medium-resolution spectrograph on the VLT (D'Odorico et al. 2006; Vernet et al. 2011). By combining lensing and dynamical results, we are able to obtain more precise dark-matter mass fractions ($f_{\rm DM}$) than ever before, in order to ultimately correlate these with ETG masses and investigate the relation between baryonic and non baryonic matter during the mass-assembly and structure formation processes. With XLENS we are also able to study the stellar content of the systems in great detail from high signal-to-noise (S/N) spectra and simple stellar population modelling. We can constrain precise mass-to-light ratios ($\Upsilon_\star$), placing constraints on the low-mass end of the IMF and, for the first time, infer the value of the lower-mass turnover of the IMF directly from galaxy spectra in combination with gravitational lensing and stellar dynamics.

In this chapter we provide an overview of the survey, highlighting its scientific motivations, main goals and techniques. We present the current sample, briefly describing the data reduction and analysis process, and we present the first results on spatially resolved kinematics.

2.1 Introduction

Understanding the evolution and the internal structure of massive early-type galaxies (ETG), as well as their stellar and dark-matter distributions, is crucial to fully comprehend the processes in hierarchical galaxy formation (e.g. White & Rees 1978; Davis et al. 1985; Frenk et al. 1985).

Hierarchical structure formation models predict that massive galaxies form through mergers of lower-mass galaxies (Blumenthal et al. 1984). This naturally implies that more massive systems should form later in time than less massive galaxies. However, stellar population studies show that massive ETGs have evolved, old stellar populations (see Renzini 2006 and Conroy 2013 for recent reviews). In addition, analysis of the evolution of the stellar mass and luminosity

functions have found that high-stellar-mass, passive galaxies show relatively little evolution in their co-moving space density since $z \sim 1$ (Cimatti et al. 2004; McCarthy et al. 2004; Glazebrook et al. 2004; Daddi et al. 2005; Saracco et al. 2005; Pérez-González et al. 2008; Marchesini et al. 2009; Ferreras et al. 2009).

To reconcile these apparently paradoxical results, the prevailing idea is that ETGs formed the bulk of their stars early in the evolution of the Universe (cluster ETGs $z > 3$, field ETGs at $z > 1.5 - 2$, Thomas et al. 2005; Renzini 2006; Cimatti et al. 2008) and then only at lower redshift (e.g., $z < 1$) may have merged together to build the massive ETGs that we see today in the nearby Universe. Moreover, a further complication to this situation is represented by AGN feedback: this astrophysical process is often proposed in galaxy formation recipes to explain the lack of very massive blue galaxies (i.e. the cutoff in the luminosity function, Bower et al. 2006), blowing out part of their baryonic reservoir (e.g. Hopkins et al. 2006).

In the last two decades, enormous effort has been expended to unravel some of these issues and paint a more robust physical picture by studying the relative contributions of baryonic, dark-matter and black hole constituents of ETGs through stellar dynamical tracers, X-ray studies, and gravitational lensing (e.g. Fabbiano 1989; Mould et al. 1990; Saglia, Bertin & Stiavelli 1992; Bertin et al. 1994; Franx, van Gorkom & de Zeeuw 1994; Carollo et al. 1995; Arnaboldi et al. 1996; Rix et al. 1997; Matsushita et al. 1998; Loewenstein & White 1999; Gerhard et al. 2001; Seljak 2002; Borriello, Salucci & Danese 2003; Romanowsky et al. 2003; Cappellari & Emsellem 2004; Treu & Koopmans 2004; Treu et al. 2006; Cappellari et al. 2006; Thomas et al. 2007; Czoske et al. 2008; Auger et al. 2010a,b; Coccato et al. 2010; Das et al. 2010, 2011; Treu 2010). In fact, a variety of recent observations suggest that baryonic luminous matter, which dominates astrophysical observables, and dark-matter, which dominates most of the dynamics during galaxy formation, are strongly linked. As a consequence, progress in understanding ETGs and more generally the theory of galaxy formation and evolution requires the precise measurement of their stellar and dark-matter density profiles, together with a detailed understanding of how these quantities depend upon properties such as mass and age of the stellar assembly.

The picture emerging from studies of the inner regions of massive ETGs ($\geq 200\,\mathrm{km\,s^{-1}}$), where baryonic and dark-matter are both present, is that to first order the total mass density profile inside several effective radii ($R_{\rm eff}$) can be well-described by a power-law form close to an isothermal profile with $\gamma \approx 2$ for $\rho_{\rm tot} = r^{-\gamma'}$, although with a $\sim 10\%$ intrinsic scatter in the density profile (e.g.

Gerhard et al. 2001; Treu & Koopmans 2004; Koopmans et al. 2006, 2009; Coccato et al. 2009; Auger et al. 2010a; Barnabè et al. 2009b, 2011; Napolitano et al. 2011). The dark-matter density profile in the same region, however, is far less well constrained although it seems consistent with a density slope $1.0 < \gamma_{\rm DM} < 1.7$ (e.g. Treu & Koopmans 2004; Dye & Warren 2005; Grillo 2012; Sonnenfeld et al. 2012).

In addition, while the innermost regions of early-type galaxies are expected to be dominated by the stellar mass component, the dark-matter mass component is usually found to play a non-negligible role, with mass fractions ranging from 10 to 40 percent of the total mass within one effective radius (e.g. Gerhard et al. 2001; Cappellari et al. 2006; Gavazzi et al. 2007; Weijmans et al. 2008). Even more recently, observations, as well as theoretical studies based on stellar population and dynamical models (e.g. Bullock et al. 2001; Padmanabhan et al. 2004), indicate that, *for a constant IMF*, the dark-matter fraction ($f_{\rm DM}$) in the internal region increases monotonically with the mass of the galaxy (e.g. Zaritsky, Gonzalez & Zabludoff 2006b; Auger et al. 2010b), a trend that is more conspicuous in the case of slow-rotator ellipticals (Tortora et al. 2009). On the other hand, it has also been shown that the luminous stellar mass-to-light ratio ($\Upsilon_\star$) scales with the luminous mass of the system (Davis et al. 1985; Bardeen et al. 1986; Bell & de Jong 2001; Girardi et al. 2002; Napolitano et al. 2005; Grillo et al. 2009; Auger et al. 2010a). The only way to unambiguously disentangle the contributions of stellar and dark-matter inside the effective radius ($R_{\rm eff}$) is to have a precise measurement of the total mass and then determine independently the value of $\Upsilon_\star$ via stellar population studies.

A severe observational issue is that information from stellar kinematics is often limited to the central regions (a few $R_{\rm eff}$) because of the lack of bright kinematic tracers at large radii. Alternative tracers of stellar kinematics have to be used to recover the line-of-sight velocities and velocity dispersions in the outskirts of galaxies. An example is planetary nebulae (PNe), whose strong emission from the [O III] 5007 Å line makes them easy to identify even out to very large radii (up to $\sim 10\ R_{\rm eff}$) and at very low surface brightnesses, and makes it easy to measure their radial velocities from the Doppler shift in the line (Douglas et al. 1997, 2002)[1].

[1] See, e.g., results from the Planetary Nebula Spectrograph (PN.S project, Douglas et al. 1997, 2002), a special-purpose instrument at the William Herschel Telescope (WHT) of the Isaac Newton Group in La Palma, designed to carry out identification and kinematic measurement of PNe in a single efficient step (Romanowsky et al. 2003; Douglas et al. 2007; Coccato et al. 2009; Napolitano et al. 2009, 2011).

Moreover the total mass determination from dynamics suffers from the well-known degeneracy between the mass density profile of the galaxy and the anisotropy of its stellar velocity dispersion tensor (mass-anisotropy degeneracy, Binney & Mamon 1982). Higher-order velocity moments, which potentially allow one to disentangle this degeneracy by providing additional constraints (Gerhard 1993; van der Marel & Franx 1993), can generally only be measured with sufficient accuracy in the inner parts of nearby galaxies with current instruments.

A new technique to to obtain sufficient signal-to-noise in the outskirts of the galaxies (up to 4–5$R_{\rm eff}$) consists of using the integral field spectrograph as a "photon collector", by co-adding the individual spectra of each lenslet into one single spectrum. In this way it is possible to measure the stellar velocity profiles up to the fourth Gauss-Hermite moment, which allows one to break the mass-anisotropy degeneracy when constructing dynamical models of the galaxies (see, e.g. Weijmans et al. 2009).

Valuable additional information on distant ETGs, can be provided by gravitational lensing. Strong gravitational lensing is by far the most accurate (i.e. few percent precision, Kochanek 1991) mass-measurement technique available for the central regions of ETGs, providing a one-shot, purely gravity-dependent measurement of the mass enclosed by the lensed images (Maoz & Rix 1993; Rusin & Ma 2001; Koopmans & Treu 2002; Treu & Koopmans 2004; Rusin & Kochanek 2005; Dye & Warren 2005; Brewer & Lewis 2006, 2008). However, the mass-sheet (Falco, Gorenstein & Shapiro 1985) and the related mass-profile (Wucknitz 2002) degeneracies do not always allow one to accurately determine the slope of the galaxy density profile and to unambiguously disentangle the luminous and dark-matter components.

Gravitational lensing becomes more powerful in combination with stellar dynamics. These two complementary approaches are particularly effective to break many of these degeneracies, when they are applied in combination in the analysis of the internal structure of distant early-type galaxies (up to $z \sim 1$). They allow, when combined self-consistently, the robust determination of the mass profile of the lens galaxy (Koopmans & Treu 2002, 2003; Treu & Koopmans 2002, 2003, 2004; Jiang & Kochanek 2007; Barnabè & Koopmans 2007; Czoske et al. 2008; Barnabè et al. 2009a; Koopmans et al. 2009; Grillo et al. 2009; Treu 2010; Barnabè et al. 2011).

However, it remains difficult to separate the stellar and dark-matter components, mostly due to a still relatively poor understanding of the precise shape of the stellar IMF and its associated $\Upsilon_\star$. Uncertainties related to the latter can easily lead to a factor of a few uncertainty in the inferred stellar mass.

Understanding the shape of the stellar IMF is an important open issue with a broad range of astrophysical implications. Although it is commonly assumed that the IMF is universal and independent of cosmic time (e.g., Kroupa 2001; Chabrier 2003; Bastian, Covey & Meyer 2010), several authors have suggested during the last years that the IMF might evolve (Davé 2008; van Dokkum 2008) or depend on the stellar mass of the system (e.g. Worthey 1992; Trager et al. 2000b; Treu et al. 2010; Graves, Faber & Schiavon 2009; Graves & Faber 2010; Auger et al. 2010b; Napolitano, Romanowsky & Tortora 2010).

Recently, van Dokkum & Conroy (2010), hereafter vDC10, suggested that low-mass stars ($M < 0.3\,M_{\odot}$) could be far more dominant in massive ETGs than previously thought. These results, based on single stellar population (SSP) modelling of galaxy spectra, indicate that stars that contribute little to the spectral light in the central region of ETGs increase more rapidly in number than high-mass stars with galaxy mass (van Dokkum & Conroy 2010; Spiniello et al. 2011, 2012; Cappellari et al. 2012; Tortora, Romanowsky & Napolitano 2013; Ferreras et al. 2013; La Barbera et al. 2013). This could imply that part of the increase in the value of $\Upsilon_{\star}$ of galaxies with galaxy mass can be due to a changing stellar IMF rather than only an increasing dark-matter fraction, consistent with the suggestions by Treu (2010) and Auger et al.(2010b, Fig. 2.1).

Indeed, lensing and dynamics studies suggest that the value of $\Upsilon_{\star}$ of massive ETGs increases monotonically with the velocity dispersion of the galaxy, under the assumption of standard Navarro-Frenk-White (NFW, Navarro, Frenk & White 1996) dark-matter profiles (e.g. Auger et al. 2010a; Treu et al. 2010). A varying low-mass end of the stellar IMF could however be partially responsible for this change in the value of $\Upsilon_{\star}$ rather than a varying dark-matter mass fraction. Consequently the shape of the IMF and the internal fraction of dark-matter inside massive ETGs cannot be both universal, but it is very hard to break the degeneracy between these two effects.

The X-Shooter Lens Survey (XLENS, Spiniello et al. 2011, 2012) aims to take these analyses one step further. Within the XLENS project, we are able to disentangle the stellar and dark-matter content of galaxies and, for the first time, directly constrain the normalization, shape and turn-over mass ($M_{\rm low}$) of the low-mass end of the IMF, through combined strong gravitational lensing, dynamical and spectroscopic stellar population studies, and correlate these results with other galaxy properties (e.g., Chapters 3-6, Spiniello et al. 2011, 2012, 2013; Barnabè, Spiniello et al. 2013).

Our methodology consists of combining spatially resolved kinematics with high-precision strong-gravitational-lensing measurements of the total mass and

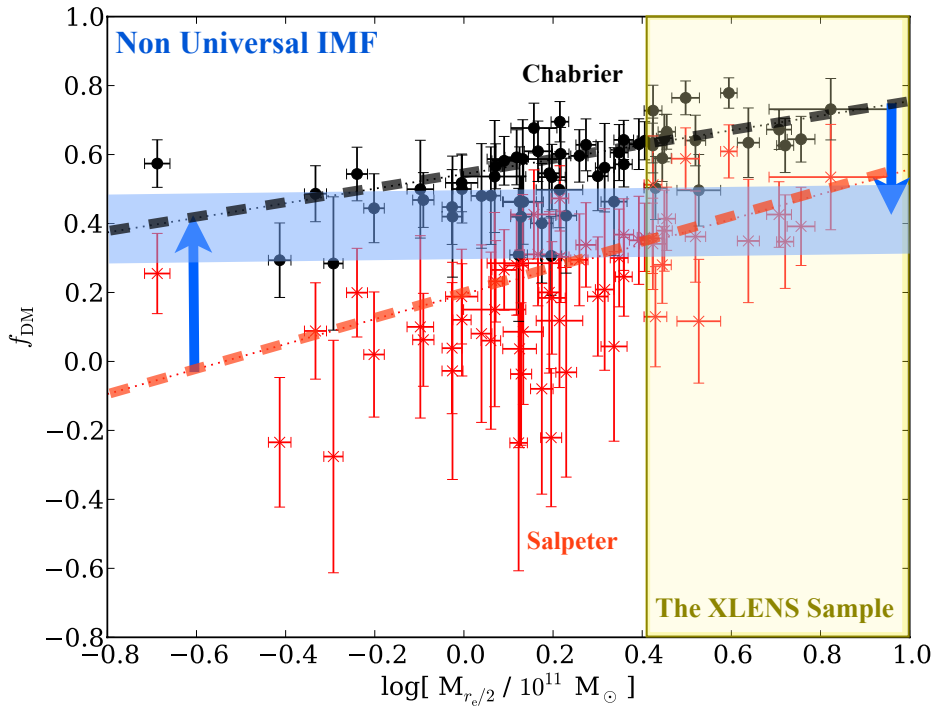

Figure 2.1: Relation between the projected dark-matter fraction within half the effective radius and the mass enclosed within the same radius (based on Auger et al. 2010b). Red points are for an assumed Salpeter IMF and black points are for a Chabrier IMF. The blue band and arrows pictorially show that a non-universal IMF, which steepens from Chabrier to Salpeter, with increasing galaxy mass (as suggested in Spiniello et al. 2012, 2013), flattens the internal dark-matter fraction with increasing galaxy mass. The yellow box roughly indicates the mass range targeted by the XLENS Survey.

mass profile near the lens Einstein radius ($R_{\rm Ein}$), to obtain precise internal dark-matter fractions inside one effective radius and to search for possible correlations between these quantities and e.g. galaxy mass or stellar velocity dispersion. The lensing and dynamics constraints on the galaxy mass distribution are complementary and, when combined self-consistently, have proven to be a powerful method to robustly determine the mass profile of the lens galaxy (Barnabè & Koopmans 2007; Barnabè et al. 2011). If stellar population analysis is added, an independent measurement of the stellar mass can be obtained, and

therefore it is possible to disentangle the contributions of stellar and dark-matter to the mass in the inner regions of ETGs.

In this chapter we give an overview of the on-going survey, focusing on the data reduction and analysis process. In Section 2.2, we introduce the XLENS Survey, highlighting its main purposes and characteristics and we present its sample selection criteria. In Section 2.3, we focus on the observations and data reduction process. In Section 2.4 we present the spatially resolved kinematics up to $\sim 1\ R_{\rm eff}$ obtained from VLT X-shooter spectra of 10 ETGs with $\sigma_\star \geq 250\,{\rm km\,s^{-1}}$. We summarize our findings and present our preliminary conclusions in Section 2.5.

We assume $H_0 = 70\,{\rm km\,s^{-1}\,Mpc^{-1}}$, $\Omega_{\rm m} = 0.3$ and $\Omega_\Lambda = 0.7$ throughout the thesis.

2.2 Overview of the XLENS Survey

The X-shooter Lens Survey (XLENS) aims to study spectroscopically the stellar population of strong early-type lens galaxies, for which exquisite HST multi-band images and very detailed lens models are available. The major goal of the survey is to disentangle the dark-matter and stellar mass distributions, as well as to constrain the slope and the cutoff (or turn-over) mass of the low-mass end of the stellar IMF directly from spectra, by combining the lensing and dynamical results with spectroscopic stellar population studies.

By taking advantage of the wide wavelength coverage and throughput of the X-Shooter spectrograph[2], we are able to obtain high-resolution spectra from the UVB to the near-IR for detailed stellar-population and kinematics studies of the high-mass end of the early-type galaxies (ETGs) up to redshift $z \sim 0.7$. We combine these data with high-precision strong gravitational lensing determinations of the total masses to obtain their precise dark-matter fractions ($f_{\rm DM}$) inside approximately one effective radius ($R_{\rm eff}$) and to test possible correlations between the non-visible matter (baryonic matter, i.e. low-mass end

[2]X-Shooter is a powerful, multi wavelength (3000–25000 Å), medium resolution spectrograph mounted at the UT2 Cassegrain focus of the Very Large Telescope. It consists of three arms, each of them is an independent cross dispersed echelle spectrograph equipped with optimized optics, dispersive elements, detectors, its own shutter and/or slit mask. The incoming light is split into the three different spectrographs through two dichroics (transition wavelengths 5595 Å and 10240 Å for the separation of the UVB-VIS light and VIS-NIR light, respectively) resulting in a huge final wavelength spectral coverage.

of the IMF, or non-baryonic matter, i.e. dark-matter) and galaxy mass and size (Auger et al. 2010a; van Dokkum & Conroy 2010; Spiniello et al. 2011, 2012, 2013; Cappellari et al. 2012; Tortora, Romanowsky & Napolitano 2013).

A crucial result of our approach is that it allows us to tackle the long-standing problem of constraining the low-mass cutoff ($M_{\rm low}$) for the IMF. In fact, we can break the degeneracy between slope and $M_{\rm low}$ by comparing two independent estimation of the stellar mass (Barnabè, Spiniello et al. 2013, Chapter 6). The first one comes from a fully self-consistent lensing+dynamics analysis (e.g. Barnabè et al. 2011), and the other from spectroscopy and SSP modelling (Spiniello et al. 2013, Chapter 5) .

In previous studies, the value of $M_{\rm low}$ has always been treated as a relatively unconstrained parameter, despite being critical to determine the value of $\Upsilon_\star$. Stars with masses below $\sim 0.15\ M_\odot$ have very little effect on the spectral lines and on the line-index measurements in the optical and near-infrared for any assumed IMF slope (Conroy & van Dokkum 2012a), but they provide a substantial contribution to the total mass budget of the system (Worthey 1994). Therefore, to constrain the value of $M_{\rm low}$ it is necessary to support spectroscopic studies with a combined lensing and dynamics analysis (see Chapter 6).

2.2.1 Candidate Selection

Our current sample has been selected from the SLACS survey. We provide a brief description of that survey, focusing on the candidate selection criteria.

The Sloan Lens ACS Survey (Bolton et al. 2006, 2008a,b; Treu et al. 2006, 2009; Koopmans et al. 2006; Gavazzi et al. 2007, 2008; Auger et al. 2009, 2010b; Newton et al. 2011) is a SDSS spectroscopically-selected lens survey with imaging follow-up conducted with the Advanced Camera and Spectrograph (ACS) aboard the Hubble Space Telescope (HST). The SLACS survey was initiated in 2003 with the purpose of confirming and imaging galaxies that act as strong gravitational lenses of emission-line background sources. The survey has greatly extended the number of strong gravitational lens galaxies at redshift $z \leq 0.5$ with complete redshift information, providing an ideal sample of systems to be analysed with joint lensing and dynamics techniques.

Lens candidates were originally selected from the Sloan Digital Sky Survey (SDSS, York et al. 2000). The SDSS is a large project that in a decade of operations (SDSS-I: Abazajian et al. 2003, 2004, 2005; SDSS-II: Adelman-McCarthy et al. 2006, 2007, 2008; Abazajian et al. 2009) imaged more than one-

quarter of the sky in five optical bands and obtained deep, multi-color images and spectroscopic follow-up observations of 10^6 galaxies and 10^5 quasars.

In particular, half of the lenses were selected from the luminous red galaxy (LRG) spectroscopic sample of the SDSS (Eisenstein et al. 2001). The LRG sample is defined by photometric selection cuts that very efficiently select massive ETGs in the redshift range $0.15 < z \leq 0.5$, as confirmed by SDSS spectroscopy. These galaxies are very homogeneous in their spectral, photometric, and morphological properties.

The method by which lens candidate were selected is described in Bolton et al. (2006). Briefly, they subtracted best-fit principal-component analysis (PCA) templates (a by-product of the redshift pipeline) from the observed SDSS target galaxy spectra. They required the SDSS continuum to be well fit by the template, which effectively yielded a parent sample of galaxies with well-behaved absorption-dominated spectra and very secure redshifts (z_{FG}, FG denoting "foreground"). The residual spectra were then scanned for nebular line emission at greater redshifts (z_{BG}, BG denoting "background"). Spectra in which such emission was significantly detected for at least three separate common atomic transitions at a single background redshift were taken as lens candidates. Using the values of z_{FG}, z_{BG} and the measured stellar velocity dispersion, the strong-lensing cross section for each system in the source plane was determined (to first order) using a singular isothermal sphere (SIS) model. To maximize the number of strong lenses in the survey, they selected candidates with the highest predicted lensing cross section.

The remaining targets were selected with the same spectroscopic selection procedure from within the MAIN galaxy sample of SDSS (Strauss et al. 2002). The MAIN sample is more heterogeneous, and therefore the SLACS team imposed a quiescent, absorption-dominated spectral criterion by requiring their lens candidates to have rest-frame equivalent widths in $H\alpha$ of $\mathrm{EW}_{H\alpha} < 1.5$ Å (Bolton et al. 2006).

The current SLACS sample consists of 131 strong gravitational lens candidates[3] (Bolton et al. 2008a; Treu et al. 2009; Auger et al. 2009). The catalog of the largest single confirmed strong gravitational lens sample to date, includes 85 "grade-A" and 15 "grade-B" (likely lenses) strong galaxy-galaxy lens systems complete with lens and source redshifts, F814W lens-galaxy photometry, gravitational lens models, and measured stellar velocity dispersions (Auger et al.

[3] An additional ~ 50 genuine SLACS lenses have recently been found but are as of yet unpublished.

2009). Approximately 80% of the "grade-A" systems have elliptical morphologies while ∼ 10% show some spiral structure; the remaining lenses have lenticular morphologies. Such a large and high-quality lens sample provides a unique resource for the quantitative study of massive early-type galaxies.

2.2.2 The XLENS sample

From the final SLACS sample of ∼ 100 confirmed lenses, the XLENS sample includes only "grade-A" systems with elliptical morphology and that lie above the knee of the luminosity function ($\sigma_{\star,\mathrm{SDSS}} > 250$ km s^{-1}). The velocity dispersion cut has been made because of recent findings (Treu et al. 2010; Auger et al. 2009, 2010a) that internal dark-matter fraction is a monotonically increasing function of the velocity dispersion of the system, and recent indications (vDC10) that very massive early-type galaxies could have an initial mass function steeper than the universally-assumed Milky Way IMF (Kroupa 2001; Chabrier 2003).

The current XLENS-SLACS sample consists of twelve luminous red galaxies with V-magnitudes between $-15.8-18.1$, high-resolution and high signal-to-noise HST imaging in B/V, I and H-bands, and with detailed lensing models constructed by the SLACS collaboration. VLT X-shooter spectra were collected in a total of 30^h of Observation Time (OT), awarded in two periods (P086 and P089)[4]. Among these, ten have complete observations at the date of writing (first results are presented in Chapters 4 and 6, published as Spiniello et al. 2012; Barnabè, Spiniello et al. 2013), while two have only been partially observed at the present time. High-resolution HST F814W images together with models of a selection of the systems in the XLENS sample are shown in Figure 2.2.

In addition to the twelve galaxies selected from the SLACS sample, another system has been observed in Guaranteed Time (GTO, P087.A-0620): SDSSJ1148+1930, also known as "The Cosmic Horseshoe". This lens at redshift $z = 0.444$ was analysed as a "pilot program" of the survey. Results on this extremely massive galaxy ($\langle\sigma_\star\rangle(\leq R_{\mathrm{eff}}) = 352 \pm 10 \pm 16$ km s^{-1}) are presented in Chapter 3 (Spiniello et al. 2011).

We plan to extend the current sample, observing lenses within the same range of velocity dispersions ($\sigma_{\star,\mathrm{SDSS}} > 250$ km s^{-1}) at higher redshift (up to $z \sim 1$) in the future to test possible evolution of the IMF with cosmic time. We also plan to observe low-mass ETGs to build a complementary dataset to our more

[4] 15^h OT during P86 (P086.A-0312, PI: Koopmans) and 15^h OT during P89 (P089.A-0364, PI: Spiniello). The latter is still in "carryover" status and more data are expected.

Table 2.1: Properties of observed systems.

SLACS System	z_{lens}	z_{BG}	R_{eff}(kpc)	R_{Ein} (kpc)	m_V (mag)
Completed					
SDSSJ0037-0942	0.1955	0.6322	7.03	4.95	16.90
SDSSJ0044+0113	0.1196	0.1965	5.56	1.72	16.32
SDSSJ0216-0813	0.3317	0.5235	12.6	5.53	18.36
SDSSJ0912+0029	0.1642	0.3239	10.8	4.58	16.56
SDSSJ0935-0003	0.3475	0.4670	20.7	4.26	17.71
SDSSJ0936+0913	0.1897	0.5880	6.61	3.45	17.12
SDSSJ0946+1006	0.2219	0.6085	8.33	4.95	17.78
SDSSJ1143-0144	0.1060	0.4019	9.21	3.27	15.83
SDSSJ1627-0053	0.2076	0.5241	6.66	4.18	16.91
SDSSJ2343-0030	0.1810	0.4630	8.27	4.62	17.17
On-going					
SDSSJ1112+0826	0.2730	0.6295	6.20	6.19	17.97
SDSSJ020+1122	0.2822	0.5530	6.73	5.12	18.12
XLENS-Pilot Program					
SDSSJ1148+1930	0.4440	2.3815	12.5	29.0	20.02

massive ETGs with the purpose of cover a wider stellar mass range (see Future work, Chapter 8 for further details). The current sample of lens ETGs with their photometric parameters and physical properties is presented in Table 2.1. In the following sections, we limit our discussion to the twelve SLACS-selected XLENS systems (with $0 \leq z \leq 0.4$).

2.3 Observations and data reduction

X-Shooter observations of the systems presented here were carried out in slit mode during two programs between 2011 and 2013, splitting the beam over three arms: UVB (R=3300 with $1.''6$ slit); VIS (R=5400, with $1.''5$ slit); and NIR (R=3300 with $1.''5$ slit), covering a wavelength range from 3000 to 25000 Å simultaneously. The $11''$ long slit was always centred on the lens galaxy with the position angle (PA) aligned with the major axis of the systems or with an angle that minimizes contamination from the source and leaves enough sky region to facilitate accurate sky subtraction. A different number of Observation Blocks (OBs) have been

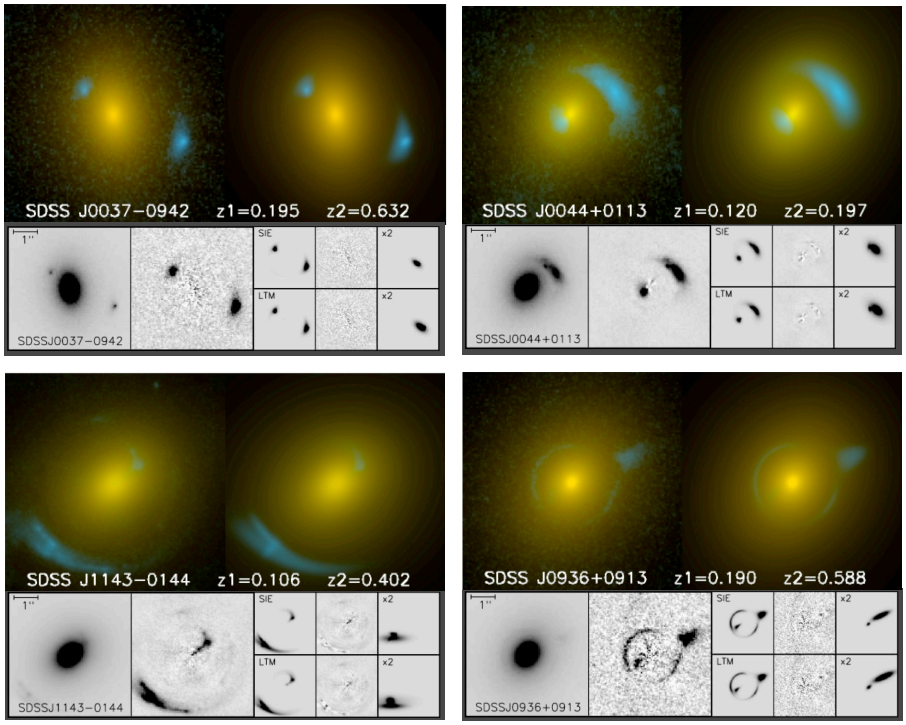

Figure 2.2: *Upper rows:* $6'' \times 6''$ HST ACS-WFC F814W imaging of four of the gravitational lenses selected from the SLACS survey (Bolton et al. 2008a; Auger et al. 2009). The colors of the foreground elliptical galaxies have been assigned based upon the g-r colors measured by the SDSS, and the lensed background-galaxy features have been enhanced in blue. The upper-left panel in each cell is based on multi-color HST data, while the upper-right panel shows a model used to describe the foreground and background galaxies, including the lensing effect that distorts the image of the latter. The foreground and background redshifts in each system are given as z1 and z2 respectively. *Lower rows:* Lens models for the strong gravitational lens system. Left-most larger panels show the F814W images, $5'' \times 5''$ to a side, with North up and East left. The following large panels show the same images, with the B-spline model of the foreground galaxy subtracted, showing lensed features. Top rows of smaller panels: Left: model prediction of the best-fit SIE strong lens model for features in the residual data image; Center: "double-residual" image, after subtraction of B-spline and SIE models; Right: unlensed source-plane for best-fit SIE lens model, evaluated over a $2.5'' \times 2.5''$ region and convolved with a 2× de-magnified HST PSF for display purposes. Bottom rows of smaller panels: Same as top row, but for best-fit light-traces-mass (LTM) lens models.

observed for each system to reach a S/N high enough to perform detailed stellar population analyses (S/N ~ 50 per Å). Each OB has the same layout with three scientific exposures for a total exposure time on target for each arm of ~ 2500 sec per OB[5]. The seeing varied during the observations from ~ 0.″6 to ~ 0.″9. Standard calibration frames and standard stars for flux calibration were obtained after each OB.

Data reduction was performed using the ESO X-Shooter pipeline v. 2.0.0 (Goldoni et al. 2006) and the Gasgano data file organiser developed by ESO. The pipeline reduction uses calibration spectra, taken during the commissioning run, for bias subtraction and flat-fielding of the raw spectra. Cosmic rays are removed using LACosmic (van Dokkum 2001). For each arm, the orders are extracted and rectified in wavelength space using a wavelength solution previously obtained from the calibration frames. The resulting rectified orders are shifted and co-added to obtain the final two-dimensional (2D) spectrum. We extract a one dimensional spectrum (1D) from the resulting 2D merged spectrum, using our own IDL code that implements the optimal-extraction algorithm of Horne (1986). It also produces the corresponding error file and bad pixel map. The final S/N in the UVB+VIS spectrum varies from system to system, with a minimum of ~ 10 and a maximum of ~ 25 per pixel (0.2 Å/pix). We finally perform an iterative sigma-clipping to clean the spectrum of any residual bad pixels, sky lines and cosmic rays. No telluric correction was applied so that prominent atmospheric absorption bands can still be seen in the final UVB+VIS spectra shown in rest-frame wavelengths in Figure 2.3. For some of the systems, it is also possible to see emission lines from the background source, although the chosen PA minimizes their contribution to the stellar spectra. We mask these lines as well as telluric absorption during spectra fitting, when extracting the spatially resolved kinematic profile, as described in the next section.

Because the near-infrared spectrum suffers seriously from sky-line residuals that are difficult to remove using the current pipeline, we limit ourselves in this thesis to the UVB-VIS region of the spectrum and defer to future publications for a full analysis of the infrared data.

[5]In the NIR arm, the total exposure time is the product of DIT (Detector Integration Time), NDIT (Number of DITs) and NINT (Number of INTegrations): T = DIT × NDIT × NINT. We used for each of the 3 scientific exposure 3 DITs of 278 sec.

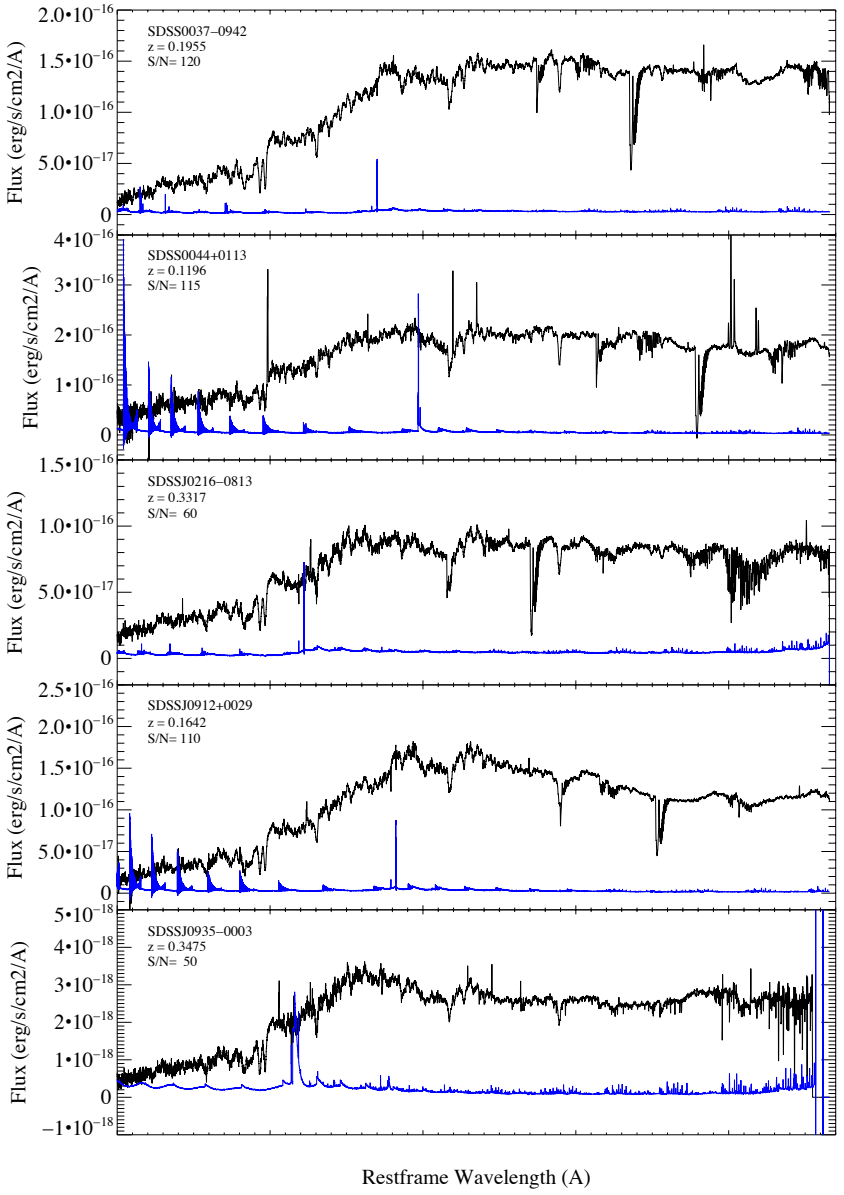

Figure 2.3: Final luminosity-weighted UVB–VIS 1D X-Shooter spectra (in black) and respective errors (in blue) extracted from a rectangular aperture of $\sim 2'' \times 1.''5$ centered on the galaxies, shifted to the rest-frame and smoothed (3-pixel boxcar) for displaying purposes only. ID names, redshifts of the lens and average S/N (per Å) are shown in the panels. Telluric absorption lines and emission coming from the background source have not been removed from the spectra. The peak in the error spectra between 4500 - 5500 Å, shows the point at which UVB and VIS 1D final spectra have been joined.

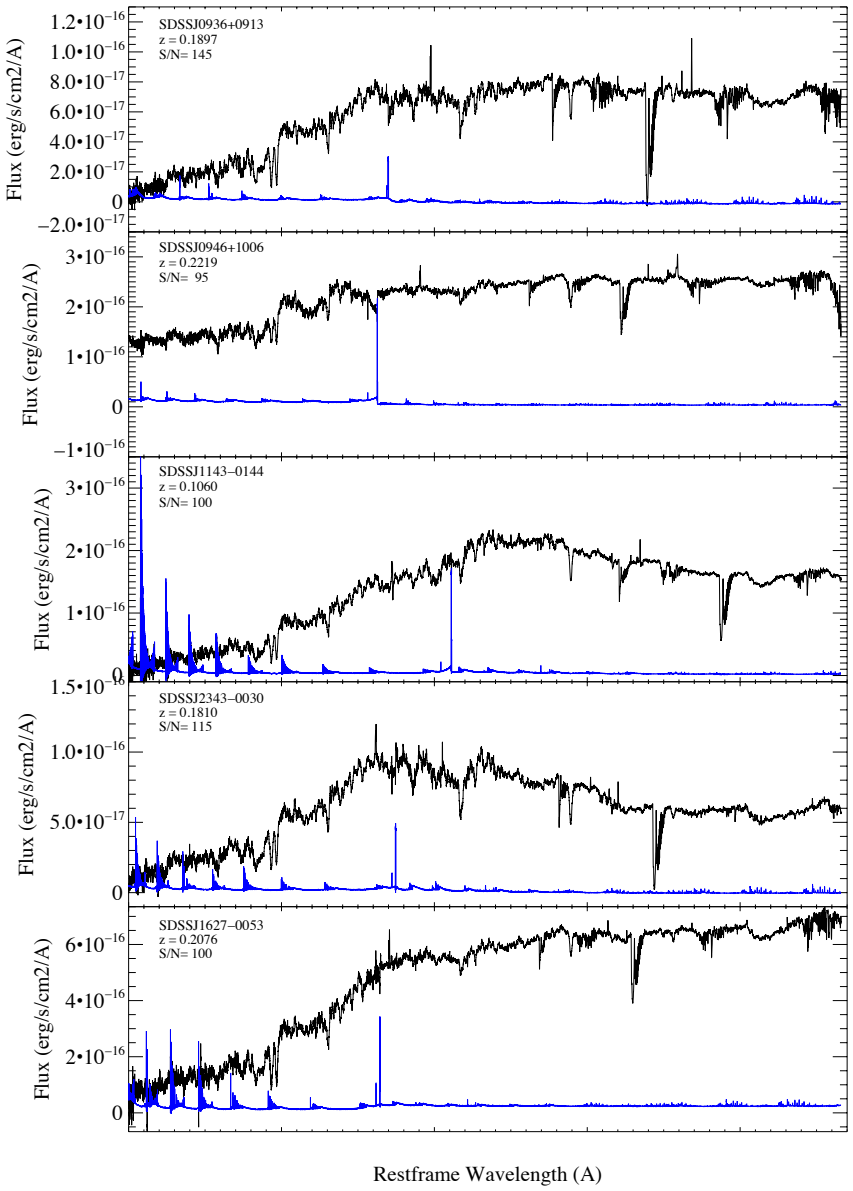

Figure 2.3: continued

2.4 Stellar Kinematics

We measure a luminosity-weighted line-of-sight velocity dispersion (LOSVD) of the lens galaxies from the final 1D UVB–VIS spectra extracted from a rectangular aperture of 2" × 1.″5 centered on the galaxy. We use the Penalized Pixel Fitting (pPXF) code of Cappellari & Emsellem (2004) to determine the combination of stellar templates which, when convolved with an appropriate line-of-sight-velocity distribution (LOSVD), best reproduces the galaxy spectrum. The best-fitting parameters of the LOSVD are determined by minimizing a χ^2 penalty function, yielding the mean velocity and the velocity dispersion (v and $\sigma_\star$, respectively), plus their uncertainties.

We focus on absorption lines between 3500–6500 Å (including Ca K and H, G4300, H_β, Mg_b, strong Fe lines, NaD and some TiO molecular absorption bands). To minimize errors due to mismatch between the resolution of the templates and the galaxy spectrum, we use X-Shooter spectra obtained as part of the X-Shooter Stellar Library (XSL) survey (Chen et al. 2013, in prep.), with similar instrumental resolution (for the galaxy spectrum we use a 1.5-arcsecond slit, corresponding to $\langle\sigma_{\rm instr}\rangle \sim 35$ km s^{-1}, while for the stellar templates the slit width is 0.7 arcsecond, corresponding to $\langle\sigma_{\rm instr}\rangle \sim 12$ km s^{-1}). As a test of the accuracy of our measurements, we use the more heterogeneous MILES[6] stellar template library (Sánchez-Blázquez et al. 2006). We select 100 stars (F, G, K, M) in the range 3525–7500 Å, with 2.5 Å FWHM spectral resolution (corresponding roughly to $30 \leq \sigma_{MILES} \leq 70$ km s^{-1} in the selected wavelength range), which is comparable to the XLENS spectra resolution in the selected region ($\sigma_{XSH} \sim 35$ km s^{-1}) that have been smoothed to the same spectral resolutions with a Gaussian. Fitting with different stellar templates does not appreciably change (i.e. well within the errors) the resulting LOSVD. As a second test, we fit the same stellar templates to two different spectral regions for each galaxy separately (blue region: $[3800-5000]$ Å and red region: $[5000-6500]$ Å). Only for two systems (SDSSJ0936+0913 and SDSSJ1143-0144) do we find slightly different results between the blue and the red part of the spectrum, but always consistent within 2σ. The scatter between the different fits is used to estimate additional systematic uncertainties related to template mismatch and spectral coverage. We report our results and the comparison with other published velocity dispersion results for each ETG in Table 2.2. We find a very good agreement between our values extracted from a rectangular aperture of 2" × 1.″5 and the SDSS velocity-dispersion

[6] http://www.iac.es/proyecto/miles/pages/stellar-libraries/miles-library.php

Table 2.2: Luminosity-weighted stellar kinematics of the lenses. $\langle\sigma_{XSH}\rangle$ has been extracted from a rectangular aperture of 2" × 1.″5 centered on the galaxies, while σ_{SDSS} is measured within an aperture with a diameter of 3". VIMOS velocity dispersions were measured from aperture-integrated spectra from data from the VIMOS Integral-Field Unit (with a field-of-view of 27" × 27", Czoske et al. 2012).

ID name	$\langle\sigma_{XSH}\rangle$ (km s^{-1})	σ_{SDSS} (km s^{-1})	σ_{VIMOS} (km s^{-1})
SDSSJ0037-0942	277 ± 6	279 ± 14	$245.3^{+6.9}_{-7.2}$
SDSSJ0044+0113	260 ± 8	266 ± 13	...
SDSSJ0216-0813	327 ± 19	333 ± 23	$340.7^{+7.8}_{-7.7}$
SDSSJ0912+0029	325 ± 10	326 ± 16	$306.5^{+10.9}_{-11.4}$
SDSSJ0935-0003	380 ± 22	396 ± 35	$330.4^{+9.0}_{-8.5}$
SDSSJ0936+0913	256 ± 18	243 ± 12	...
SDSSJ0946+1006	300 ± 22	263 ± 21	...
SDSSJ1143-0144	287 ± 18	269 ± 10	...
SDSSJ1627-0053	303 ± 23	290 ± 20	$272.6^{+7.8}_{-8.9}$
SDSSJ2343-0030	298 ± 21	269 ± 16	...

measurements obtained in the 3"-diameter spectroscopic fiber (for most of the systems within 1σ error). We also find relatively good agreement with the results of Czoske et al. (2012) obtained from aperture-integrated spectra from the Integral Field data on five systems that overlap with the XLENS sample. In Figure 2.4 we show examples of pPXF fitting for the two best and worst cases.

2.4.1 Spatially-Resolved Kinematics

To extract the spatially-resolved kinematic information, we define for each galaxy a number of spatially-varying apertures (with adequate S/N ratio) along the radial direction, and we sum the signal within each aperture. Apertures are always defined to be larger than the seeing in order to have relatively independent kinematic measurements for each aperture. The stellar rotation velocity and velocity dispersion are measured from each spatially-resolved spectrum using pPXF as described above. Also in this case we perform tests to check our error determinations: we fit the blue and red spectral regions separately, masking out the most prominent telluric lines in the VIS-red range; we use different stellar templates from the two different stellar libraries (eleven XSL stars of G, K and M spectral types and a sub-selection of MILES stars of the same spectral types). The uncertainties on the inferred kinematics are estimated by adding in quadrature

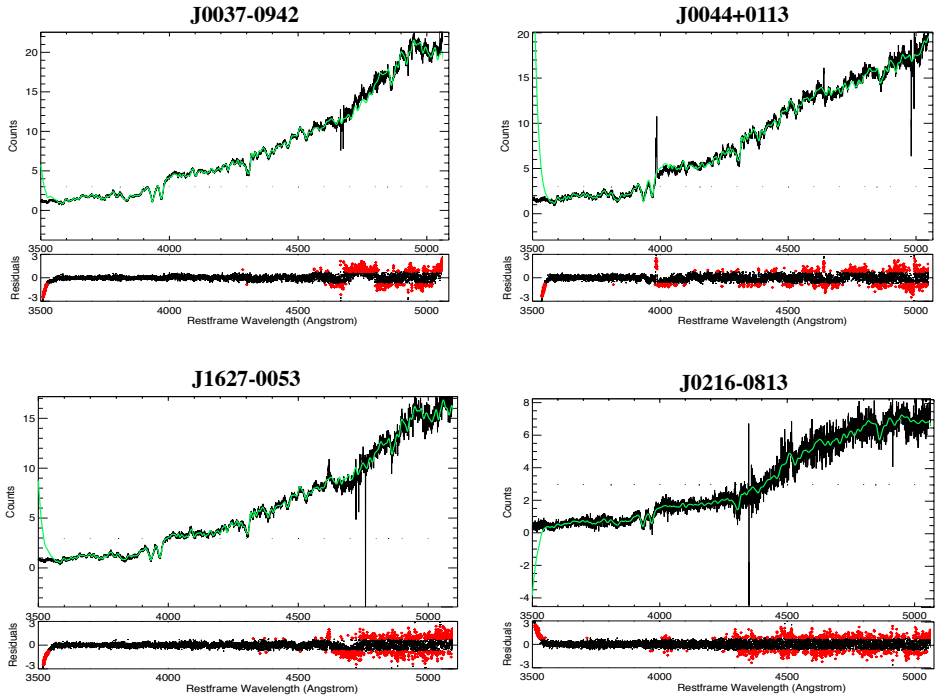

Figure 2.4: Some example of pPXF fitting. The upper row shows two of the best cases (χ^2/DOF ~ 1.15), while the lower raw shows the worst cases (χ^2/DOF ~ 1.65). *Top panels:* UVB+VIS galaxy spectrum (black) and correspondent best-fit template (green), both in restframe wavelength. *Bottom panels:* Residuals from the fit. Bad-pixels excluded from the fitting procedure (sky line, telluric lines) are shown in red. See the text for more information.

the formal uncertainty given by pPXF and the scatter in the results for different templates and spectral regions.

Our goal is to determine the kinematic profiles up to ~ 1 $R_{\rm eff}$ for all the systems. When spatially resolved stellar kinematics is combined with detailed strong gravitational lensing modelling, it is possible to obtain a precise measurement of the logarithmic slope of the total mass density profile of the lens galaxy (e.g. Barnabè et al. 2011, 2013; Spiniello et al. 2011). The lens models for all these systems have been constructed by the SLACS collaboration using high S/N HST multi-band images. The joint lensing and dynamics code for the analysis of ETGs (CAULDRON, Barnabè & Koopmans 2007; Barnabè et al. 2009b, 2012)

will be used in the future to perform the analysis of the total mass distributions for the XLENS systems. A pilot-program in which we analysed two XLENS systems is presented in Chapter 6 (Barnabè et al. 2013).

The rotation and the velocity dispersion profiles for the ten XLENS-SLACS galaxies with complete observations are shown in Figure 2.5, for systems that show an almost-flat velocity profile up to the effective radius, and in Figure 2.6, for those showing moderate rotation.

The weighted average values are always consistent within the formal error with the luminosity weighted values for an aperture of $2'' \times 1.5''$.

2.5 Summary & Conclusions

In this chapter we have introduced a new on-going spectroscopic follow-up survey of massive early-type lens galaxies: The X-Shooter Lens Survey (XLENS).

In particular, we have

- highlighted the scientific motivations and main goals of XLENS.
- presented the current sample of thirteen massive early-type lens galaxies, discussed the selection criteria and described the data reduction process for the twelve XLENS-SLACS galaxies. The remaining lens, also known as "The Cosmic Horseshoe", has been used as pilot program of the survey and is the subject of Chapter 3 (Spiniello et al. 2011).
- presented the spatially resolved kinematic profiles up to $\simeq 0.8 - 1.5\ R_{\rm eff}$ for the ten galaxies with complete observations. We found luminosity-weighted velocity dispersions mostly within 1σ agreement with those calculated from SDSS. Our velocity dispersions also agree with the results of Czoske et al. (2012) extracted from VIMOS integral-field spectra. Small differences could be due to the different apertures within which the LOSVD has been extracted.

The combination of high S/N spectroscopy from X-Shooter with a strong-gravitational-lensing mass determination will enable us to conduct an in-depth study of the dark and luminous matter within $\sim 1R_{\rm eff}$. Combining stellar population studies, with these lensing and kinematic data allow us to disentangle the stellar and dark-matter content of galaxies (Chapters 3, and 4) and for the first

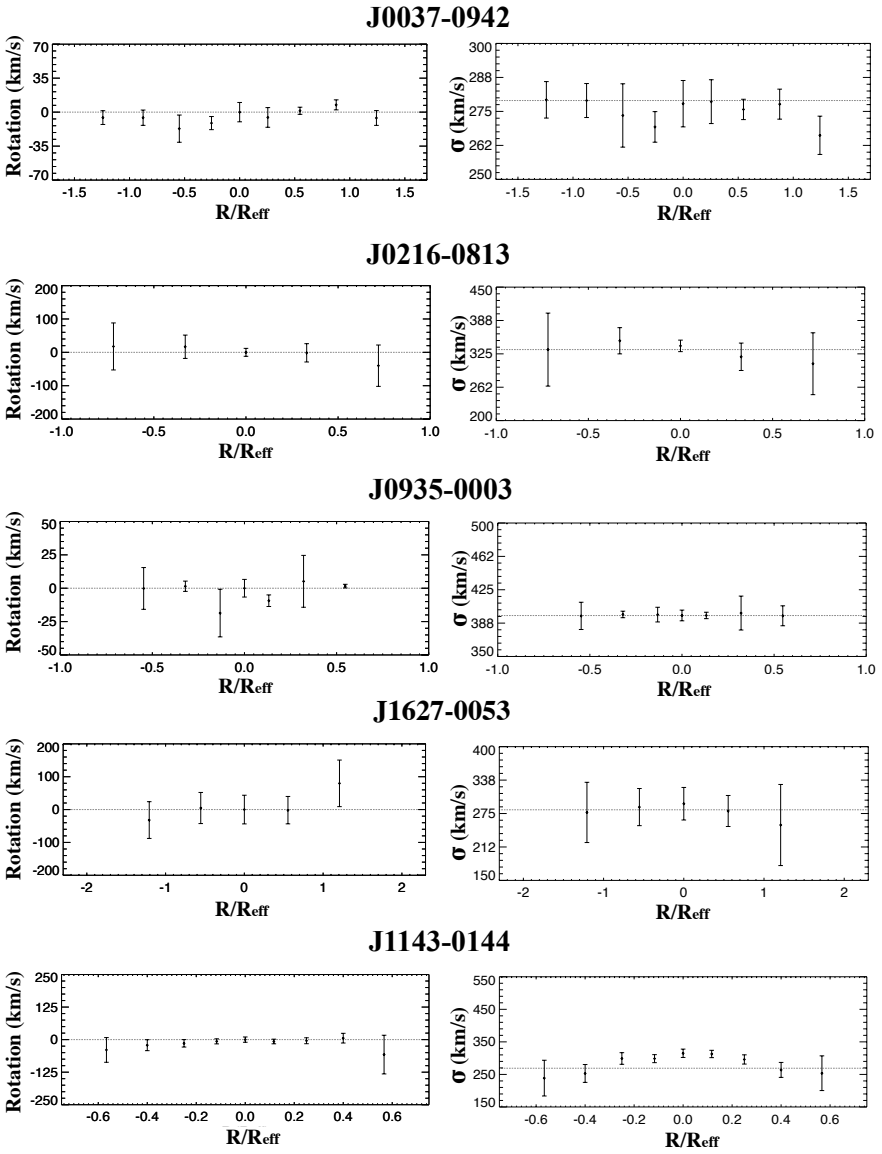

Figure 2.5: Spatially-resolved kinematics of systems which do not show rotation. Dotted lines represent the rotation inferred from the central bin, used as zero-point (left panels), and the SDSS velocity dispersions (right panels).

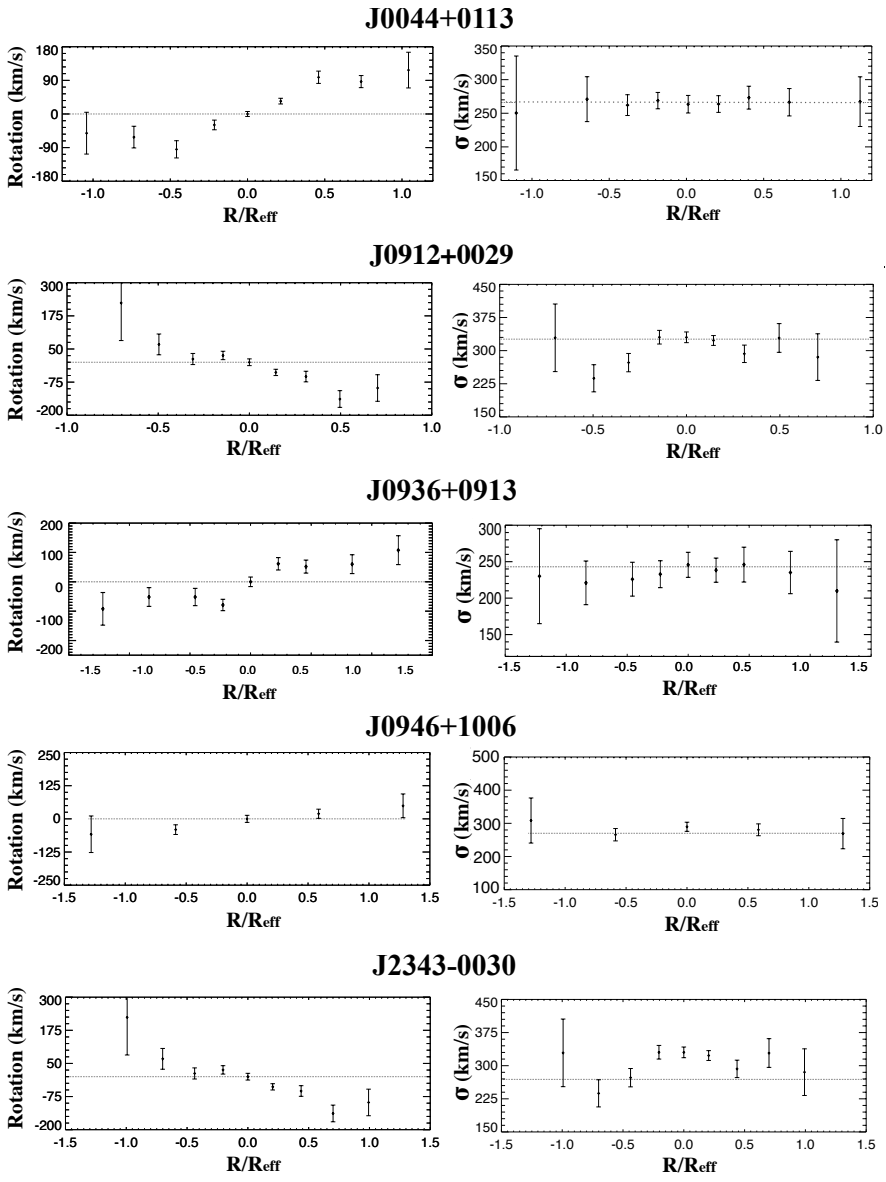

Figure 2.6: Spatially-resolved kinematics of systems which show rotation. Dotted lines represent the rotation inferred from the central bin, used as zero-point (left panels), and the SDSS velocity dispersions (right panels).

time constrain the normalization, shape and turnover mass ($M_{\rm low}$) of the low-mass end of the IMF (Chapter 6).

In the following chapters we will present results of the survey, focusing predominantly on stellar population analysis and IMF constraints.

3 A pilot program: dark matter domination and a Salpeter-type IMF in The Cosmic Horseshoe.

If the facts don't fit the theory, change the facts.

Albert Einstein

Published as:

C. Spiniello, L.V.E. Koopmans, S.C. Trager, O.Czoske and T. Treu,
"The X-Shooter Lens Survey - I. dark matter Domination and a Salpeter-type IMF in a Massive Early-type Galaxy," 2011, MNRAS, 417, 3000

In this chapter, we present the first results from the X-Shooter Lens Survey (XLENS) in order to demonstrate the validity and power of our method: An analysis of the "Cosmic Horseshoe" (SDSSJ1148+1930), an almost complete Einstein ring with a diameter of $\sim 10\farcs2$ around a very massive early-type galaxy (ETG) at $z = 0.444$.

We combine the galaxy extended kinematic profile – derived from spectra obtained with X-Shooter on ESO *Very Large Telescope* – with strong gravitational lensing and multi-color information derived from Sloan Digital Sky Survey (SDSS) images. Our main results are (i) the luminosity-weighted stellar velocity dispersion is $\langle\sigma_\star\rangle(\leq R_{\rm eff}) = 352 \pm 10 \pm 16\,{\rm km\,s^{-1}}$, extracted from a rectangular aperture of $1\farcs8 \times 1\farcs6$ centered on the galaxy, more accurate and considerably lower than a previously published value of $\sim 450\,{\rm km\,s^{-1}}$; (ii) a single-component (stellar plus dark) mass model of the lens galaxy yields a logarithmic total-density slope of $\gamma' = 1.72^{+0.05}_{-0.06}$ (68% C.L.; $\rho_{\rm tot} \propto r^{-\gamma'}$) within a projected radius of $\sim 2\farcs16$; (iii) the projected stellar mass fraction, derived solely from the lensing and dynamical data, is $f_\star(<R_{\rm Ein}) = 0.19^{+0.04}_{-0.09}$ (68% C.L.) inside the Einstein radius for a Hernquist stellar profile and no anisotropy. The dark matter fraction inside the effective radius is $f_{\rm DM}(<R_{\rm eff}) = 0.60^{+0.15}_{-0.06} \pm 0.1$ (68% C.L.), where the latter error is systematic; (iv) based on the SDSS colors, we find $f_{\star,{\rm Salp}}(<R_{\rm Ein}) = 0.17 \pm 0.06$ for a Salpeter Initial Mass Function (IMF) and $f_{\star,{\rm Chab}}(<R_{\rm Ein}) = 0.07 \pm 0.02$ for a Chabrier IMF. The lensing and dynamics constraints on the stellar mass fraction agree well with those independently derived from the SDSS colors for a Salpeter IMF, which is preferred over a Chabrier IMF at variance with standard results for lower mass galaxies. Dwarf-rich IMFs in the lower mass range of 0.1–0.7 $M_\odot$, with $x \geq 3$ (with $dN/dM \propto {\rm M}^{-x}$) – such as that recently suggested for massive ETGs with $x = 3$ in the mass range $0.1 - 1\,M_\odot$ – are excluded at the $> 90\%$ C.L. and in some cases violate the total lensing-derived mass limit. We conclude that this very massive lens galaxy is dark matter dominated inside one effective radius, consistent with the trend recently found from massive SLACS (Sloan Lens ACS) galaxies, with a total density slope shallower than isothermal and a IMF normalization consistent with Salpeter.

3.1 Introduction

In the ΛCDM cosmological model, early-type galaxies (ETGs) play a fundamental role because they contain more than half of the stellar mass in the universe (e.g. Bell et al. 2003). A variety of observations suggest that ETGs are dominated by

stars in their central regions and are increasingly dominated by massive dark-matter (DM) halos in their outskirts. This indicates that a strong relationship between baryonic luminous matter and DM must exist, which plays a crucial role in the dynamics of galaxy formation (e.g. Blumenthal et al. 1984). The details of ETG structure and dynamics therefore provide key quantitative tests of the ΛCDM paradigm. Progress in understanding ETGs and consequently the theory of galaxy formation requires the precise measurement of their stellar and DM density profiles and a detailed understanding of how these structures depend upon properties such as mass and age of the stellar-assembly and the shape of the low-mass end of the stellar initial mass function (IMF). With the XLENS Survey we are for the first time probing variations of the IMF shape and unambiguously disentangling luminous and dark matter in the internal region of lens ETGs, thanks to a powerful joint lensing+dynamics+stellar population (SP) analysis.

In this chapter we present the result of the pilot program of the XLENS project: an analysis of the massive early-type galaxy SDSS J1148+1930 at redshift $z = 0.444$. The system was discovered by Belokurov et al. (2007) in the Sloan Digital Sky Survey Data Release 5 (DR5, Adelman-McCarthy et al. 2007). The source is a star-forming galaxy at $z = 2.381$ (Dye et al. 2008; Quider et al. 2009). Properties and characteristics of the Cosmic Horseshoe are listed in Table 3.1 and a composite SDSS image of the system is shown in Figure 3.1.

The chapter is organized as follows: In Section 3.2, we present the observations and data reduction. In Section 3.3, we discuss our kinematic analysis. In Section 3.4, we discuss the luminous and dark matter distributions of the lens galaxy. We summarize our findings and we present our conclusions in Section 3.6.

3.2 Observations and Data reduction

X-Shooter observations of SDSSJ1148+1930 were carried out during a GTO run between 17–24 March 2010 in slit mode[1], splitting the beam over three arms: UVB (R=3300, with 1.″6 slit); VIS (R=5400, with 1.″5 slit); and NIR (R=3300 with 1.″5 slit), covering a wavelength range from 3000 to 25000 Å simultaneously. The 11″ long slit was centered on the lens galaxy with a position angle (PA) of 163°. The latter minimizes contamination from the source and leaves enough sky region to facilitate accurate sky subtraction. Two Observation Blocks (OBs) were not used because of bad seeing and/or an incorrect positioning of the slit

[1] P084.A-0289(A); PI: Koopmans

Table 3.1: Properties of the cosmic Horseshoe[1].

	Parameter	**Values**
Lens	RA	11h 48m 33.15s
Galaxy	Dec	19° 30′ 03.″5
	Redshift	0.444
	Effective radii	$1.''96 \pm 0.''02$
	g_L	(20.84 ± 0.06) mag
	r_L	(19.00 ± 0.02) mag
	i_L	(18.22 ± 0.01) mag
	z_L	(17.75 ± 0.04) mag
	Axis ratio, g	0.8 ± 0.1
Source	Redshift[2]	2.38115 ± 0.00012
	Star formation rate	$\sim 100\, M_\odot\, \mathrm{yr}^{-1}$
	Dynamical mass	$M_{vir} \simeq 10^{10}\ M_\odot$
Ring	Diameter	$10.''2$
	Length	$\sim 300°$
	u_L	21.6 mag
	g_L	20.1 mag
	i_L	19.7 mag
	Mass enclosed[3]	$(5.02 \pm 0.09) \times 10^{12}\, M_\odot$

[1] Belokurov et al. (2007) measured the redshift of the source to be $z = 2.379$. We find a systematic shift that brings the source redshift to be $z = 2.3811$ in agreement with Quider et al. (2009).

[2] The mass within the Einstein radius or, more precisely, within the ring diameter, is taken from Dye et al. (2008).

[3] Parameters obtained from images taken with the 2.5 m Isaac Newton Telescope (INT). Magnitudes are taken from SDSS DR7. See Belokurov et al. (2007)

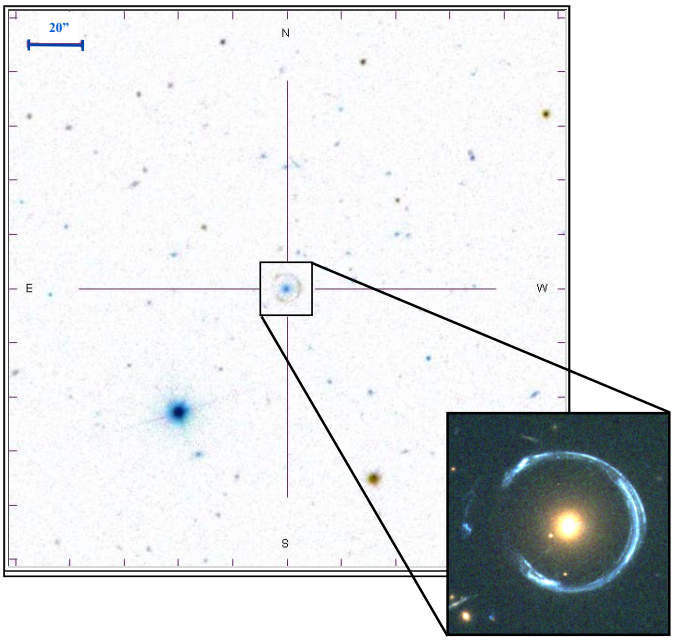

Figure 3.1: SDSS color composite image of the sky region around the Cosmic Horseshoe and a HST $\sim 20'' \times 20''$ zoom centered on the gravitational lens.

on the object. The total exposure time on target for each arm is $\sim$ 7389 sec and the typical seeing is $\sim 0.''6$. Standard calibration frames were obtained after each corresponding OB. A summary of the observing blocks is given in Table 3.2 .

Data reduction was done using the ESO X-Shooter pipeline v1.2.1 (Goldoni et al. 2006) and the Gasgano data file organiser developed by ESO[2]. The pipeline reduction uses calibration spectra, taken during the commissioning run, for bias subtraction and flat-fielding of the raw spectra. Cosmic rays are removed using LACosmic (van Dokkum 2001). For each arm, the orders are extracted and rectified in wavelength space using a wavelength solution previously obtained from the calibration frames. The resulting rectified orders are shifted and coadded to obtain the final two-dimensional (2D) spectrum. We extract a one dimensional spectrum (1D) from the resulting 2D merged spectrum, using an IDL code that uses the optimal-extraction algorithm of Horne (1986). It also produces the corresponding error file and bad pixel map. The final signal-to-noise ratio (S/N)

[2]http://www.eso.org/gasgano

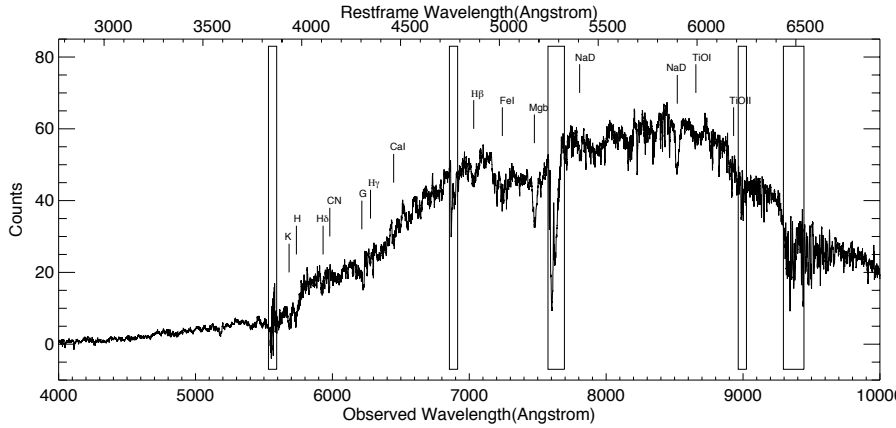

Figure 3.2: The final luminosity-weighted UVB–VIS 1D X-Shooter spectrum extracted from a rectangular aperture of $1.''8 \times 1.''6$ centered on the galaxy (see text). Spectral features the lens galaxy are marked. Telluric absorption lines have not been removed from the spectrum nor has the spectrum been flux calibrated. The boxes indicate parts of spectrum that are affected by sky or telluric lines.

in the UVB+VIS spectrum is ~ 7 per pixel. No telluric correction was applied, so that prominent atmospheric absorption bands can still be seen in the final spectrum in Figure 3.2.

Because the near-infrared spectrum suffers seriously from sky-line residuals using the current pipeline, we limit our analysis to the UVB-VIS region of the spectrum and defer a full analysis of the infrared data to future work.

In this chapter, we base our stellar mass determinations solely on the broad-band colors from the SDSS plus the stellar kinematic and lensing data. We will present our spectroscopic stellar-population analysis in the following chapters.

3.3 Stellar Kinematics

We measure the luminosity-weighted velocity dispersion (LOSVD) of the lens galaxy from the final 1D UVB–VIS spectrum using the Penalized Pixel Fitting (pPXF) code of Cappellari & Emsellem (2004), already described in Chapter 2. pPXF extract the stellar mean velocity and velocity dispersion (v and $\sigma_\star$, respectively), plus their uncertainties from absorption-line spectra of galaxies,

Table 3.2: Observational details of the Cosmic Horseshoe

Observation Block	Date	Exp. time (sec)	Seeing
200200337	17-3-2010	3 x 821(UVB - VIS) 3 x 3 x 274(NIR)	0.″62
200200343	17-3-2010	3 x 821(UVB - VIS) 3 x 3 x 274(NIR)	0.″56
200200436	19-3-2010	3 x 821(UVB - VIS) 3 x 3 x 274(NIR)	0.″66

using a maximum penalized likelihood approach. The S/N ratio of the data is inadequate to measure the higher order Gauss-Hermite moments h_3 and h_4, which quantify the asymmetric and symmetric departures of the LOSVD from a pure Gaussian (related to the skewness and kurtosis respectively). pPXF also allows the user to mask noisy or bad regions of the galaxy spectrum. We also perform an iterative sigma-clipping in order to clean the spectrum of residual bad pixels, sky lines and cosmic rays. We focus on absorption lines between 3500–5500 Å (including Ca K and H, G4300, H_β, Mg_b and some Fe lines). To minimize errors due to mismatch between the resolution of the templates and the galaxy spectrum, we use X-Shooter stellar spectra obtained as part of the X-Shooter Stellar Library (XSL) survey (Chen et al. 2014 in prep.), with similar instrumental resolution (for the galaxy spectrum we use a 1.″5 slit, corresponding to $\sigma_{\rm instr} \sim 25\,{\rm km\,s^{-1}}$, while for the stellar templates the slit width is 0.″7,corresponding to $\sigma_{\rm instr} \sim 12\,{\rm km\,s^{-1}}$). An excellent fit is obtained with a weighted linear combination of a K1 giant template (57%) and a G2 star template (43%). The selected region of the galaxy spectrum used for the fit and the corresponding best fit stellar template are shown in Figure 3.3.

3.3.1 Luminosity-Weighted Kinematics

The measured luminosity-weighted velocity dispersion for the central aperture of $1.''8 \times 1.''6$ is $\langle\sigma_\star\rangle = 352 \pm 10 \pm 16\,{\rm km\,s^{-1}}$. The only velocity dispersion value previously published for the Cosmic Horseshoe is from Belokurov et al. (2007). They perform fits of Gaussian line profiles to the Ca H and K absorption lines from a much lower resolution spectrum (FWHM~ 10 Å). They find a higher velocity dispersion estimation of $430 \pm 50\,{\rm km\,s^{-1}}$, inconsistent with our high-quality data. The formal error on the dispersion includes both the random error

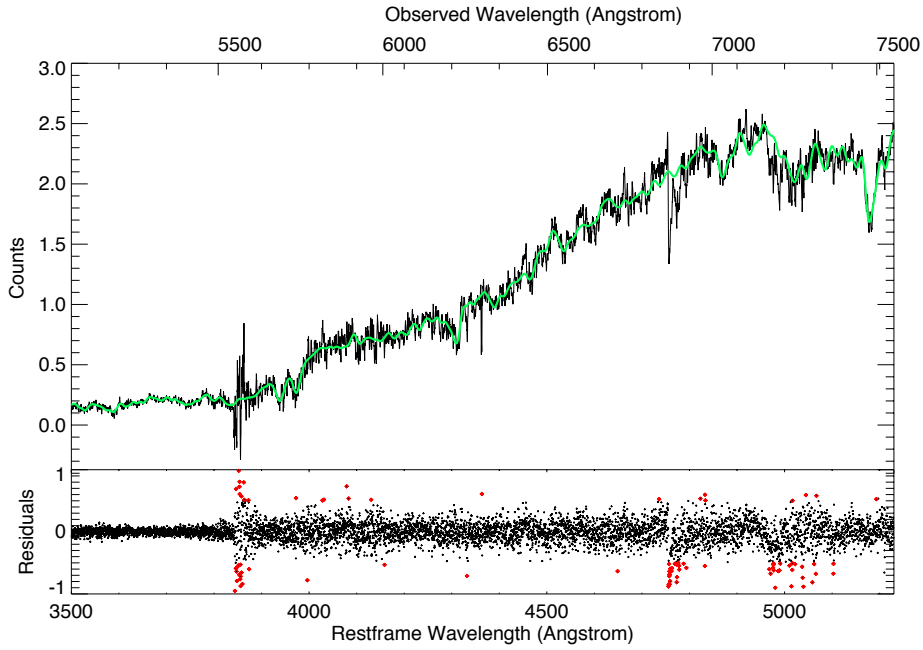

Figure 3.3: *Top panel:* Logarithmically rebinned UVB+VIS galaxy spectrum (black) and logarithmically rebinned best-fit template (green), both in restframe wavelength. *Bottom panel:* Residuals from the fit. Bad-pixels excluded from the fitting procedure (sky line, telluric lines) are shown in red. See the text for more information.

contribution and the systematic uncertainties due to spectral range differences, template mismatch and continuum fitting as discussed below. Figure 3.3 shows the best fitting template of the pPXF routine superimposed on the galaxy spectrum as well as the residuals of the fit.

As a first test of the accuracy of our measurements, we use the more heterogeneous MILES[3] stellar template library of Sánchez-Blázquez et al. (2006)). We select 100 stars (F, G, K, M) in the range 3525–7500 Å, with 2.3 Å FWHM spectral resolution. The measured luminosity-weighted stellar velocity dispersion of $\langle\sigma_\star\rangle = 358 \pm 31$ km s^{-1}, after instrumental correction, is consistent with the

[3] http://www.iac.es/proyecto/miles/pages/stellar-libraries/miles-library.php

above estimate, based on XSL templates, but has larger errors due to the lower resolution of the MILES library. As a second test, we fit templates to two different spectral regions. We find slightly different results between the blue and the red part of the spectrum, but always consistent within 2σ (not including systematics). The scatter in these fits is used to estimate additional systematic uncertainties related to template mismatches and spectra coverage.

3.3.2 Spatially-Resolved Kinematics

To preserve the spatially-resolved kinematic information, we define seven spatially-varying apertures (with adequate S/N ratio) along the radial direction and we sum the signal within each aperture. Apertures are defined to be larger than the seeing, in order to have independent kinematics measurements for each aperture. The stellar rotation velocity and velocity dispersion are measured in each aperture using pPXF, as described above. Again, we use different spectral regions, excluding the most prominent telluric lines in the VIS range and a range of seven XSL stellar templates (G, K and M stars). The uncertainties on the inferred kinematics are estimated by adding in quadrature the formal uncertainty given by pPXF and the scatter in the results for different templates and spectral regions. Details of the aperture sizes and the kinematic profiles are listed in Table 3.3. The rotation and the velocity dispersion profiles are shown is Figure 3.4.

We find an almost flat velocity dispersion profile beyond the effective radius ($R_{\rm eff}$). The weighted average value of 344 ± 25 km s^{-1} is consistent within the formal error with the luminosity weighted value for an aperture of $1.8'' \times 1.6''$ (see Tab. 3.3), as expected. The velocity profile shows some mild rotation, with a projected rotation velocity of ~ 140 km s^{-1} at $1\,R_{\rm eff}$. Because the second moment ($v^2_{\rm rms} = \sqrt{v^2 + \sigma^2}$; see Cappellari 2008) is well within the errors on σ, the effect of rotation can be neglected in our spherical Jeans analysis and we will ignore rotation in the remainder of this chapter.

3.4 Stellar and dark matter

In the following Section we derive the slope of the total density profile and calculate the fraction of dark matter inside one effective radius.

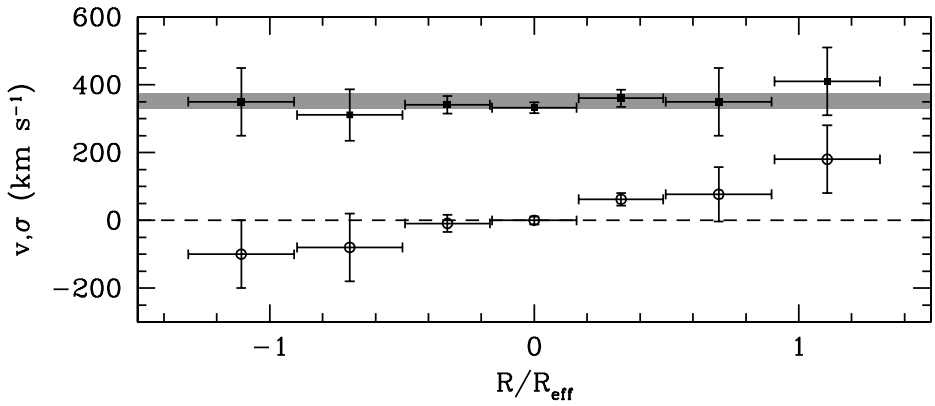

Figure 3.4: Kinematic profiles of the Cosmic Horseshoe. Rotation (bottom) and velocity dispersion (top). Grey line shows the light-weighted value for the central aperture.

3.4.1 The Galaxy Mass Model

To derive the stellar mass inside the Einstein radius, we follow Treu & Koopmans (2002, 2004); Koopmans & Treu (2003). We model the mass distribution as a superposition of the stellar and the dark matter components. For the stellar mass distribution we use two different spherical models, described by the equation:

$$\rho_\star(r) = \frac{(3-n)M_\star r_\star}{4\pi r^n (r+r_\star)^{4-n}} \tag{3.1}$$

The Hernquist (1990) luminosity-density profile has $n = 1$, and the Jaffe (1983) luminosity-density profile has $n = 2$. The total stellar mass is $M_\star$ and the break-radius is $r_\star$.

We model the dark matter distribution as a generalized spherical NFW profile (Frenk et al. 1985, using a break radius of $r_b = 50\,\mathrm{kpc}$, typical of massive ETGs (although the result is insensitive to its exact value), and an outer slope of $\gamma_{\mathrm{out}} = 3$ (Gavazzi et al. 2007; Auger et al. 2010a), following the prediction from numerical simulations of dark matter halos (Ghigna et al. 2000):

$$\rho_{\mathrm{DM}}(r) = \frac{\rho_{d,0}}{(r/r_b)^{-\gamma}[1+(r/r_b)^2]^{(\gamma-3)/2}} \tag{3.2}$$

The break radius and the density scale ($\rho_{d,0}$) determine the virial mass of the dark matter halo (Bullock et al. 2001).

For completeness, we also use a single mass component model where the stellar and dark matter mass densities add to a power-law with an effective density slope γ' for $\rho_{\rm tot} \propto r^{-\gamma'}$ and the stars are treated as trace particles (see Koopmans & Treu 2003).

The most accurately known constraint from the lens mass model is the mass inside the Einstein radius ($R_{\rm Ein}$). We use $M_{\rm Ein} = (5.02 \pm 0.09) \times 10^{12}\, M_{\odot}$ inside $R_{\rm Ein} = 5\farcs1$ derived by Dye et al. (2008). The mass components must add to $M_{\rm E}$ within the $R_{\rm Ein}$. The error in radius is folded into the error in mass so that a fixed radius can be used (the mass and Einstein radius are coupled in the modeling). We use the average of the two effective radii from the g and i band images reported in Belokurov et al. (2007), $R_{\rm eff}$= 1.96 ± 0.02 arcsec (Table 3.1). The effective radius is uniquely related to $r_{\star}$ (see Hernquist 1990 and Jaffe 1983).

We also assume a constant orbital anisotropy parameter β and allow it to range between 0.0 and 0.5, which is typical for massive ETGs (e.g. Gerhard et al. 2001). The parameters of the model without a strong prior are then the stellar mass ($M_{\star}$) and the dark matter density slope (γ), or only γ' for the single-component model. We subsequently solve the spherical Jean equations and compare the models to the kinematic data, taking the aperture sizes and seeing into account.

For the single component model, we find an effective density slope of γ' = $1.72^{+0.05}_{-0.06}$ (68% C.L.) when marginalizing over β = 0.0–0.5, shallower than isothermal (see Koopmans et al. 2006, 2009). This slightly low value for the logarithmic total-density slope may suggest that this object can be a group, or a small cluster of galaxies, where the overall efficiency of converting gas into stars is lower, and where typically the overall mass density profile in the corresponding region is shallower than isothermal (e.g. Newman et al. 2011). Changing the luminosity-density profile also does not change the final logarithmic slope significantly. The more interesting case of the two component model will now be discussed.

3.4.2 The Stellar Mass Fraction from Lensing and Kinematic Constraints

To derive the stellar mass fraction inside the Einstein radius, we create a densely sampled grid of likelihood values by comparing the kinematic profiles to the data for a projected stellar mass fraction within the Einstein radius [$f_{\star}(<R_{\rm Ein})$] ranging between 0 and 1 and a dark matter density slope (γ) ranging between 0.0 and 2.0. We assume flat priors on both quantities and marginalize over γ to derive the probability density function of $f_{\star}(<R_{\rm Ein})$. The results for the Hernquist and

Table 3.3: Spatially resolved kinematics of the Cosmic Horseshoe.

Aperture center ($''$)	**Aperture dimension($''$)**	v ($\mathrm{km\,s^{-1}}$)	$\sigma_\star$ ($\mathrm{km\,s^{-1}}$)
0.00, 0.00	1.80×1.60	0 ± 15	352 ± 10
$-2.16, 0.00$	0.80×1.60	-100 ± 100	350 ± 100
$-1.36, 0.00$	0.80×1.60	-80 ± 100	311 ± 76
$-0.64, 0.00$	0.64×1.60	-9 ± 25	341 ± 26
$0.00, 0.00$	0.64×1.60	0 ± 12	332 ± 16
$+0.64, 0.00$	0.64×1.60	62 ± 18	360 ± 25
$+1.36, 0.00$	0.80×1.60	77 ± 80	350 ± 100
$+2.16, 0.00$	0.80×1.60	180 ± 100	410 ± 100

Jaffe profiles are shown in Figure 3.5 for $\beta = 0$ and a more extreme case of radial anisotropy with $\beta = 0.5$. Taking as reference the best fit parameters of the Sersic profile computed in Dye et al. (2008): $n = 5.40 \pm 0.04$, $r_0 = 3.9 \pm 0.1$, $L_{1/2} = 61.2 \pm 0.4$), with the form :

$$L = L_{1/2} \exp\{-B(n)[(r/r_0)^{1-n} - 1]\} \tag{3.3}$$

we conclude that Hernquist and Jaffe profiles fit well the observed luminosity profile of the galaxy within the effective radius (with a slight preference for the Hernquist model).
We find a fraction of stellar mass within the Einstein radius for the two luminosity profiles of:

$$f_{\star,\mathrm{HQ}} = 0.19^{+0.04}_{-0.09} \text{ and } f_{\star,\mathrm{JF}} = 0.13^{+0.03}_{-0.05} \text{ for } \beta = 0$$

and

$$f_{\star,\mathrm{HQ}} = 0.13^{+0.04}_{-0.07} \text{ and } f_{\star,\mathrm{JF}} = 0.11^{+0.02}_{-0.05} \text{ for } \beta = 0.5$$

We note that in projection, the lens galaxy is already fully dark matter dominated inside ~ 2.5 effective radii. For comparison with previous work, we also derive the dark matter fraction inside the effective radius and find $f_{\mathrm{DM}}(<R_{\mathrm{eff}}) = 0.60^{+0.15}_{-0.06} \pm 0.1$ [68% confidence level (C.L.)] for $\beta = 0$, including a systematic uncertainty of 0.1. The random error is based on the marginalized probability densities shown in Figure 3.5 and a systematic error is included based on the maximum range of possible dark matter density slopes. Although the latter is constrained by

the models, we extrapolate inward from $R_{\rm Ein}$ to $R_{\rm eff}$, where this slope could be somewhat different. We note though that the systematic error is rather conservative. The dark matter fraction increases by ~ 0.1 for $\beta = 0.5$ and the difference between the Hernquist and Jaffe profiles is negligible (by construction, since they both contain equal fractions of mass inside that radius). This high dark matter fraction inside the effective radius is consistent with the result found in Auger et al. (2010b) for SLACS systems and is consistent with the dark matter fraction within the effective radii being a monotonically-increasing function of galaxy mass.

3.4.3 Stellar Mass Fraction from Stellar Population Constraints

We independently calculate the projected stellar mass fraction inside the Einstein radius using stellar population synthesis models and the SDSS colors (see Table 3.1) of the lens galaxy. A comparison between this fraction and that derived from lensing and stellar kinematics provides a direct constraint on the stellar IMF (see also, e.g. Treu et al. 2010; Auger et al. 2010b).

We use GALAXEV, a library of evolutionary stellar population synthesis models computed using the isochrone synthesis code of Bruzual & Charlot (2003). This code allows one to compute the spectral evolution of stellar populations for a wide range of ages and metallicities. Here we use the 2007 version of GALEXEV kindly provided by S. Charlot (a version commonly known as 'CB07'). We use six Simple Stellar Populations (SSP) models computed with a Salpeter IMF (Salpeter 1955) or a Chabrier IMF (Chabrier 2003) for a range of metallicities from $Z = 0.0001$ to $Z = 0.05$, all of them with lower mass cutoff of $M_{\rm low} = 0.1\,M_\odot$ and upper mass cutoff of $M_{\rm up} = 100\,M_\odot$. The spectral resolution is 3 Å across the wavelength range of 3200–9500 Å.

We compute the spectral evolution of the stellar population and the redshift dependence of colors and magnitudes in the SDSS filters g, r, i, and z for all SSP models and for a range of ages and star formation histories (SFH). For the SFH model, we use an exponentially declining star formation rate (SFR) with time-scales $\tau = 0.1$ to 0.4 Gyr and as extreme cases an instantaneous burst with $\tau = 0$ or a constant SFR. We compute the redshift evolution of the galaxy colors and magnitudes for a start of star formation between 12 to 5 Gyr, corresponding to a formation redshift of between roughly $z \sim 5$ and ~ 0.5. By comparing the model magnitudes to the SDSS magnitudes, we subsequently determine a grid (as function of age, metallicity and SFH duration) of likelihood values for each model

as well as the total stellar mass. We do this for both the Salpeter and Chabrier IMFs.

We use the standard Bayesian approach, as outlined in Auger et al. (2009), to determine the posterior probability distribution function and the marginalized errors on the total stellar mass of the galaxy, assuming flat priors on all parameters in logarithmic space (e.g. a prior $\propto 1/\tau$ for τ). The latter assumption is not critical, but given that the time-scale of the SFH, etc., are unknown *a priori*, this prior is a better description of our ignorance before making the observations (and modeling). From the resulting cumulative probability function, we calculate the median of the total stellar mass and its 68% confidence interval for both IMFs. Using the observed brightness profile of the galaxy modeled as a Hernquist, Jaffe or de Vaucoulers profile (the precise choice is not critical), we determine the fraction of the stellar mass (assuming a constant mass-to-light ratio, Υ) within the Einstein radius. The results of this analysis are listed in Table 3.4, where we report the inferred total stellar mass fraction for each assumed IMF as well as that from lensing and kinematics.

We find that, for the range of assumed luminous profiles and anisotropies, the stellar mass fraction from lensing agrees remarkably well with that from stellar population modelling assuming a Salpeter IMF (Fig. 3.5). This result further supports the results found by Treu et al. (2010) that the IMF slope of massive early-type lens galaxies is well-matched by an evolved Salpeter IMF. They found a tentative trend of the IMF slope with galaxy velocity dispersion, with a 'light' IMF such as a Chabrier IMF is inappropriate for systems with $\sigma_\star \geq 200\mathrm{km\,s^{-1}}$. This trend may imply a non-universal IMF, perhaps dependent on metallicity, age, or abundance ratios of the stellar populations. Alternatively, it may imply non-universal dark matter halos with inner density slope increasing with velocity dispersion. While the degeneracy between the two interpretations cannot be broken without additional information, the Treu et al. data imply that massive ETGs cannot have both a universal IMF and universal dark matter halos. This is confirmed by the expanded analysis of Auger et al. (2010b), who added weak-lensing data to constrain the halo model, finding that the data for massive galaxies are inconsistent with a Chabrier universal IMF for a range of realistic halo profiles, including various recipes to account for baryonic effects. The same result is also confirmed by the following chapters of this thesis.

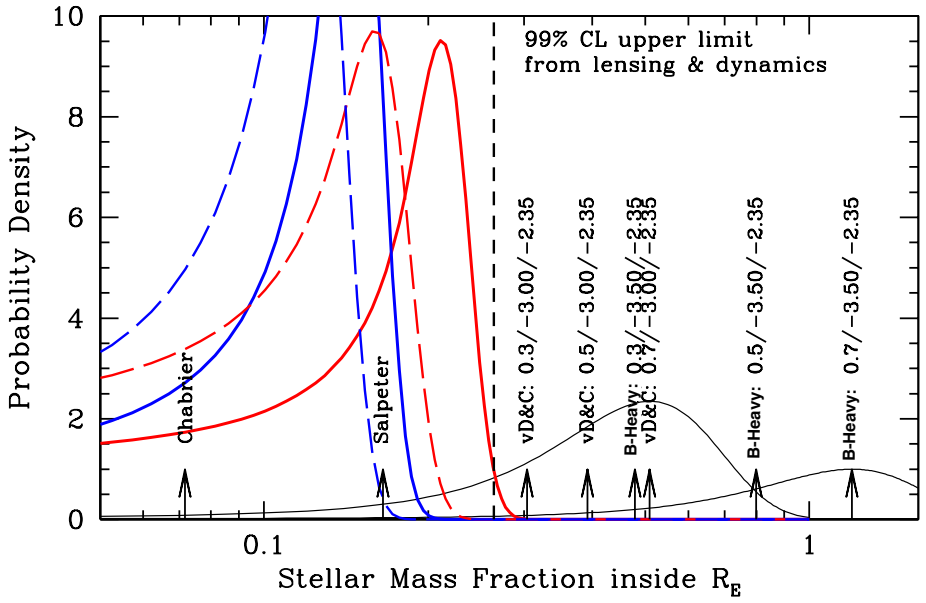

Figure 3.5: Marginalised PDF for the Hernquist model (red lines) and the Jaffe model (blue lines) from our lensing and dynamics model. Solid lines are for an anisotropy parameter of $\beta = 0.0$, and dashed lines for $\beta = 0.5$. Black arrows show the internal stellar mass fractions with different IMFs from our stellar population analysis. Black lines represent PDFs of vDC10 IMF and of the most extreme bottom-heavy IMFs. In the labels, the first number represents the break radius, the second is the IMF slope at lower masses ($m \leq m_{\rm break}$) and the last number is the slope at higher masses (fixed to Salpeter slope). We exclude the Chabrier IMF and the $x = 3$ IMFs at a confidence level of $\geq 90\%$ and the extreme bottom-heavy ($x = 3.5$) IMFs at a confidence level of 99%, while the Salpeter IMF is fully consistent with lensing data.

3.5 Bottom-heavy IMFs

Recently, van Dokkum & Conroy (hereafter vDC10; 2010) have suggested the presence of a large number of stars with masses $\leq 0.3\,M_{\odot}$ in the central regions of massive early-type galaxies. By measuring the strength of the NaI doublet and the Wing-Ford molecular FeH band in the spectra of eight of the most luminous and massive ETGs in the Virgo and Coma clusters, they infer that the IMF for these systems might even be steeper than Salpeter, with a slope as steep as $x = 3$. They also test even more 'bottom-heavy' IMF with $x = 3.5$ and 'bottom-light' (dwarf deficient) IMF but they find the best fit between stellar population synthesis models and spectrum around the NaI doublet with the $x = 3$ IMFs, although the uncertainties are large and Salpeter cannot be excluded with high-confidence.

Here, we investigate this claim by assuming a broken power-law IMF, with the Salpeter slope in the high-mass regime that dominates the SDSS magnitides (i.e. changes in the IMF below this break do not affect the stellar-population analysis carried out above) and a steeper profile in the low-mass range. We test three different values of the break point in the mass function: $m_{\rm break} = 0.3, 0.5$ and $0.7\,M_{\odot}$, respectively. Changing the IMF for stars with $M \leq m_{\rm break}$ does not change the SDSS colors because $\geq 90\%$ of the light in the spectral region we studied here is coming from stars with $M \geq 0.7\,M_{\odot}$. On the other hand, it dramatically changes the total stellar mass of the system, because stars with masses of 0.1–$0.3\,M_{\odot}$ can contribute at least 60% of the stellar mass for these bottom-heavy IMFs (Worthey 1994).

We calculate the change in total stellar mass arising from the change in the slope of the IMF:

$$\Delta M = \int_{0.1\,M_{\odot}}^{m_{\rm break}} \left[\left.\frac{dN}{dm}\right|_{\rm IMF} - \left.\frac{dN}{dm}\right|_{\rm Salp} \right] m\,dm, \tag{3.4}$$

where

$$\left.\frac{dN}{dm}\right|_{\rm IMF} = \begin{cases} \left(\frac{m}{m_{\rm break}}\right)^{-\eta} & \text{if } m_{\rm break} < m \leq 100\,M_{\odot} \\ \left(\frac{m}{m_{\rm break}}\right)^{-x} & \text{if } 0.1\,M_{\odot} < m \leq m_{\rm break} \end{cases}, \tag{3.5}$$

with $\eta = 2.35$ (Salpeter slope), $x = 3$ for the bottom-heavy IMFs suggested by van Dokkum & Conroy (2010) or $x = 3.5$ in the most extreme case.

Our results for the bottom-heavy stellar mass fraction are listed in Table 3.4. We also list the likelihood ratios between the nominal isotropic Hernquist model lensing and dynamic stellar mass fraction and the stellar mass fractions obtained

from stellar populations and colors for the different IMFs (equivalent to $\Delta\chi^2$ if the distribution was Gaussian, which we assume as a first approximation), comparing their maximum *a posteriori* difference with the no-difference hypothesis. Vertical arrows in Figure 3.5 show the stellar mass fractions predicted by stellar population synthesis models and SDSS color by these different IMFs and the stellar mass fraction obtained with lensing and dynamics. Using $m_{\rm break} = 0.7\,M_\odot$ and a bottom-heavy IMF, we find that inferred stellar mass fraction exceeds unity for $x = 3.5$, inconsistent with the lensing mass. An extreme 'bottom-heavy' IMF with slope of $x = 3.5$ is inconsistent at the $> 90\%$ C.L. with the lensing and kinematic results. The $x = 3$ model is only marginally consistent for $m_{\rm break} = 0.3\,M_\odot$ but is also excluded at the $> 90\%$ confidence level for $m_{\rm break} = 0.7\,M_\odot$. A Salpeter IMF gives the best agreement with the lensing and kinematics. It is important to mention that we do not include any possible effects of large-scale structure line-of-sight (LOS) contamination (e.g. from a group elongated along the line of sight), that would decrease the total mass assumed here. Recalling Treu et al. (2009) and Guimarães & Sodré (2011), SLACS lenses are shown to be an unbiased sample in relation to a random LOS, despite the fact that the lenses are elliptical galaxies, which are often found in dense regions. Moreover, other possible explanations, such as a top-heavy IMF with more black holes and neutron stars remnants, are still possible. As discussed in van Dokkum (2008), top-heavy IMFs have fewer low-mass stars than a standard Salpeter IMF but many more high-mass stars. Nevertheless, it is important to clarify that since our method only infers the overall Υ, we cannot distinguish a Salpeter IMF from a bottom-light IMF like a Chabrier IMF due to the presence of remnants (Treu et al. 2010; Auger et al. 2010b).

Table 3.4: The stellar mass fractions within the Einstein Radius derived from lensing plus stellar kinematics and from stellar population synthesis models, respectively. The likelihood ratio compares the maximum a-posteriori difference between the SSP model and the no-difference (null-hypothesis) model with the isotropic Hernquist model, which has the highest inferred stellar mass fraction. The IMF slope is assumed to be $x = 2.35$ beyond the break $m_{\rm break}$ in the mass function. The probabilities in between parentheses represent for each IMF the fraction probability that a given PDF (P_0) matches the max probability.

Lensing and Kinematic model	**Anisotropy**	**Stellar Mass Fraction**
Hernquist	$\beta = 0.0$	$0.19^{+0.04}_{-0.09}$
	$\beta = 0.5$	$0.13^{+0.04}_{-0.07}$
Jaffe	$\beta = 0.0$	$0.13^{+0.03}_{-0.05}$
	$\beta = 0.5$	$0.11^{+0.02}_{-0.05}$

Stellar Population Model	$\mathbf{m_{break}}$ ($M_\odot$)	**Stellar Mass Fraction**	$\mathbf{2\ln(P_{max}/P_0)}$ (HQ versus SSP)
Chabrier $x = 1.8$	0.07 ± 0.02	3.0 (0.08)	
Salpeter $x = 2.35$	0.17 ± 0.06	0.1 (0.75)	
vDC10 $x = 3.0$	0.3	0.30 ± 0.11	1.0 (0.32)
vDC10 $x = 3.0$	0.5	0.39 ± 0.15	1.9 (0.17)
vDC10 $x = 3.0$	0.7	0.51 ± 0.18	3.0 (0.08)
Bottom-heavy $x = 3.5$	0.3	0.48 ± 0.17	2.8 (0.09)
Bottom-heavy $x = 3.5$	0.5	0.80 ± 0.29	4.5 (0.03)
Bottom-heavy $x = 3.5$	0.7	1.19 ± 0.43	5.0 (0.03)

3.6 Summary & Conclusions

In this chapter we presented the first results from the new spectroscopic survey of massive early-type lens galaxies presented in this thesis: the X-Shooter Lens Survey (XLENS). The combination of high-fidelity UVB+VIS spectroscopy from

the X-Shooter instrument on the VLT, with the strong gravitational lensing mass determination has enabled us to conduct an in-depth study of the internal structure of the luminous elliptical galaxy SDSS J1148+1930 at $z = 0.444$. We find the following:

- The luminosity-weighted stellar velocity dispersion is $\langle\sigma_\star\rangle(\leq R_{\rm eff}) = 352 \pm 10 \pm 16$ km s^{-1}, more accurate and considerably lower than a previously published value of ~ 450 km s^{-1}.

- A single-component (stellar plus dark) mass model of the lens galaxy yields a logarithmic total-density slope of $\gamma' = 1.72^{+0.05}_{-0.06}$ (68% C.L.; $\rho_{\rm tot} \propto r^{-\gamma'}$).

- The projected stellar mass fraction, derived solely from the lensing and dynamical data, is $f_\star(<R_{\rm Ein}) = 0.19^{+0.04}_{-0.09}$ (68% C.L.) inside the Einstein radius for a Hernquist profile and no anisotropy. The dark matter fraction inside the effective radius is $f_{\rm DM}(\leq R_{\rm eff}) = 0.60^{+0.15}_{-0.06} \pm 0.1$ (68% C.L.), where the latter error is systematic.

- Based on the SDSS colors, we find $f_{\star,{\rm Salp}}(<R_{\rm Ein}) = 0.17 \pm 0.06$ for a Salpeter IMF and $f_{\star,{\rm Chab}}(<R_{\rm Ein}) = 0.07 \pm 0.018$ for a Chabrier IMF. A Salpeter IMF gives the best agreement between lensing and dynamics constraints on the stellar mass fraction, therefore it is preferred to a Chabrier IMF. Dwarf-rich IMFs with $x \geq 3$ (with $dN/dM \propto M^{-x}$) in the lower mass range of 0.1–0.7 $M_\odot$, – such as those recently suggested by vDC10 for massive early-type galaxies ($x = 3$) – are excluded at the $> 90\%$ C.L. and in some cases ($x = 3.5$) violate the total lensing-derived mass limit.

This massive lens ETG lies at the extreme end of the trend found by, e.g., Auger et al. (2010b) that the dark matter fraction within the effective radii is a monotonically increasing function of galaxy mass. In fact SDSS J1148+1930 is already dark matter dominated within that region. We find that a Salpeter IMF agrees best with the total stellar mass derived from lensing and stellar kinematics as well as with its SDSS colors. As in Treu et al. (2010) and Grillo & Gobat (2010), a Salpeter IMF appears to be the best option for very massive early-type galaxies. Although slightly more massive IMFs cannot be excluded given the typical uncertainties. A bottom-light IMF such as a Chabrier (or Kroupa) IMF agrees only marginally and we exclude a steep 'dwarf-rich' IMF with $x = 3.5$ at $> 90\%$ C.L. Somewhat shallower IMFs with $x \approx -3.0$, as suggested by vDC10, are marginally acceptable. We conclude that our data are *fully* consistent with SDSS

J1148+1930 being a massive early-type galaxy that is dark matter dominated inside its effective radius and having a Salpeter IMF. No strong evidence for an even more bottom-heavy IMF is found, consistent with previous results (Treu et al. 2010), although uncertainties are still large.

Further studies are required to break the degeneracy between the central dark matter fraction and distribution and the stellar IMF. In forthcoming chapters, based on published papers of the XLENS survey, we present results in which we extended the study to more systems, performed more detailed stellar population analyses using the full UV-optical spectrum and obtained independent contraints on the the physical parameters that may correlate with IMF normalization (i.e., age and metallicity and effective temperature of the red-giant branch) or that may be the cause of the correlation between dark matter content and velocity dispersion.

4 Evidence for a mild steepening and bottom-heavy IMF in massive galaxies from Sodium and Titanium-Oxide indicators

The greatest challenge to any thinker is
stating the problem in a way that will allow a solution.

Bertrand Russell

Published as:

C. Spiniello, S.C. Trager, L.V.E. Koopmans, Y.P. Chen,
"Evidence for a mild steepening and bottom-heavy IMF in massive galaxies from Sodium and Titanium-Oxide indicators" 2012, ApJL, 753, L32

We measure equivalent widths (EW) – focussing on two unique features (Na I doublet and TiO2 molecular band) of low-mass stars ($\leq 0.3\,M_{\odot}$) – for luminous red galaxy spectra from the the Sloan Digital Sky Survey (SDSS) and X-Shooter Lens Survey (XLENS) in order to study the low-mass end of the IMF. We compare these EWs to those derived from simple stellar population models computed with different IMFs, ages, [α/Fe], and elemental abundances. We find that models are able to simultaneously reproduce the observed NaD λ5895 and Na I λ8190 features for the lower-mass ($\sim \sigma_{\star}$) ETGs but deviate increasingly for more massive ETGs, due do strongly mismatching NaD EWs. The TiO2 λ6230 feature and the Na I λ8190 feature, may be a powerful IMF diagnostic, with age and metallicity effects orthogonal to the effect of IMF on the feature's strength. We find that both features correlate strongly with galaxy velocity dispersion. The XLENS ETG (SDSSJ0912+0029) and one SDSS ETG (SDSSJ0041-0914) appear to require both an extreme dwarf-rich IMFs and a high sodium enhancement. However, lensing constraints on the total mass of the XLENS system within its Einstein radius limit a bottom-heavy IMF with a power-law slope to $x \leq 3.0$ at the 90% C.L. We conclude that Na I and TiO2 features, in comparison with state-of-the-art SSP models, suggest a mildly steepening IMF from Salpeter ($dN/dM \propto M^{-x}$ with $x = 2.35$) to $x \approx 3.0$ for ETGs in the range $\sigma_{\star} = 200 - 335\,\mathrm{km\,s^{-1}}$.

4.1 Introduction

When constraining the star formation, metallicity and gas/dust content of galaxies often the initial mass function (IMF) is assumed universal and equal to that of the solar neighborhood (Kroupa 2001; Chabrier 2003; Bastian, Covey & Meyer 2010). However, evidence has recently emerged that the IMF might evolve (Davé 2008; van Dokkum 2008) or depend on the stellar mass of the system (e.g. Worthey 1992; Trager et al. 2000b; Graves, Faber & Schiavon 2009; Treu et al. 2010; Auger et al. 2010b; Napolitano, Romanowsky & Tortora 2010; van Dokkum & Conroy 2010).

van Dokkum & Conroy (2010; hereafter vDC10) suggested that low-mass stars ($\leq 0.3\,M_{\odot}$) could be more prevalent in massive early-type galaxies. The increase in the mass-to-light ratio (Υ) of galaxies with galaxy mass may thus be partly due to a changing IMF rather than an increasing dark matter fraction, consistent with previous suggestions (Treu et al. 2010; Auger et al. 2010b; Barnabè et al. 2011; Dutton, Mendel & Simard 2012; Cappellari et al. 2012).

vDC10 showed that some spectral features, such as the Na I λ8183,8195 doublet (called NaI0.82 by vDC10), depend strongly on surface gravity at fixed effective temperature, betraying the presence of faint M dwarfs in integrated light spectra. If correct, the low-mass end of the IMF can be inferred directly from red/near-IR spectra of old populations. Hence, the strength of the Na I doublet versus another sodium feature, such as the NaD doublet (called Na0.59 by vDC10), should provide a powerful means for separating the IMF from other effects. Specifically for the purpose of determining the low-mass initial mass function (IMF) down to $\sim 0.1\,M_{\odot}$ for metal-rich stellar populations with ages of 3–13.5 Gyr, Conroy & van Dokkum (2012; hereafter CvD12) presented a new population synthesis model. The NaD feature responds more strongly to Na-enhancement than IMF in the CvD12 models (see also Chapter 7), while the Na I doublet is strong in stars with mass $< 0.3\,M_{\odot}$ and weak or absent in all other types of stars. Unfortunately, NaI is also sensitive to to age and metallicity, and NaD is influenced by interstellar medium present in a galaxy. It is therefore necessary to test these models over a range of age and metallicitity indicators, as well as against other lines caused by low-mass stars.

In this chapter, we focus on the NaI feature as indicator of low-mass stars. We use NaD as indicator of a change in sodium abundance and Hβ and [MgFe] [1] as indicators of age and metallicity, respectively. This allows us to assess model degeneracies and deficiencies. We propose the use of the TiO feature at λ6230 as indicator of the presence of low-mass stars. We find that both of these features (NaI and TiO) correlate with galaxy velocity dispersion, implying a steepening of the IMF slope in ETGs with $\sigma > \sigma_{\star}$.

4.2 The data

As part of the XLENS[2] project, we obtained UVB-VIS X-shooter spectrum of the massive and luminous early-type SLACS (Sloan Lens ACS Survey, Bolton et al. 2006) lens galaxy SDSS J0912+0029 at $z = 0.1642$, with high enough signal-to-noise to perform stellar population analyses. The lens galaxy shows a surprisingly deep Na I feature (Fig.4.1), making it an extremely interesting target for studying the low-mass end of the IMF in ETGs. We measure the luminosity-weighted velocity dispersion of the lens galaxy from the final reduced flux-calibrated 1D UVB–VIS spectrum using the Penalized Pixel Fitting (pPXF) code of Cappellari

[1] [MgFe] = $\sqrt{(\mathrm{Fe5270} + \mathrm{Fe5335})/2 \times \mathrm{Mg}b}$, González (1993)

[2] The X-Shooter Lens Survey, Spiniello et al. (2011) and Chapter 2

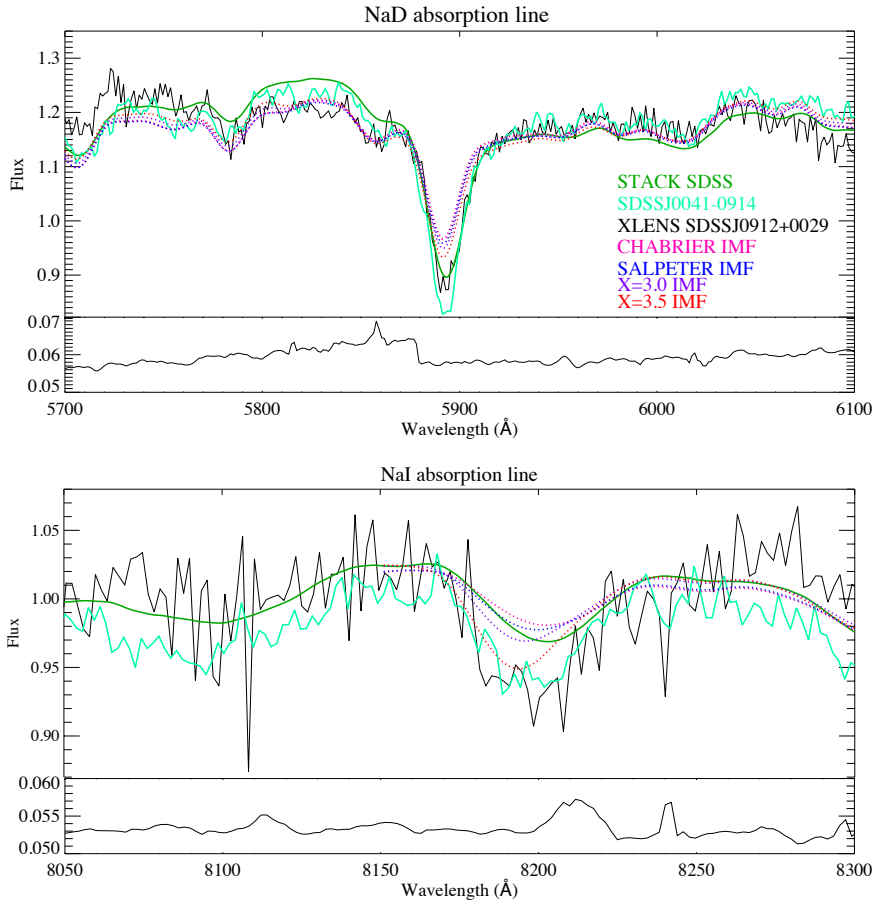

Figure 4.1: Galaxy (continuous lines) and model (dashed lines) spectra in the regions of the NaD (top) and NaI (bottom) features. The observed NaD EWs do not match the models for the most massive ETGs ($\geq 300\,\mathrm{km\,s^{-1}}$). Na I absorption is stronger in the XLENS system and SDSSJ0041-0914 and appears in both cases to require an IMF steeper than Salpeter, while the stacked SDSS spectrum shows a weaker Na I feature that matches a model with a Salpeter IMF. The bottom panels show the noise spectrum of the XLENS system.

& Emsellem (2004). We obtain $\langle\sigma_\star\rangle(\leq R_{\rm eff}) = 325 \pm 10 \pm 12\,{\rm km\,s^{-1}}$, in agreement with the previously published value ($\sigma_\star \simeq 313 \pm 12\,{\rm km\,s^{-1}}$; Bolton et al. (2006). We also used the spectra of ~50 galaxies with similar morphology and colors (all LRGs) from the Sloan Digital Sky Survey DR8 (SDSS; Aihara et al. 2011, in five velocity-dispersion bins spread over $200 - 335\,{\rm km\,s^{-1}}$. We examine one system, SDSSJ0041-0914, separately because it has a Na I feature comparably deep to the XLENS system.

4.3 Stellar Population Synthesis Modeling

We use the synthetic spectra of CvD12 to analyze the stellar populations of these galaxies. The models make use of two separate empirical libraries, the MILES library covering 3500–7400 Å (Sánchez-Blázquez et al. 2006) and the IRTF library of cool stars covering 8100–24000 Å (Cushing, Rayner & Vacca 2005; Rayner, Cushing & Vacca 2009). They also incorporate synthetic spectra with the purpose of investigating changes in the overall metallicity or changes in the abundances of individual elements and to cover the gap in wavelength between the two empirical libraries. We refer to CvD12 for details. The abundance variations of single elements are implemented at fixed [Fe/H], which implies that the total metallicity Z varies from model to model. We measure line-strength indices in the range 4000–8400 Å, including the standard Lick indices Hβ, Mgb, Fe5270, Fe5335, NaD and a TiO index (TiO2) using the definitions of Trager et al. (1998), and the commonly-used [MgFe] combination from González (1993). We define a modified index around the Na I doublet 8183, 8195 Å, which seems to be strongly dependent on the low-mass end of the IMF (Table 4.1). This index is slightly different from that used by vDC10 and CvD12, having a wider central index bandpass and slightly wider pseudo-continua. Our definition is more stable against velocity dispersion variations and more suitable for massive ETGs. We convolve all the galaxy and model spectra to an effective velocity dispersion of $\sigma_\star = 335\,{\rm km\,s^{-1}}$ (the upper limit in our sample) to correct for kinematic broadening, before measuring indices. Indices in both the observed and synthetic spectra are measured with the same definitions and method (SPINDEX2; Trager, Faber & Dressler 2008). We do not place our indices on the zero-point system of the Lick indices and quote them as equivalent widths (EWs) in units of Å, except for TiO2, which is given in magnitudes. Following Worthey (1994), an EW is

$$\mathrm{EW} = (\lambda_{\rm red} - \lambda_{\rm blue})(1 - F_I/F_C) \tag{4.1}$$

Table 4.1: Definition of the index around the Na I doublet

Index	Central band	Pseudocontinua
NaI	8168.500 – 8234.125	8150.000 – 8168.400
		8235.250 – 8250.000

where $\lambda_{\rm red}$ and $\lambda_{\rm blue}$ are the red and blue wavelength bounds of the index passband, F_C is the continuum flux and F_I is the continuum flux minus the absorption. An index expressed in magnitudes is instead:

$$\mathrm{Mag} = -2.5\log(F_I/F_C)\,. \tag{4.2}$$

4.4 Results and discussion

Hβ is primarily an age indicator, while a combination of Mgb, Fe5270, and Fe5335 yields information on the mean metallicity [Z/H] of the population (Worthey 1994) while minimizing the effects of abundance ratio variations (e.g. González 1993; Trager et al. 2000a). These indices (Panel (a), Fig. 4.2) show a good agreement between the models and the galaxies EWs for old stellar populations, with an age of 13.5 ± 3 Gyr for $\sigma_\star \geq 300\,\mathrm{km\,s^{-1}}$ (black points) and younger ages for lower mass ETGs. The statistical error is deduced directly from variations in Hβ[3]. The most massive ETGs have values of [α/Fe] between solar and super-solar (~0.2), in good agreement with the prediction that massive galaxies have significantly super-solar abundance ratios because of a rapid, high efficiency star formation (Trager et al. 2000b; Thomas et al. 2005; Spolaor et al. 2009, 2010). Given the uncertainties in the line-strengths of the two individual galaxies (SDSSJ0912+0029 and SDSSJ0041-0914), we are unable to determine their ages and metallicities precisely, but their line strengths are similar to the mean of the highest-mass SDSS sample, with a deviation from the average EW smaller than 1σ in both age and metallicity. The NaI and NaD indices can in principle be used to constrain the IMF slope (CvD12), and this relation is shown in Figure 4.2b. Although the data match the models for low-dispersion systems ($\leq 250\,\mathrm{km\,s^{-1}}$), the models with solar [Na/Fe] abundance do not match the NaD strengths and only models with [Na/Fe] = $+0.3 - 0.4$ dex match the NaD

[3]For stellar populations with ages > 10 Gyr, an uncertainty of 0.1 Å in Hβ corresponds to 1 Gyr uncertainty in the age (cf.Worthey 1994).

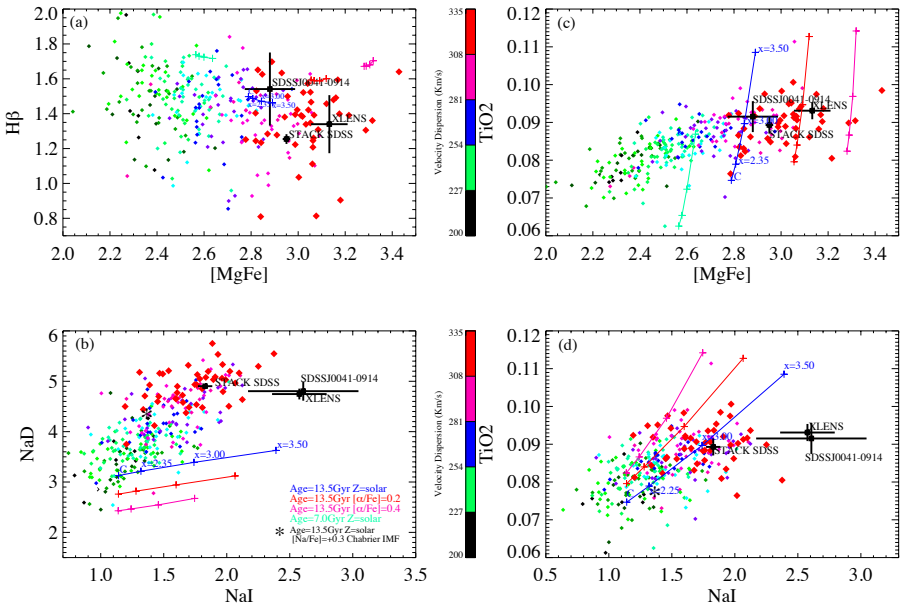

Figure 4.2: Index-index plots of the main absorption features. Lines and crosses are different SSP models from CvD12 with increasing IMF (Chabrier, Salpeter with a slope of $x = 2.35$, a bottom-heavy IMF with slope of $x = 3.0$ and an extremely dwarf-rich IMF with a slope of $x = 3.5$). Points colored according to their velocity dispersions are individual SDSS galaxies, with index errors similar to SDSS J0041-0914. In the plots showing sodium, the XLENS system SDSSJ0912+0029 requires a very steep IMF, violating lensing contraints on its total mass (see the text for further details). *Panel (a):* Hβ as a function of [MgFe]. The most massive ETGs ($> 300\,\mathrm{km\,s^{-1}}$) best match an old stellar population (13.5 Gyr) with super-solar total metallicity. Lower-mass systems are younger. *Panel (b):* NaD as a function of NaI. Only low-mass ($< 250\,\mathrm{km\,s^{-1}}$) systems match the models. More massive ETGs require a higher [Na/Fe] and the XLENS system and SDSSJ0041-0914 also require a very steep IMF slope. *Panel (c):* TiO2 as a function of [MgFe]. The most massive ETGs require an IMF slope slightly steeper than Salpeter. A Chabrier-type IMF systematically underestimates the SDSS TiO2 EWs. *Panel (d):* TiO2 as a function of NaI. The ETGs match with the models using a Salpeter or slightly steeper IMF, but the XLENS system and SDSSJ0041-0914 still do not match the SSP models well.

Table 4.2: Variation with IMF of $\Upsilon_\star$ and stellar mass fraction within the Einstein radius.

IMF slope	$(\Upsilon_\star)_{DSEP,B}$ ($[\alpha/\mathrm{Fe}]=0.0$)	$(\Upsilon_\star)_{DSEP,V}$ ($[\alpha/\mathrm{Fe}]=0.0$)	$f_B^\star$	$f_V^\star$
2.35	10.2 ± 3	7.2 ± 2	0.75 ± 0.2	0.59 ± 0.18
3.00	22 ± 6	16 ± 5	1.6 ± 0.5	1.4 ± 0.4
3.50	43 ± 13	29 ± 9	2.4 ± 0.8	2.4 ± 0.7

[1] The constraints on the mass and luminosity within the Einstein radius are taken from Auger et al. (2009) and Barnabè et al. (2009b). All quantities are calculated in the rest-frame V- and B-band.
[3] The IMF slope x is defined as: $dN/dM = M^{-x}$
[2] The fraction of stars within the Einstein radius is calculated as: $f^\star_{\mathrm{band}} = (L_{\mathrm{Ein}}/M_{\mathrm{Ein}}) \times (\Upsilon_\star)_{\mathrm{band}}$

indices for higher-mass ETGs. We suggest two possible explanations for this behavior. NaD could be highly contaminated by the interstellar medium (ISM) for higher mass ETGs; for example, dust lanes provide additional absorption in this resonance line (Sparks, Carollo & Macchetto 1997). Or these very massive ETGs have higher [Na/Fe] abundances (> 0.3 dex) *and* a bottom-heavy IMF that correlate with their stellar velocity dispersions. In both cases, the models seem consistent with a Salpeter IMF at the low-dispersion end, if these effects are accounted for, but the models predict a steeper IMF slope of $x \sim 3.0-3.5$ for both the XLENS galaxy SDSSJ0912+0029 and SDSSJ0041-0914. We note that a TiO feature at 8199 Å could partly contaminate NaI, although this feature should not vary strongly (CvD12). Overall we conclude that the NaD EWs and its trend with stellar mass remains unexplained for systems with $\sigma_\star \geq 250\,\mathrm{km\,s^{-1}}$. We find that SSP models predict that TiO features also depend strongly on the slope of the low-mass end of the IMF, such as TiO2, shown in Figure 4.2, panels (c) and (d). This indicator gives more support to the conclusion that the sodium strengths of the XLENS ETG, SDSSJ0912+0029, still remain somewhat difficult to explain by current stellar population models, although most SDSS systems can be matched in NaI for most ETGs (if not in NaD). Together the TiO2 and NaI indices both imply a bottom-heavy IMF, steepening from Salpeter to possibly $x \approx 3$ for the most massive SDSS ETGs. As in Treu et al. (2010), a bottom-light IMF such as Chabrier IMF is inappropriate for the most massive ETGs.

4.4.1 Limits on the IMF from Strong Lensing

A strong case against an extreme bottom-heavy IMF can be made using that system with the strongest NaI EW (Fig. 4.2), the XLENS galaxy SDSSJ0912+0029. This system provides a hard upper limit on the stellar mass inside its Einstein radius, no matter the IMF model. If we assume that the SSP models are correct and this galaxy has a high [Na/Fe] abundance, we infer an IMF with a power-law slope $x = 3$–3.5 at the low-mass end (where the IMF follows $dn/dm = m^{-x}$, and the Salpeter slope is $x = 2.35$). To assess whether these steep IMF slopes are consistent with the upper limit on the total mass, we calculate the total luminosity and the SSP stellar $\Upsilon_\star$ in stars for each assumed IMF to infer the stellar mass fraction inside the Einstein radius ($R_{\rm Ein} = 4.55 \pm 0.23$ kpc; Koopmans et al. 2006). Changes in the IMF of stars with $M \leq 0.3\,M_\odot$ change the total luminosity of the lens galaxy by at most $\sim 10\%$. Conversely, stars with masses of 0.1–$0.3\,M_\odot$ contribute $\geq 60\%$ of the stellar mass for bottom-heavy IMFs with slopes steeper than Salpeter (see, e.g., Fig. 2 of CvD12). To determine the stellar $\Upsilon_\star$, we use the isochrones at solar [Fe/H] and [α/H] for a 13.5 Gyr population from the Dartmouth Stellar Evolution Program (DSEP), a state-of-the-art stellar evolution code (Chaboyer, Green & Liebert 1999; Chaboyer et al. 2001). We compare three different IMFs: Salpeter ($x = 2.35$), a bottom-heavy IMF ($x = 3.0$) and a very bottom-heavy IMF ($x = 3.5$). CvD12 use the same isochrones in their SSP for the bulk of the main sequence and red giant branch, except at $M < 0.2\,M_\odot$, where they use the Baraffe et al. (1998) isochrones. For each IMF we compute the quantity

$$f^\star_{\rm Ein} = M^\star / M_{\rm Ein} = (L_{\rm Ein} / M_{\rm Ein}) \times \Upsilon_{\star,{\rm DSEP}},$$

where $M_{\rm Ein}$ is a robust measurement of the total mass enclosed within the physical Einstein radius [$M_{\rm Ein} = (39.6 \pm 0.8) \times 10^{10}\,M_\odot$], $L_{\rm Ein}$ is the luminosity enclosed within the Einstein radius, evaluated using B-spline luminosity models, as a fraction of de Vaucouleurs total model luminosity [$L_{\rm Ein} = (4.49 \pm 0.2) \times 10^{10}\,L_\odot$, from Bolton et al. (2008a)], and $\Upsilon_{\star,{\rm DSEP}}$ is the mass-to-light ratio from the DSEP isochrone using the appropriate IMF. The $\Upsilon_\star$ includes the contribution from stellar remnants and gas ejected from stars at the end of their life-cycles. We list the results of this calculation in Table 4.2. For a Salpeter IMF, the stellar mass fraction of SDSSJ0912+0029 in the restframe V-band is $f^\star_{\rm Ein,Salp} = 0.59 \pm 0.15$, in agreement with previous results (0.60 ± 0.09, Auger et al. 2009). The mass-to-light ratio calculated from the DSEP isochrone for a Salpeter IMF is $\Upsilon_{\star,V} = 7.2 \pm 2\,(\Upsilon_\star)_\odot$ in the V band and $\Upsilon_{\star,B} = 10.2 \pm 3\,(\Upsilon_\star)_\odot$ in the B band. The latter value is consistent with the upper limit of $\Upsilon_{\star,B} \leq 9.08\,(\Upsilon_\star)_\odot$ derived from

dynamical models of Barnabè et al. (2009b) under the maximum bulge hypothesis. An IMF slope of $x = 3.5$ yields $\Upsilon_{\star,V} = 29 \pm 9\,(\Upsilon_\star)_\odot$, and $\Upsilon_{\star,B} = 43 \pm 13\,(\Upsilon_\star)_\odot$ corresponding to $f^\star_{\mathrm{Ein},3.5} = 2.4 \pm 0.8$, inconsistent with the total lensing mass within the Einstein radius at the $> 95\%$ confidence level. An IMF of $x = 3.0$ in B-band also excluded at the $> 90\%$ level, as this corresponds to a fraction $f^\star_{\mathrm{Ein},3.0,B} = 1.6 \pm 0.5$. For both of the bottom heavy IMFs in B-band and for the $x = 3.5$ IMF in V-band, we therefore obtain a stellar mass fraction within the Einstein radius in excess of unity, thereby violating the lensing constraint on the total mass of the system at the $> 90\%$ CL. The $x = 3$ model is only marginally consistent in V-band, but $f^\star_{\mathrm{Ein},3.0,V} = 1.4 \pm 0.4$ implies that there is no dark matter within the Einstein radius.

4.4.2 Systematic uncertainties

The uncertainty on the value of $f^\star_{\mathrm{Ein}}$ has a number of contributions. However, the uncertainties in the mass and luminosity determinations from lensing are much smaller than differences in the values of $\Upsilon_\star$ arising from the use of different stellar population evolution models. The emerging picture is that, for a fixed IMF, it is difficult to constrain $\Upsilon_\star$ estimates to much better than 0.1 dex (Gallazzi et al. 2008; Marchesini et al. 2009; Longhetti & Saracco 2009; Conroy, Gunn & White 2009; Conroy, White & Gunn 2010). We study mass-to-light ratio values predicted for different IMF from different stellar population models in the rest-frame V- and B-bands and compare predictions from Worthey (1994); Bruzual & Charlot (2003); Maraston (2005), and Vazdekis et al. (2010) for single stellar populations with ages 11.2–14.1 Gyr, solar ($Z = 0.02$) or super-solar metallicity ($Z = 0.05$). For each SSP and each IMF, we calculate an average value and a standard deviation that we associate with the inferred values of $\Upsilon_\star$. Changing the [Fe/H] abundance from 0. to 0.22 yields a $\sim 9\%$ uncertainty on $\Upsilon_\star$, while changing the age of the stellar population changes $\Upsilon_\star$ by $\sim 20\%$ at fixed IMF. The latter is the dominant contribution to the final uncertainties. We propagated these errors in to the stellar mass fraction. The errors on the stellar mass fractions in Table 4.2 include both the random error contribution and the systematic uncertainties due to the use of different set of isochrones, bands, and stellar population age and metallicity uncertainties.

4.5 Conclusions

In this chapter we have studied the Na I λ8190 and TiO λ6230 features – both indicators of low-mass ($< 0.3\,M_{\odot}$) stars in massive ETGs – as a function of each other, of age and metallicity indicators (Mgb, Fe, Hβ), of NaD, and of stellar velocity dispersion. We find the following:

- The observed NaI-NaD trend depends strongly on stellar velocity dispersion of ETGs and only match current state-of-the-art SSP models for ETGs with $\sigma_{\star} \leq 250\,\mathrm{km\,s^{-1}}$. The most extreme NaI index strength in our sample is found in a gravitational lens system, which should have an IMF slope $x \geq 3.0$ based on the best current SSP models. The total enclosed mass of this system, however, excludes slopes steeper than $x = 3.0$ at the $> 90\%$ C.L. or slopes steeper than $x = 3.5$ at the $> 95\%$ C.L. We conclude that the NaD feature is still affected by as-of-yet not understood processes in the more massive ETGs ($\sigma_{\star} > 250\,\mathrm{km\,s^{-1}}$). A full spectral comparison, in combination with lensing and dynamical constraints, is planned to further strengthen these results and assess whether NaI and NaD (in some instances) are contaminated.

- We find that the TiO feature at $\lambda \sim 6230$Å (TiO2) is a particularly promising feature to decouple the IMF from stellar population, age, metallicity, and abundance pattern, especially when combined with metallicity-dependent indices. We find that this feature correlates well with NaI, if the two most extreme cases as discussed in the text, are excluded.

- We find a clear trend of an increasing IMF slope between $\sigma_{\star} = 200$ to $335\,\mathrm{km\,s^{-1}}$ from Salpeter ($x = 2.35$) to $x \approx 3.0$, in agreement with the XLENS system that excludes steeper IMFs at the high mass end.

Our results are the first SSP-based indications of a steepening of the low-mass end of the IMF with increasing galaxy mass *within* the class of LRG/ETGs. Our results (i) support a similar trend first found by Treu et al. (2010), (ii) extend the evidence based on SSP models that the IMF steepens from spiral to early-type galaxies (vDC10), and (iii) support a similar trend found by Cappellari et al. (2012) based on stellar kinematics. The upper limit of $x \leq 3.0$, based on one of the most massive ETG system in our sample, a gravitational lens, also supports our previous similar finding (Spiniello et al. 2011).

5 The stellar IMF in early-type galaxies from a non-degenerate set of optical line indices.

Real is what can be measured.
Max Planck

Based on:

C. Spiniello, S.C. Trager, L.V.E. Koopmans, C.Conroy
"The stellar IMF determined in early-type galaxies from a non-degenerate set of optical line indices" 2013, submitted to MNRAS

We investigate the optical spectral region of spectra of ∼ 1000 stars searching for IMF-sensitive features to constrain the low-mass end of the initial mass function (IMF) slope in elliptical galaxies. The use of indicators bluer than NIR features (NaI, CaT, Wing-Ford FeH) is crucial if we want to compare our observations to optical simple stellar population (SSP) models. We use the MILES stellar library (Sánchez-Blázquez et al. 2006) in the wavelength range 3500–7500 Å to select indices that are sensitive to cool dwarf stars and that do not or only weakly depend on age and metallicity. We find several promising indices of molecular TiO and CaH lines. In this wavelength range, the response of a change in the effective temperature of the cool red giant (RGB) population is similar to the response of a change in the number of dwarf stars in the galaxy. We therefore investigate the degeneracy between IMF variation and $\Delta T_{\rm eff,RGB}$ and show that it is possible to break this degeneracy with the new IMF indicators defined here. In particular, we define a CaH1 index around λ6380 Å that arises purely from cool dwarfs, does not strongly depend on age and is anti-correlated with [α/Fe]. This index allows the determination of the low-mass end of the IMF slope from integrated-light measurements when combined with different TiO lines and age- and metallicity-dependent features such as Hβ, Mgb, Fe5270 and Fe5335. The use of several indicators is crucial to break degeneracies between IMF variations, age, abundance pattern and effective temperature of the cool red giant (RGB) population. We measure line-index strengths of our new optical IMF indicators in the Conroy & van Dokkum (2012a) SSP models and compare these with index strengths of the same spectral features in a sample of stacked Sloan Digital Sky Survey (SDSS) early-type galaxy (ETG) spectra with varying velocity dispersions. Using 10 different indicators, we find a clear trend of a steepening IMF with increasing velocity dispersion from 150 to 310 km s^{-1} described by the linear equation $x = (2.3 \pm 0.1) \log \sigma_{200} + (2.13 \pm 0.15)$, where x is the IMF slope and σ_{200} is the central stellar velocity dispersion measured in units of 200 km s^{-1}. We compute the "IMF mismatch" parameter as the ratio of stellar mass-to-light ratio predicted from the $x-\sigma_{200}$ relation to that inferred from SSP models assuming a Salpeter IMF and find good agreement with independent published results.

5.1 Introduction

The stellar contribution to the mass budgets of early-type galaxies (ETGs) is a crucial ingredient to fully understand the internal structure, the formation and the

evolution of these massive galaxies (e.g. Blumenthal et al. 1984). In ETGs the stellar mass-to-light ratio ($\Upsilon_\star$) scales with the luminous mass of the system (Grillo et al. 2009; Barnabè et al. 2011; Dutton, Mendel & Simard 2012; Cappellari et al. 2012; Tortora, Romanowsky & Napolitano 2013), but it has also been shown recently that, for the assumption of a universal initial mass function (IMF), the dark matter (DM) fraction in the internal region of these systems increases with the mass of the galaxy (e.g. Zaritsky, Gonzalez & Zabludoff 2006b; Auger et al. 2010a; Treu et al. 2010; Barnabè et al. 2011). Disentangling the relative contributions of baryonic and dark matter constituents of ETGs is therefore crucial to fully comprehend the processes that shape the hierarchical galaxy formation scenario (e.g. White & Rees 1978; Davis et al. 1985; Frenk et al. 1985).

A quantitative study of the luminous unresolved stellar content of distant galaxies requires the use of stellar population synthesis models (Worthey 1994; Renzini 2006; Conroy 2013). By comparing colors, line-strength indices or full spectral energy distributions (SEDs) in galaxy spectra with predictions from single stellar population (SSP) models (which assume a single epoch of star formation rather than an extended SFH), it is possible to derive stellar parameters such as luminosity-weighted age, metallicity, $\Upsilon_\star$, IMF slope and elemental abundances for a galaxy (Worthey 1994; Trager et al. 2000a,b). However, it remains difficult to trace a galaxy's full star formation history (SFH), to break the age-metallicity degeneracy (Worthey 1994) and to study possible correlation of IMF slope and $\alpha-$enhancement variation with galaxy masses (Spinrad 1962; Spinrad & Taylor 1971; Cohen 1978; Frogel et al. 1978; Frogel, Persson & Cohen 1980; Faber & French 1980; Carter, Visvanathan & Pickles 1986; Hardy & Couture 1988; Couture & Hardy 1993; Worthey 1994; Cenarro et al. 2003).

In the last two decades a crucial assumption has been made in constraining the star formation history of galaxies through SSPs: the IMF is assumed to be universal and equal to that of our Milky Way (Kroupa 2001; Chabrier 2003; Bastian, Covey & Meyer 2010). In the past years, evidence has emerged that the IMF might evolve (Davé 2008; van Dokkum 2008) and may depend on the (stellar) mass of the system (e.g. Treu et al. 2010; Auger et al. 2010b; Napolitano, Romanowsky & Tortora 2010; van Dokkum & Conroy 2010; Spiniello et al. 2011, 2012). Recently, van Dokkum & Conroy (2010), hereafter vDC10, have suggested that low-mass stars ($\leq 0.3\,M_\odot$) could be much more prevalent in massive early-type galaxies (ETGs) than previously thought. This could imply that the increase in the $\Upsilon_\star$ with galaxy mass is due to a steeper low-mass end of the IMF rather than an increasing fraction of internal DM (Treu et al. 2010; Auger et al. 2010a; Barnabè et al. 2011; Dutton, Mendel & Simard 2012; Cappellari et al. 2012;

Spiniello et al. 2012).

Strong absorption features that vary with surface gravity at fixed effective temperature and that can be used to count stars with masses $\leq 0.3\,M_{\odot}$ (M dwarfs) are mainly present in the red-optical and near-infrared spectral region (vDC10, Smith, Lucey & Carter 2012). At these wavelengths galaxy stellar emission is dominated by evolved stellar populations, i.e. red giant branch (RGB) and asymptotic giant branch (AGB) stars (e.g. Worthey 1994; Renzini 2006), whose physics is not yet well understood, because their lifetime is very short and mass-losses are very high (e.g. Reimers 1975). Moreover, AGB stars are also highly variable (e.g. Blöcker 1995). In the optical spectral region, on the other hand, M dwarfs contribute at most 5% to the total light of the integrated spectrum, despite dominating the total stellar mass budget in galaxies (Worthey 1994). The light in ETGs is dominated by K and M giants, that, to the first order, have spectra similar to the one of an M dwarf, because of the similar spectral type. However the spectra of M dwarfs and M giants with similar effective temperature show minor but important differences. Careful line-index strength measurements of multiple spectral indices (or full spectral fitting: Conroy & van Dokkum 2012b) are necessary to reveal these spectral differences at the percent level and to break degeneracies, enabling one to observe variations of IMF with galaxy mass if present.

Two new SSP models have recently been published specifically for the purpose of measuring the IMF slope down to $\sim 0.1\,M_{\odot}$ for old, metal-rich stellar populations. Conroy & van Dokkum (2012a), hereafter CvD12, built models over the wavelength interval $0.35\,\mu m < \lambda < 2.4\,\mu m$ at a resolving power of R $\sim$ 2000, using a combination of two empirical stellar libraries (MILES, Sánchez-Blázquez et al. 2006; and IRTF, Cushing, Rayner & Vacca 2005) and three sets of isochrones. Vazdekis et al. (2012) recently built the MIUSCAT models, an extension in wavelength of the Vazdekis et al. (2003a,b, 2010) models.

All other available models in the NIR are based on theoretical atmospheres and stellar libraries (Maraston 2005; Bruzual & Charlot 2003), which have only been tested by fitting broadband colors and do not reproduce line indices measurements of clusters and galaxies (Lyubenova et al. 2012). The CvD12 and MIUSCAT models are therefore the state-of-the-art of SSP models.

Both models allow for different IMF slopes and a range of ages, but while the CvD12 models use solar metallicity isochrones and synthesize models with different abundance patterns, MIUSCAT models use different total metallicities but do not allow one to change the abundances which are fixed to solar. Non-solar abundance patterns appear to be a necessary ingredient to properly assess the non-

universality of the IMF, especially in massive ETGs, which may have undergone a star formation histories different from the solar-neighbourhood (Peterson 1976; Peletier 1989; Worthey 1992; Trager et al. 2000b; Arrigoni et al. 2010). The CvD12 models allow for a variation in [α/Fe] as well as the abundance pattern of 11 different elements. This is particularly important in the case of sodium lines, especially when including the NaD index. As shown in Conroy & van Dokkum (2012a,b) and confirmed in Spiniello et al. (2012) (Chapter 4), more massive systems seem to be Na-enhanced ([Na/Fe] $\sim$ 0.3–0.4 dex), consistent with values obtained for the bulge of the Milky Way (on average [Na/Fe] $\sim$ 0.2, Fulbright, McWilliam & Rich 2007; see Chapter 7 (Spiniello et al., in prep.) for a detailed study of the impact of models with and without variable abundance patterns on the determination of the low-mass IMF slope in ETGs. We therefore use the CvD12 models in this study to have the required ability to decouple IMF variations from abundance variations. Moreover, CvD12 also include the possibility to change the effective temperature of the red giant branch (RGB), taking into account that the isochrones should change with abundance pattern.

In the blue region (3500–7500 Å) the CvD12 and MIUSCAT models use the same empirical spectral library (MILES), while in the red and NIR they make use of two different libraries (CVD12 uses IRTF, MIUSCAT uses Indo-US, Valdes et al. 2004, and CaT, Cenarro et al. 2001). The use of optical indicators allows us to reduce the uncertainties caused by different assumptions of different SSP models in the synthesis process (e.g. their spectral libraries).

Conroy & van Dokkum (2012b) clearly show that there is information on the IMF slope in the blue spectral range, the goal of this work is to recover and quantify this information. We find a set of optical IMF-sensitive spectral indicators that allow us to decouple the effects of a varying IMF from age, metallicity and/or elemental abundance variations, and the effective temperature of the RGB, when studying the stellar populations of massive ETGs. A direct comparison of the variation of index strengths with IMF slope predicted from the SSP models with the variation of index strengths determined from SDSS spectra allows us to understand whether the recent suggestion that the IMF steepens with increasing galaxy velocity dispersion is genuine or arises from a misunderstanding of the main ingredients of SSP models.

In this work (i) we focus on line-index measurements rather than full spectral fitting, which avoids issues with spectral calibration when comparing to observations that might have been poorly calibrated and (ii) we assume an SSP, rather than an extended SFH, which is still a strong assumption and will be properly addressed in future works. The Chapter is organized as follows.

In Section 5.2 we present a new set of IMF-sensitive indicators along with a brief introduction of the MILES library. In Section 5.3 we compare line-index variations as function of the IMF slope from single MILES stars and the CvD12 SSP model. In Section 5.4 we compare the models with SDSS galaxies. We summarize our findings and discuss our conclusions in Section 5.5.

5.2 New optical IMF-sensitive indices

Stellar spectral features that show different strengths in M-dwarfs and cool giants, including NaI, Wing-Ford FeH, CaT and CaI, can potentially reveal a galaxy's low-mass stellar content in spectra of unresolved stellar populations (e.g. Spinrad 1962; Faber & French 1980; Schiavon et al. 1997; Schiavon, Barbuy & Singh 1997; Schiavon, Barbuy & Bruzual A. 2000; Cenarro et al. 2003). These are mainly present in the red-optical and near-infrared part of the spectra. However, optical spectra are easier to obtain with current spectrographs than NIR (1–2 μm) spectra. Moreover, near-infrared spectra are contaminated by the presence of strong sky lines and telluric absorption arising from water vapour (e.g. Stevenson 1994). A proper measurement of equivalent widths (EW) in the red part of the spectrum relies heavily on the correct removal of these lines. It is therefore important to search for IMF-sensitive features in the blue-optical spectral region, where the SSP models are less affected by these uncertainties and different assumptions. However one has to keep in mind that blue-optical spectral features are more sensitive to stars of earlier spectral types.

5.2.1 Searching for IMF-sensitive features in the MILES Library

We searched for spectral features that would be sensitive to IMF variations in SSPs by searching for features that appear solely in cool dwarf stars in the the MILES empirical spectral stellar library (Sánchez-Blázquez et al. 2006), the same library used by the CvD12 and MIUSCAT models. The MILES library consists of $\sim$ 1000 stellar spectra obtained at the 2.5m INT telescope. It covers the wavelength range 3525–7500 Å with 2.51 Å (FWHM) spectral resolution and spans a large range in atmospheric parameters: [Fe/H]= [−2.86, 1.65], $\log g$=[−0.2, 5.5] and $T_{\rm eff}$= [2747, 36000]. Using these spectra, we identified a number of potentially interesting stellar features that could be used to constrain the low-mass end of the IMF. We plotted the ratio between spectra of a cool giant ($T_{\rm eff} \sim 3300K$) and a cool dwarf ($T_{\rm eff} \sim 2800K$), both with roughly solar metallicity, to select these spectral features. We inspected this ratio looking for wavelength regions with

large residuals. We identified seven interesting regions, including four new and previously unidentified features, and defined absorption-line indices for these. Moreover, we ran a principal component analysis on the SSP models to isolate features that strongly depend on temperature and gravity. The final IMF-sensitive indices we have found and use here are listed in Table 5.1. We note that TiO and CaH indices are measured in magnitudes, while NaD is measured in Å.

Figures 5.1 and 5.2 show index strengths of these indices for single MILES stars as a function of temperature (left panels), gravity (middle panels) and metallicity (right panels). The figures clearly show that all the selected stellar absorption features are very weak in main-sequence stars (MS) and intermediate-temperature stars and are strong in cool dwarfs and giants – except CaH1, which is only strong in cool dwarfs–.

More than half of the selected indices come from TiO molecular absorption bands (Fig. 5.1). The effect of TiO lines in stellar atmospheres has been extensively studied over the years (Jorgensen 1994; Allard, Hauschildt & Schwenke 2000; Valenti, Ferraro & Origlia 2010) and red TiO lines have already been recognized to be good IMF indicators (Chapter 4, Spiniello et al. 2012, Chen et al. 2013, in prep.). Our bluest feature is around $\lambda \sim 4770$ Å: we call it blue-TiO and define a new index (bTiO, Table 5.1). Although a similar index was already used in Serven, Worthey & Briley (2005), who named it Mg4780, we are confident that this absorption is due to TiO molecular lines, whose strength is very large in very cool dwarf and giant stars and smaller for intermediate-mass M stars, as shown in the middle panel of Figure 5.1. The aTiO index, defined around the α-TiO feature (Jorgensen 1994), is also strongly IMF-sensitive. A possible issue with this feature is the presence in its central bandpass of the very strong [OI] λ5577 Å sky emission line. Any contamination from sky lines could affect the response to gravity of the spectral index defined around aTiO. However from Figure 5.1 it appears that the subtraction of the emission line in the library stars is sufficient, as the behaviour of aTiO seems to be similar to that of bTiO and TiO2 (i.e., stronger EWs for cool giants and dwarfs). The TiO2 feature ($\lambda \sim 6230$ Å) was already found to be promising in constraining the low-mass end of the IMF slope (see Chapter 4, Spiniello et al. 2012), but it also shows a weak dependence on metallicity and α-element variation (Chen et al. 2013, in prep). The NaD feature, although gravity-sensitive, also depends strongly on abundance (in particular this index is ~ 4 times more sensitive to variation in the [Na/Fe] abundance than to variation of the IMF slope, as shown in Chapter 7 (Spiniello et al., 2013, in prep.) and may be contaminated by the interstellar medium (see Chapter 4, Spiniello et al. 2012).

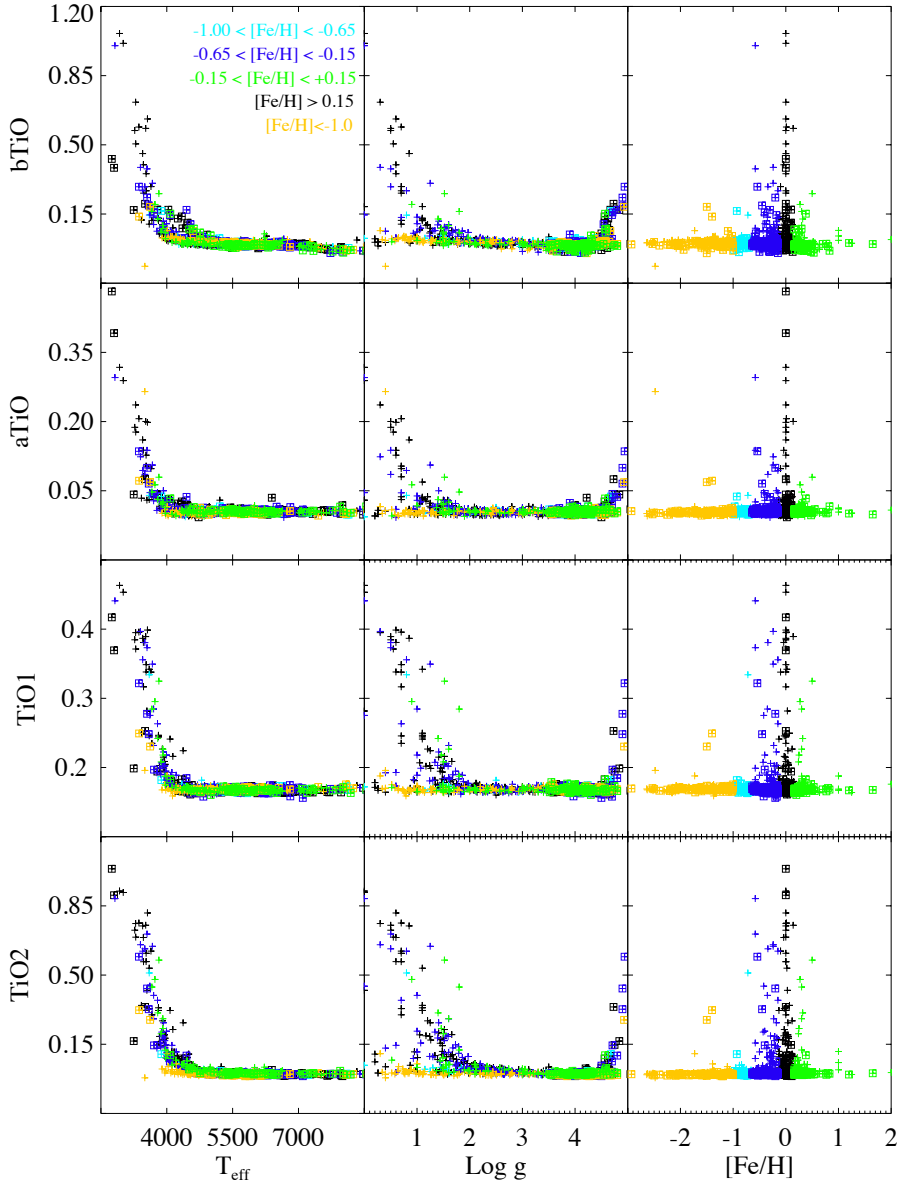

Figure 5.1: Index strengths of TiO indices for single stars from the MILES library plotted as function of temperature, gravity, and [Fe/H], at the original MILES resolution. The points are coded by $\log g$: crosses are mostly giants, and squares are dwarfs. The colors refer to [Fe/H], as seen in the upper-left panel. All TiO indices are very strong in cool stars ($T < 4100K$). From the middle panel, it is clear that the indices are stronger in giants (i.e. $\log g < 3.0$) and M dwarfs (i.e. $\log g > 3.8$) than in warmer main-sequence stars.

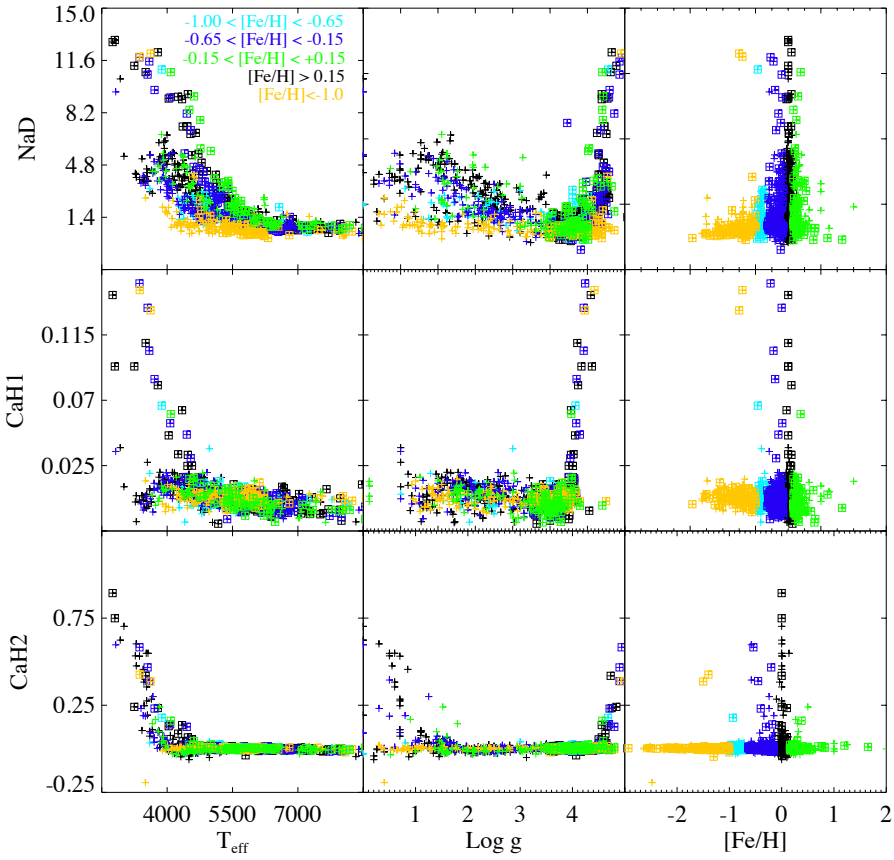

Figure 5.2: EWs of CaH and NaD indices for single stars from the MILES library plotted as function of temperature, gravity, and [Fe/H], at the original MILES resolution. The points are coded by $\log g$: crosses are mostly giants, and squares are dwarfs. The colors refer to [Fe/H], as seen in the upper-left panel. The middle row shows the only feature which is very strong only in cool stars ($T < 4500K$) with high gravity (i.e. $\log g > 3.8$): CaH1. This index allows us to count the M-dwarf population in a galaxy spectrum.

Table 5.1: Definition of the IMF-sensitive indices used in this Chapter. TiO and CaH indices are measured in magnitudes, while NaD is measured in Å

Index	Central band (Å)	Pseudo-continua (Å)
bTiO	4758.500 – 4800.000	4742.750 – 4756.500
		4827.875 – 4847.875
aTiO	5445.000 – 5600.000	5420.000 – 5442.000
		5630.000 – 5655.000
NaD	5876.875 – 5909.375	5860.625 – 5875.625
		5922.125 – 5948.125
TiO1	5936.625 – 5994.125	5816.625 – 5875.625
		6038.625 – 6103.625
TiO2	6189.625 – 6272.125	6066.625 – 6141.625
		6372.625 – 6415.125
CaH1	6357.500 – 6401.750	6342.125 – 6356.500
		6408.500 – 6429.750
CaH2	6775.000 – 6900.000	6510.000 – 6539.250
		7017.000 – 7064.000

As a sanity check, we show spectra of single dwarf stars with similar gravity ($\log g$ = 4.6–5) at different values of $T_{\rm eff}$ in the left panels of Figure 5.3 in order to ensure that these indices are stronger in cool dwarfs than in warm ones. The right panels of Figure 5.3 show instead spectra of single cool giants with a range of effective temperatures. bTiO and TiO2 are clearly stronger in cool stars but they behave similarly in giants and dwarfs, therefore they do not allow one to disentangle between these two classes of stars and between a top-heavy and a bottom-heavy IMF by themselves.

However, the CaH1 index around λ6380 Å (Fig. 5.2), is strong only in cool dwarfs. We believe that this feature is the most robust optical feature to estimate the IMF in this particular wavelength region, because it allows us to disentangle the contribution of RGB stars from the cool M-dwarf population when combined with age- and metallicity-sensitive features. CaH features were first detected in spectra of M dwarfs by Fowler (1907) and then studied in detail by Öhman (1934). Already in that paper Öhman pointed out that the CaH band at 6390 Å (corresponding to our CaH1 index) is strong in M-dwarf spectra and almost absent in M giants. Mould (1976) realized that the behaviour of CaH in stellar atmospheres is strongly influenced by gas pressure over the formation of

the molecule, and therefore he used the CaH band as a luminosity indicator of cool stars in low resolution spectra. He also studied the sensitivity of the CaH band strength to gravity, clearly confirming that CaH bands are very weak or absent in giants. Finally, Barbuy et al. (1993) presented a study of the intensity of CaH bands as a function of stellar temperature and gravity. Their results are qualitatively consistent with ours in the sense that CaH absorption lines are stronger in dwarfs and tend to disappear in giants. We refer to section 5.4 of Conroy & van Dokkum (2012a) for a useful sketch of the basic physics involved.

This brief historical overview demonstrates that it has been known for a hundred years that certain spectral features depend strongly on surface gravity at fixed effective temperature and therefore betray the presence of faint M dwarfs in integrated light spectra.

From Figure 5.3, it is clear that the spectrum of a cool giant is similar to that of a cool dwarf. We therefore also investigate the response of variation in the effective temperature of red-giant branch versus the response in variation of the IMF slope, to ensure that the degeneracy between $T_{\rm eff,RGB}$ and IMF slope can be broken by our optical IMF indicators. Indeed, one of the problems that one faces when using indices bluer that ~ 7500 Å is that the effects of a varying IMF and of a varying $T_{\rm eff}$ of the isochrones are very similar, as shown in Figure 5.4.

In the figure we plot the continuum normalized response to IMF variation and variation of the value of $T_{\rm eff}$ of the RGBs as a function of wavelength. As expected, the IMF variation is *almost* completely overwhelmed by $T_{\rm eff}$ variation. However, the two curves differ in their responses around bTiO, aTiO and CaH1. Therefore only the use of the full set of lines allows one to separate IMF and $T_{\rm eff}$ effects. By combining blue spectral features that strongly depend on age, metallicity and elemental abundance with surface-gravity-sensitive features, such as TiO and CaH lines, we can jointly constrain these effects and the low-mass end of the IMF in integrated optical-light spectra of distant ETGs.

5.3 SSP models

After the recent suggestion by vDC2010 that the low-mass end of the IMF slope may be not universal and might depend on the stellar mass of the system (Treu et al. 2010; Spiniello et al. 2011, 2012; Cappellari et al. 2012, CvD12), new SSP models with varying IMFs have been developed. One of these is CvD12, who presented SSP models with variable abundance patterns and stellar IMFs suitable for studying the integrated-light spectra of galaxies with ages > 3 Gyr.

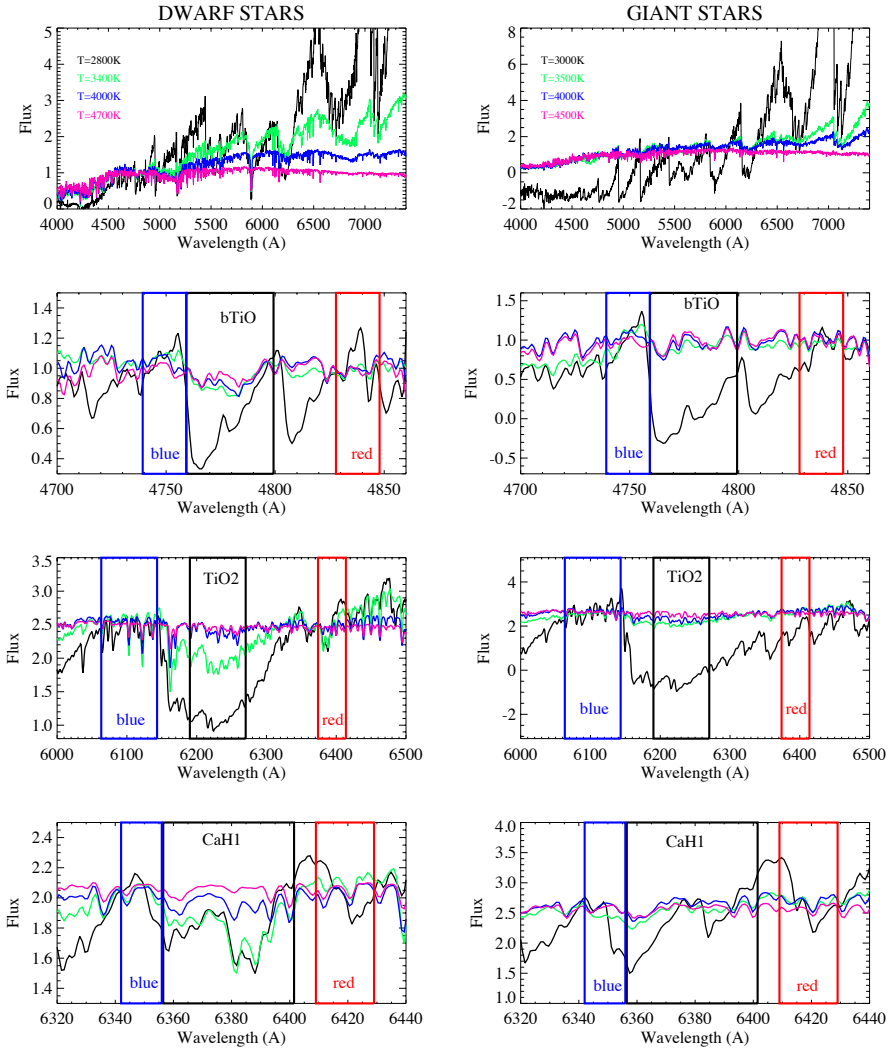

Figure 5.3: *Left panels:* Individual MILES dwarf stars with similar surface gravities ($\log g \sim 5$) and different $T_{\rm eff}$. *Right panels:* Individual MILES giants with similar surface gravities ($\log g \sim 0.5$) and different $T_{\rm eff}$. In the bottom three rows, we show a zoom into different absorption feature regions. Red and blue boxes are the blue and red pseudo-continua bands of the indices. Both bTiO and TiO2 absorption are stronger in cool stars but are present in both dwarfs and giants. The CaH1 index instead only comes from cool dwarfs.

CvD12 synthesized stellar atmospheres and spectra using the combination of three different isochrones to describe separate phases of stellar evolution: the Dartmouth isochrones (Dotter et al. 2008) for the main sequence and the red giant branch (RGB); the Padova isochrones (Marigo et al. 2008) to describe AGB evolution and the horizontal branch (HB); and the Lyon isochrones (Chabrier & Baraffe 1997; Baraffe et al. 1998) for the lower-mass main sequence ($M_\star \leq 0.2\,M_\odot$). All of the CvD12 models use *solar* metallicity isochrones, even when synthesizing with different abundance patterns or different [α/Fe].

The models are based on empirical stellar libraries, modified using theoretical stellar atmosphere models and their emergent synthetic spectra, and therefore they are somewhat restricted in their SSP parameter coverage (especially at high metallicity and for non-solar abundance ratios) and poorly-calibrated against mass loss in advanced stages, such as the asymptotic giant branch (AGB). Stars in these phases provide a non-negligible contribution to the red spectrum of galaxies (Worthey 1994). This contribution is however hard to quantify because RGBs and AGBs are so short-lived that good statistics are hard to obtain from color-magnitude diagrams of globular and open clusters. Moreover, mass loss, which is a crucial ingredient to calculate the precise evolutionary path of AGB, is very hard to model and therefore is a main source of uncertainties in the models (e.g. Blöcker 1995).

The CvD12 models explore variations in age in the range 3–13.5 Gyr, $\alpha-$enhancement of 0–0.4 dex, individual elemental abundance variations and four different IMFs: a bottom-light Chabrier (2003) IMF, a Salpeter (1955) IMF with a slope of $x = 2.35$ (where x is the IMF slope, using $dN/dm \propto m^{-x}$), and two bottom-heavy IMFs with slopes of $x = 3.0$ and $x = 3.5$.

Fig 5.5 shows index strengths versus IMF slope for different ages (different colors) and [α/Fe] (symbols) for a number of features from the CvD12 SSP models. Most of the classical blue Lick indices (e.g. Hβ, [MgFe]: González 1993; Worthey 1994; Trager et al. 2000a) do not show a strong variation with the IMF slope, although they are important in constraining the age and metallicity of galaxies. Index strengths of the newly defined bTiO and aTiO and the redder TiO indices clearly increase with steeper IMF slopes, but they also increase for higher [α/Fe]. On the other hand, the CaH1 index strength decreases with increasing [α/Fe]. This makes the combination of TiO lines and CaH1 absorption a very good IMF probe, as the effects of [α/Fe] and varying IMF slope are orthogonal in a TiO-CaH plot.

We note that other models, such as Thomas et al. (2011), do not find a strong sensitivity of the TiO indices to [α/Fe]. The reason why previous models for

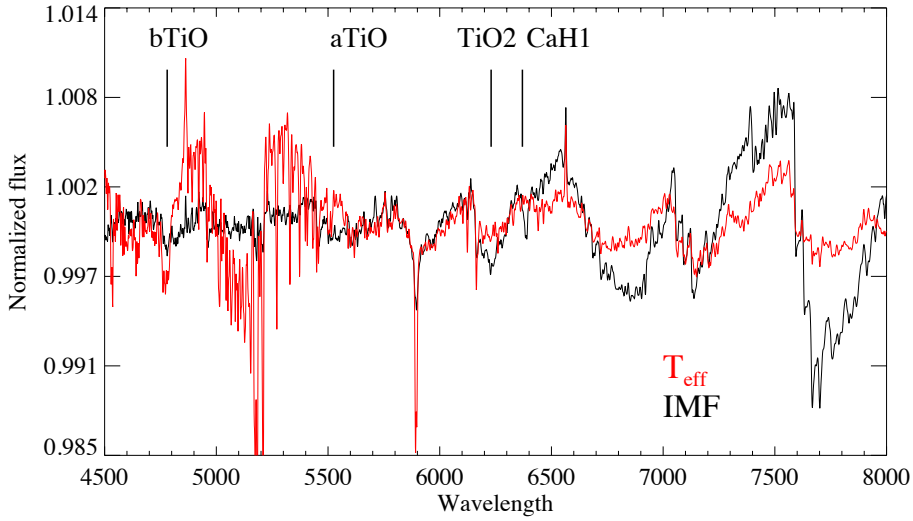

Figure 5.4: Relative effect on the spectrum of IMF and $T_{\rm eff}$ variations. Blueward of $\sim$ 7500 Å the effects are almost perfectly degenerate while they decouple redward of TiO2 and CaH1. The response of the two curves however is different around specific features. This makes their combination a powerful tool to decouple the variations.

TiO indices differ from CvD12 is that the old response functions (including Korn, Maraston & Thomas 2005, used in e.g., Thomas et al. 2011) do not include TiO molecules, so they will not be able to reproduce the TiO sensitivities.

The dependence on age of index strengths is smaller for almost all the indicators if we restrict ourself to ages $\geq$ 7 Gyr. A caveat of our analysis is that the response functions of CvD12 do not currently include the CaH molecule. However observations of Ca indices indicate a nearly solar [Ca/Fe] abundance in galaxies (Vazdekis et al. 1997; Worthey 1998; Trager et al. 1998; Cenarro et al. 2003; Smith et al. 2009) and therefore this limitation in the response functions is unlikely to impact our results.

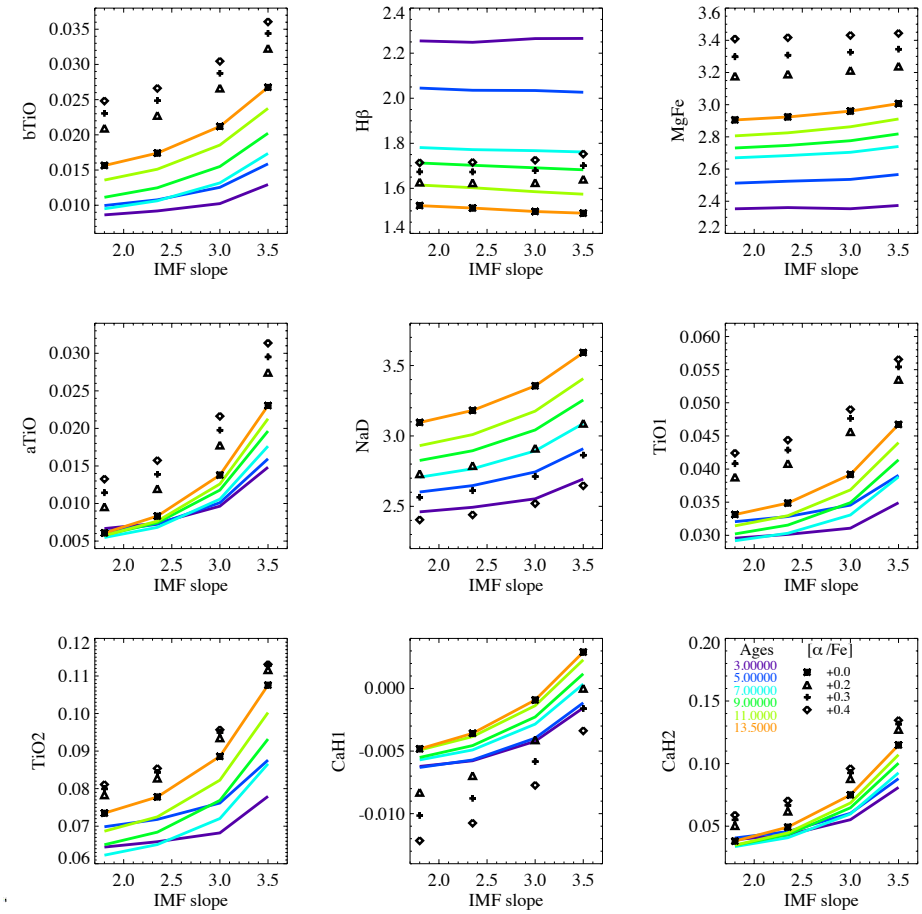

Figure 5.5: Variation of index strengths with IMF slope for CvD12 models in the MILES wavelength range and with a resolution of $\sigma = 350\,\mathrm{km\,s^{-1}}$. In each panel, different colors represent SSP models with different ages, while different symbols are SSP models with an age of ~ 13.5 Gyr and with different [α/Fe] ratios. The models predict a generally weak dependence of TiO features on age and an increase of all TiO strengths with increasing IMF. The CaH1 index strength also increases with steepening IMF and age but decreases with increasing [α/Fe]. In all plots, a Salpeter IMF (Salpeter 1955) has a slope of $x = 2.35$.

5.4 Constraining the low-mass end of the IMF slope using ETGs optical spectra

We now compare the CvD12 models to early-type galaxies (ETGs), for which they are specifically designed.

We selected ETGs from the Sloan Digital Sky Survey DR8 (SDSS; Aihara et al. 2011) in five velocity-dispersion bins spread over 150–310 $\mathrm{km\,s^{-1}}$, each with a width of $\sim 30\,\mathrm{km\,s^{-1}}$. To select ETGs and to minimize contamination of our sample by late-type galaxies, we select systems for which the galaxy's surface brightness profile has a likelihood of a de Vaucouleurs' model fit higher than the likelihood of an exponential model fit. This requirement reduces approximately to requiring that the surface brightness profile should be better fitted by the de Vaucouleurs' model than by an exponential. We also visually inspected spectra of all the selected galaxies removing that showing emission lines (specifically, all the cases in which H_β, O[III] or O[II] emission is visible). Moreover, we select systems with very low star-formation rate (SFR $< 0.3\,M_\odot\,\mathrm{yr^{-1}}$) using the MPA/JHU value-added galaxy catalog containing results from the galaxy spectral fitting code described in Tremonti et al. (2004) and star formation rates based on the technique discussed in Brinchmann et al. (2004). Finally we set an upper limit on the redshift range ($z \leq 0.05$) to cover the entire wavelength range of interest. In each bin we stack spectra together in order to increase the final signal-to-noise (S/N), which is of the order of $\sim 300/\text{Å}$ over the wavelength range 4000–7000 Å. We use CvD12 models with varying IMF slopes, ages = [7–13.5] Gyr, [α/Fe] = [0, 0.2], and solar abundances. We convolve the galaxy and model spectra to an effective velocity dispersion of $\sigma = 350\,\mathrm{km\,s^{-1}}$ to correct for kinematic broadening before measuring indices. We also normalize the spectra using a second-order polynomial fit. In Figure 5.6, we show the stacked SDSS spectra for each velocity dispersion bin as well as a set of models with solar [α/Fe] and varying IMF slope. Boxes show the IMF-sensitive indices used in this work.

We measure line-strength indices in the range 4000–7400 Å, including the standard Lick indices Hβ, Mgb, Fe5270, Fe5335, NaD and TiO2 (e.g., Trager et al. 1998), and the commonly-used [MgFe] combination[1], as well as our newly defined IMF-sensitive features bTiO, aTiO and CaH1. Indices in both the galaxy and the model spectra are measured with the same definitions and methods[2]. We

[1] [MgFe] = $\sqrt{(\mathrm{Fe5270} + \mathrm{Fe5335})/2 \times \mathrm{Mg}b}$, González (1993)

[2] We use the code SPINDEX from Trager, Faber & Dressler (2008)

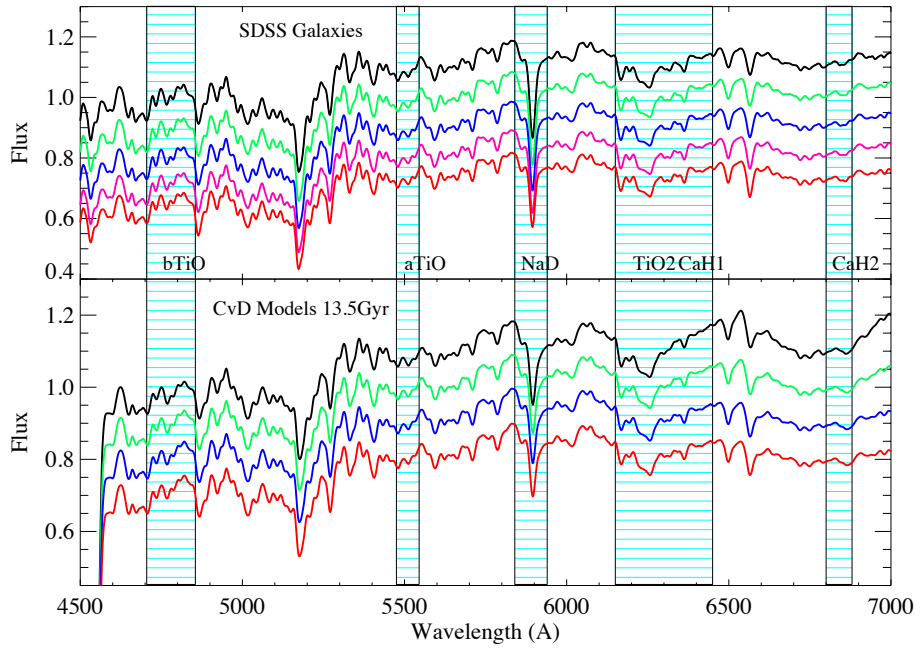

Figure 5.6: *Upper panel:* Stacked spectra of SDSS galaxies with different observed velocity dispersions, increasing from bottom to top (150, 190, 230,280, 310 $\mathrm{km\,s^{-1}}$ respectively) and offset for clarity. *Lower panel:* CvD12 SSP models with same age (13.5 Gyr) and solar [α/Fe] but different IMF slopes, from Chabrier (at the bottom) to the most bottom-heavy ($x = 3.5$, at the top). Boxes show IMF-sensitive features. All observed and model spectra are normalized with a polynomial fitting and convolved to a common resolution of $\sigma = 350\,\mathrm{km\,s^{-1}}$.

do not place our indices on the zero-point system of the Lick indices and quote the new TiO and CaH indices as index strengths in units of magnitudes.

To investigate the IMF variation with galaxy mass, we produce index-index plots for the selected optical indicators. Panel (a) of Figure 5.7 shows the Hβ–[MgFe] diagram, used to constrain age and metallicity of galaxies. The different colors represent CvD12 SSP models with different ages and solar [α/Fe]. We observe an increase in age with increasing velocity dispersion, consistent with previous stellar population studies of early-type galaxies that suggest that more massive galaxies predominantly have older, more evolved, stellar populations (e.g. Renzini 2006). The reader might notice that contrary to many other SSP models

(Worthey 1994; Bruzual & Charlot 1993, 2003; Leitherer et al. 1999; Vazdekis et al. 1996, 1997; Maraston 2005; Thomas et al. 2005), in the CvD12 models the [MgFe] index depends on [α/Fe]. This is because in the CvD12 models the abundance variations of single elements are implemented at fixed [Fe/H][3]. All selected galaxies are consistent with populations of 9 Gyr or older, and therefore in the other panels we only plot SSP models with ages of 9, 11, 13.5 Gyr. We plot models with solar [α/Fe] (solid lines) and supersolar [α/Fe] (= 0.2 dex, dotted lines); we note that the predicted variation of IMF slopes is orthogonal to the [α/Fe] enrichment for the selected IMF-sensitive indicators (Spiniello et al. 2012). Panels (b), (c) and (d) of Figure 5.7 show some of our selected IMF indicators in the optical. In each panel we plot one of the TiO lines against CaH1, which is the only feature that is strong only in cool dwarfs. The combination of TiO lines (whose strengths increase with steepening of the IMF *and* with increasing [α/Fe]) and CaH1 absorption (whose index strength instead decreases with increasing [α/Fe]) allows us to break the IMF slope–[α/Fe] degeneracy. Several TiO lines are necessary to further break the IMF–$T_{\rm eff,RGB}$, as described below.

Remarkably, all indicators clearly show a steeper IMF slope with increasing galaxy mass: they imply a Chabrier IMF for the least-massive galaxies ($\langle\sigma_*\rangle \sim 150\,{\rm km\,s^{-1}}$), Salpeter for the intermediate-mass galaxies ($\langle\sigma_*\rangle \sim 230\,{\rm km\,s^{-1}}$) and possibly a bottom-heavy IMF with $x \lesssim 3$ for the most massive SDSS ETGs ($\langle\sigma_*\rangle \sim 310\,{\rm km\,s^{-1}}$). We quantify this further in section 5.4.3.

5.4.1 Variation in the $\Delta T_{\rm eff}$ of the red-giant branch versus IMF variations

Here we investigate further the IMF–$\Delta T_{\rm eff,RGB}$ degeneracy, showing that the data are consistent with a non-universal IMF even when we take into account the possible uncertainty on the exact temperature of the red giant branch in ETGs. We

[3] Schiavon (2007) has already seen the same effect in his models which have also been cast in terms of [Fe/H], and not total metallicity [Z/H]. This reflects the choice to deal explicitly with quantities that can be inferred from measurements taken in the integrated spectra of galaxies. Total metallicity is not one of them, given our current inability to use integrated spectra of stellar populations to constrain the most abundant of all metals, oxygen. As clearly discussed in Graves & Schiavon (2008), an advantage with casting models in terms of [Fe/H] is that each elemental abundance can be treated separately, so that the effect of its variation can be studied in isolation from every other elemental abundance at the cost, however, of varying the total metallicity. In the case of models cast in terms of [Z/H], it is impossible to vary the abundance of a single element, because enhancing one element means decreasing the abundances of all other elements to keep the total metallicity constant.

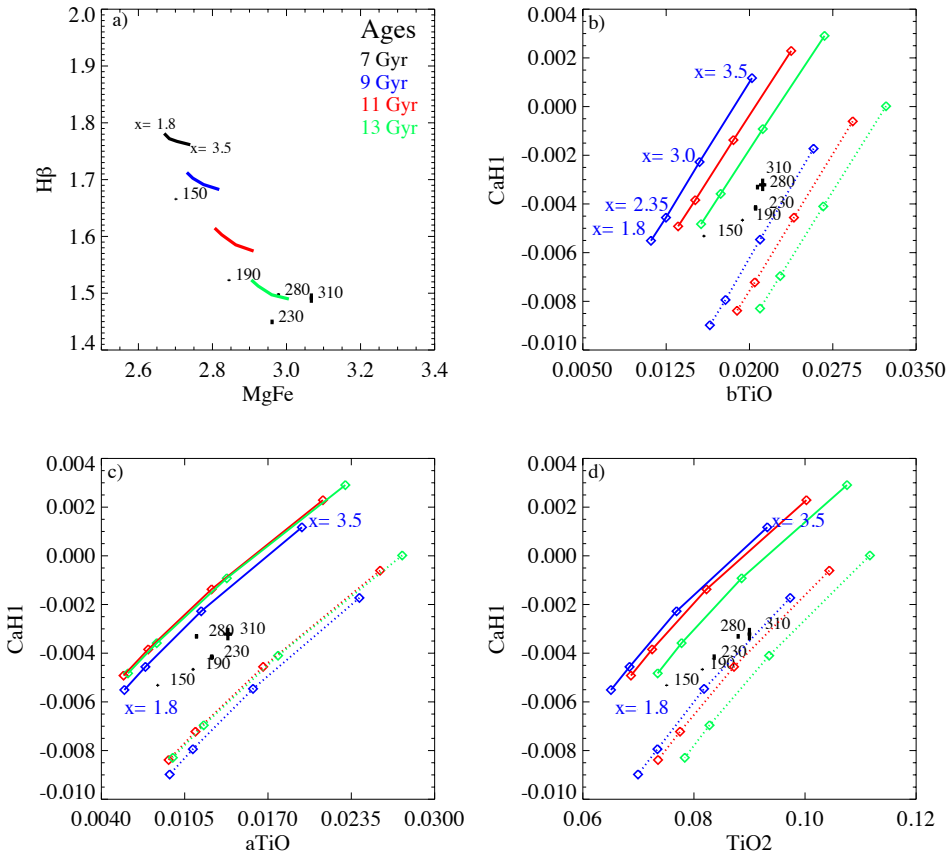

Figure 5.7: Index-index plots of the main absorption features in the optical. Solid lines are CvD12 models with different ages (colors) and different IMF slopes (points on each line are models with IMF slopes of 1.8, 2.35, 3.0, 3.5). Dotted lines are the same models with $[\alpha/\mathrm{Fe}] = +0.2$ dex. All models have solar metallicity. Points with error bars are stacked spectra of SDSS galaxies, in five velocity-dispersion ($\sigma_\star$) bins. The value shown is the average $\sigma_\star$ in $\mathrm{km\,s^{-1}}$ for each bin. Galaxies and models are convolved to a final common resolution of $350\,\mathrm{km\,s^{-1}}$ before measuring index strengths. *Panel (a):* The Hβ–[MgFe] diagram. In this plot IMF dependence is minimal, and the ages and metallicities of the galaxies can be inferred. All the galaxies show populations older than 9 Gyr. *Panels (b, c, d):* IMF-sensitive index-index plots; CaH1 as a function of bTiO, aTiO and TiO2 respectively. The TiO lines are strong in cool giants and dwarfs and become strong with increasing [α/Fe]. CaH1 comes only from M dwarfs and becomes weaker for super-solar [α/Fe]. The combination of these indices is therefore particularly effective at constraining the low-mass end of the IMF slope. All the indicators agree and confirm a steepening of the IMF slope with galaxy mass. In these panels, galaxies prefer models with slightly super-solar [α/Fe].

use 13.5 Gyr old CvD12 models in which we change the temperature of the RGB in the isochrones. In each index-index plot of Figure 5.8 we show the standard-temperature model with solar and super-solar [α/Fe], a solar-abundance model with $\Delta T_{\rm eff,RGB}$ increased by 50 K, and three solar-abundance models with $\Delta T_{\rm eff,RGB}$ decreased by respectively 50 K, 100 K, and 150 K. On each line, different symbols indicate different assumed IMFs. Figure 5.8 clearly shows that the combination of our preferred optical IMF-dependent indicators allows us to break also the IMF-$\Delta T_{\rm eff,RGB}$ degeneracy. It is also clear from the figure that ETGs are slightly α-enhanced, and that the degeneracy between IMF, $\Delta T_{\rm eff,RGB}$ and [α/Fe] can be completely broken by using several TiO lines in combination with the CaH1 feature.

In principle the NaD index at 5900 Å could be used to constrain the IMF (Conroy & van Dokkum 2012b; Ferreras et al. 2013), but, as shown in panel (f) of Figure 5.8, this index is more sensitive to variation of the effective temperature of the RGB stars than to variation of the IMF slope in these models. However, this feature is above all sensitive to [Na/Fe] abundance, as we will show in the next section.

5.4.2 The Na features

NaD and NaI indices are both very strong absorption features in the optical-NIR spectrum and have been the subject of numerous studies of the IMF slope as well as of the interstellar medium (ISM). The first claim of a non-universal low-mass end of the IMF was made by Spinrad & Taylor (1971) using the NaI feature ($\lambda \sim 8190$ Å). They compared the observed line strength of the NaI doublet in the centers of M31, M32 and M81 with population synthesis models, finding a substantial fractional contribution by dwarf stars to the integrated light of these galaxies. More recently, van Dokkum & Conroy (2010) demonstrated indeed that the NaI doublet depends strongly on surface gravity at fixed effective temperature, betraying the presence of faint M dwarfs in integrated light spectra. Figure 5.2 shows that the bluer NaD feature ($\lambda \sim 5900$ Å) is also very strong in dwarf stars at relatively low temperatures ($T_{\rm eff} \leq 4200$K). Hence, its strength as a function of the redder sodium feature should provide a powerful means for separating the IMF from the sodium abundance, assuming that the two features react in the same way to changes in the [Na/Fe] abundance. However, it has been argued that the NaD index could be highly contaminated by the ISM, even though the dominant process is under great debate (cool gas in the disk, galactic wind in actively star-forming

galaxies or AGN activity are the most common candidates, e.g. Heckman, Armus & Miley 1990; Lehnert et al. 2011).

Here we show that the NaD strength is not *solely* driven by IMF variation: we find that this index is more sensitive to [Na/Fe] abundance variations than to IMF slope variations (Chapter 7, Spiniello et al. 2013, in prep.), and it varies strongly with $T_{\rm eff,RGB}$. In Chapter 4 we show that CvD12 models with solar [Na/Fe] abundance do not match the NaD strengths for high-mass ETGs. This is also confirmed by Conroy & van Dokkum (2012b) who find that massive ETGs require models with [Na/Fe] = 0.3–0.4. When *only* sodium indicators are used these systems require also extremely steep IMFs, $x \geq 3.5$. For the gravitational lens analysed in Chapter 4, with $\sigma_\star \sim 300\,{\rm km\,s^{-1}}$, such steep slopes are ruled out at the 99.9 per cent confidence level (C.L.) from lensing constraints. We therefore conclude that Na lines are highly sensitive to both IMF variation and [Na/Fe] variation, and are therefore complicated to interpret when considered in isolation.

Furthermore, in a recent paper, Smith & Lucey (2013) found a giant elliptical ($\sigma_\star \sim 330\,{\rm km\,s^{-1}}$) lens galaxy with a "lightweight" IMF. From their lensing analysis, an IMF heavier than Salpeter is disfavoured at the > 99.8 per cent level. However, when looking at the dwarf-sensitive NaI feature in the spectrum of that galaxy, a SSP with age of 13.5 Gyr, super-solar [α/Fe] *and* bottom-heavy IMF ($x = 3.0$) is required to match the observed galaxy spectrum. Also in this case, the stellar mass inferred from this SSP model violates the limits on the total mass of that particular system, set by gravitational lensing. Even when considering models with an enhancement of sodium, Smith & Lucey (2013) cannot completely reconcile the SSP Na-based result and the lensing result on the IMF slope *for this* particulat giant elliptical.

Additional evidence showing that the NaD strengths in ETGs are not exclusively IMF-driven is provided by Jeong et al. (2013). These authors identified NaD excess objects (NEOs) from the SDSS DR7 (Abazajian et al. 2009) and found that NaD features are too strong in many massive ETGs even when using SSP models with a bottom-heavy IMFs (and solar abundance). They studied a plausible range of stellar parameters (from CvD12 SSP models) that could reproduce the observed values of NaD, Mgb and Fe5270, finding that the majority of the early-type NEOs are α-enhanced, metal-rich and especially Na-enhanced ([Na/Fe] $\sim$ 0.3).

To further complicate this situation, we note that large differences exist when comparing the behaviour of Na features predicted from different SSP models, as pointed out in La Barbera et al. (2013). The authors compared the [α/Fe] sensitivity of the NaD for different SSP models finding a strong discrepancy. They

showed that the CvD12, Coelho et al. (2007) and Cervantes et al. (2007) models predict that NaD weakens as [α/Fe] increases, while the Thomas et al. (2011) models predict a mild increase with enhancement.

Given this unresolved situation about the level of sodium abundance in ETGs, we therefore think that it is currently prudent not to draw any strong conclusion about the low-mass end of the IMF slope based *solely* on Na features, and to concentrate on indices such as those from TiO and CaH, which appear to be less subject to abundance-ratio variation effects and give mutually consistent predictions for the trend of IMF slope with galaxy mass.

In the following section we give a quantitative expression for the relation between IMF slope and velocity dispersion, showing that the relation inferred from sodium lines is systematically different than the relation inferred from any other combination of the above-mentioned IMF-sensitive spectral indices.

5.4.3 IMF slope versus velocity dispersion

Our results confirm that it is possible to constrain the low-mass end of the IMF slope from optical spectra of ETGs and provide increasing support to the emerging notion of the non-universality of the IMF. We observe that the steepness of the low-mass end of the IMF increases with galaxy velocity dispersion, consistent with other chapters of this thesis (Chapters 3, 4), and previously-published works (van Dokkum & Conroy 2010; Spiniello et al. 2011, 2012; Conroy & van Dokkum 2012b; Cappellari et al. 2012; Ferreras et al. 2013; Tortora, Romanowsky & Napolitano 2013; La Barbera et al. 2013). To constrain the IMF slope of each galaxy and concurrently break the degeneracies between age, metalicity, abundance ratio and temperature, we use the following indices: Hβ, Mgb, Fe5270, Fe5335, bTiO, aTiO, TiO1, TiO2, CaH1, and CaH2. The first four indicators are almost IMF-independent and they are mainly used to constrain age and [α/Fe], while the combination of CaH1 with TiO features is used to count dwarfs stars and to break the degeneracy with effective temperature (see Figs. 5.7 and 5.8).

We now give a quantitative expression for the variation of the IMF slope with velocity dispersion. We compare each stacked SDSS spectrum with grids of interpolated SSPs spanning a range of ages (log(age) = [0.8 − 1.15] Gyr, with a step of 0.01 Gyr), [α/Fe] (between −0.2 and +0.4 dex, with a step of 0.05 dex), and changes in the effective temperature of the RGB ($\Delta T_{\rm eff,RGB}$ between −200 K and 50 K, with a step of 50 K) for different values of the IMF slope ($x = 1.8 - 3.5$, with a step of 0.1 in the slope). Using a bspline interpolation, we build a grid of $8 \times 13 \times 18 \times 9$ models in log(age), [α/Fe], IMF slope and $\Delta T_{\rm eff,RGB}$, and for each

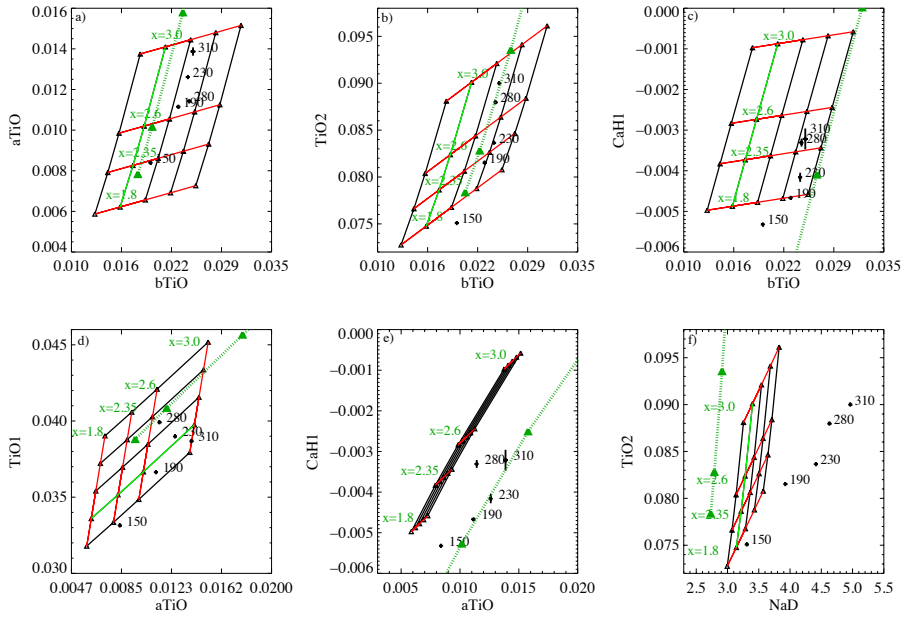

Figure 5.8: The effect of $\Delta T_{\rm eff,RGB}$ on CvD12 models with ages of 13.5 Gyr. In each panel, the green solid line shows the standard-temperature model with solar [α/Fe] while the black lines are models in which $\Delta T_{eff,RGB}$ has been increased or decreased by 50 K. The green dotted line shows the standard-temperature model with [α/Fe]= +0.1. We plot models with $\Delta T_{eff,RGB}$ = 50 K, −50 K, −100 K and −150 K. Red lines represent therefore ΔT$_{\rm eff,RGB}$ variations, while different symbols on the same black line indicate different IMF slopes for a model with a given temperature. Points with error bars are stacked spectra of SDSS galaxies, in five velocity-dispersion ($\sigma_\star$) bins whose average is shown in $km\,s^{-1}$. *Panels a–d):* The combination of these indicators allow the degeneracy between RGB temperature and IMF to be broken. A mild variation of $\Delta T_{\rm eff,RGB}$ with galaxy mass can be detected, but a clear trend of increasing IMF with galaxy mass is present in all three panels. *Panel e):* CaH1–aTiO does not allow simultaneous constraints on the IMF slope and $\Delta T_{\rm eff,RGB}$. From this panel it is clear that models with slightly super-solar [α/Fe] better fit the data. The same result is also visible in Figure 5.7 (c) and (d) and is consistent with the best-fit models of Table 5.2. *Panel f):* NaD strengths in the stacked galaxies show a strong variation with galaxy mass. This variation cannot be entirely explained via non-universality of the IMF (Spiniello et al. 2012). The data suggest that NaD is highly dependent on the temperature of the RGB.

Table 5.2: Best-fit stellar population models for SDSS galaxies in different velocity dispersion bins. $\Delta T_{\rm eff}$ shifts are given with respect to the effective temperature of the RGB of solar-scaled models.

SDSS $\sigma_\star$ ($km\,s^{-1}$)	**Best-fit age (Gyr)**	**Best-fit [α/Fe]**	**Best-fit IMF slope (Salpeter:** $x = 2.35$**)**	**Best-fit** $\Delta T_{\rm eff}$ **(K)**
150 ± 20	10 ± 2	-0.11 ± 0.04	1.85 ± 0.2	-50 ± 30
190 ± 20	11 ± 2	$+0.05 \pm 0.02$	2.08 ± 0.2	-98 ± 36
230 ± 20	13 ± 2	$+0.11 \pm 0.02$	2.33 ± 0.4	-115 ± 29
280 ± 20	12 ± 2	$+0.16 \pm 0.04$	2.40 ± 0.3	-80 ± 30
310 ± 20	13 ± 3	$+0.14 \pm 0.02$	2.62 ± 0.4	-131 ± 40

galaxy spectrum we compute the χ^2 values for our 10 optical indicators as

$$\chi^2_n = \sum_{ind=1}^{10} \chi^2_{ind,n} = \sum_{ind=1}^{10} \frac{(EW^{obs}_{ind} - EW^{mod}_{ind,n})^2}{\sigma^2_{EW^{obs}_{ind}}}, \tag{5.1}$$

where n is the SSP model of interest. We obtain a probability density function (PDF) for each model via the likelihood function $L \propto \exp(-\chi^2/2)$. We then marginalize over age, ΔT_{eff} and [α/Fe] to obtain a best-fitting slope of the IMF and its uncertainty (1σ error on the cumulative probability distribution) for each velocity dispersion bin, assuming flat priors on all parameters.

We present our SSP analysis results in Table 5.2. We plot the percentile deviation of the EWs measured in the stacked SDSS galaxy spectra ($EW_{\rm SDSS}$) from the values measured in the correspondent SSP best-fit model ($EW_{\rm BF}$) and Figure 5.9.

In Figure 5.11 we show the best-fit IMF slope as a function of central stellar velocity dispersion. We determine the parameters of a linear regression model, $x = a \times \log \sigma_{200} + b$, for the stacked SDSS spectra to be

$$x = (2.3 \pm 0.1) \log \sigma_{200} + (2.13 \pm 0.15)\,, \tag{5.2}$$

where x is the IMF slope and σ_{200} is the central stellar velocity dispersion measured in units of $200\,{\rm km\,s^{-1}}$.

To test the robustness of the IMF–σ relation, we repeat the above statistical procedure several times eliminating each time one or more indices and calculating a new likelihood function for each model and the inferred stellar population

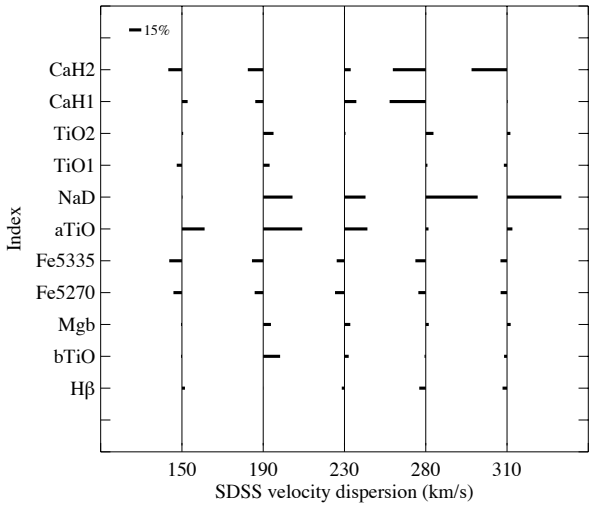

Figure 5.9: Deviation of the EWs measured in the stacked SDSS galaxy spectra ($EW_{\rm SDSS}$) from the values measured in the corresponding SSP best-fit model ($EW_{\rm BF}$). For each velocity dispersion bin, shown on the x-axis, the vertical lines indicate the model values of the fitted indices, indicated on the y-axis. Horizontal lines departing from these indicate the percentile variations of the given index. As reference, we show the length of a line corresponding to a deviation of 15 per cent on the upper-left corner. When the value of the $EW_{\rm SDSS}$ is bigger than the value of the $EW_{\rm BF}$, the horizontal line goes to the right, as for NaD. The $EW_{\rm SDSS}$ of the NaD feature in the more massive galaxies are systematically underestimated by the SSP models, because we are restricting the analysis to solar [Na/Fe] (see Sec. 5.4.2).

parameters for each stacked spectrum. We always keep $H\beta$, our only age-dependent and IMF-independent feature. Our inferred IMF slopes are consistent within 1σ if we use CaH1, $H\beta$, Mgb, at least one of the iron lines, one of the blue TiO indices (bTiO or aTiO) and one of the redder TiO features (TiO1 or TiO2). If we use the [MgFe] as a single indicator we still recover the IMF variation with velocity dispersion, but we do not recover the well-established [α/Fe]–$\sigma_\star$ relation (Trager et al. 2000a; Arrigoni et al. 2010). If we do not include CaH1 we are not able to break the degeneracy between [α/Fe] and IMF slope. In this case, all the IMF-sensitive features increase both with steepening of the IMF slope and increasing of [α/Fe]. The aTiO index does not significantly affect the IMF slope if we include or exclude it, confirming that the [OI] sky line does not

Table 5.3: Summary of the parameters of the inferred best-fit IMF slope as a function of central stellar velocity dispersion (though the linear equation $x = a \log \sigma_{200} + b$) using different sets of indices. The first row represents our preferred set. The non-universality of the IMF slope is confirmed in all the tested combinations. However, the trend of the IMF slope with $\sigma_\star$ gets steeper when NaD is used. See the text for further details.

Set ID (see Fig.5.10)	**Used indices**	**a**	**b**
1	$H\beta$, Mgb, Fe5270,Fe5335, bTiO, aTiO,TiO1, TiO2, CaH1 and CaH2	2.3 ± 0.1	2.1 ± 0.2
2	$H\beta$, Mgb, Fe5270,Fe5335, bTiO, aTiO,TiO1, TiO2, CaH1	2.3 ± 0.1	2.1 ± 0.2
3	$H\beta$, Mgb, Fe5270,Fe5335, bTiO, aTiO,TiO1, TiO2, CaH2	2.3 ± 0.2	2.1 ± 0.2
4	$H\beta$, Mgb, Fe5270,Fe5335, bTiO, aTiO,TiO1, TiO2	2.2 ± 0.3	2.3 ± 0.3
5	$H\beta$, Mgb, Fe5270, bTiO, aTiO,TiO1, CaH1	2.3 ± 0.3	2.1 ± 0.3
6	$H\beta$, Mgb, Fe5270, bTiO, aTiO,TiO2, CaH2	2.4 ± 0.3	2.2 ± 0.3
7	$H\beta$, Mgb, Fe5270,Fe5335, bTiO, aTiO,TiO1, TiO2, CaH1, CaH2 and NaD	2.6 ± 0.2	2.3 ± 0.2
8	$H\beta$, Mgb, Fe5270,Fe5335, bTiO, aTiO,TiO1, TiO2, CaH1 and NaD	2.9 ± 0.2	2.1 ± 0.1
9	$H\beta$, Mgb, Fe5270,Fe5335, bTiO, aTiO,TiO1, TiO2, CaH2 and NaD	3.2 ± 0.2	2.2 ± 0.2
10	$H\beta$, Mgb, Fe5270,Fe5335, bTiO, aTiO,TiO1, TiO2, and NaD	3.2 ± 0.2	2.4 ± 0.2

have a significant effect on the inference of the IMF slope from this absorption feature. However, if we exclude aTiO from the analysis we find RGB effective temperatures systematically higher than those inferred by including aTiO.

The situation changes when NaD is included: the slope of the linear relation becomes significantly steeper when we include this index. In Figure 5.10 we show this effect by plotting the resulting value of the slope of the linear relation $x = a \log \sigma_{200} + b$ inferred from different sets of indicators noted in Table 5.3. We note that we are restricting this particular analysis to solar Na abundances. A trend of increasing [Na/Fe] abundance with galaxy mass can *partially* mimic the IMF steepening. We address this in a forthcoming paper. It is important to note that we are assuming [Na/Mg] = 0.0, which may not be a good assumption for these very massive ETGs. A full spectral fitting approach as in Conroy & van Dokkum (2012b) and Conroy, Graves & van Dokkum (2013) might be necessary to investigate in detail the effect of a single non-solar element abundance.

5.4.4 Comparison with other works

In this section we compare our spectroscopic stellar population-based results on the IMF–$\sigma_\star$ relation with results obtained from similar SSP-based methods by other authors and from dynamically-based and lensing-based results.

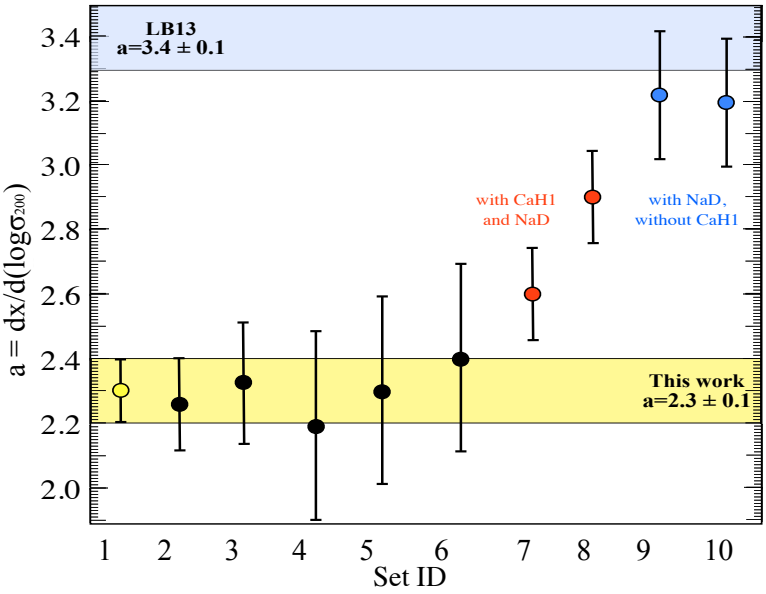

Figure 5.10: The slope of the linear relation $x = a \log \sigma_{200} + b$ inferred by using the different sets of indices as given in Table 5.3. The yellow point and the yellow horizontal box show the slope recovered by using our preferred set of indicators (ID = 1), while the blue upper box represents the slope found by La Barbera et al. (2013). The results are robust and stable against systematics arising from single indicators. Only when using NaD do we find a steep relation.

Ferreras et al. (2013, hereafter F13) and La Barbera et al. (2013, hereafter LB13) also found a correlation between central velocity-dispersion and IMF slope for a large sample of SDSS ETGs. F13 combined spectra of $\sim 40,000$ galaxies in velocity-dispersion bins, obtaining a final set of 18 stacked spectra at very high signal-to-noise ratio ($S/N \sim 400$ Å^{-1}). They compared spectral line strengths sensitive to age, metallicity, and IMF slope of these galaxies with the population synthesis models of Vazdekis et al. (2012). Using TiO1, TiO2 and NaI (λ8190 Å), they found $x = 4.87 \log \sigma_{200} + 2.33$. Qualitatively the general trends are similar to what we have found above, but their analytical fit has a much steeper slope and therefore predicts a larger variation of the IMF slopes with galaxy mass. For galaxies with $\sigma \geq 300\,\mathrm{km\,s^{-1}}$, they inferred a very steep IMF slope of $x \sim 3.2$. F13 only used three indicators to constrain the stellar population parameters, two of them coming from TiO lines that are sensitive to α-enrichment, as shown in our

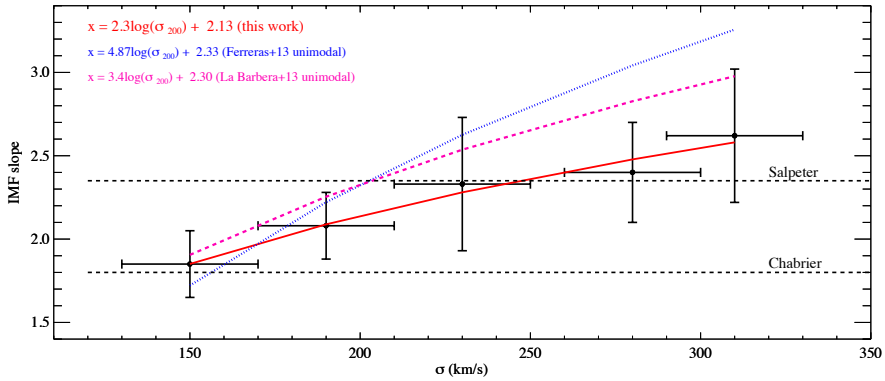

Figure 5.11: Variation of the IMF slope as a function of stellar velocity dispersion. Points are SDSS ETGs stacked by velocity dispersion. The red solid line represents a least-squares fit to the data. The blue dotted line is the linear fit obtained by F13, and the magenta dashed line is the linear fit obtained by LB13 for a unimodal IMF. The Chabrier and Salpeter cases are shown as horizontal dashed lines.

analysis. Disentangling IMF variations from age, metallicity and [α/Fe] variations and breaking the degeneracies is very difficult if only a few IMF-sensitive features are used. We therefore believe that our result is more robust because it is based on the combination of more IMF-sensitive indices, and it infers IMF slopes that do not violate lensing constraints on the total masses of massive ETG lenses (see Chapters 3 and 4). In fact, LB13 find a relation similar to that we found in this work (within 1σ, see Fig. 5.11) when analysing a variety of spectral indices, combining IMF-sensitive features with age- and metallicity-sensitive indices and considering the effect of non-solar abundance variations. LB13 and F13 test two different cases of a single power-law (unimodal) and a low-mass ($< 0.5\,M_{\odot}$) tapered IMF (bimodal), showing that bimodal IMF shapes do not provide such high $\Upsilon_{\star}$ ratios even for very steep slopes.

In order to compare our SSP-based results to lensing and dynamics-based results, and our unimodal IMF to the bimodal IMF of LB13, we translate the IMF slope–$\sigma_{\star}$ relation into a $\Upsilon_{\star}$–$\sigma_{\star}$ relation. For each SDSS velocity-dispersion bin, we calculate the stellar $\Upsilon_{\star}$ in the R-band using the Dartmouth Stellar Evolution Program (Chaboyer et al. 2001), selecting the IMF slope, age, and [α/Fe] inferred from the line-strength analysis. We then calculate the ratio of this value and the $\Upsilon_{\star}$ that the same population (i.e. same age and [α/Fe]) will have assuming a Salpeter IMF (a single power law with $x = 2.35$). In this way, we define an "IMF

mismatch" parameter $\alpha_{\rm IMF}$, following an approach similar to the one proposed by Treu et al. (2010) and used by Cappellari et al. (2013):

$$\alpha_{\rm IMF} = \frac{(\Upsilon)^{\star}_{x}}{(\Upsilon)^{\star}_{\rm Salp}}. \tag{5.3}$$

In Fig. 5.12 we plot $\log(\alpha_{\rm IMF})$ as a function of $\log\sigma_{\star}$ and compute the corresponding linear regression for the SDSS points (black points)

$$\log(\alpha)_{\rm IMF} = (1.05 \pm 0.2)\log\sigma_{\star} - (2.5 \pm 0.4)\,. \tag{5.4}$$

Moreover, we show linear fits to the gravitational-lensing-based results of SLACS (blue, Treu et al. 2010) and to stellar population-based results (green: Conroy & van Dokkum 2012b; magenta: La Barbera et al. 2013). Finally we plot the sample of 260 ATLAS3D galaxies (red points, Cappellari et al. 2011, 2013). The linear fit of LB13 is obtained using the linear relation between best-fit slope of the IMF and central velocity dispersion given in their Figure 12. We use the mass-to-light ratios in the Johnson R-band (Vega system) predicted from the MIUSCAT SSP models[4] with an age of 12.6 Gyr, solar metallicity and bimodal IMFs to convert the IMF slope–$\sigma_{\star}$ relation into a $\Upsilon_{\star}$–$\sigma_{\star}$ relation. In particular we use the bimodal IMF slopes obtained by fitting spectral indices with two SSP plus X/Fe models. These models consist of a linear combination of two extended MIUSCAT SSPs with the same IMF but different ages and metallicities. In addition, the models incorporate three free parameters describing the [Ca/Fe], [Na/Fe], and [Ti/Fe] abundances.

In Fig. 5.12, we also draw two horizontal lines showing the $\alpha_{\rm IMF}$ for a Chabrier-like (single power-law with $x = 1.8$) and a Salpeter IMF (i.e. $\log(\alpha_{\rm IMF}) = 0$). We note that a bottom-heavy IMF with slope of $x = 3.0$ falls out of the plot, predicting a value of $\log(\alpha_{\rm IMF}) \sim 0.6$. The good agreement between the stacked SDSS data points and these completely independent analyses (at least at the massive end of the different samples) gives confidence that our spectroscopic analysis and our inferred variation of the IMF slope with velocity dispersion are robust, and the trend we observe depends neither on the SSP model chosen nor on our statistical analysis.

5.5 Discussion and Conclusions

In this Chapter, we have defined a new set of indices which are strong in cool giants and dwarfs and almost absent in main sequence stars, in a spectral

[4] http://miles.iac.es/pages/photometric-predictions/based-on-miuscat-seds.php

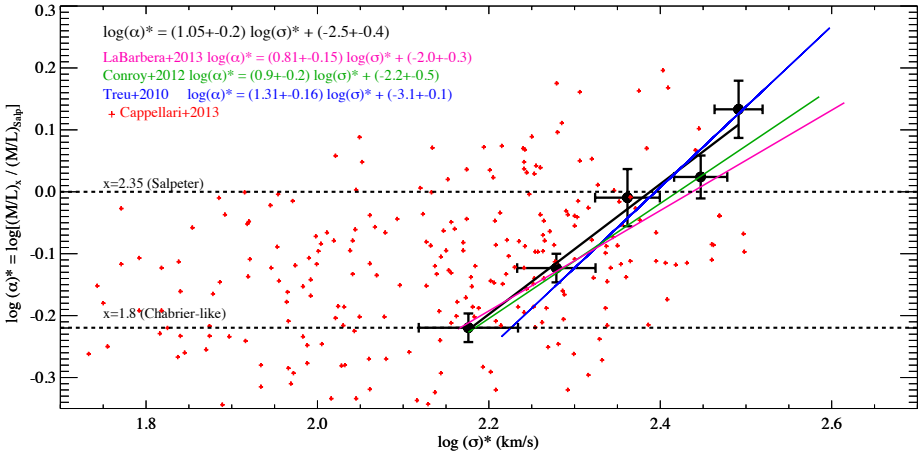

Figure 5.12: The $\alpha_{\rm IMF}$-$\sigma_\star$ relation. Our points and their error bars are shown in black, and a linear least-squares fit to these points is shown as the black line. Red points are single galaxies from the ATLAS3D sample. Colored lines are least-squares fits to the $\alpha_{\rm IMF}$–$\sigma_\star$ relation derived from the spectroscopic analysis of CvD12b, of LB13 with a bimodal IMF slope, and the lensing+dynamic analysis from Treu et al. (2010). The plot highlights the excellent agreement between these independent studies in their common velocity dispersion range. The Chabrier and Salpeter cases are shown as horizontal dotted lines. A bottom-heavy IMF with slope of $x = 3.0$ predicts $\log(\alpha_{\rm IMF}) \sim 0.6$.

region where single-stellar population (SSP) models have been most extensively studied. These features arise from TiO and CaH molecular absorption bands in the wavelength range $\sim$ 4700–7000 Å. We have calculated the strengths of these indices for stars in the MILES empirical library. In particular we have shown that all the TiO indicators are strong in cool giants and dwarfs and almost absent in warm main-sequence stars, allowing the study of their variation with temperature, gravity and [Fe/H]. However, the strength of the TiO lines increases with the increasing of the IMF but also with increasing [α/Fe]. The feature around CaH1 λ6380, which is strong only in M dwarfs, decreases instead with increasing α-enhancement and therefore allows us, in combination with the TiO indicators, to break the degeneracy between IMF and [α/Fe] variations and thus to constrain the low-mass end of the IMF slope.

We have used the Conroy & van Dokkum (2012a) SSP models constructed specifically for the purpose of measuring the IMF slope down to $\sim 0.1\,M_\odot$ for old, metal-rich stellar populations. We have measured SSP index strengths for our new

set of IMF indicators, and we have compared these to strengths of stacked spectra of SDSS DR8 ETGs in five different velocity dispersion bins between 150 and $310\,\mathrm{km\,s^{-1}}$. Finally we also investigated in detail the response of a change in the effective temperature of the red giant branch in the isochrones versus the response in variation of the IMF slope for the wavelength range where these responses are shown to be mostly degenerate.

In this work, we focused only on line-index measurement and we restricted the analysis to solar metallicity. Element abundance is a fundamental parameter that has to be fully and quantitatively explored in order to further isolate and test the suggested variation of IMF normalization with galaxy mass. A full spectral fitting approach can help to further investigate possible IMF variations with galaxy masses and to trace the complete star formation history of a galaxy (Conroy, Graves & van Dokkum 2013).

Our main conclusions are the following.

- CvD12 SSP models predict a minimal variation of the aTiO and CaH1 EWs with age (at least for old ages) and a minimal dependence of [α/Fe] on TiO2.

- The predicted variation of IMF slopes is orthogonal to [α/Fe] enrichment for all the presented IMF-sensitive index-index plots.

- Our set of IMF-sensitive indicators is able to break the IMF–$T_{\mathrm{eff,RGB}}$ degeneracy. The index strengths of SDSS galaxies match better those of SSP models with a population of RGB stars slightly cooler than the default isochrones. However this cannot explain the trend of IMF slope with galaxy velocity dispersion.

- A variation of the IMF with galaxy velocity dispersion, consistent with previous works (Treu et al. 2010; Spiniello et al. 2011, 2012; Cappellari et al. 2012; Tortora, Romanowsky & Napolitano 2013; La Barbera et al. 2013) is visible in all the index-index plots for the SDSS stacked spectra of galaxies in different $\sigma_\star$ bins from 150 to $310\,\mathrm{km\,s^{-1}}$. We find $x = (2.3 \pm 0.1)\log\sigma_{200} + (2.13 \pm 0.15)$, in disagreement with Ferreras et al. (2013), who found a significantly steeper relation at least when using an IMF characterized by a single power-law, but within 1σ of La Barbera et al. (2013), who performed a detailed analysis using more IMF-sensitive indicators than F13, two SSP models and a correction for the effect of non-solar abundance patterns (X/Fe).

- Our fit predicts an IMF slope that is more shallow than 3.0 for the most massive σ-bin. This is in agreement with the upper limit sets by gravitational lensing studies on the analysis of one very massive lens ETG presented in Chapter 4 (Spiniello et al. 2012)

- We translate the IMF–σ_{star} relation into a $\Upsilon_\star$–$\sigma_\star$ relation and compute an "IMF mismatch" parameter ($\alpha_{\rm IMF}$). This allows us to compare our results with Cappellari et al. (2013), Treu et al. (2010) La Barbera et al. (2013) and Conroy & van Dokkum (2012b). The studies, based on three completely independent methods, and two different SSP models are in excellent agreement.

In conclusion, the newly defined optical IMF indicators bTiO, aTiO, TiO1, TiO2, CaH1, and CaH2, represent useful probes for decoupling the IMF from stellar population age, metallicity, bulk abundance ratio [α/Fe], and the effective temperature of the RGB, when used in combination with age and metallicity indicators. These features are in a region of the spectrum less affected by sky lines or atmospheric absorption lines than the NIR features previously used. This region is also easier to observe as it lies in the wavelength region of the majority of the optical spectrographs, including integral-field instruments, that could be used to spatially resolve the low-mass stellar population of galaxies (see Future work in Chapter 8).

In this work, we focussed only on line-index measurements and we restricted our analysis to solar metallicity and abundances. Element abundance is a fundamental parameter that has to be fully and quantitatively explored in order to completely isolate and test the suggested variation of IMF normalization with galaxy mass (in particular [Na/Fe] will be studied in Chapter 7). A full spectral fitting approach might also be necessary to further investigate possible IMF variations with galaxy masses and to trace the complete star formation history of a galaxy (Conroy, Graves & van Dokkum 2013).

6 A low-mass cut-off near the hydrogen burning limit for Salpeter-like IMF in early-type galaxies

The important thing is not to stop questioning.
Curiosity has its own reason for existing.

Albert Einstein

Based on:

M. Barnabè, C. Spiniello, L.V.E. Koopmans, S.C. Trager, O.Czoske and T. Treu, *"A low-mass cut-off near the hydrogen burning limit for Salpeter-like initial mass functions in early-type galaxies"* 2013, accepted for publication to MNRAS

We conduct a detailed investigation of the properties of the stellar initial mass function (IMF) in two massive early-type lens galaxies with velocity dispersions of $\sigma \simeq 250\,\mathrm{km\,s^{-1}}$ and $\sigma \simeq 330\,\mathrm{km\,s^{-1}}$, for which both *HST* imaging and X-Shooter spectra are available. We compare the inferences obtained from two fully independent methods: (i) a combined gravitational lensing and stellar dynamics (L&D) analysis of the data sets employing self-consistent axisymmetric models, and (ii) a spectroscopic simple stellar population (SSP) analysis of optical line-strength indices, assuming single power-law IMFs. The results from the two approaches are found to be in agreement within the 1σ uncertainties. Both galaxies are consistent with having a Salpeter IMF (power-law slope of $x = 2.35$), which is strongly favoured over a Chabrier IMF ($x = 1.8$), with probabilities inferred from the joint analysis of 89% and 99%, respectively. Bottom-heavy IMFs significantly steeper than Salpeter ($x \geq 3.0$) are ruled out with decisive evidence (Bayes factor $B > 1000$) for both galaxies, as they exceed the total mass derived from the L&D constraints. Our analysis allows, for the first time, the inference of the low-mass cut-off, or turnover, of the IMF ($M_{\rm low}$). Combining the joint L&D and SSP analyses of both galaxies, we infer an IMF slope of $x = 2.22 \pm 0.14$, consistent with Salpeter IMF, and a low-mass limit $M_{\rm low} = 0.13 \pm 0.03\,M_{\odot}$, just above the hydrogen burning limit.

6.1 Introduction

The stellar initial mass function is a fundamental quantity to understand the evolution and structure of galaxies, since it is crucial in determining many key properties of stellar populations and galaxies, such as star formation rates and galaxy stellar masses. While it has long been assumed that the IMF is universal, given that the IMF appears to be largely invariant throughout the Local Group (Kroupa 2001; Chabrier 2003; Bastian, Covey & Meyer 2010; Kroupa et al. 2013), in recent years numerous extra-galactic studies have provided mounting evidence that the steepness of the IMF profile might vary with galaxy mass, stellar velocity dispersion or morphological type (e.g. Trager et al. 2000b; Graves, Faber & Schiavon 2009; Treu et al. 2010; van Dokkum & Conroy 2010; Auger et al. 2010b; Barnabè et al. 2012, hereafter B12; Geha et al. 2013; Dutton et al. 2013). In particular, there are strong indications that massive elliptical galaxies are characterized by a classic single power-law IMF (Salpeter 1955, $dN/dM \propto M^{-x}$ with slope $x = 2.35$, where N is the number of stars of mass M), possibly becoming steeper with increasing total galaxy mass (see e.g. Grillo et al. 2009;

van Dokkum & Conroy 2010; Barnabè et al. 2009b, 2011; Cappellari et al. 2012; Spiniello et al. 2011, 2012, 2013; Conroy & van Dokkum 2012b; Sonnenfeld et al. 2012; Ferreras et al. 2013; Tortora, Romanowsky & Napolitano 2013).

Understanding the trend in the IMF slope is necessary to determine how the dark matter content of galaxies changes with mass, and thus to provide important insight into galaxy evolution mechanisms. Several works (e.g. Padmanabhan et al. 2004; Tortora et al. 2009; Graves & Faber 2010; Barnabè et al. 2011) have shown that, under the assumption of a universal IMF, the inferred dark matter fraction within the inner regions of early-type galaxies (ETGs) increases with the total mass. However, it remains unclear whether (and how much) this effect can be countered by the observed variation in the IMF slope, and consequently to what extent (if at all) the actual dark matter content of ETGs scales with total mass.

The combination of gravitational lensing with stellar (or gas) dynamics has been proven to be a very robust and powerful method to investigate the mass structure of both early- and late-type galaxies beyond the local Universe (e.g. Treu & Koopmans 2004; Jiang & Kochanek 2007; Czoske et al. 2008; Koopmans et al. 2009; Barnabè et al. 2010; Suyu et al. 2012). When lensing and kinematic data of sufficient quality are available, this technique can also make it possible to put firm constraints on the stellar mass of the analyzed galaxy (see van de Ven et al. 2010; Dutton et al. 2011; B12), which can then be compared to the results of SSP modelling to draw inferences for the shape of the IMF of the galaxy. In this chapter we follow an analogous approach: by taking advantage of high-quality X-Shooter spectroscopic observations, we perform a fully self-consistent joint L&D analysis of two massive lens ETGs: SDSS J0936+0913 ($\sigma \simeq 250\,\mathrm{km\,s^{-1}}$ at $z = 0.164$) and SDSS J0912+0029 ($\sigma \simeq 330\,\mathrm{km\,s^{-1}}$ at $z = 0.190$), hereafter J0936 and J0912, respectively. The inferences for the stellar masses are then compared against the corresponding results from a completely independent method, viz., a spectroscopic SSP study of the same two systems based on line-strength indices analysis, thus yielding secure constraints on the IMF slope and, for the first time, on the IMF low-mass cut-off.

The value of M_{low} is an essential but often unappreciated parameter when determining the stellar mass-to-light ratio ($\Upsilon_\star$) from stellar population evolutionary codes. In fact, different codes adopt a different choice for M_{low}, implying different results for $\Upsilon_\star$ (e.g., Conroy & van Dokkum 2012a, hereafter CvD12, use $0.08\,M_\odot$, Bruzual & Charlot 2003 and Vazdekis et al. 2012 adopt $0.10\,M_\odot$, while all models based on the *Padova 2000* isochrones use $0.15\,M_\odot$).

6.2 The Dataset

Both galaxies were originally observed with *HST* as part of the Sloan Lens ACS Survey (SLACS). We refer to Bolton et al. (2008a) and Auger et al. (2009) for a detailed presentation of all the SLACS spectrophotometric data sets. For the analysis presented here, we make use of the high-resolution *F814W* images of the lens systems. An elliptical B-spline model of the surface brightness distribution of the deflector is used to produce the galaxy-subtracted image that is used for the lensing modelling (e.g. Bolton et al. 2008a).

For both systems, UVB–VIS X-Shooter spectra with signal-to-noise high enough to perform SSP analysis (S/N > 50) were obtained as part of the X-Shooter Lens Survey (XLENS, Chapter 2, Spiniello et al. 2011). X-Shooter observations of J0912 and J0936 were carried out during two runs between 2011 and 2013 in slit mode (UVB: R = 3300 with $1\farcs6 \times 11''$ slit; VIS: R = 5400, with $1\farcs5 \times 11''$ slit). The total exposure time on target was ∼ 2500 sec for J0912 and ∼ 5000 sec for J0936, with a typical seeing for both observations of $\sim 0\farcs65$. The data were reduced using the ESO X-Shooter pipeline v1.5.7. Stellar kinematic parameters were measured with the Penalized Pixel Fitting (pPXF) code of Cappellari & Emsellem (2004).

6.3 Stellar population synthesis modelling

For our analysis we use the SSP models of CvD12. To constrain the IMF slope, age and [α/Fe] of the stellar populations, we follow the approach described in Chapter 5 (Spiniello et al. 2013). We use the nearly IMF-independent indicators Hβ, Mgb, Fe5270, and Fe5335 to constrain age and [α/Fe], while the combination of CaH1 and four TiO features are used to measure the low-mass end of the IMF. We compare the indices of each galaxy with grids of SSPs spanning a range of $\log_{10}(\mathrm{age/Gyr}) = [0.8, 1.15]$ and $[\alpha/\mathrm{Fe}] = [-0.2, +0.4]$ dex for different values of the IMF slope ($x = 1.8 - 3.5$). In CvD12 the abundance variations of single elements are implemented at fixed [Fe/H], which implies that the total metallicity Z varies from model to model. For each model we calculate the χ^2 and obtain a probability distribution function (PDF) via the likelihood function and assuming uniform priors over the above described ranges. We then marginalize over age and [α/Fe] to obtain the best-fitting slope of the IMF and its uncertainty for each system: $x_{\mathrm{J0936}} = 2.10 \pm 0.15$ and $x_{\mathrm{J0912}} = 2.60 \pm 0.30$. The final marginalized PDFs for each system are shown in Figure 6.1

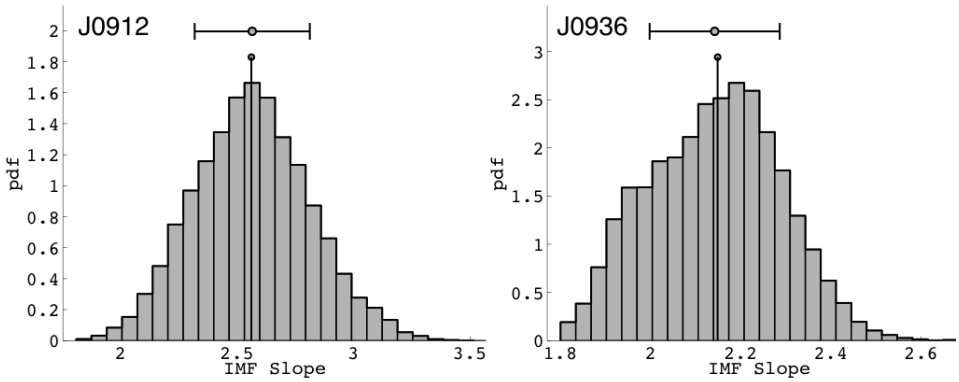

Figure 6.1: PDFs of the best-fit SSP model for each galaxy marginalized over age and [α/Fe] to obtain the best-fitting slope of the IMF and its uncertainty for each system ($x_{\rm J0936} = 2.10 \pm 0.15$ and $x_{\rm J0912} = 2.60 \pm 0.30$) from spectroscopic stellar population analysis alone.

Table 6.1: SSP analysis results and inferred stellar masses for the two different $M_{\rm low}$ values for both lens systems.

System	**Log(Age) (Gyr)**	**[α/Fe]**	**IMF slope**	$M^{\star}_{\rm M_{low}=0.115}$ ($\times 10^{11}\,M_{\odot}$)	$M^{\star}_{\rm M_{low}=0.08}$ ($\times 10^{11}\,M_{\odot}$)
J0912+0029	1.1 ± 0.05	0.1 ± 0.03	2.6 ± 0.3	12.8 ± 0.4	17.8 ± 0.4
J0936+0913	0.9 ± 0.05	0.05 ± 0.02	2.1 ± 0.15	3.01 ± 0.03	3.56 ± 0.03

To determine $\Upsilon_{\star}$, we use the isochrones at solar [Fe/H] from the stellar evolution code DSEP (Dartmouth Stellar Evolution Program, Chaboyer et al. 2001), selecting IMF slope, age, and [α/Fe] inferred from the line-strength analysis (see Table 6.1). Each $\Upsilon_{\star}$ includes the contribution from stellar remnants and gas ejected from stars at the end of their life-cycles. The lowest mass limit in the DSEP isochrones is $M_{\rm low}$= $0.115\,M_{\odot}$. We extrapolate the luminosities for lower stellar masses down to the hydrogen burning limit of $M_{\rm low}$= $0.08\,M_{\odot}$ (e.g. Kumar 1963; Grossman 1970), using a spline. We note that stars below $\sim 0.115\,M_{\odot}$ remain mostly invisible in current spectral lines for any reasonable IMF slope (CvD12) and therefore we can move $M_{\rm low}$ without any real impact on the spectra and on the line-strength measurements. Finally, we use the luminosities derived in Auger et al. (2009) to translate these numbers into stellar masses. The results are presented in Table 6.1.

Table 6.2: Summary of the adopted priors and of the posterior PDFs inferred from the combined lensing and dynamics analysis.

parameter	prior J0936	posterior J0936	prior J0912	posterior J0912
$v_{\rm vir}/{\rm km\,s^{-1}}$	$\mathcal{N}(350, 150)$	124^{+160}_{-88}	$\mathcal{N}(475, 200)$	470^{+160}_{-130}
γ	U(0, 2)	$0.92^{+0.72}_{-0.64}$	U(0, 2)	$0.46^{+0.41}_{-0.30}$
c_{-2}	U(0, 50)	$6.3^{+18.4}_{-4.1}$	U(0, 50)	$7.2^{+3.8}_{-2.7}$
$q_{\rm h}$	L$\mathcal{N}(1, 0.3)$	$0.93^{+0.25}_{-0.18}$	L$\mathcal{N}(1, 0.3)$	$0.54^{+0.10}_{-0.08}$
$M_\star/10^{11}\,M_\odot$	U(0, 10)	$3.31^{+0.18}_{-0.30}$	U(0, 35)	$10.28^{+0.57}_{-0.62}$
b	U(0, 5)	$0.89^{+0.37}_{-0.31}$	U(0, 5)	$1.94^{+0.24}_{-0.21}$

In the prior columns, $U(a, b)$ denotes a uniform distribution over the open interval (a, b). $\mathcal{N}(a, b)$ and $L\mathcal{N}(a, b)$ denote a normal and lognormal distribution, respectively, with a being the central value for the variable and b the standard deviation (for the log of the variable, in the case of $L\mathcal{N}$). In the posterior columns we list, for each parameter, the median value of the corresponding marginalized posterior PDF and the uncertainty quantified by taking the 68% credible interval (i.e., the 16th and 84th percentiles). See Sect. 6.4 for a description of the six free model parameters.

6.4 Gravitational lensing and stellar kinematics modelling

We carry out an in-depth analysis of the mass and dynamical structure of the two lens systems by employing the fully Bayesian CAULDRON code (detailed by Barnabè & Koopmans 2007 and B12), which is designed to conduct a self-consistent combined modelling of both the lensing and kinematic constraints.

We adopt a flexible two-component axially-symmetric mass model for the lens galaxy. For the dark matter component, motivated by the findings of cosmological simulations, we use a generalized Navarro-Frenk-White (gNFW) halo characterized by four free parameters, namely the inner density slope γ, the axial ratio $q_{\rm h}$, the halo concentration parameter c_{-2} and the virial velocity $v_{\rm vir}$ (i.e. the circular velocity at the virial radius). The density profile of the luminous mass component is obtained by deprojecting the multi-Gaussian expansion (MGE) fit to the observed surface brightness distribution of the galaxy, a technique that has become the *de facto* standard in state-of-the-art dynamical studies of galaxies

(e.g. the ATLAS^{3D} project, Cappellari et al. 2011). The free parameter $\Upsilon_\star$, or equivalently the total stellar mass $M_\star \equiv \Upsilon_\star L_{\rm tot}$, sets the normalization of the stellar mass distribution.

This mass profile is then used to simultaneously model both the lensing data set, by employing a pixelated source reconstruction method, and the stellar kinematic observables, i.e. the quantity $v_{\rm rms}(R) = \sqrt{v_{\rm rot}^2(R) + \sigma^2(R)}$, where $v_{\rm rot}$ and σ denote the line-of-sight projected stellar rotation velocity and velocity dispersion, respectively. The construction of the dynamical model is based on the flexible Jeans anisotropic MGE technique (JAM, see Cappellari 2008), which allows for orbital anisotropy, specified by the meridional plane anisotropy parameter $b = \sigma_R^2/\sigma_z^2 = 1/(1-\beta_z)$.

The adopted prior distributions for the six free parameters are presented in Table 6.2, together with the one-dimensional marginalized posterior PDFs derived from the combined L&D analysis. As discussed by B12, we choose very broad uninformative priors encompassing the entire range of realistic parameter values and allowing for a wide variety of galaxy models. In particular, the prior on $v_{\rm vir}$ is based on the velocity dispersion-halo virial mass relationship as determined by, e.g., Bundy, Treu & Ellis (2007) for massive ellipticals, allowing for a broad standard deviation.

6.5 Results and discussion

In this chapter we focus on the inferences for the total stellar mass of the two analyzed systems. The posterior PDFs for the quantity $\log_{10} M_\star/M_\odot$ are shown in Fig. 6.2 as histograms. The values are tightly constrained: we find $\log_{10} M_\star/M_\odot = 11.52^{+0.02}_{-0.04}$ for J0936 and $\log_{10} M_\star/M_\odot = 12.01^{+0.03}_{-0.03}$ for J0912. The corresponding dark matter fractions within one effective radius $R_{\rm eff}$ are $f_{\rm DM} = 0.06^{+0.10}_{-0.05}$ and $f_{\rm DM} = 0.18^{+0.08}_{-0.08}$, respectively. These values are in agreement within the uncertainties with the findings from the most accurate dynamical studies of local ellipticals, which measure median $f_{\rm DM} \approx 0.10-0.25$ (see Williams, Bureau & Cappellari 2009; Thomas et al. 2011; Cappellari et al. 2013). We note that J0936 is at the lower limit of these values and is marginally consistent with having no dark matter contribution within its inner regions.

From the SSP analysis described in Sect. 6.3 we obtain a direct measurement of the IMF slope for the two systems, inferring $x_{\rm J0936} = 2.10 \pm 0.15$ and $x_{\rm J0912} = 2.60 \pm 0.30$ respectively, suggestive of a slight steepening of x with increasing galaxy mass. From these values we derive the total $M_\star$ of the two objects and

we compare them with the corresponding $M_\star$ independently determined from the lensing and dynamics study, as illustrated in Figure 6.2. As clearly seen, the stellar masses inferred from the two methods are consistent within the one-sigma uncertainties for both galaxies.

The first result is that both galaxies are consistent with a Salpeter-like IMF: for J0912, $x = 2.35$ is within the 1-sigma uncertainties derived from the SSP analysis, and is actually preferred over the *maximum a posteriori* (MAP) slope $x_{\rm J0912} = 2.6$ with an 84% probability (Bayes factor $B = 5.2$). For J0936, a Salpeter IMF is slightly disfavoured with respect to the MAP slope $x_{\rm J0936} = 2.1$, albeit only marginally ($B = 0.40$). In general, even though we see a weak steepening of the best-fit IMF when going from the slightly sub-Salpeter J0936 ($x \simeq 2.1$) to J0912 (best-fit slope $x \simeq 2.6$), there is no compelling indication of an IMF slope trend with galaxy mass from this data set.

A Chabrier IMF, on the other hand, is ruled out for both systems with a high degree of confidence. A Salpeter-like IMF is preferred over a Chabrier-like one at 89% probability ($B = 8$) for J0936, and at 99% probability ($B = 96$) for J0912, corresponding in the second case to very strong evidence.[1] This confirms the findings of this thesis (Chapters 3 and 4, Spiniello et al. 2011, 2012) and of several other studies of ETGs, using a variety of methods, e.g. Grillo et al. 2009; Cappellari et al. 2012).

We note that the SSP results are obtained under the assumption of a single power-law IMF. A broken power-law (as proposed by Kroupa 2001) or a log-normal IMF (as in Chabrier 2003), both described by two different slopes for different mass ranges ("tapered IMFs"), will be considered in future works. In particular, we plan to apply the method presented here for the analysis of the entire XLENS sample (Spiniello et al. 2014, in prep.) testing different assumptions for the IMF with the value of $M_{\rm low}$ as well as the peak mass characterizing a tapered IMF as free parameters.

Some works based on absorption-line strengths (e.g., Ferreras et al. 2013) have suggested that the most massive ETGs ($\sigma \gtrsim 200\,{\rm km\,s^{-1}}$) might have increasingly bottom-heavy IMFs, with slopes significantly steeper than Salpeter, i.e. $x = 3.0 - 3.5$. Even though one might have concluded from the inferences drawn from the spectroscopic SSP analysis alone that the massive galaxy J0912 is consistent with an $x = 3.0$ super-Salpeter IMF, that scenario is clearly ruled out when also the results of the combined L&D analysis are brought into the picture. In fact, for

[1] Very similar values of the Bayes factors are obtained if we compare the Chabrier IMF with the MAP slopes rather than with Salpeter.

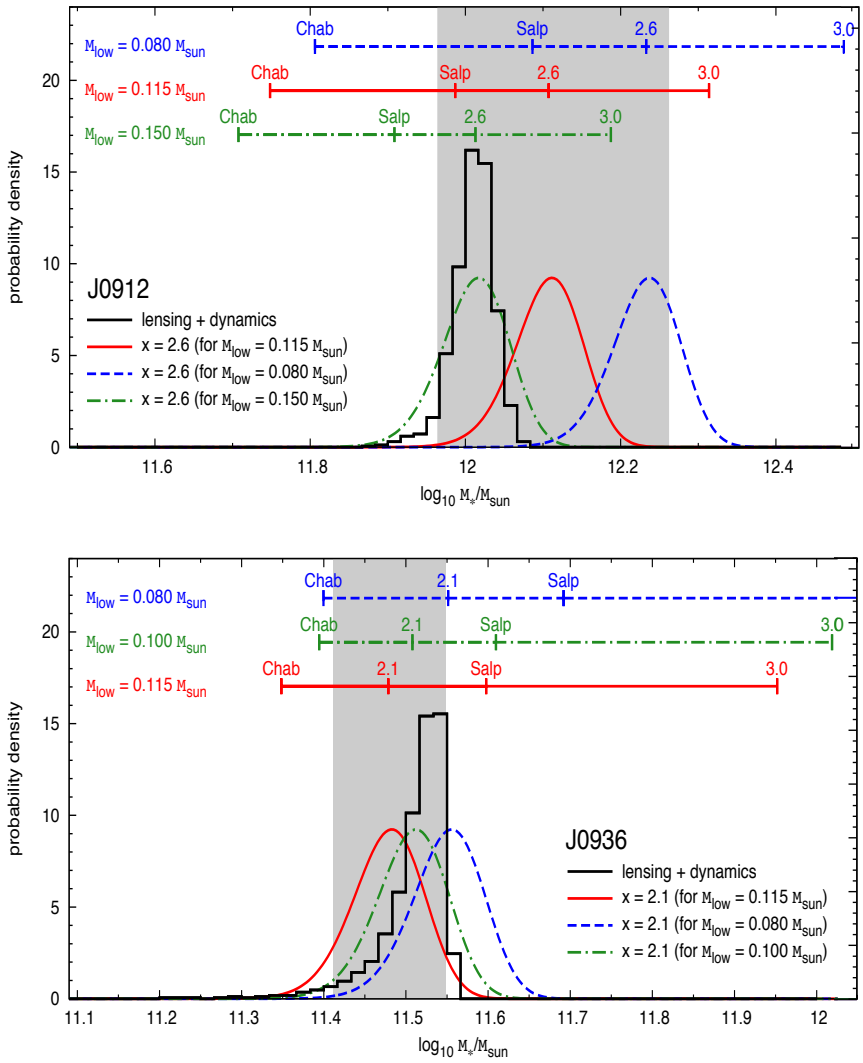

Figure 6.2: Comparison of the total stellar masses $M_\star$ inferred from the combined lensing and dynamics analysis (histogram) with the $M_\star$ determined from the spectroscopic SSP modelling of line-strength indices, for different values of the IMF slope (indicated above the tics on the horizontal bars). The solid red curve and the grey band denote, respectively, $M_\star$ for the MAP slope and the corresponding 1σ uncertainties around that value (i.e., $x_{\rm J0936} = 2.10 \pm 0.15$ in the left panel and $x_{\rm J0912} = 2.60 \pm 0.30$ in the right panel), derived by adopting the low-mass IMF cut-off $M_{\rm low} = 0.115\,M_\odot$ from DSEP. The dashed blue curve shows $M_\star$ obtained for the MAP slope when we adopt the value $M_{\rm low} = 0.080\,M_\odot$ assumed by CvD12. The dash-dotted green curve gives the inference for $M_\star$ when using the MAP slope and the best-fit $M_{\rm low}$ value.

J0912 (and even more so for J0936) a Salpeter IMF is favoured over a steep $x = 3.0$ IMF by a Bayes factor $B > 1000$, corresponding to decisive evidence.[2] More intuitively, adopting a super-Salpeter IMF results in a stellar mass exceeding the galaxy total mass predicted by the combined model, and therefore this scenario must be ruled out as unphysical.

Finally, the approach presented in this chapter allows for the first time a resolution of the long-standing problem of constraining the low-mass cut-off for the IMF. In previous studies, $M_{\rm low}$ has been treated as a fully unconstrained parameter, despite being critical to determine $\Upsilon_\star$. Stars with masses below $\sim 0.15\,M_\odot$ have very little effect on the spectral lines in the optical and near-infrared for any assumed IMF slope (CvD12) but they give a non-negligible contribution to the total mass budget of the system (Worthey 1994). Therefore, it is impossible to determine $M_{\rm low}$ from spectroscopic studies alone, since varying this parameter does not have any real impact on the spectra and on the line-index measurements. Luckily, this degeneracy can be broken when adding the information from the combined L&D analysis. The analysis conducted so far in this chapter has assumed the cut-off mass value $M_{\rm low}^{\rm D} = 0.115\,M_\odot$ assumed by DSEP. However, when adopting a lower value $M_{\rm low}^{\rm H} = 0.08\,M_\odot$, corresponding to the hydrogen burning limit (as suggested by, e.g., CvD12), the inferred total stellar mass increases significantly for the steeper IMF slopes, i.e. around 25% for $x = 2.35$ (Salpeter) and 50% for $x = 3.0$. For J0936 the constraints on $M_\star$ are not good enough to discriminate between the two possibilities; on the other hand, in the case of J0912 (considering the MAP slope $x_{\rm J0912} = 2.6$), there is decisive evidence in favour of ${M_{\rm low}}^{\rm D}$ with $B = 401$, corresponding to 99.8% probability.

We combine the results of the L&D and SSP analyses of both galaxies to derive the joint inferences on the IMF slope and cut-off. To this purpose, we use the DSEP isochrones extrapolated down to $0.06\,M_\odot$ to compute the V-band $\Upsilon_\star$ for different values of the IMF slope and $M_{\rm low}$ for both ETGs; these $\Upsilon_\star$ values are used to convert the observed luminosities into stellar masses. The probability density for this stellar mass is then determined from the posterior PDF of the L&D analysis (see Fig. 6.2), which acts as prior at this level of inference. In addition, we assume a Gaussian PDF for the IMF slope, as determined from the SSP modelling in this chapter, and similarly a Gaussian PDF for the ETG luminosity, determined by Auger et al (2009), which both act as priors. We adopt a flat prior U(0.06, 0.25) on $M_{\rm low}/M_\odot$. We then run a Markov Chain Monte Carlo with 10^5 samples drawn

[2] It has been argued that $B > 1000$ is high enough to be used as conclusive forensic evidence in criminal trials, cf. Kass & Raftery (1995) and references therein.

by varying x, $M_{\rm low}$ and ETG luminosity, to sample the joint lensing, dynamics and SSP posterior. Finally we combine the posteriors derived from the two galaxies, and marginalize over luminosity to obtain the joint 2-D posterior PDF, which is shown in Fig.6.3. The resulting marginalized MAP values are $x = 2.22 \pm 0.14$ for the IMF slope, and $M_{\rm low} = 0.13 \pm 0.03\, M_{\odot}$ for the low-mass cut-off.

6.6 Conclusions

In this work, for the first time, we compare the results of a state-of-the-art combined lensing and dynamics analysis of two early-type galaxies with the corresponding inferences from a spectroscopic SSP study of line-strength indices. This is made possible by the exquisite quality of the data sets available for the two systems, J0936 and J0912, including *HST* high-resolution imaging and high signal-to-noise X-Shooter spectra.

We model simultaneously the lensing and kinematic data sets by adopting a flexible, axisymmetric, two-component mass distribution for the dark halo and the luminous profile (both self-gravitating), and solving the anisotropic Jeans equations. We derive tight constraints on the total stellar mass and dark matter fractions (within one $R_{\rm eff}$) of the two galaxies, i.e. $\log_{10} M_{\star}/M_{\odot} = 11.52^{+0.02}_{-0.04}$ (and $f_{\rm DM} = 0.06^{+0.10}_{-0.05}$) for J0936 and $\log_{10} M_{\star}/M_{\odot} = 12.01^{+0.03}_{-0.03}$ (and $f_{\rm DM} = 0.18^{+0.08}_{-0.08}$) for J0912, independent of the IMF. These dark matter contents are in agreement, within the uncertainties, with the findings of dynamical studies of local ellipticals (e.g. Cappellari et al. 2013). By comparing the posterior PDFs for $M_{\star}$ derived from this combined analysis with the completely independent results from the spectroscopic SSP study of the two systems, we draw the following conclusions on the properties of their IMFs:

- The modelling of the line-strength indices (adopting solar metallicity and a cut-off mass $M_{\rm low} = 0.115\, M_{\odot}$) provides a direct determination of the IMF slopes for the two lenses, namely $x_{\rm J0936} = 2.10 \pm 0.15$ and $x_{\rm J0912} = 2.60 \pm 0.30$. The total stellar masses inferred from this method are completely consistent within the one-sigma uncertainties with the results obtained from the combined lensing and dynamics analysis, which is a fully independent approach that makes no assumptions on the IMF.

- For both galaxies, an IMF with slope close to Salpeter ($x = 2.35$) provides a much better description than a Chabrier profile: statistical analysis based on the calculation of evidence ratios (i.e., Bayes factor) shows that a Salpeter

IMF model is preferred over a Chabrier one with 89% and 99% probability for J0936 and J0912, respectively.

- Bottom-heavy IMFs significantly steeper than Salpeter, i.e. with slopes $x \geq 3.0$, are ruled out with decisive evidence (Bayes factor $B > 1000$) for both galaxies. The values for $M_\star$ implied by these super-Salpeter IMFs unphysically exceed the total galaxy mass derived from the combined lensing and dynamics analysis. This result contradicts the findings from absorption line spectroscopy studies (see e.g. Ferreras et al. 2013) which support IMF slopes $x = 3.0-3.5$ for massive ETGs such as those considered here ($\sigma_{\rm J0936} \simeq 250\,{\rm km\,s^{-1}}$ and $\sigma_{\rm J0912} \simeq 330\,{\rm km\,s^{-1}}$).

- For the system J0912, a low-mass IMF cut-off of $M_{\rm low} = 0.08\,M_\odot$ (corresponding to the hydrogen burning limit) is ruled out with a probability of 99.8% in favor of the value $M_{\rm low}{}^{\rm D} = 0.115\,M_\odot$ assumed by DSEP. For J0936, instead, it is not possible to reliably discriminate between the two values.

- By combining the L&D and SSP inferences of the two lenses, we obtain the marginalized MAP values $x = 2.22 \pm 0.14$ for the IMF slope and $M_{\rm low} = 0.13 \pm 0.03\,M_\odot$, consistent with a Salpeter-like IMF and a low-mass cut-off slightly higher than the hydrogen burning limit.

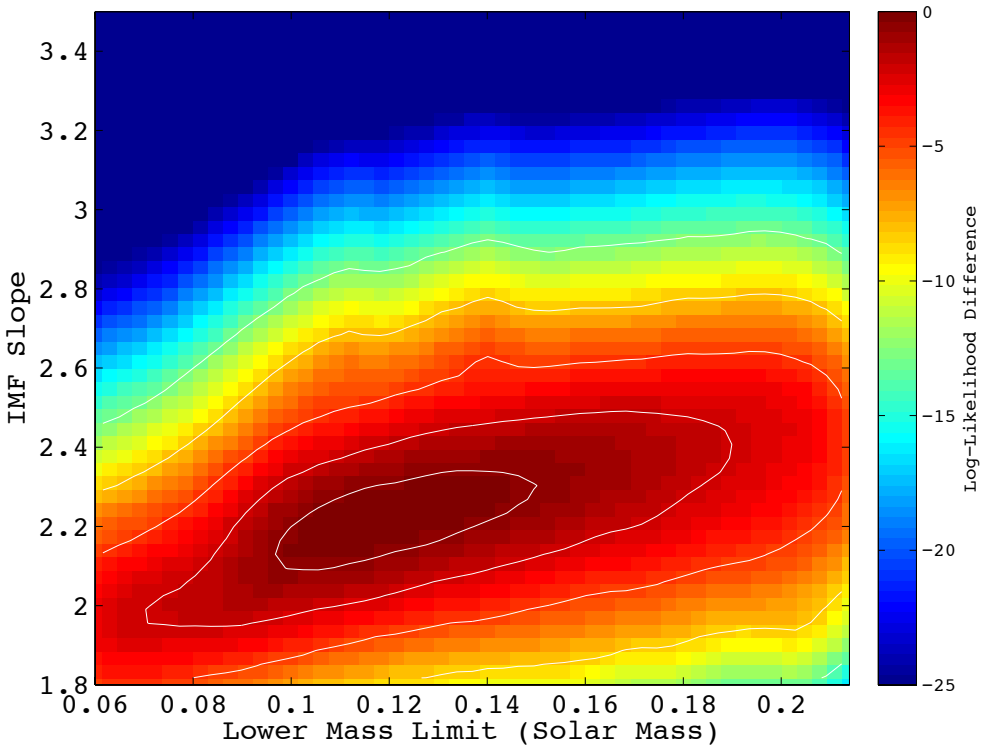

Figure 6.3: Joint two-dimensional posterior PDF of the IMF slope and $M_{\rm low}$ for the two galaxies combined using both L&D and SSP constraints. The contours denote the equivalent of $\exp(-\chi^2/2)$ for $\chi = 1, 2, 3, 4$ and 5.

7 A detailed comparison of the effects of low-mass stars in Single Stellar Population models.

Science is facts;
just as houses are made of stones, so is science made of facts;
but a pile of stones is not a house
and a collection of facts is not necessarily science.

Jules Henri Poincare

Based on:
C. Spiniello, S.C. Trager, L.V.E. Koopmans, 2013b, in prep.

In this chapter we perform a direct comparison between two new single stellar population (SSP) models that have been constructed specifically for the purpose of measuring the Initial Mass Function (IMF) slope down to $\sim 0.1\,M_{\odot}$ for old, metal-rich stellar populations by Conroy & van Dokkum (2012a, hereafter CvD12), and Vazdekis et al. (2012, hereafter MIUSCAT). Our goal is to show how important the underlying model assumptions and ingredients such as stellar libraries (e.g. stellar spectral library parameter coverage especially at high metallicity and for non-solar abundance ratios) or isochrones are in constraining the IMF slope for massive early-type galaxies (ETGs).

In both models, we study equivalent widths (EWs) of several stellar features with varying ages, metallicity and elemental abundances, as a function of the IMF slope. We use the IMF-sensitive features defined in Chapter 5 (Spiniello et al. 2013) in the wavelength range 4000–7400 Å where the two SSP models make use of the same empirical spectral library (the MILES Library, Sánchez-Blázquez et al. 2006) plus the redder Na I (λ8190 Å, with the definition given in Chapter 4) and CaT (λ8484–8642, Cenarro et al. 2001) features that have already been shown to be M-dwarf-sensitive (Cenarro et al. 2003; van Dokkum & Conroy 2010; Smith, Lucey & Carter 2012; Spiniello et al. 2012), which arise from different spectral libraries in the models. We show that the use of optical indices, coming mainly from TiO and CaH molecular absorption lines, permits us to eliminate the uncertainty caused by the different stellar libraries used in the synthesis process.

Neither of the two SSP models are able to simultaneously reproduce all the optical stellar features in SDSS ETGs with $\sigma_{ETG} \geq 250\,\mathrm{km\,s^{-1}}$ if we restrict the analysis to solar abundance patterns and to line-index measurements. The sodium indices (e.g. NaD λ5895 and Na I λ8190) in galaxies do not follow the solar-abundance models well, as shown in Spiniello et al. (2012), presented in Chapter 4 of this thesis. The MIUSCAT models do not allow for non-solar abundance patterns. They are able to reproduce the galaxy's indices in a Na I–NaD plot, but these indices alone seem to predict an extremely bottom-heavy IMF for very massive ETGs. When examining Na I–TiO2, however, the data follow the CvD12 models, and these models also can fit NaD indices of very massive ETGs when models with [Na/Fe] ≥ 0 are considered. We also find that predictions of IMF slope variations and abundance patterns arising from the two different models are very different, especially when sodium lines are used. In particular, we investigate the variation of the two sodium indices with IMF slope and [Na/Fe] abundance in CvD12, thanks to the flexibility of these models to single element abundance patterns. We show that the NaD feature is very sensitive to [Na/Fe] variations

whereas the Na I index depends mainly on the IMF slope and only weakly on elemental abundance. Unfortunately a complete and flexible set of models that allows us to investigate at the same time variations in age, IMF, metallicity, [α/Fe] and abundance patterns is not currently available. However, in this thesis we have shown that we can constrain the low-mass end of the IMF in massive ETGs using the models of CvD12 and a large set of indicators that allow us to break the degeneracies between IMF slope, age and abundance patterns.

7.1 Introduction

A quantitative study of the luminous stellar content of unresolved stellar populations requires the use of stellar population synthesis models. Many of the fundamental properties of unresolved stellar populations are encoded in their spectral energy distributions (SEDs). The characterization of the full SED allows one to derive relevant stellar parameters such as age, metallicity, IMF shape, element abundance, and the physical state and quantity of dust and gas of galaxies (e.g. Conroy 2013). The evolutionary population synthesis approach was first implemented by Tinsley (Tinsley 1968, 1972; Tinsley & Gunn 1976). This approach is based on stellar evolution theory to constrain all the phases of stellar evolution for a range of different stellar types at a given age and metallicity.

Since Tinsley's work, more detailed models have been constructed (e.g. Buzzoni 1989; Bressan, Chiosi & Fagotto 1994; Worthey 1994; Bruzual & Charlot 1993, 2003; Leitherer et al. 1999; Maraston 2005) to extract information from the SEDs of galaxies. All stellar population synthesis models are mainly based on three ingredients, which determine the quality of the predictions: i) a prescription for the initial mass function (IMF), ii) a set of stellar evolutionary isochrones and iii) one or more stellar spectral libraries, either theoretical or empirical. The quality of the resulting spectral energy distribution (SEDs) model relies to a great extent on the atmospheric parameters coverage of the library (temperature, gravity and metallicity).

Historically the IMF has been considered universal and the same as that of the Milky Way (e.g. Kroupa 2001; Bell & de Jong 2001; Chabrier 2003). However, in the last years increasingly more observational and theoretical evidence (e.g. van Dokkum & Conroy 2010; Treu et al. 2010; Conroy & van Dokkum 2012b; Thomas et al. 2011; Cappellari et al. 2012; Tortora, Romanowsky & Napolitano 2013) supports the idea of a non-universal IMF whose slope could steepen with galaxy mass (Spiniello et al. 2012, 2013). Recently, two new stellar population

models have been developed specifically for the purpose of testing the low-mass end of the initial mass function (IMF) down to $\sim 0.1\,M_{\odot}$ in old, metal-rich stellar populations: Conroy & van Dokkum (2012a, hereafter CvD12), and Vazdekis et al. (2012, hereafter MIUSCAT). The aim of this chapter is to directly compare these two SSP models in the study of the stellar population of massive ETGs. In fact, even though the two sets of models are based on different assumptions, both are built for the same purpose of measuring low-mass stars ($\leq 0.3\,M_{\odot}$) in the same class of systems. If one plans to use these SSP models to study observational data and stellar population in unresolved spectra of old, evolved galaxies, as we have done in this thesis, it is essential to demonstrate that the conclusions and previsions on the galaxy parameters do not depend on the assumptions of the model itself. A direct comparison of these two state-of-the-art SSP models is therefore useful to understand whether the recent suggestions that the IMF steepens with galaxy velocity dispersion does not arise from a misunderstanding of the main ingredients of the models.

The chapter is organized as follows: in Section 7.2 we give a brief introduction on the two sets of models that we compare and highlight their similarities and differences. In Section 7.3 we compare both models with absorption-line indices of SDSS galaxies (used already in Chapters 4 and 5). Finally in Section 7.4 we present our findings and we discuss our conclusions.

7.2 Simple Stellar Population Models

In this section we provide a brief introduction to the two sets of SSP models. We first describe the main ingredients and the space of stellar parameters that are explored, before proceeding to compare them.

7.2.1 Conroy & van Dokkum SSP models

Conroy & van Dokkum (2012a) presented new SSP models with variable abundance patterns and stellar IMFs, suitable to study integrated light spectra of galaxies with ages ≥ 3 Gyr. They use the combination of three different isochrones to explore the separate phases of stellar evolution. They use: i) the Dartmouth isochrones (Dotter et al. 2008) for the main sequence and the red giant branch (RGB); ii) the Padova isochrones (Marigo et al. 2008) to describe AGB evolution and the horizontal branch (HB); iii) and the Lyon isochrones (Chabrier & Baraffe 1997; Baraffe et al. 1998) for stars with masses $M \leq 0.2 M_{\odot}$. All models have solar metallicity, even when synthesizing models with different

abundance patterns. The wavelength interval covered by the final fiducial model is $0.35\,\mu m < \lambda < 2.4\,\mu m$, at a resolution of $R \simeq 2000$. The CvD12 models use two separate empirical libraries: the MILES library from $0.35\,\mu m < \lambda < 0.74\,\mu m$ (Sánchez-Blázquez et al. 2006), and the IRTF library of cool stars, which covers the wavelength range $0.81\,\mu m < \lambda < 2.4\,\mu m$ (Cushing, Rayner & Vacca 2005), plus synthetic stellar spectra to cover the gap and to investigate spectral variations due to changes in individual elemental abundances. In the version of the code that we examined, the model allows for variation in the elements C, N, Na, Mg, Si, Ca, Ti, Cr, Mn, and Fe, whereas O, Ne, S are varied in lock-step.

With the isochrones and stellar libraries described above, they construct integrated light spectra via the equation:

$$f(\lambda) = \int_{m_l}^{m_h(t)} s(\lambda, m)\,\phi(m)\,dm \tag{7.1}$$

where the integral over stellar masses ranges from the hydrogen burning limit (assumed to be $m_l = 0.08\,M_\odot$), to the most massive star still alive at time t. In the equation, s represents the spectrum of an individual star, f is the integrated spectrum and $\phi(m) = dN/dm$ is the IMF. They explore variations in age between 3–13.5 Gyr, four different IMFs – a bottom-light Chabrier-like, Salpeter ($x = 2.35$), and two bottom-heavy IMFs with slopes of $x = 3.0$ and $x = 3.5$ – $\alpha-$enhancement and individual element abundances.

7.2.2 The MIUSCAT SSP models

The MIUSCAT models are an extension of stellar population synthesis models based on the MILES (Sánchez-Blázquez et al. 2006) and CaT (Cenarro et al. 2001) empirical stellar spectral libraries to cover the spectral range $0.346\,\mu m < \lambda < 0.947\,\mu m$. They use the Indo-U.S. library (Valdes et al. 2004) to join the stellar spectra and to extend the spectral coverage of their model SEDs to the blue and red. In order to determine which stars to include in the synthesis and to assign masses to them, they use the solar-scaled theoretical isochrones of Girardi et al. (2000), which cover a wide range of ages, 0.063 to 17.8 Gyr, and six metallicity bins. These isochrones include the latest stages of the stellar evolution, including a simple synthetic prescription for incorporating the thermally pulsing AGB regime to the point of complete envelope ejection (Bertelli et al. 1994). The physics of these models was updated with respect to Bertelli et al. (1994) with an improved version of the equation of state, the opacities of Alexander & Ferguson (1994) and a milder convective overshoot scheme. Several IMFs are considered: the

unimodal and bimodal power-law IMFs defined in Vazdekis et al. (1996), and the multi-part power-law IMFs of Kroupa (2001). The Salpeter (1955) IMF is obtained by adopting the unimodal case with slope $\Gamma = x - 1 = 1.3$. The spectra of the stars are integrated along the isochrone taking into account their number per mass bin according to the adopted IMF. Here we only study the unimodal power-law IMFs, to perform a fair comparison with CvD12.

7.3 Comparing model predictions

Both models test different assumptions for the IMF and are created for the specific purpose of examining the stellar content of massive ETGs. They are both mainly based on empirical libraries that generally provide good fits to line-strengths and full spectra of populations of Solar neighbourhood stars (e.g. Carter, Visvanathan & Pickles 1986). However, empirical stellar libraries are often not able to reproduce consistently the spectral features of systems which have undergone a star formation history (SFH) different than the solar-neighbourhood (for instance, in the case of ellipticals, which are shown to be overabundant in α-elements relative to the Sun: Peterson 1976; Peletier 1989; Worthey 1992). This happens because, by construction, the abundance pattern of models based on empirical libraries is dictated by stars in the library, which are mainly observed in the solar-neighbourhood (McWilliam 1997). On the other hand, a clear advantage of using real stars is that they do not rely on our knowledge of the physics of stellar atmospheres and databases of atomic and molecular transitions.

Moreover, CvD12 and MIUSCAT make use of different isochrones, and also a different method to attach stars to the isochrones at low mass (see following subsection). In the red-VIS and NIR regions the two SSP models use two different libraries (CVD12 uses IRTF; MIUSCAT uses CaT and Indo-US), while in the blue region (3500–7400 Å) they use the same empirical spectral library, although in slightly different ways. The new set of blue IMF-sensitive indicators defined and used in Chapter 5 (Spiniello et al. 2013) are therefore essential in this context to eliminate differences arising from the use of different stars.

In order to directly compare predictions from the two different models, we calculate index variations as functions of the IMF slope and age of some of the VIS optical indices for both MIUSCAT and CvD12 models. In Figure 7.1, we show the predicted index variations for a range of CvD12 models (upper panels) and MIUSCAT models (lower panels) with different ages (lines of different colors).

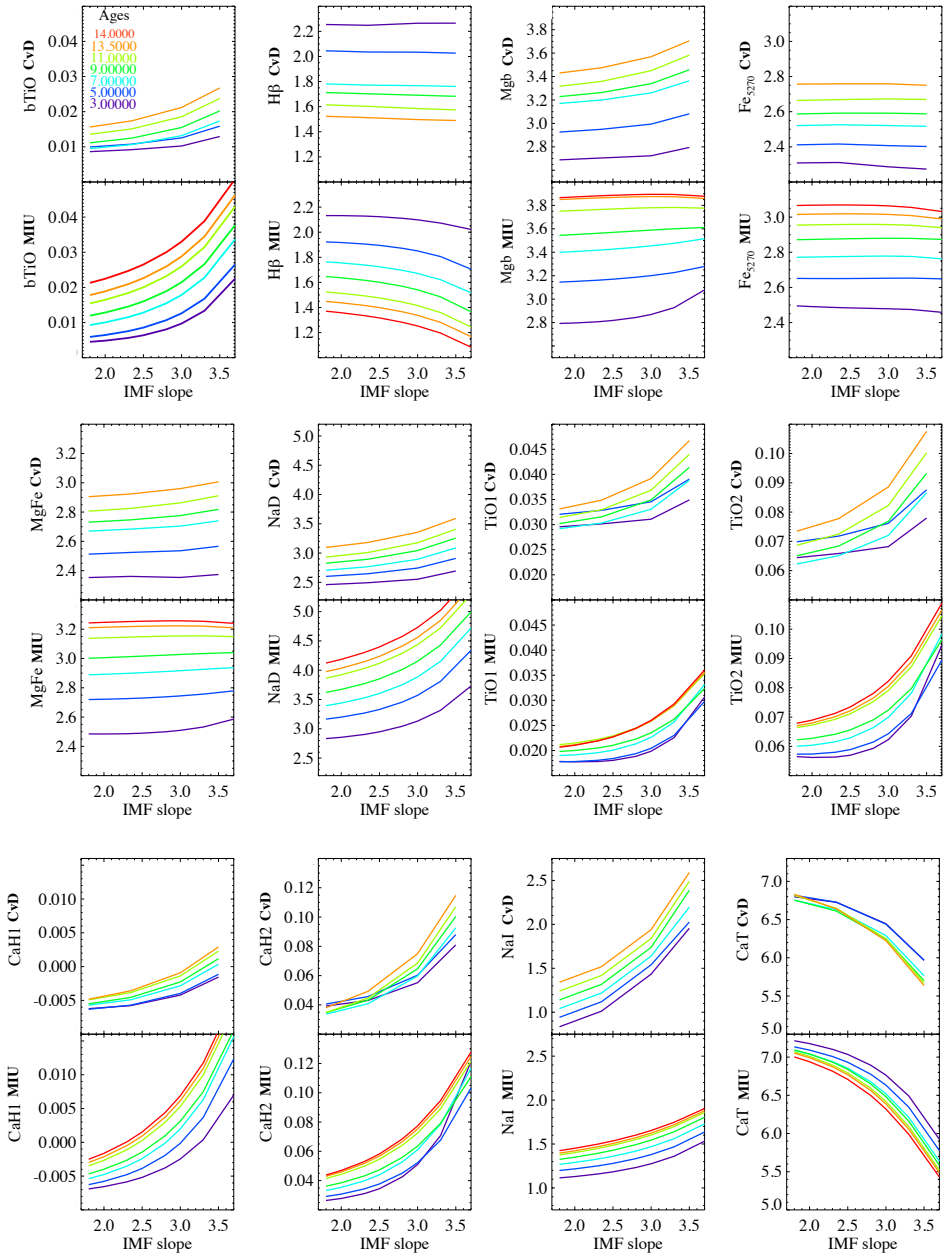

Figure 7.1: Variation of index strengths with IMF slope for CvD12 models (upper panels) and MIUSCAT models (lower panels) convolved to a common resolution of σ = 350 km s^{-1}. In each panel, different colors represent SSP with different ages, as indicated in the legend on the first panel. TiO and CaH indices are given in magnitudes, while all the other indices are given in Å.

Because of the different approach in dealing with metallicity and [α/Fe] (see following section), we restrict our comparison to solar abundances and metallicity.

Most of the blue classical Lick indices (Burstein et al. 1984; Worthey 1994; Trager et al. 1998) do not depend (or depend only weakly) on the IMF slope, while the Na, TiO and CaH indices increase from a Chabrier-like IMF to a bottom-heavy IMF for both models (as already shown in previous chapters). The only IMF-sensitive feature weaker for more bottom-heavy IMFs is the Ca Triplet (as already shown in previous studies, e.g. Cenarro et al. 2003; Conroy & van Dokkum 2012a). For the majority of the indices, the qualitative slope of the variation is similar, although generally slightly milder for the CvD12 models than for the MIUSCAT models. For some indices, however, the two SSP models give quite different predictions for IMF variations. CaH1 is an extreme case, and in addition bTiO and both the sodium indices (Na I and NaD) behave differently in the two sets of models. We further investigate the behaviour of these particular indices in the following sections. Predictions for the Hβ index are also different, although this index depends only weakly on the IMF slope. On the other hand, index variations with IMF slope of the redder TiO features predicted from the two SSP models appear to be similar. Remarkably, variations of the CaH2 and the CaT index are even more similar. Moreover, for some indices, there is also a shift in the zero-point: for a Chabrier IMF, NaD indices in CvD12 models with *solar abundance* are systematically lower than MIUSCAT models while TiO indices are systematically higher. Small differences in the metallicity-sensitive features could be due to the different ways the two sets of models deal with metallicity and/or [α/Fe]. This will be briefly addressed in the following subsection.

7.3.1 Effects of Metallicity and/or [α/Fe]

The CvD12 models use solar-metallicity isochrones even when synthesizing models with different abundance patterns. The abundance variations of single elements are implemented at fixed [Fe/H], which implies that the total metallicity Z varies from model to model. Each MIUSCAT SSP has instead a fixed total metallicity, and in total they explore six metallicity bins ($Z = 0.0004, 0.001, 0.004, 0.008, 0.019$ and 0.03), where 0.019 represents the solar value. Therefore, if a direct comparison is possible between the models, it has to be done at solar metallicity and solar [α/Fe]. Obviously this is very restrictive and may be problematic if one aims to disentangle element enhancement (or metallicity changes) and IMF variations.

7.3.2 Effect of Isochrones

A significant difference between the models is the set of isochrones used to calculate stellar parameters and spectra. A large number of isochrones exist in the literature (see Conroy 2013 for a review), spanning a wide range of ages and chemical compositions for stars with masses between the hydrogen burning limit ($\sim 0.08\,M_\odot$) and $\sim 100\,M_\odot$. Different sets of isochrones are tailored for different mass ranges and different evolutionary phases of stellar evolution. Some are more effective in tracking the high-mass stars, others focus on the main sequence, red giant branch (RGB), and horizontal branch (HB) evolution of low-mass stars ($M < 0.3\,M_\odot$), such as the Dartmouth models (Dotter et al. 2008). Others are particularly effective at describing the very low-mass end of the IMF down to the brown dwarf regime, such as the Lyon models (Chabrier & Baraffe 1997; Baraffe et al. 1998). Since no single set of available isochrones covers a full range of ages, metallicity and evolutionary phases, most of the stellar population synthesis models use a combination of different isochrones. Combining various sets of isochrones is not trivial because different groups can make different physical assumptions (for instance convection, rotation, etc.), and consequently the age at which stars evolve away from the main sequence can vary between models.

Commonly-used isochrones for the bulk of the age and metallicity range of elliptical galaxies include the Padova isochrones (Bertelli et al. 1994; Girardi et al. 2000; Marigo et al. 2008) or the BaSTI models (Pietrinferni et al. 2004; Cordier et al. 2007). These are often supplemented with the Geneva models (Schaller et al. 1992; Meynet & Maeder 2000) at younger ages. Little attention has been paid in the past to the lowest-mass portion of the isochrones, since low-mass stars contribute only few percent of the light of an old stellar population (in the optical, e.g. Worthey 1994; Renzini 2006; Conroy 2013). However, if one wants to test the non-universality of the low-mass end slope of the IMF, this 1–5% contribution is crucial. It is for this reason that CvD12 decided to use the Lyon models for stars with masses below $0.2\,M_\odot$, The Lyon models use the surface boundary condition of the base of the atmosphere (rather than at $T = T_{\rm eff}$) which is better for stellar interior codes that are not ideally suited to compute the physical conditions for high-density, low-temperature environments down to $T = T_{\rm eff}$ (CvD12). Using only the solar-scaled theoretical Padova isochrones of Girardi et al. (2000), the MIUSCAT library is forced to cut off at $0.15\,M_\odot$, since the Padova isochrones do not extend to lower masses. This is one of the reasons why in this thesis we have chosen to use the CvD12 rather than the MIUSCAT SSP models. We will discuss our choice further and list other reasons at the end of this chapter.

In Figure 7.2, we focus on the blue and red optical TiO features. Because CvD12 and MIUSCAT make use of the same empirical stellar library (MILES), in this spectral region the main difference between the two sets of models are the isochrones they use. We plot variations predicted for the bTiO and TiO2 indices (both IMF-sensitive indices) by changing the IMF slope for an old ($\sim 12 - 14$ Gyr) SSP model with solar metallicity and solar [α/Fe] for both MIUSCAT and CvD12. Although qualitatively the predictions of the two SSP models agree, the MIUSCAT models suggest a steeper variation of both indices with IMF slope which affects the inference on the IMF slopes in ETGs. Based on the MIUSCAT models, Ferreras et al. (2013) give an analytical fit describing the correlation between central stellar velocity dispersion ($\sigma_{star,ETG}$) and IMF slope for a large sample of SDSS ETGs, which we find in Chapter 5 (Spiniello et al. 2013) to be shallower when using the CvD12 models. To test the importance of isochrones in constraining the IMF slope from TiO indices, we built new CvD12 models using Padova isochrones for all stellar evolutionary phases[1]. In Figure 7.2 the dashed black line shows the prediction on the variation of the two TiO indices with varying IMF for a CvD12 model with Padova isochrones. As expected, the discrepancy between MIUSCAT and CvD12 becomes smaller when the two models make use of the same stellar isochrones. However, the models do not predict exactly the same variation of TiO indices with IMF slope, even when they make use of the same empirical stellar library and set of isochrones. This difference is primarily due to the different methods used in the CvD12 and MIUSCAT models to attach stars to the isochrones at low mass. The MIUSCAT models use the theoretical parameters of the isochrones ($T_{\rm eff}, \log g, [{\rm Z/H}]$) to obtain stellar fluxes on the basis of empirical relations between colours and stellar parameters (temperature, gravity and metallicity, respectively). It finds the closest stars and weights them according to the distance to the target point ($T_{\rm eff,0}$, $\log g_0, [{\rm Fe/H}]_0$) in the stellar parameter space, using the interpolation algorithm described in Vazdekis et al. (2003a, 2010). The CvD12 SSP models use an M–$L_{\rm bol}$ relation, choose the closest observed stellar spectrum from the IRTF library with the appropriate bolometric luminosity, and then match it to a MILES spectrum at shorter wavelengths. Any residual differences could be due to the small offset in age between the two sets of models: we are comparing CvD12 model of 13.5 Gyr with MIUSCAT models with ~ 12.6 Gyr and ~ 14.1 Gyr.

[1] This work has been done in collaboration with C. Conroy, who kindly provided his models and collaborated to change the isochrones. We are very grateful to Prof. Conroy for his help in the realization of this chapter.

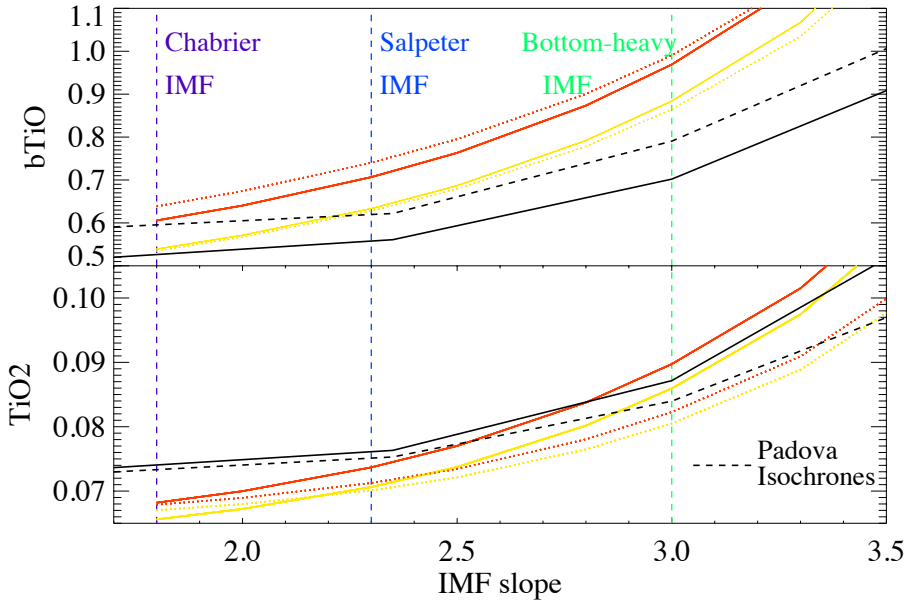

Figure 7.2: Variation of bTiO and TiO2 indices with IMF slope. Black solid lines are a CvD12 SSP model of 13.5 Gyr and solar [α/Fe], and black dashed lines are a CvD12 model with same age and [α/Fe], built using Padova isochrones for all the stellar evolutionary phases. Coloured lines are MIUSCAT SSP models with ages of ~ 14.1 (red) and ~ 12.6 (yellow). Solid lines have solar metallicity, while dotted have super-solar metallicity. Vertical lines show different IMFs.

7.3.3 Comparison to data

We now compare the CvD12 and MIUSCAT models with data on ETGs, for which they are specifically designed. We use the same sample of SDSS spectra selected in Chapter 5 stacked in five velocity-dispersion bins spread over 150–310 $\mathrm{km\,s^{-1}}$, to increase the final S/N in each bin. Here we also include a lower sigma-bin with an average value of 110 $\mathrm{km\,s^{-1}}$; however we limit our analysis to galaxies with $\sigma_\star \geq 150\,\mathrm{km\,s^{-1}}$. Below this value contamination from spiral galaxies becomes larger and emission lines affect our results prominently[2].

[2]To minimize spiral galaxy contamination in our sample and to select only ETGs, we select systems for which the likelihood of the de Vaucouleurs' model is 1.05 times larger than the likelihood of the exponential model. We select systems with very low star-formation rate and we

For the CvD12 and MIUSCAT models, as well as for the stacked spectra, we measure line-strength indices in the range 4000–8500 Å, including the standard Lick indices Hβ, Mgb, Fe5270, Fe5335, NaD and TiO2 using the definitions of Trager et al. (1998), the commonly-used [MgFe] combination[3] and the IMF-sensitive set of optical indicators described in Chapter 5 (Spiniello et al. 2013). Finally we use the modified Na I index defined in Chapter 4 (Spiniello et al. 2012) and the CaT index, even though we are aware that in this wavelength range the two models make use of different stellar libraries. We convolve all the galaxy and model spectra to an effective velocity dispersion of $\sigma = 350\,\mathrm{km\,s^{-1}}$ to correct for kinematic broadening before measuring indices. We also normalize the spectra using a second order polynomial fit. Indices in both the galaxies and the two sets of model spectra are measured with the same definitions and methods[4]. We do not place our indices on the zero-point system of the Lick indices and quote them as equivalent widths (EWs) in units of Å, except for TiO and CaH indices, which are given in magnitudes.

Figure 7.3 shows a zoom-in of the galaxy and SSP model spectra in the bTiO region, the bluest IMF-sensitive feature, with the index bandpass as well as the blue and red pseudo-continua bands shown as boxes. A clear increase of bTiO line-strength is visible in all panels, although the data show a somewhat stronger variation, probably due to the fact that this index is not only gravity-sensitive but also depends on age and possibly element abundance. For the CvD12 models, which allow a variation of the Ti abundance pattern, we investigate whether a non-solar [Ti/Fe] abundance could significantly vary the bTiO index. In Panel b) it is clear that the variation due to IMF is stronger than that due to non-solar Ti abundance. However only with full-spectrum fitting can one completely break the degeneracy between IMF variation and non-solar abundances (Conroy, Graves & van Dokkum 2013).

In order to have a fair comparison between the models, we restrict ourselves to solar metallicity (the only choice for CvD12) and solar [α/Fe] (the only choice for MIUSCAT). However, because very massive ETGs are known to be α-enriched and to have slightly super-solar metallicity, we also plot models with different metallicity or [α/Fe] in order to compare each set of models separately with our more massive galaxy spectra bins. Once again, we stress that the two sets of models change the metallicity of the SSPs in different ways. We choose the ages

set an upper limit to the redshift range ($z \leq 0.05$) to cover the wavelength range of interest. See Chapter 5 for further details on the selection criteria

[3] [MgFe] = $\sqrt{(\mathrm{Fe5270} + \mathrm{Fe5335})/2 \times \mathrm{Mg}b}$, González (1993)

[4] We use the code SPINDEX from Trager, Faber & Dressler (2008)

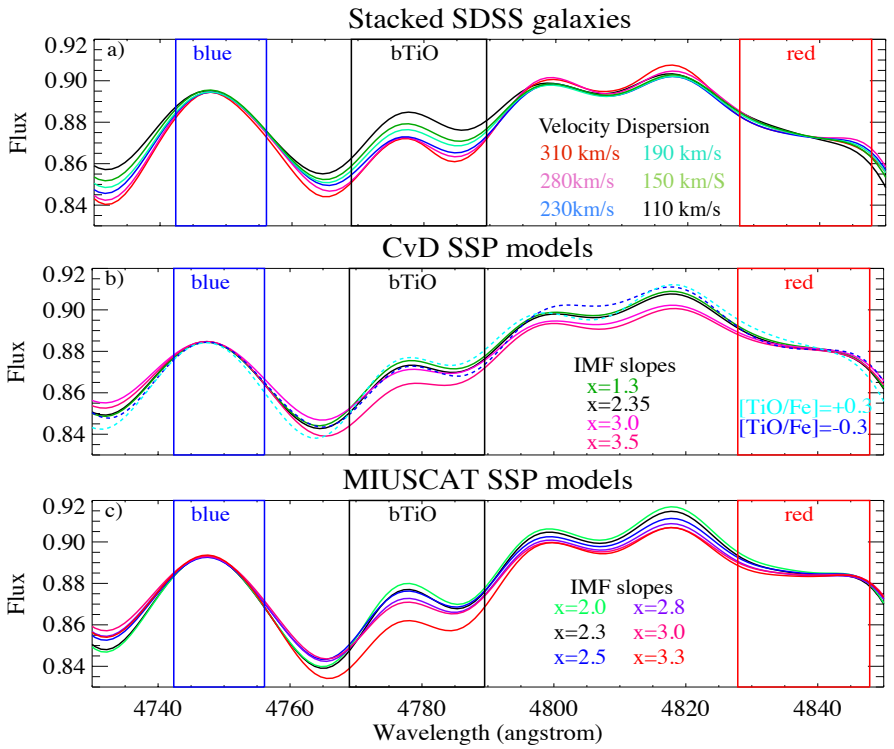

Figure 7.3: Galaxy (Panel a) and SSP model (Panel b and c) spectra in the regions of the bTiO absorption feature. A clear trend of increasing bTiO is visible in both data and models, although data show a stronger variation (see text). The bandpass of the index, as well as the blue and red pseudo-continua, are shown as boxes in the plots. *Panel a):* Stacked spectra of SDSS galaxies with different velocity dispersions over the range 110 – 310 $\mathrm{km\,s^{-1}}$. *Panel b):* CvD12 SSP models with same age (13.5 Gyr) and solar [α/Fe] but different IMF slopes, from Chabrier to very bottom-heavy (x = 3.5). Dotted lines show models with Chabrier IMF and different [Ti/Fe] abundances. Panel C): MIUSCAT SSP models with the same age (14.2 Gyr) and solar metallicity, but different IMF slopes, from an IMF with a slope of x = 2 to an extremely bottom-heavy IMF with a slope of x = 3.3. All spectra are normalized by a polynomial matching the flux at a point in each of the blue and red pseudo-continua bands.

of the two models to be as close as possible. Finally we limit ourselves to an unimodal IMF slope, the only choice for the CvD12.

Panel (a) of Figure 7.4 shows our preferred IMF indicators in the optical (see Chapter 5). The bTiO–TiO2 diagram shows a good agreement between the two set of models and the galaxies for old stellar populations (with an age of 12.5 ± 1 Gyr). These indicators clearly show a steepening of the IMF slope with galaxy mass: they imply a Chabrier IMF for the least-massive galaxies ($\langle\sigma_\star\rangle = 150\,\mathrm{km\,s^{-1}}$), Salpeter for the intermediate-mass galaxies and possibly a bottom-heavy IMF with $x \sim 3$ for the most massive SDSS ETGs[5]. In Panel (b), we plot TiO2 versus the Calcium triplet index (CaT λ8484–8642). The variation of indices with IMF slope is consistent between the two SSP models with similar age and solar abundance and the steepening of the IMF slope from Chabrier to Salpeter to bottom-heavy is confirmed. We can also confirm that the CaT index is almost metallicity independent (Cenarro et al. 2002) but is strongly dependent on [α/Fe]. In this wavelength range, the two models use different libraries. Since CvD12 models with solar [α/Fe] provide the best match with data for all the mass bins, one could argue that perhaps the IRTF library is a better choice to study the low-mass star population than the CaT library of Cenarro et al. (2001) used by MIUSCAT.

However, when sodium lines are used [Panels (c) and (d) of Figure 7.4], the situation is different. As discussed in Chapter 4 (Spiniello et al. 2012), CvD12 models with solar abundances only match the low-mass systems, while more-massive ETGs require higher [Na/Fe] *and* steep (Salpeter or slightly steeper) IMF slopes. In Panel (c), MIUSCAT models do a better job in matching the data at all velocity dispersions, but the most massive bin requires an IMF slope as steep as $x = 3.8$, in disagreement with the other indicators, other spectroscopic studies (Conroy & van Dokkum 2012b) and gravitational lens observations (Spiniello et al. 2011, 2012, 2013; Barnabè et al. 2013). In Panel (d), the MIUSCAT SSP models do not match the indices of very massive systems, while the CvD12 models with solar abundances do.

We conclude that the CvD12 SSP models with solar [Na/Fe] abundances predict a different variation of sodium indices with IMF slopes than the MIUSCAT models, while they agree when using other gravity-dependent indices, such as TiO2 and CaT. We emphasize that NaD lies in a part of the spectrum for which the two sets of models use the same stellar library, while Na I lies in the redder

[5] This is in agreement with the results presented in previous chapters of this thesis, and published in Spiniello et al. (2012, 2013) and Barnabè et al. (2013)

part where the models make use of two different stellar libraries. Therefore this difference cannot be attributed to the different stars used when constructing the SSP models.

We now investigate further the disagreement between the model predictions arising from sodium lines. In particular, using CvD12 models with different [Na/Fe] abundances we study the behaviour of the NaD and the Na I indices when varying the IMF slopes at fixed sodium abundance and when varying the [Na/Fe] at fixed IMF slope. In Figure 7.5 we show the CvD12 models with an age of 13.5 Gyr zooming on the regions of the NaD (top panel) and Na I (bottom panel) features. In both panels different colors show models with different [Na/Fe], varying between −0.3 and +0.3, while different line-styles represent models with different IMF slopes, between 1.8 and 3.5. The figure clearly demonstrates that the NaD absorption is more sensitive to [Na/Fe] than the redder Na I feature, which varies much more with the IMF slope. This sensitivity is also quantitatively expressed in Table 7.1, were we compute the quantity:

$$\left(\frac{\Delta\mathrm{IMF}}{\Delta[\mathrm{Na/Fe}]}\right)_i = \frac{I_i(x=3.5)_{[\mathrm{Na/Fe}]=0} - I_i(x=1.8)_{[\mathrm{Na/Fe}]=0}}{\langle\, I_i([\mathrm{Na/Fe}]=+0.3) - I_i([\mathrm{Na/Fe}]=-0.3)\,\rangle_{x=[1.8-3.5]}} \qquad (7.2)$$

for both indices. In the equation, the numerator measures the variation of the index i with IMF slope from a Chabrier-like IMF to an extremely bottom-heavy IMF (slope of $x = 3.5$), while the denominator is the average of the index variation with sodium abundances in the range $[-0.3, +0.3]$ for the two IMFs. The larger the value of $\Delta\mathrm{IMF}/\Delta[\mathrm{Na/Fe}]$ is, the larger the sensitivity to IMF steepening is compared to the sensitivity on Na-abundance. As shown in Conroy & van Dokkum (2012a,b) and confirmed in Spiniello et al. (2012), more massive systems seem to require larger values of [Na/Fe] ($\sim 0.3 - 0.4$ dex), and this is also consistent with values obtained for the bulge of the Milky Way, which is Na-enhanced like massive ellipticals (on average [Na/Fe] ~ 0.2; (Fulbright, McWilliam & Rich 2007). The flexibility of the CvD12 models, allowing for non-solar abundance patterns, is therefore crucial to disentangle IMF variations from elemental abundance variations.

7.4 Conclusions

In this chapter, we have compared SSP models by Conroy & van Dokkum (2012a) and Vazdekis et al. (2012) constructed specifically for the purpose of measuring the IMF slope down to $\sim 0.1 M_\odot$ for old, metal-rich stellar populations. We have

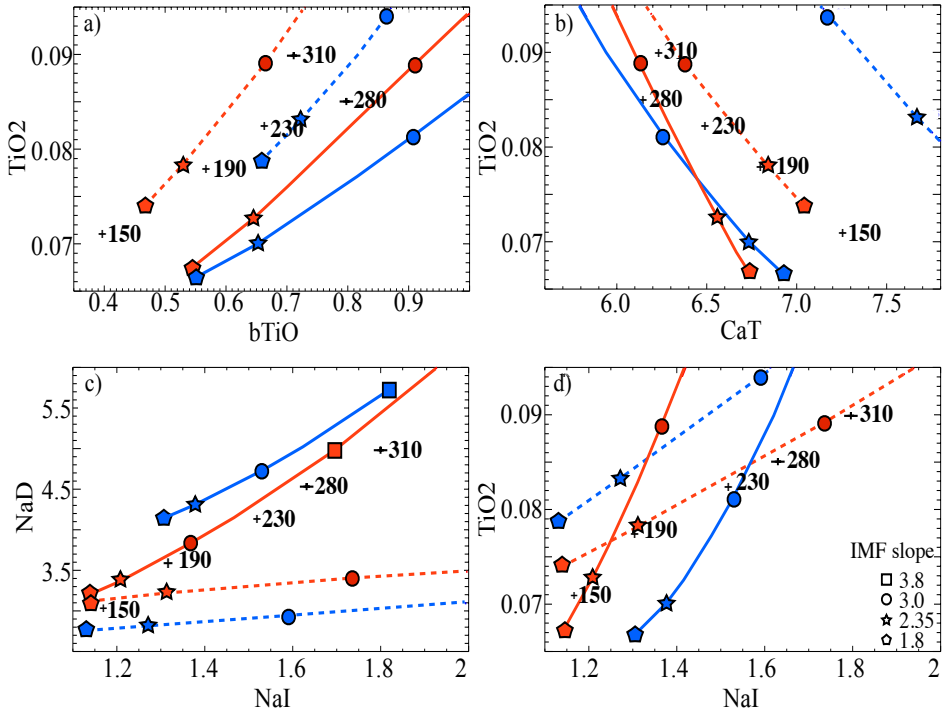

Figure 7.4: Index-index plots of the main IMF-sensitive absorption features in the optical. Solid lines are MIUSCAT SSP models with ~ 12 Gyr: red lines have solar metallicity, and blue lines have $Z = +0.22$. Dotted lines are SSP models from CvD12 with ~ 13.5 Gyr, red lines are SSP models with solar [α/Fe], and blue lines are α-enhanced models. Given the different assumptions on metallicity and α-element abundances, a fair comparison can be made between red lines from different models. Symbols on each line represents different IMF slopes (see legend). Black points with error bars are SDSS galaxies, stacked by velocity dispersions expressed in $\mathrm{km\,s^{-1}}$. In the plots showing sodium indices, the two sets of models give completely different predictions for IMF variations. *Panel (a):* Our preferred IMF indicators in the optical, TiO2 as a function of bTiO. This diagram shows a good agreement between the two models and the galaxies for old stellar populations. *Panel (b):* TiO2 as a function of CaT. A clear trend of the low-mass slope of the IMF with mass is visible from both models. The most massive ETGs require an IMF slope slightly steeper than Salpeter. *Panel (c):* NaD as a function of Na I. Solar-metallicity MIUSCAT models do better in matching the data at all $\sigma_\star$ than solar-composition CvD12 models, but the most massive bin with $\langle\sigma\rangle = 310\,\mathrm{km\,s^{-1}}$ requires an extremely steep IMF with a slope of $x = 3.8$ (square symbol), in disagreement with previous observations based on lensing and stellar populations (Spiniello et al. 2012). A sodium over-abundance with [Na/Fe] = 0.3–0.4 (also consistent with values found from previous studies) in more massive galaxies can explain the disagreement between CvD12 models and the most massive galaxies bin. *Panel (d):* TiO2 as a function of Na I. Here MIUSCAT SSP models do not match the index strengths of very massive systems, while the CvD12 models do. As shown in Figure 7.5 and Table 7.1, Na I does not strongly depend on abundance.

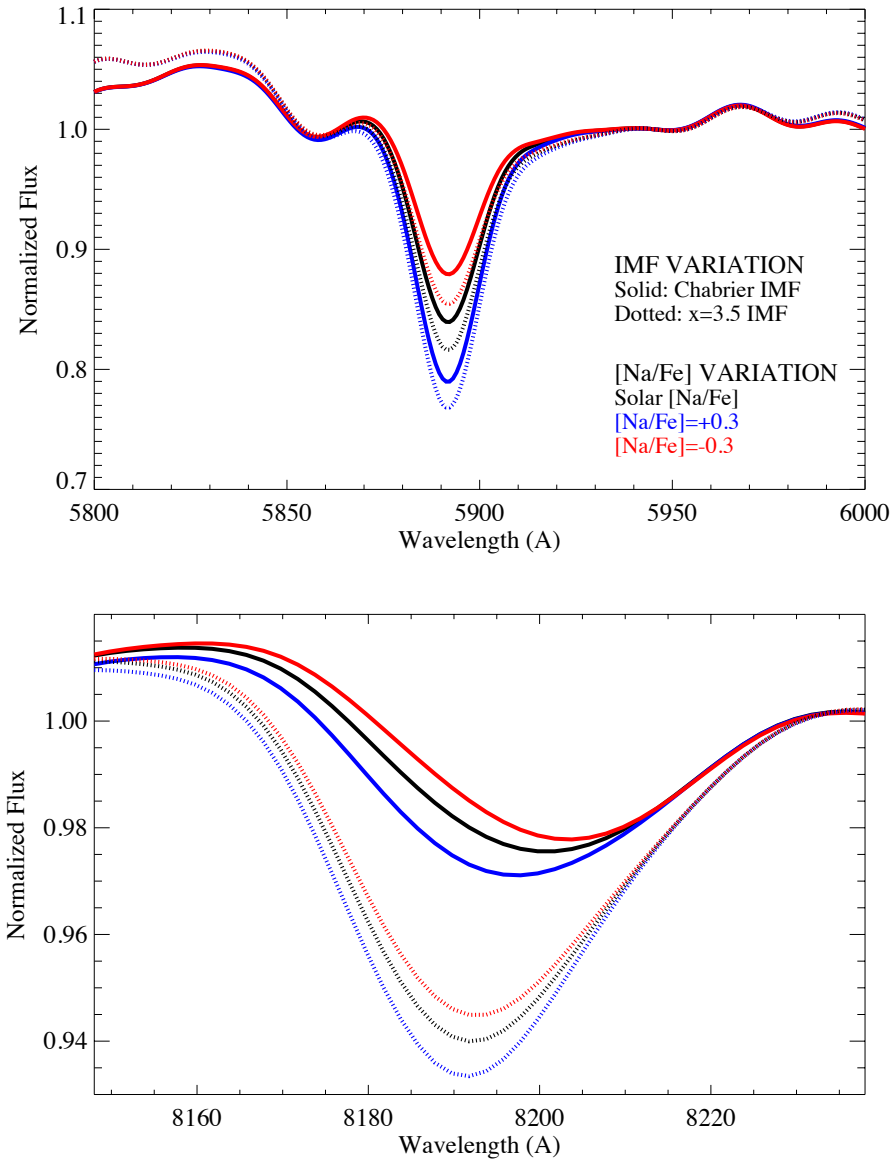

Figure 7.5: Spectra of a CvD12 model with age of 13.5 Gyr in the regions of the NaD (top) and Na I (bottom) features. Different colors are models with different [Na/Fe] abundances (between −0.3 and +0.3), solid lines are models with a Chabrier-like IMF (single power-law with a slope of $x = 1.8$), while dotted lines represent models with an extremely bottom-heavy IMF ($x = 3.5$). The NaD feature is more sensitive to abundance variations than to IMF, whereas the Na I is much more sensitive to variations in the IMF slope. Because the MIUSCAT models only have solar abundance pattern, we cannot repeat this test for these models.

Table 7.1: Ratio between the fractional changes in indices with IMF slope and with sodium abundances, predicted from the CvD12 SSP models. Na I is ~ 4 times more sensitive to variations in IMF slope than to variations in sodium abundances, whereas NaD is more sensitive to [Na/Fe] than to IMF slope.

Index	ΔIMF/Δ[Na/Fe]
NaD	0.29
Na I	4.21

shown how crucial the underlying model assumptions and ingredients like stellar libraries or isochrones (especially at high metallicity and for non-solar abundance ratios) are in constraining the IMF slope for massive ETGs. Our main conclusions are the following:

- CvD12 and MIUSCAT models predict slightly different variations of indices with IMF slope even in a wavelength region where they make use of the same empirical spectral library. We investigate the reason of this disagreement and find that one of the largest differences is the use of different isochrones. In collaboration with C. Conroy, the author of the models, we rebuilt the CvD12 models using the same isochrones used in MIUSCAT models and find better agreement between the models. However, even when the two sets of models use the same library and the same isochrones, we still find small differences in the predictions of the IMF slopes for some indices. We attribute these difference to the different methods that the CvD12 and the MIUSCAT models use to attach stars (i.e. spectral templates) to the isochrones.

- A mild variation of the IMF slope with galaxy velocity dispersion (consistent with the results presented in previous chapters of this thesis and in other works, Treu et al. 2010; Spiniello et al. 2012; Cappellari et al. 2012; Tortora, Romanowsky & Napolitano 2013; Ferreras et al. 2013; La Barbera et al. 2013; Spiniello et al. 2013) is visible in all the index-index plots. Following CvD12, the data do not seem to require super-solar [α/Fe]. Using the MIUSCAT models, we can conclude that more massive systems are in general more metal-rich (e.g. Trager et al. 2000a; Arrigoni et al. 2010).

- The pair of indices bTiO and TiO2 appears to be very promising to constrain the IMF slope, as already demonstrated in previous chapters. Here the

models agree, and there seems to be a minimal dependence on age (at least for old ages) and metallicity. In this wavelength range both models use the same empirical stellar library. Moreover, the variation of IMF slope is orthogonal to the [α/Fe] enrichment (at least in the CvD12 models). The dependence of bTiO on age and metallicity is very small (especially for old populations), as can be seen in Figure 7.4, Panel (a).

- The qualitative trends of the IMF-sensitive features in the two models is similar: both predict an increase in the index strengths from a Chabrier-like IMF to a bottom-heavy IMF. However quantitatively, the variation is generally milder for CvD12 and can be very different for some indices (e.g. CaH1, Fe5270 and the sodium indices). In fact, Ferreras et al. (2013) find a more rapidly increasing IMF slope with velocity dispersion when comparing high S/N stacked spectra of ETGs to MIUSCAT models.

- The two different sets of models give different predictions on the IMF-$\sigma_\star$ relation for some indices, specifically, NaD and Na I. Observed Na I–NaD values only match CvD12 SSP models with solar metallicity and abundances for ETGs with $\sigma_\star < 250\,\mathrm{km\,s^{-1}}$, while MIUSCAT models with solar metallicity and abundances match the data in all mass bins (Fig. 7.4c). The CvD12 models allow one to change the elemental abundances. If one uses models with [Na/Fe] = 0.3 – 0.4 dex, the models better reproduce higher-mass ETGs with a Salpeter, or slightly steeper ($x \sim 2.5$), IMF slope. On the other hand, in the Na I–TiO2 plot (Fig. 7.4d), the CvD12 models do a good job in matching the galaxies' index strengths in all the mass bins without the need for non-solar abundance ratios. Moreover, both models (if we only consider solar Na abundance) predict an extremely strong variation of the IMF slope, with a maximum of $x = 3.8$ for the most massive mass bin. This result goes against inferences from all the indices and the other results of this thesis (Spiniello et al. 2011, 2012, 2013; Barnabè et al. 2013). Therefore the Na indices cannot be used alone to constrain the IMF if one limits oneself to solar-scaled models. NaD is especially problematic in this context because it is highly affected by [Na/Fe] abundance, as shown in Figure 7.5. In fact, although the models also differ in the Na I–TiO2 plot, if one assumes that giant ETGs are Na-enriched, then at least the prediction for the IMF slope variation are comparable and milder than in the NaD–Na I plot. This plot agrees with conclusions of previously published works (Cappellari et al. 2012; Conroy & van Dokkum 2012a; Spiniello et al. 2012; Smith, Lucey & Carter 2012; Tortora, Romanowsky & Napolitano 2013).

- bTiO, TiO2 and CaT index strengths seem to give the same predictions for the IMF slope for the two different models (at least partially, given the differences in metallicity and [α/Fe]). For CaT, CvD12 models with solar [α/Fe] provide the best match with the data (in all mass bins). This suggests that the stellar coverage of the IRTF library is perhaps more representative low-mass stars than the CaT library, used by MIUSCAT. This provides further support for our choice of using the CvD12 models instead of the MIUSCAT models.

- TiO2 plotted as a function of CaT shows how crucial the different underlying model assumptions on the metallicity and [α/Fe] abundance are. It is well-known that CaT is almost metallicity-independent[6] as visible in Panel (d) of Fig. 7.4 from the MIUSCAT models, while it increases with increasing [α/Fe] for CvD12 models.

In conclusion, all IMF-sensitive indicators in both models give support to the idea of a non-universality of the IMF slope, which increases with increasing galaxy mass. Using either CvD12 or MIUSCAT SSP models, a bottom-light IMF such as Chabrier IMF is inappropriate for the most massive ETGs, as also shown in Treu et al. (2010); Spiniello et al. (2012); Barnabè et al. (2013).

7.4.1 The choice of CvD12 SSP models over MIUSCAT SSP models.

For the spectroscopic stellar population analysis presented in this thesis, we decided to use CvD12 rather than MIUSCAT. There are several reasons that led us to adopt this choice.

First, we consider [α/Fe] a fundamental and necessary parameter to recover the non-universality of the IMF, because of the well-established [α/Fe]-$\sigma_\star$ relation (e.g. Trager et al. 2000b; Arrigoni et al. 2010). As described in this chapter, MIUSCAT models do not allow one to change the relative abundance of the α-elements and are therefore restricted to the solar abundance pattern, although they build models with different metallicities. On the other hand, CvD12 are more flexible in varying [α/Fe] as well as the abundance pattern of 11 different elements. This is particularly important in the case of sodium lines, especially for the NaD λ5900 index. We note that elemental abundance is a fundamental parameter that has to be further explored to isolate and test a possible variation of IMF normalization with galaxy mass. A full-spectrum fitting approach should

[6] This is true only when $[Z/\mathrm{H}] \geq -0.5$, which is almost always the case for the giant ETGs considered here.

be the final goal to investigate possible IMF variations with galaxy mass and to disentangle IMF from age, metallicity and elemental abundances (see Conclusions & Outlook, Chapter 8). However the approach taken in this thesis focuses on using specific indices such that one better understands how different parts of the spectrum react to changes in age, metallicity, abundance ratios, effective temperature of the RGB and the IMF slope. In addition, it avoids potential issues with spectral calibration.

Perhaps the IRTF library, used by the CvD12 models in the red optical region, is a better choice to study the low-mass stars population than the CaT library of Cenarro et al. (2001) used by the MIUSCAT models. This can be deduced from Panel (b) of Figure 7.4 showing TiO2 versus the CaT index where CvD12 models with solar [α/Fe] provide the best match with data for all mass bins.

Finally, another important reason is that CvD12 created their integrated spectra using several separate evolutionary calculations (a combined set of different isochrones, empirical and theoretical libraries), allowing a more accurate treatment of the low-mass stars down to the hydrogen burning limit ($M_{\rm low}$= $0.08\,M_{\odot}$). From a spectroscopic point of view the adoption of a slightly higher value of $M_{\rm low}$ does not have a large impact on the line-strength measurements, although it can have a visible contribution for some spectral features (see for example Fig. 15 in Conroy & van Dokkum 2012a). As discussed in Chapter 6, the IMF and in particular the value of $M_{\rm low}$ is an essential parameter when determining $\Upsilon_{\star}$ from stellar population codes. It is well established today that M-dwarfs contribute only little to the integrated optical light of ETGs[7]. However, the debate remains open whether dwarf stars ($M_{\star} \sim M_{\rm low}$) can contribute > 1% of the integrated optical light. This difference might seem subtle but it is actually of fundamental importance not only for questions regarding the universality of the IMF slope but also to the inference of the relative amount of dark and luminous matter in the central regions of galaxies.

[7]Note that the situation has changed remarkably since the early papers of Spinrad & Taylor (1971) and Faber & French (1980), who claimed that dwarfs contributed ~ 30% to the V-band light of old populations, because this would imply a $\Upsilon_{\star} \sim 40$, strongly ruled out by dynamical and lensing studies (e.g. Cappellari et al. 2006; Treu et al. 2010)

8 Conclusions and outlook

Remember to look up at the stars and not down at your feet.
Try to make sense of what you see and
wonder about what makes the universe exist.
Be curious.
And however difficult life may seem,
there is always something you can do and succeed at.
It matters that you don't just give up.

Stephen Hawking

The mass assembly and stellar population properties of the class of very massive 'red and dead' galaxies puts the hierarchical structure formation model in the ΛCDM paradigm to the test. In-depth knowledge of the internal structure, luminous and dark-matter distribution, as well as the detailed study of the integrated stellar population of ETGs is therefore vital to paint a more physical picture of the mixture of complex processes in action during galaxy formation.

Recent observations indicate that the internal dark-matter fraction of ETGs increases rapidly with galaxy mass. At the same time, recent observations have also shown evidence for a varying IMF, where the low-mass end of the stellar IMF steepens with galaxy mass. With the X-Shooter Lens Survey (XLENS) we can, for the first time, disentangle the two scenarios. In this thesis we have presented spectroscopic evidence for a varying low-mass end of the stellar IMF slope in ETGs, which steepens with increasing galaxy stellar velocity dispersion. Moreover, we have shown that the combination of strong gravitational lensing, stellar kinematics and spectroscopic stellar population information is uniquely powerful to disentangle the contribution of stellar and dark matter in the inner regions of ETGs and thus to directly measure their stellar mass-to-light ratios ($\Upsilon_\star$).

Expanding on the result of this thesis, I envision five main directions for future works: (i) complement our observational results with theoretical modelling to investigate the physical processes that could be responsible for the steepening of the IMF slope; (ii) investigate spatial gradients in the IMF shape; (iii) extend our sample of lens ETGs to lower velocity dispersions ($\sigma_\star \sim 170$–$250\,\mathrm{km\,s^{-1}}$), to scrutinize the non-universality of the IMF slope and its relation to galaxy mass; (iv) extend the SSP analysis to the NIR and for non-solar abundance patterns, investigating also the differences and issues with varying abundances and/or varying total metallicity; and (v) push (even further) the redshift boundary, to test possible cosmic evolution of the IMF shape. Certainly, we also need to test different IMF shapes (i.e. bimodal or tapered IMFs) and extended star formation rather than single instantaneous burst of star formation.

8.1 Summary and main results

In this thesis, I have focused mainly on the stellar IMF, whose recently suggested non-universality (e.g. van Dokkum & Conroy 2010; Conroy & van Dokkum 2012b; Cappellari et al. 2012; La Barbera et al. 2013), if confirmed, could

have profound implications for our understanding of galaxy assembly and star formation. Although until now it has almost always been assumed that the IMF is universal, equal to the one measured in our Milky Way and independent of cosmic time, it is remarkable to note that this universality does not directly stem from an *a priori* theory (Bastian, Covey & Meyer 2010).

In the present Section, we provide a brief review of the most significant outcomes of this work.

8.1.1 The X-Shooter Lens Survey: An overview

In Chapter 2, we presented the current sample of the XLENS Survey: thirteen very massive lens galaxies, i.e. with velocity dispersions $\sigma_{\rm ETGs} > 250\,{\rm km\,s^{-1}}$. Thanks to the wide wavelength range covered by X-Shooter, we obtained high-signal-to-noise spectra (S/N$\sim$ 50–120/Å) of ten ETGs and derived their spatially-resolved kinematic profiles up to $\sim 1\ R_{\rm eff}$. In combination with multi-band HST images and lensing constraints on the total masses, this data will lead to a precise determination of the internal dark-matter mass fractions, which will then be directly compared to those predicted by numerical simulations in order to improve our understanding on how dark matter behaves in these galaxies and how it influences the formation of luminous structure in the Universe (e.g., Davis et al. 1985; Frenk et al. 1985; White & Frenk 1991). The possibility to accurately infer the slope of the IMF from spectroscopic stellar population studies is crucial in this context because internal dark-matter fractions depend on the IMF normalization (e.g. Auger et al. 2010b).

8.1.2 A pilot program: The Cosmic Horseshoe

The analysis of the internal structure and mass distribution of a very massive lens at redshift $z = 0.444$ (SDSSJ1148+1930, Spiniello et al. 2011) demonstrated the robustness of this new approach (Chapter 3). We measured the stellar mass fraction inside the effective radius ($f_*(< R_{\rm eff}) = 0.19^{+0.04}_{-0.09}$, 68% C.L.), using the spatially resolved kinematic profile of this galaxy obtained from a UVB-VIS X-Shooter spectrum, in combination with a stellar plus dark-matter mass model and the total mass inside the Einstein radius from lensing. This fraction agrees with an independent measurement based on SDSS colors for a Salpeter IMF slope, and it clearly shows that this massive ETG is dark-matter-dominated inside one effective radius ($R_{\rm eff}$). Extremely dwarf-rich IMFs with slope $x > 3$ in the lower mass range of 0.1-0.7 $M_\odot$ – such as those suggested by van Dokkum & Conroy

(2010), Ferreras et al. (2013) and La Barbera et al. (2013) for very massive ETGs ($\sigma_\star \geq 280\,\mathrm{km\,s^{-1}}$) – are also excluded at the > 90% C.L. for this particular lens galaxy (and also for the other lenses analysed in the previous chapters) and in some cases ($x = 3.5$) violate the total lensing-derived mass limit (Spiniello et al. 2011).

8.1.3 Evidence of a steepening of the low-mass end of the IMF with stellar velocity dispersion.

This thesis presents the first lensing plus Single Stellar Population (SSP) model based evidence that the IMF slope steepens from low to high-mass early-type galaxies. We have shown that more massive galaxies have a substantial population of M-dwarfs stars with masses $M \approx 0.2$–$0.3\,M_\odot$ (Chapter 4), from line-index measurements of optical spectra of a lens galaxy in the current XLENS sample (SDSSJ0912+0029, $\sigma_\star = 312 \pm 12\,\mathrm{km\,s^{-1}}$) and SDSS spectra of red and dead galaxies stacked in different $\sigma_\star$-bins (Spiniello et al. 2012).

In Chapter 5 we defined a set of optical IMF-sensitive spectral indicators that allowed us to decouple the effects of a varying IMF from age, metallicity effective temperature of the RGB, and, up to some extent, element abundance variations, when studying the stellar populations of massive ETGs. Our approach is based on line-index measurements and consists of the combination of blue gravity-insensible features, used to constrain age and metallicity, with the classical red-optical and near-infrared M-dwarfs indicators *and* with a number of newly defined IMF-sensitive features in the blue optical spectral region. At wavelengths in the range 4500–7500 Å, cool low-mass stars give a smaller, but still measurable, contribution to the spectrum, and it is much easier to obtain high S/N galaxy spectra in this range with current spectrographs than in the NIR (Spiniello et al. 2013). Combining IMF-sensitive spectral features in the red with IMF-insensitive blue features dominated by the same element is also the most promising means to separate IMF and abundance effects. We highlight that element abundance is the main source of uncertainties (especially when comparing different SSP models, see Chapter 7) and therefore has to be further explored to definitively isolate the effect of IMF variation and probe its steepening with galaxy mass (Spiniello et al., in prep.).

In Chapter 5 we measured line-index strengths of our new optical IMF indicators in the Conroy & van Dokkum (2012a) SSP model spectra with ages between 3.0 and 13.5 Gyr, [α/Fe]=[−0.2,+0.4] dex and $\Delta T_{\mathrm{eff,RGB}}$=[−200, +50] K. We compared these to index strengths of the same spectral features in a sample of

the stacked SDSS ETG spectra with varying velocity dispersions, as described in Chapter 4. Using several different indicators, we found a clear trend of steepening IMF with increasing velocity dispersion from 150 to 310 $\mathrm{km\,s^{-1}}$, described by the linear equation $x = (2.3 \pm 0.1) \log \sigma_{200} + (2.13 \pm 0.15)$, where x is the IMF slope and σ_{200} is the central stellar velocity dispersion measured in units of 200 $\mathrm{km\,s^{-1}}$. We computed the "IMF mismatch" parameter as the ratio of the value of $\Upsilon_\star$ predicted from the IMF$-\sigma_{200}$ relation to that inferred from SSP models assuming a Salpeter IMF. We compared our results with independent published results (Treu et al. 2010; Conroy & van Dokkum 2012b; Cappellari et al. 2013; La Barbera et al. 2013), finding very good agreement (Spiniello et al. 2013).

Finally, in Chapter 7, we demonstrated that this result is robust and does not arise from the underlying assumptions of the chosen SSP model.

8.1.4 Constraining the low-mass cut-off of the IMF in ETGs from lensing+dynamics+SSP modelling

Thanks to a novel approach presented in Chapter 6 of this thesis we have been able, for the first time, to tackle the problem of constraining the low-mass cut-off of the IMF (M_{low}). The value of M_{low} has always been treated as a fully unconstrained parameter, despite being critical to determine $\Upsilon_\star$. Stars with masses below $\sim 0.15\,M_\odot$ have very little effect on the spectral lines in the optical and near-infrared for any reasonable assumed IMF slope (Conroy & van Dokkum 2012a) but they give a non-negligible contribution to the total mass budget of the system (Worthey 1994). Accordingly, it is impossible to infer the value of M_{low} from spectroscopic studies alone, since varying this parameter does not have any real impact on the spectra and on the line-index measurements. Luckily, this degeneracy can be broken when adding the information from the combined gravitational lensing and stellar dynamics (L&D) analysis, as we showed in Chapter 6. In this chapter, we obtained two completely independent inferences on the total mass of the most and the least massive lens galaxies in the XLENS survey. The combined L&D analysis and the spectroscopic SSP analysis gave values of stellar masses which agreed within the 1σ uncertainties. This shows the robustness of the method and the absence of major hidden systematics. Combining the L&D and the SSP analyses of both galaxies in a Bayesian framework, we inferred an IMF of $x = 2.23 \pm 0.14$, consistent with a Salpeter IMF, and a low-mass limit mass cut-off of $M_{\mathrm{low}} = 0.13 \pm 0.03\,M_\odot$, just above the hydrogen burning limit.

8.2 Future work

The emerging idea of a non-universal IMF, if shown to be correct, will impact our understanding of galaxy formation and evolution. The natural step forward is to study the physical processes possibly driving a bottom-heavy IMF in high velocity dispersion ETGs. In fact, despite the compelling observational evidence for a steepening of the low-mass end of the IMF, arising from many different and independent techniques (i.e. lensing and dynamics, Treu et al. 2010; spectroscopy, van Dokkum & Conroy 2010; Conroy & van Dokkum 2012b; La Barbera et al. 2013; or dynamics and stellar population studies, Cappellari et al. 2012), the physical origin of this variation still remains an open question. It is therefore crucial to test theoretical predictions of the IMF slope as function of their formation history against the data. A considerable amount of work, both from the theoretical and SSP-modelling point of view, is required.

Here we single out some of the possible directions that one could take going beyond the current limitations and further address the fundamental scientific questions addressed in Chapter 1.

8.2.1 Unravelling the physics driving steep low-mass end of the IMF in massive ETGs

From a theoretical point of view, it is not clear yet what physical mechanisms in galaxies could cause star-forming clouds to make stars that follow a different IMF (i.e. with higher or lower fragmentation). There is strong theoretical evidence that the stars in the innermost region of ETGs (1 kpc) have formed via inflows of gas to large densities in nuclear merger-induced starbursts (the same process seen in action in the centers of local ULIRGs, Hopkins et al. 2006). During a merger event, giant, high-density, molecular clouds rapidly fall into the center of the merging galaxies (remnants) where they collide, increasing their density and forming stars very efficiently. According to recent theoretical work (e.g. Hennebelle & Chabrier 2008, 2009; Offner & Krumholz 2009; Chabrier & Hennebelle 2011; Offner et al. 2012; Hennebelle 2012; Hopkins 2012), high density, temperature and turbulence of the gas are key parameters that drive the fragmentation of molecular clouds. Thus, more massive ETGs, for which it has been shown that mergers play a major role (Bender, Burstein & Faber 1992; Khochfar & Burkert 2003; Naab, Khochfar & Burkert 2006; Hopkins et al. 2009; Khochfar & Silk 2009; Cappellari et al. 2013), could possibly form many more

stars with masses below 0.2–0.3 $M_{\odot}$ and therefore result in a final integrated stellar population described by a bottom-heavier IMF.

In the near future, I plan to combine the XLENS observations with semi-analytic models (SAMs)[1] to investigate whether this theoretical physical-motivated picture is able to reproduce the observations and to give consistent predictions for the variation of the IMF slope with stellar velocity dispersion.

8.2.2 Spatial variation of the IMF slope

If mergers and accretion of galaxies with pre-enriched gas are indeed the physical parameters that drive the non-universality of the IMF shape, from an observational point of view we would expect to observe a radial gradient in the IMF slope within a single massive galaxy, with stellar populations following a bottom-heavy IMF located in the center of galaxies. Subsequent star formation episodes should increase the metallicity and, as a consequence, the IMF would gradually tend to produce a larger relative number of low-mass stars. The only issue is that in systems supported by random motions such as slow rotators, stars move over a wide range of radii and therefore this effect could smooth out in radius. Hence measuring this expected spatial gradient in the IMF would require high S/N measurements quite far away from the galaxy center. A possible way around this limitation is provided by stacking. We will stack the spectra of the full XLENS sample to increase the S/N enough and to perform line-index analysis on the spectra of different spatial regions in order to test for the presence of possible radial gradients in the IMF slope. A more extensive and complete work is also planned in the future using exquisite CALIFA (Sánchez et al. 2012; Husemann et al. 2013) spatially resolved spectra of galaxies with different velocity-dispersion and morphology. We will measure line-indices of IMF-sensitive features on spatially resolved spectra of single galaxies, constraining the IMF as function of radius for a conspicuous amount of systems.

[1] Semi-analytic models (SAMs) of galaxy formation apply simple physically motivated recipes for physical processes that drive the formation and evolution of galaxies within the framework of a ΛCDM cosmology. These models provide predictions of global galaxy properties (such as SFR, size, stellar mass and luminosity, gas content, metal enrichment) for large numbers of galaxies. Furthermore, they easily explore the physical processes involved to reproduce the growing number of observations over the full range of wavelengths probed. Specifically, we plan to use the SAM to be published in Somerville, Popping & Trager, in prep.

8.2.3 Extending the XLENS mass range

The XLENS sample is currently limited to very massive ETGs for which high-fidelity HST deep images and high S/N spectra from X-Shooter are available. We are planning to complement our more massive ETGs with lower-velocity dispersion ETGs $\sigma_\star = 170$–$210\,\mathrm{km\,s^{-1}}$, covering in this way a substantially increased stellar mass range to further scrutinize the non-universality of the IMF slope and its possible relation to galaxy mass using the joint lensing+dynamics+SP analysis presented in Chapter 6.

To achieve this goal, we will select a number of ETGs lens discovered by the *'SLACS for the Masses'* project (HST, Cycle 18, PI: A. Bolton) using HST snapshots obtained with ACS-WFC snapshots. Although snapshots are sufficient for lens confirmation and crude modeling, detailed lensing analysis requires deep, higher-resolution imaging data in order to separately model the images of the lensing and lensed galaxies. Better image sampling and increased S/N is necessary to fully separate the lens and the source and to determine projected total masses within a few percent accuracy. We will request HST time to observe a number of candidates for one orbit with ACS-WFC and obtain a statistically-comparable sample to the higher-mass XLENS current sample with data of comparable quality. In parallel, we will request X-shooter (and/or Keck) time to follow up these systems spectroscopically and to perform stellar population modeling as described in Chapter 5.

With a complete sample of ETGs lens galaxies in the final velocity dispersion range $\sigma_\star = 170$–$400\,\mathrm{km\,s^{-1}}$, we will be able to better probe the steepening of the stellar IMF with galaxy mass[2]. If the non-universality of the IMF is proven to be correct, this implies that the relation between the internal fraction of DM and galaxy velocity dispersion, thus far obtained under the assumption of a universal IMF, would require a correction. Remarkably, in that case, the DM fraction only seems to weakly depend on galaxy mass, and the observed increase of the total M/L in more-massive galaxies is purely due to a variation in IMF slope. These results will have a profound impact on our understanding of galaxy-formation and how feedback plays a role.

[2]The on-going *Sloan WFC Edge-on Late-type Lens Survey* (SWELLS, Treu et al. 2011) is also investigating the normalization of the stellar IMF in *spiral galaxies* with a similar lensing+SP approach. Brewer et al. (2012) (SWELLS III) found that for the lower mass SWELLS systems (i.e. $\sigma_* < 230\,\mathrm{km\,s^{-1}}$), adoption of a Salpeter IMF leads to estimates of a stellar mass fraction that exceed unity, which is obviously unphysical. This result further strengthens the evidence against a universal stellar IMF, but these are however morphologically and physically very different systems from our sample, which are purposely selected against having any signs of a disk.

8.2.4 Extending stellar population models

A step towards a better understanding of the effect of a variation in the low-mass end of the IMF predicted from SSP modelling requires the expansion of these models into the NIR and to non-solar abundances. This is necessary to reproduce massive ETGs absorptions features and to break the degeneracies between various stellar population parameters.

Stellar spectral features that depend strongly on surface gravity, and hence distinguish giants from dwarf stars, often show degeneracies with age, metallicity and element abundances. In this regard, it is crucial to use as much spectroscopic information as possible, and therefore to find new IMF-sensitive indices, as well as fully characterize the behaviour of the classical spectral indices as a function of IMF variations. The wide wavelength coverage of X-shooter is essential here. Features that are strong in M-dwarfs and not present in cool giants (or vice versa), needed to detect the low-mass stellar content in unresolved stellar populations, are most prominently present in the red-optical and NIR spectrum. Until now, we have limited our stellar population analysis and kinematics measurements to the near-UVB and optical regions due to the difficulty in reducing the infrared data and especially the lack of well-calibrated NIR spectral libraries (see, e.g., the exhaustive review of Peletier 2012). The situation is also much more complicated in the NIR, because there the light is controlled by cool, late-type stars, AGB and RGB stars, whose complex evolution and physics are still not well understood (e.g. Conroy 2013). Fortunately, in the near future the X-Shooter stellar library (XSL, Chen et al., 2014, in prep) will be completed and released. XSL is an on-going project to produce the largest homogeneous library of stellar spectra covering simultaneously the entire wavelength range from 3200 Å to 2.5 μm using X-Shooter. The more indices we study, the better we can break the degeneracies. We therefore plan to expand on the same line followed in Chapter 5 (where we used stars from MILES stellar library, Sánchez-Blázquez et al. 2006, that only covers the wavelength range 3500–7500 Å) using stars from XSL to explore stellar models over a wide wavelength range in search for promising new indices to completely decouple the effect of a varying IMF slope from stellar population, age, metallicity, and abundance pattern in integrated-light measurements.

In addition, the empirical stars used in the current SSP models are approximately of solar metallicity, while the average metallicity of massive ETGs is higher and they are believed to be α-enhanced (e.g., Worthey 1992; Trager et al. 2000a). In the future, we plan to repeat our SSP analysis using synthetic spectral libraries (alone or in combination with empirical libraries) to further investigate

changes in the overall metallicity or changes in the abundances of individual elements.

Comparing different SSP models that use different stellar libraries and make different physical assumptions is of crucial importance to fully demonstrate that the increasing IMF slope with galaxy velocity dispersion is real and does not arise from a misunderstanding of the numerous degenerate ingredients and parameters involved in stellar population synthesis. Steps in this direction have already been taken in Chapter 7; however a more detailed and quantitative analysis is planned to resolve current discrepancies of different models when compared to each other and to our XLENS and SDSS data (Spiniello et al., in prep.). New SSP models with varying IMFs and spanning a wide range in ages, metallicity, abundance patterns are necessary in order to fully separate abundance effects from giant-to-dwarf ratio effects.

In this thesis we focussed on line-index measurements, rather than full spectral fitting, to avoid issues with spectral calibration when comparing to observations that might have been poorly calibrated. However we are aware that a full spectral fitting approach is necessary to further investigate possible IMF variations with galaxy masses and to trace the complete star formation history of a galaxy (Conroy, Graves & van Dokkum 2013).

In fact, it is natural to believe that very massive ETGs cannot be well described with a single stellar population model in which all stars are formed in a single burst and with the same chemical composition, since in the hierarchical galaxy formation scenario they are thought to be the final result of merger events. What will be the resulting IMF inferred from integrated light of a galaxy that is a final product of an old, metal-rich stellar population merged with a younger, metal-poorer stellar population? Can we prove that IMF variations observed in higher-mass galaxies are indeed merger-driven? In order to give an answer to these intriguing questions, we have already started a project in which we combine SSP models with different ages metallicities and IMFs, simulating in this way a combination of two different stellar populations with two different IMFs, to find a toy model able to fit simultaneously all the galaxy stellar absorption features.

8.2.5 Pushing the Redshift Boundaries.

Beyond $z = 1$, theoretical arguments suggest that star formation occurred more often in a burst mode (e.g. Hopkins et al. 2006; Lacey et al. 2008), and in star-forming clouds with lower metallicity. This would suggest a more top-heavy IMF (e.g., Worthey 1992; Hopkins et al. 2006; van Dokkum 2008). Constraining the

IMF shape directly from spectra of $1 \leq z \leq 2$ galaxies is probably now achievable with high-resolution near-infrared spectroscopy with X-Shooter, due to its high resolution and superb wavelength range, although as already mentioned, data reduction and analysis will be more challenging because of the the presence of strong telluric absorption arising from water vapour (e.g. Stevenson 1994). Proper index measurement in the red optical and NIR range relies heavily on the correct removal of these lines. Moreover, the new blue indicators defined in this thesis (Chapter 5) will be particularly important in this context because the classical red IMF-sensitive features will be redshifted out of the NIR window while these blue-optical lines will still be observable.

8.3 Concluding remarks

The shape of the low-mass end of the stellar Initial Mass Function in massive Early-Type Galaxies and the internal distribution of their dark and luminous matter are exciting open questions in modern astrophysics. With the X-Shooter Lens Survey (XLENS) we have designed, developed and applied the combination of lensing, dynamics and especially stellar-population synthesis modeling to unravel these issues and to disentangle the stellar and dark-matter content of massive ETGs.

The IMF is a fundamental ingredient in our understanding of galaxy evolution and cosmology, required to quantify the stellar density of the Universe, the stellar masses of galaxies, the star formation rates and the amount of dark matter in galaxies. In this thesis, we have shown that it is possible to constrain the low-mass end and the cut-off mass of the stellar IMF directly from galaxy spectra, through combined strong gravitational lensing, spatially resolved kinematics and spectroscopic stellar population studies. Our result shows that the low-mass end of the IMF is not universal and can be explained neither by invoking hidden systematics nor by the choice of a particular SSP model.

We have to make clear that bth the basic assumption that the IMF is described by a single power-law and the even bigger assumption that the stellar population of ETGs is described via *single* stellar population models need to be further investigated. However, despite the many uncertainties arising from the choice of different sets of SSP models and the many degeneracies between stellar population parameters (which can be broken only by using several indicators over a wide wavelength range), this thesis leads us to believe that the low-mass end of the IMF slope varies with galaxy stellar velocity dispersion. A Chabrier-like IMF

slope fits the data of spiral galaxies (Treu et al. 2011; Barnabè et al. 2012) and low-dispersion fast rotators, while the IMF slope is at least as steep as Salpeter for massive, slowly rotating ETGs with $\sigma_\star \geq 250\,\mathrm{km\,s^{-1}}$. These results will likely have a profound impact on our understanding of galaxy formation and how feedback plays a role in the cosmic history of these systems.

Bibliography

Abazajian K. et al., 2004, AJ, 128, 502

—, 2005, AJ, 129, 1755

—, 2003, AJ, 126, 2081

Abazajian K. N. et al., 2009, ApJS, 182, 543

Adelman-McCarthy J. K. et al., 2008, ApJS, 175, 297

—, 2007, ApJS, 172, 634

—, 2006, ApJS, 162, 38

Aihara H. et al., 2011, ApJS, 193, 29

Alexander D. R., Ferguson J. W., 1994, ApJ, 437, 879

Allanson S. P., Hudson M. J., Smith R. J., Lucey J. R., 2009, ApJ, 702, 1275

Allard F., Hauschildt P. H., Schwenke D., 2000, ApJ, 540, 1005

Arnaboldi M. et al., 1996, ApJ, 472, 145

Arrigoni M., Trager S. C., Somerville R. S., Gibson B. K., 2010, MNRAS, 402, 173

Auger M. W., Treu T., Bolton A. S., Gavazzi R., Koopmans L. V. E., Marshall P. J., Bundy K., Moustakas L. A., 2009, ApJ, 705, 1099

Auger M. W., Treu T., Bolton A. S., Gavazzi R., Koopmans L. V. E., Marshall P. J., Moustakas L. A., Burles S., 2010a, ApJ, 724, 511

Auger M. W., Treu T., Gavazzi R., Bolton A. S., Koopmans L. V. E., Marshall P. J., 2010b, ApJ, 721, L163

Bacon R. et al., 2001, MNRAS, 326, 23

Baraffe I., Chabrier G., Allard F., Hauschildt P. H., 1998, A&A, 337, 403

Bardeen J. M., Bond J. R., Kaiser N., Szalay A. S., 1986, ApJ, 304, 15

Barnabè M., Auger M. W., Treu T., Koopmans L. V. E., Bolton A. S., Czoske O., Gavazzi R., 2010, MNRAS, 406, 2339

Barnabè M., Czoske O., Koopmans L. V. E., Treu T., Bolton A. S., 2011, MNRAS, 415, 2215

Barnabè M., Czoske O., Koopmans L. V. E., Treu T., Bolton A. S., Gavazzi R., 2009a, MNRAS, 399, 21

Barnabè M. et al., 2012, MNRAS, 423, 1073

Barnabè M., Koopmans L. V. E., 2007, ApJ, 666, 726

Barnabè M., Nipoti C., Koopmans L. V. E., Vegetti S., Ciotti L., 2009b, MNRAS, 393, 1114

Barnabè M., Spiniello C., Koopmans L. V. E., Trager S. C., Czoske O., Treu T., 2013, ArXiv e-prints

Barnes J. E., 1992, ApJ, 393, 484

Bastian N., Covey K. R., Meyer M. R., 2010, ARA&A, 48, 339

Bell E. F., de Jong R. S., 2001, ApJ, 550, 212

Bell E. F., McIntosh D. H., Katz N., Weinberg M. D., 2003, ApJS, 149, 289

Belokurov V. et al., 2007, ApJ, 671, L9

Bender R., Burstein D., Faber S. M., 1992, ApJ, 399, 462

—, 1993, ApJ, 411, 153

Bender R., Nieto J.-L., 1990, A&A, 239, 97

Bennett C. L. et al., 2003, ApJS, 148, 1

—, 2012, ArXiv e-prints

Bernardi M. et al., 2003, AJ, 125, 1866

Bernardi M., Sheth R. K., Nichol R. C., Schneider D. P., Brinkmann J., 2005, AJ, 129, 61

Bertelli G., Bressan A., Chiosi C., Fagotto F., Nasi E., 1994, A&A, Supplement, 106, 275

Bertin G. et al., 1994, A&A, 292, 381

Bezanson R., van Dokkum P. G., Tal T., Marchesini D., Kriek M., Franx M., Coppi P., 2009, ApJ, 697, 1290

Binney J., Mamon G. A., 1982, MNRAS, 200, 361

Blandford R. D., Narayan R., 1992, ARA&A, 30, 311

Blöcker T., 1995, A&A, 297, 727

Blumenthal G. R., Faber S. M., Primack J. R., Rees M. J., 1984, Nature, 311, 517

Bolton A. S., Burles S., Koopmans L. V. E., Treu T., Gavazzi R., Moustakas L. A., Wayth R., Schlegel D. J., 2008a, ApJ, 682, 964

Bolton A. S., Burles S., Koopmans L. V. E., Treu T., Moustakas L. A., 2006, ApJ, 638, 703

Bolton A. S., Treu T., Koopmans L. V. E., Gavazzi R., Moustakas L. A., Burles S., Schlegel D. J., Wayth R., 2008b, ApJ, 684, 248

Borriello A., Salucci P., Danese L., 2003, MNRAS, 341, 1109

Bower R. G., Benson A. J., Malbon R., Helly J. C., Frenk C. S., Baugh C. M., Cole S., Lacey C. G., 2006, MNRAS, 370, 645

Bower R. G., Lucey J. R., Ellis R. S., 1992, MNRAS, 254, 589

Bressan A., Chiosi C., Fagotto F., 1994, ApJS, 94, 63

Brewer B. J. et al., 2012, MNRAS, 422, 3574

Brewer B. J., Lewis G. F., 2006, ApJ, 637, 608

—, 2008, MNRAS, 390, 39

Brinchmann J., Charlot S., White S. D. M., Tremonti C., Kauffmann G., Heckman T., Brinkmann J., 2004, MNRAS, 351, 1151

Bruzual G., Charlot S., 1993, ApJ, 405, 538

—, 2003, MNRAS, 344, 1000

Buitrago F., Trujillo I., Conselice C. J., Bouwens R. J., Dickinson M., Yan H., 2008, ApJ, 687, L61

Bullock J. S., Kolatt T. S., Sigad Y., Somerville R. S., Kravtsov A. V., Klypin A. A., Primack J. R., Dekel A., 2001, MNRAS, 321, 559

Bundy K., Treu T., Ellis R. S., 2007, ApJ, 665, L5

Burstein D., Faber S. M., Gaskell C. M., Krumm N., 1984, ApJ, 287, 586

Busarello G., Capaccioli M., Capozziello S., Longo G., Puddu E., 1997, A&A, 320, 415

Buzzoni A., 1989, ApJS, 71, 817

Cappellari M., 2008, MNRAS, 390, 71

Cappellari M. et al., 2006, MNRAS, 366, 1126

Cappellari M., Emsellem E., 2004, PASP, 116, 138

Cappellari M. et al., 2011, MNRAS, 413, 813

—, 2012, Nature, 484, 485

—, 2013, MNRAS, 432, 1862

Caputi K. I., Cirasuolo M., Dunlop J. S., McLure R. J., Farrah D., Almaini O., 2011, MNRAS, 413, 162

Carollo C. M., de Zeeuw P. T., van der Marel R. P., Danziger I. J., Qian E. E., 1995, ApJ, 441, L25

Carter D., Visvanathan N., Pickles A. J., 1986, ApJ, 311, 637

Cenarro A. J., Cardiel N., Gorgas J., Peletier R. F., Vazdekis A., Prada F., 2001, MNRAS, 326, 959

Cenarro A. J., Gorgas J., Cardiel N., Vazdekis A., Peletier R. F., 2002, MNRAS, 329, 863

Cenarro A. J., Gorgas J., Vazdekis A., Cardiel N., Peletier R. F., 2003, MNRAS, 339, L12

Cervantes J. L., Coelho P., Barbuy B., Vazdekis A., 2007, in IAU Symposium, Vol. 241, IAU Symposium, Vazdekis A., Peletier R., eds., pp. 167–168

Chaboyer B., Fenton W. H., Nelan J. E., Patnaude D. J., Simon F. E., 2001, ApJ, 562, 521

Chaboyer B., Green E. M., Liebert J., 1999, AJ, 117, 1360

Chabrier G., 2003, PASP, 115, 763

Chabrier G., Baraffe I., 1997, A&A, 327, 1039

Chabrier G., Hennebelle P., 2011, A&A, 534, A106

Chiosi C., Carraro G., 2002, MNRAS, 335, 335

Cimatti A. et al., 2008, A&A, 482, 21

—, 2004, Nature, 430, 184

Ciotti L., Bertin G., 1999, A&A, 352, 447

Ciotti L., Lanzoni B., Renzini A., 1996, MNRAS, 282, 1

Clemens M. S., Bressan A., Nikolic B., Alexander P., Annibali F., Rampazzo R., 2006, MNRAS, 370, 702

Clemens M. S., Bressan A., Nikolic B., Rampazzo R., 2009, MNRAS, 392, L35
Coccato L., Arnaboldi M., Gerhard O., Freeman K. C., Ventimiglia G., Yasuda N., 2010, A&A, 519, A95
Coccato L. et al., 2009, MNRAS, 394, 1249
Coelho P., Bruzual G., Charlot S., Weiss A., Barbuy B., Ferguson J. W., 2007, MNRAS, 382, 498
Cohen J. G., 1978, ApJ, 221, 788
Cole S., Lacey C., 1996, MNRAS, 281, 716
Cole S., Lacey C. G., Baugh C. M., Frenk C. S., 2000, MNRAS, 319, 168
Conroy C., 2013, ArXiv e-prints
Conroy C., Graves G., van Dokkum P., 2013, ArXiv e-prints
Conroy C., Gunn J. E., White M., 2009, ApJ, 699, 486
Conroy C., van Dokkum P., 2012a, ApJ, 747, 69
Conroy C., van Dokkum P. G., 2012b, ApJ, 760, 71
Conroy C., White M., Gunn J. E., 2010, ApJ, 708, 58
Cordier D., Pietrinferni A., Cassisi S., Salaris M., 2007, AJ, 133, 468
Couture J., Hardy E., 1993, ApJ, 406, 142
Cushing M. C., Rayner J. T., Vacca W. D., 2005, ApJ, 623, 1115
Czoske O., Barnabè M., Koopmans L. V. E., Treu T., Bolton A. S., 2008, MNRAS, 384, 987
—, 2012, MNRAS, 419, 656
Daddi E. et al., 2005, ApJ, 626, 680
Das P., Gerhard O., Churazov E., Zhuravleva I., 2010, MNRAS, 409, 1362
Das P., Gerhard O., Mendez R. H., Teodorescu A. M., de Lorenzi F., 2011, MNRAS, 415, 1244
Davé R., 2008, MNRAS, 385, 147
Davis M., Efstathiou G., Frenk C. S., White S. D. M., 1985, ApJ, 292, 371
de Carvalho R. R., Djorgovski S. G., 1992, in Astronomical Society of the Pacific Conference Series, Vol. 24, Cosmology and Large-Scale Structure in the Universe, de Carvalho R. R., ed., p. 135
Di Matteo T., Springel V., Hernquist L., 2005, Nature, 433, 604
Djorgovski S., Davis M., 1987, ApJ, 313, 59
D'Odorico S. et al., 2006, in Society of Photo-Optical Instrumentation Engineers (SPIE) Conference Series, Vol. 6269, Society of Photo-Optical Instrumentation Engineers (SPIE) Conference Series
Dotter A., Chaboyer B., Jevremović D., Kostov V., Baron E., Ferguson J. W., 2008, ApJS, 178, 89
Douglas N. G. et al., 2002, PASP, 114, 1234
—, 2007, ApJ, 664, 257
Douglas N. G., Taylor K., Freeman K. C., Axelrod T. S., 1997, in IAU Symposium, Vol. 180, Planetary Nebulae, Habing H. J., Lamers H. J. G. L. M., eds., p. 493

Dressler A., 1980, ApJ, 236, 351
Dressler A., Lynden-Bell D., Burstein D., Davies R. L., Faber S. M., Terlevich R., Wegner G., 1987, ApJ, 313, 42
Dutton A. A. et al., 2011, MNRAS, 417, 1621
Dutton A. A., Mendel J. T., Simard L., 2012, MNRAS, 422, L33
Dutton A. A. et al., 2013, MNRAS, 428, 3183
Dye S., Evans N. W., Belokurov V., Warren S. J., Hewett P., 2008, MNRAS, 388, 384
Dye S., Warren S. J., 2005, ApJ, 623, 31
Eggen O. J., Lynden-Bell D., Sandage A. R., 1962, ApJ, 136, 748
Eisenstein D. J. et al., 2001, AJ, 122, 2267
Emsellem E. et al., 2011, MNRAS, 414, 888
—, 2007, MNRAS, 379, 401
Fabbiano G., 1989, ARA&A, 27, 87
Faber S. M., 1977, in Evolution of Galaxies and Stellar Populations, Tinsley B. M., Larson D. Campbell R. B. G., eds., p. 157
Faber S. M., Dressler A., Davies R. L., Burstein D., Lynden-Bell D., 1987, in Nearly Normal Galaxies. From the Planck Time to the Present, Faber S. M., ed., pp. 175–183
Faber S. M., French H. B., 1980, ApJ, 235, 405
Faber S. M., Jackson R. E., 1976, ApJ, 204, 668
Faber S. M. et al., 2007, ApJ, 665, 265
Falco E. E., Gorenstein M. V., Shapiro I. I., 1985, ApJ, 289, L1
Ferrarese L., Merritt D., 2000, ApJ, 539, L9
Ferreras I., La Barbera F., de la Rosa I. G., Vazdekis A., de Carvalho R. R., Falcón-Barroso J., Ricciardelli E., 2013, MNRAS, 429, L15
Ferreras I., Lisker T., Pasquali A., Khochfar S., Kaviraj S., 2009, MNRAS, 396, 1573
Forbes D. A., Ponman T. J., Brown R. J. N., 1998, ApJ, 508, L43
Fraix-Burnet D., Dugué M., Chattopadhyay T., Chattopadhyay A. K., Davoust E., 2010, MNRAS, 407, 2207
Franx M., van Gorkom J. H., de Zeeuw T., 1994, ApJ, 436, 642
Frenk C. S., 1988, in Post-Recombination Universe, Kaiser N., Lasenby A. N., eds., pp. 367–370
Frenk C. S., White S. D. M., Davis M., Efstathiou G., 1988, ApJ, 327, 507
Frenk C. S., White S. D. M., Efstathiou G., Davis M., 1985, Nature, 317, 595
Frogel J. A., Persson S. E., Cohen J. G., 1980, ApJ, 240, 785
Frogel J. A., Persson S. E., Matthews K., Aaronson M., 1978, ApJ, 220, 75
Fulbright J. P., McWilliam A., Rich R. M., 2007, ApJ, 661, 1152
Gallazzi A., Brinchmann J., Charlot S., White S. D. M., 2008, MNRAS, 383, 1439
Gao L., Yoshida N., Abel T., Frenk C. S., Jenkins A., Springel V., 2007, MNRAS, 378, 449

Gargiulo A. et al., 2009, MNRAS, 397, 75
Gavazzi R., Treu T., Koopmans L. V. E., Bolton A. S., Moustakas L. A., Burles S., Marshall P. J., 2008, ApJ, 677, 1046
Gavazzi R., Treu T., Rhodes J. D., Koopmans L. V. E., Bolton A. S., Burles S., Massey R. J., Moustakas L. A., 2007, ApJ, 667, 176
Gebhardt K. et al., 2000, ApJ, 539, L13
Geha M. et al., 2013, ApJ, 771, 29
Gerhard O., Kronawitter A., Saglia R. P., Bender R., 2001, AJ, 121, 1936
Gerhard O. E., 1993, MNRAS, 265, 213
Ghigna S., Moore B., Governato F., Lake G., Quinn T., Stadel J., 2000, ApJ, 544, 616
Girardi L., Bressan A., Bertelli G., Chiosi C., 2000, A&A, Supplement, 141, 371
Girardi M., Manzato P., Mezzetti M., Giuricin G., Limboz F., 2002, ApJ, 569, 720
Glazebrook K. et al., 2004, Nature, 430, 181
Goldoni P., Royer F., François P., Horrobin M., Blanc G., Vernet J., Modigliani A., Larsen J., 2006, in Society of Photo-Optical Instrumentation Engineers (SPIE) Conference Series, Vol. 6269, Society of Photo-Optical Instrumentation Engineers (SPIE) Conference Series
González J. J., 1993, PhD thesis, Thesis (PH.D.)–University of California, Santa Cruz, 1993.Source: Dissertation Abstracts International, Volume: 54-05, Section: B, page: 2551.
Graham A. W., Guzmán R., 2003, AJ, 125, 2936
Graves G. J., 2009, PhD thesis, University of California, Santa Cruz
Graves G. J., Faber S. M., 2010, ApJ, 717, 803
Graves G. J., Faber S. M., Schiavon R. P., 2009, ApJ, 693, 486
Graves G. J., Faber S. M., Schiavon R. P., Yan R., 2007, ApJ, 671, 243
Graves G. J., Schiavon R. P., 2008, ApJS, 177, 446
Gregg M. D., 1992, ApJ, 384, 43
Grillo C., 2012, ApJ, 747, L15
Grillo C., Gobat R., 2010, MNRAS, 402, L67
Grillo C., Gobat R., Lombardi M., Rosati P., 2009, A&A, 501, 461
Grossman A. S., 1970, ApJ, 161, 619
Guimarães A. C. C., Sodré, Jr. L., 2011, ApJ, 728, 33
Gültekin K. et al., 2009, ApJ, 698, 198
Guzman R., Lucey J. R., Bower R. G., 1993, MNRAS, 265, 731
Guzman R., Lucey J. R., Carter D., Terlevich R. J., 1992, MNRAS, 257, 187
Hardy E., Couture J., 1988, ApJ, 325, L29
Heckman T. M., Armus L., Miley G. K., 1990, ApJS, 74, 833
Hennebelle P., 2012, A&A, 545, A147
Hennebelle P., Chabrier G., 2008, ApJ, 684, 395
—, 2009, ApJ, 702, 1428

Hernquist L., 1990, ApJ, 356, 359
—, 1992, ApJ, 400, 460
Hinshaw G. et al., 2012, ArXiv e-prints
Hopkins P. F., 2012, MNRAS, 423, 2037
Hopkins P. F., Bundy K., Hernquist L., Wuyts S., Cox T. J., 2010, MNRAS, 401, 1099
Hopkins P. F., Hernquist L., Cox T. J., Di Matteo T., Robertson B., Springel V., 2006, ApJS, 163, 1
Hopkins P. F., Hernquist L., Cox T. J., Keres D., Wuyts S., 2009, ApJ, 691, 1424
Horne K., 1986, PASP, 98, 609
Humphrey P. J., Buote D. A., 2010, MNRAS, 403, 2143
Husemann B. et al., 2013, A&A, 549, A87
Jaffe W., 1983, MNRAS, 202, 995
Jiang G., Kochanek C. S., 2007, ApJ, 671, 1568
Johansson P. H., Naab T., Ostriker J. P., 2009, ApJ, 697, L38
Jorgensen I., Franx M., Kjaergaard P., 1996, MNRAS, 280, 167
Jorgensen U. G., 1994, A&A, 284, 179
Kass R. E., Raftery A. E., 1995, J. Amer. Statistical Assoc., 90, 773
Kereš D., Katz N., Weinberg D. H., Davé R., 2005, MNRAS, 363, 2
Khochfar S., Burkert A., 2003, ApJ, 597, L117
Khochfar S., Silk J., 2006, ApJ, 648, L21
—, 2009, MNRAS, 397, 506
Kochanek C. S., 1991, ApJ, 373, 354
—, 2006, in Saas-Fee Advanced Course 33: Gravitational Lensing: Strong, Weak and Micro, Meylan G., Jetzer P., North P., Schneider P., Kochanek C. S., Wambsganss J., eds., pp. 91–268
Koopmans L. V. E. et al., 2009, ApJ, 703, L51
Koopmans L. V. E., Treu T., 2002, ApJ, 568, L5
—, 2003, ApJ, 583, 606
Koopmans L. V. E., Treu T., Bolton A. S., Burles S., Moustakas L. A., 2006, ApJ, 649, 599
Korn A. J., Maraston C., Thomas D., 2005, A&A, 438, 685
Kourkchi E. et al., 2012a, MNRAS, 420, 2819
Kourkchi E., Khosroshahi H. G., Carter D., Mobasher B., 2012b, MNRAS, 420, 2835
Kroupa P., 2001, MNRAS, 322, 231
Kroupa P., Weidner C., Pflamm-Altenburg J., Thies I., Dabringhausen J., Marks M., Maschberger T., 2013, The Stellar and Sub-Stellar Initial Mass Function of Simple and Composite Populations, Oswalt T. D., Gilmore G., eds., p. 115
Kudritzki R. P., Pauldrach A., Puls J., 1987, A&A, 173, 293
Kuijken K., 2003, ArXiv Astrophysics e-prints
Kumar S. S., 1963, ApJ, 137, 1121

La Barbera F., Ferreras I., Vazdekis A., de la Rosa I. G., de Carvalho R. R., Trevisan M., Falcón-Barroso J., Ricciardelli E., 2013, ArXiv e-prints
Lacey C., Cole S., 1993, MNRAS, 262, 627
Lacey C. G., Baugh C. M., Frenk C. S., Silva L., Granato G. L., Bressan A., 2008, MNRAS, 385, 1155
Larson R. B., 1975, MNRAS, 173, 671
Lehnert M. D., Tasse C., Nesvadba N. P. H., Best P. N., van Driel W., 2011, A&A, 532, L3
Leitherer C. et al., 1999, ApJS, 123, 3
Loeb A., Peebles P. J. E., 2003, ApJ, 589, 29
Loewenstein M., White, III R. E., 1999, ApJ, 518, 50
Longhetti M., Saracco P., 2009, MNRAS, 394, 774
Lyubenova M., Kuntschner H., Rejkuba M., Silva D. R., Kissler-Patig M., Tacconi-Garman L. E., 2012, A&A, 543, A75
Magoulas C. et al., 2012, MNRAS, 427, 245
Maoz D., Rix H.-W., 1993, ApJ, 416, 425
Maraston C., 2005, MNRAS, 362, 799
Marchesini D., van Dokkum P. G., Förster Schreiber N. M., Franx M., Labbé I., Wuyts S., 2009, ApJ, 701, 1765
Marigo P., Girardi L., Bressan A., Groenewegen M. A. T., Silva L., Granato G. L., 2008, A&A, 482, 883
Matsushita K., Makishima K., Ikebe Y., Rokutanda E., Yamasaki N., Ohashi T., 1998, ApJ, 499, L13
McCarthy P. J. et al., 2004, ApJ, 614, L9
McWilliam A., 1997, ARA&A, 35, 503
Meynet G., Maeder A., 2000, A&A, 361, 101
Mould J. R., Oke J. B., de Zeeuw P. T., Nemec J. M., 1990, AJ, 99, 1823
Naab T., Burkert A., 2003, ApJ, 597, 893
Naab T., Burkert A., Hernquist L., 1999, ApJ, 523, L133
Naab T., Jesseit R., Burkert A., 2006, MNRAS, 372, 839
Naab T., Johansson P. H., Ostriker J. P., 2009, ApJ, 699, L178
Naab T., Johansson P. H., Ostriker J. P., Efstathiou G., 2007, ApJ, 658, 710
Naab T., Khochfar S., Burkert A., 2006, ApJ, 636, L81
Napolitano N. R. et al., 2005, MNRAS, 357, 691
—, 2011, MNRAS, 411, 2035
—, 2009, MNRAS, 393, 329
Napolitano N. R., Romanowsky A. J., Tortora C., 2010, MNRAS, 405, 2351
Narayan R., Bartelmann M., 1996, ArXiv Astrophysics e-prints
Navarro J. F., Frenk C. S., White S. D. M., 1996, ApJ, 462, 563
Newman A. B., Ellis R. S., Bundy K., Treu T., 2012, ApJ, 746, 162

Newman A. B., Treu T., Ellis R. S., Sand D. J., 2011, ApJ, 728, L39
Newton E. R., Marshall P. J., Treu T., Auger M. W., Gavazzi R., Bolton A. S., Koopmans L. V. E., Moustakas L. A., 2011, ApJ, 734, 104
Nieto J.-L., Davoust E., Bender R., Prugniel P., 1990, A&A, 230, L17
Offner S. S. R., Capodilupo J., Schnee S., Goodman A. A., 2012, MNRAS, 420, L53
Offner S. S. R., Krumholz M. R., 2009, ApJ, 693, 914
Padmanabhan N. et al., 2004, New Astron., 9, 329
Pahre M. A., Djorgovski S. G., de Carvalho R. R., 1998, AJ, 116, 1591
Peebles P. J. E., 2002, in Astronomical Society of the Pacific Conference Series, Vol. 283, A New Era in Cosmology, Metcalfe N., Shanks T., eds., p. 351
Peletier R., 2012, ArXiv e-prints
Peletier R. F., 1989, PhD thesis, , University of Groningen, The Netherlands, (1989)
Pérez-González P. G. et al., 2008, ApJ, 675, 234
Peterson R. C., 1976, ApJ, 210, L123
Peterson R. C., Caldwell N., 1993, AJ, 105, 1411
Pietrinferni A., Cassisi S., Salaris M., Castelli F., 2004, ApJ, 612, 168
Planck Collaboration et al., 2013a, ArXiv e-prints
—, 2013b, ArXiv e-prints
Prugniel P., Simien F., 1996, A&A, 309, 749
Quider A. M., Pettini M., Shapley A. E., Steidel C. C., 2009, MNRAS, 398, 1263
Rayner J. T., Cushing M. C., Vacca W. D., 2009, ApJS, 185, 289
Reda F. M., Forbes D. A., Hau G. K. T., 2005, MNRAS, 360, 693
Reimers D., 1975, Memoires of the Societe Royale des Sciences de Liege, 8, 369
Renzini A., 2006, ARA&A, 44, 141
Rix H.-W., de Zeeuw P. T., Cretton N., van der Marel R. P., Carollo C. M., 1997, ApJ, 488, 702
Robertson B., Cox T. J., Hernquist L., Franx M., Hopkins P. F., Martini P., Springel V., 2006, ApJ, 641, 21
Romanowsky A. J., Douglas N. G., Arnaboldi M., Kuijken K., Merrifield M. R., Napolitano N. R., Capaccioli M., Freeman K. C., 2003, Science, 301, 1696
Rusin D., Kochanek C. S., 2005, ApJ, 623, 666
Rusin D., Ma C.-P., 2001, ApJ, 549, L33
Saglia R. P., Bertin G., Stiavelli M., 1992, ApJ, 384, 433
Salpeter E. E., 1955, ApJ, 121, 161
Sánchez S. F. et al., 2012, A&A, 538, A8
Sánchez-Blázquez P. et al., 2006, MNRAS, 371, 703
Saracco P. et al., 2005, MNRAS, 357, L40
Sawala T., Scannapieco C., Maio U., White S., 2010, MNRAS, 402, 1599
Schaller G., Schaerer D., Meynet G., Maeder A., 1992, A&A, Supplement, 96, 269
Schiavon R. P., 2007, ApJS, 171, 146

Schiavon R. P., Barbuy B., Bruzual A. G., 2000, ApJ, 532, 453
Schiavon R. P., Barbuy B., Rossi S. C. F., Milone A., 1997, ApJ, 479, 902
Schiavon R. P., Barbuy B., Singh P. D., 1997, ApJ, 484, 499
Schneider P., 2006, in Saas-Fee Advanced Course 33: Gravitational Lensing: Strong, Weak and Micro, Meylan G., Jetzer P., North P., Schneider P., Kochanek C. S., Wambsganss J., eds., pp. 1–89
Schneider P., Ehlers J., Falco E. E., 1992, Gravitational Lenses
Scodeggio M., Gavazzi G., Belsole E., Pierini D., Boselli A., 1998, MNRAS, 301, 1001
Secco L., Bindoni D., 2009, New Astron., 14, 567
Seljak U., 2002, MNRAS, 334, 797
Sérsic J. L., 1963, Boletin de la Asociacion Argentina de Astronomia La Plata Argentina, 6, 41
—, 1968, Atlas de galaxias australes
Serven J., Worthey G., Briley M. M., 2005, ApJ, 627, 754
Smith R. J., Lucey J. R., 2013, ArXiv e-prints
Smith R. J., Lucey J. R., Carter D., 2012, MNRAS, 421, 2982
Smith R. J., Lucey J. R., Hudson M. J., Bridges T. J., 2009, MNRAS, 398, 119
Sonnenfeld A., Treu T., Gavazzi R., Marshall P. J., Auger M. W., Suyu S. H., Koopmans L. V. E., Bolton A. S., 2012, ApJ, 752, 163
Sparks W. B., Carollo C. M., Macchetto F., 1997, ApJ, 486, 253
Spiniello C., Koopmans L. V. E., Trager S. C., Czoske O., Treu T., 2011, MNRAS, 417, 3000
Spiniello C., Trager S., Koopmans L. V. E., Conroy C., 2013, ArXiv e-prints
Spiniello C., Trager S. C., Koopmans L. V. E., Chen Y. P., 2012, ApJ, 753, L32
Spinrad H., 1962, ApJ, 135, 715
Spinrad H., Taylor B. J., 1971, ApJS, 22, 445
Spolaor M., Hau G. K. T., Forbes D. A., Couch W. J., 2010, MNRAS, 408, 254
Spolaor M., Proctor R. N., Forbes D. A., Couch W. J., 2009, ApJ, 691, L138
Springel V., Di Matteo T., Hernquist L., 2005a, ApJ, 620, L79
—, 2005b, MNRAS, 361, 776
Springob C. M. et al., 2012, MNRAS, 420, 2773
Stevenson C. C., 1994, MNRAS, 267, 904
Strateva I. et al., 2001, AJ, 122, 1861
Strauss M. A. et al., 2002, AJ, 124, 1810
Suyu S. H. et al., 2012, ApJ, 750, 10
Tegmark M., Silk J., Rees M. J., Blanchard A., Abel T., Palla F., 1997, ApJ, 474, 1
Terlevich R., Davies R. L., Faber S. M., Burstein D., 1981, MNRAS, 196, 381
Thomas D., Maraston C., Bender R., Mendes de Oliveira C., 2005, ApJ, 621, 673
Thomas J., Saglia R. P., Bender R., Thomas D., Gebhardt K., Magorrian J., Corsini E. M., Wegner G., 2007, MNRAS, 382, 657

Thomas J. et al., 2011, MNRAS, 415, 545
Tinsley B. M., 1968, ApJ, 151, 547
—, 1972, ApJ, 178, 319
—, 1980, Fund. Cosmic Phys., 5, 287
Tinsley B. M., Gunn J. E., 1976, ApJ, 206, 525
Toomre A., Toomre J., 1972, ApJ, 178, 623
Tortora C., Napolitano N. R., Romanowsky A. J., Capaccioli M., Covone G., 2009, MNRAS, 396, 1132
Tortora C., Napolitano N. R., Romanowsky A. J., Jetzer P., 2010, ApJ, 721, L1
Tortora C., Romanowsky A. J., Napolitano N. R., 2013, ApJ, 765, 8
Trager S. C., Faber S. M., Dressler A., 2008, MNRAS, 386, 715
Trager S. C., Faber S. M., Worthey G., González J. J., 2000a, AJ, 120, 165
—, 2000b, AJ, 119, 1645
Trager S. C., Worthey G., Faber S. M., Burstein D., Gonzalez J. J., 1998, ApJS, 116, 1
Tremonti C. A. et al., 2004, ApJ, 613, 898
Treu T., 2010, ARA&A, 48, 87
Treu T., Auger M. W., Koopmans L. V. E., Gavazzi R., Marshall P. J., Bolton A. S., 2010, ApJ, 709, 1195
Treu T., Dutton A. A., Auger M. W., Marshall P. J., Bolton A. S., Brewer B. J., Koo D. C., Koopmans L. V. E., 2011, MNRAS, 417, 1601
Treu T., Gavazzi R., Gorecki A., Marshall P. J., Koopmans L. V. E., Bolton A. S., Moustakas L. A., Burles S., 2009, ApJ, 690, 670
Treu T., Koopmans L., 2003, in Bulletin of the American Astronomical Society, Vol. 35, American Astronomical Society Meeting Abstracts, p. 1314
Treu T., Koopmans L. V., Bolton A. S., Burles S., Moustakas L. A., 2006, ApJ, 640, 662
Treu T., Koopmans L. V. E., 2002, ApJ, 575, 87
—, 2004, ApJ, 611, 739
Trujillo I., Burkert A., Bell E. F., 2004, ApJ, 600, L39
Trujillo I. et al., 2006, ApJ, 650, 18
Valdes F., Gupta R., Rose J. A., Singh H. P., Bell D. J., 2004, ApJS, 152, 251
Valenti E., Ferraro F. R., Origlia L., 2010, MNRAS, 402, 1729
van de Sande J. et al., 2013, ApJ, 771, 85
—, 2011, ApJ, 736, L9
van de Ven G., Falcón-Barroso J., McDermid R. M., Cappellari M., Miller B. W., de Zeeuw P. T., 2010, ApJ, 719, 1481
van der Marel R. P., Franx M., 1993, ApJ, 407, 525
van Dokkum P. G., 2001, PASP, 113, 1420
—, 2008, ApJ, 674, 29
van Dokkum P. G., Conroy C., 2010, Nature, 468, 940
Van Waerbeke L., Mellier Y., 2003, ArXiv Astrophysics e-prints

Vazdekis A., Casuso E., Peletier R. F., Beckman J. E., 1996, ApJS, 106, 307

Vazdekis A., Cenarro A. J., Gorgas J., Cardiel N., Peletier R. F., 2003a, MNRAS, 340, 1317

Vazdekis A., González J. J., Olguín L., Gorgas J., Cenarro J., Cardiel N., Sánchez-Blázquez P., Pedraz S., 2003b, in Revista Mexicana de Astronomia y Astrofisica Conference Series, Vol. 16, Revista Mexicana de Astronomia y Astrofisica Conference Series, Rodriguez Espinoza J. M., Garzon Lopez F., Melo Martin V., eds., pp. 103–107

Vazdekis A., Peletier R. F., Beckman J. E., Casuso E., 1997, ApJS, 111, 203

Vazdekis A., Ricciardelli E., Cenarro A. J., Rivero-González J. G., Díaz-García L. A., Falcón-Barroso J., 2012, MNRAS, 424, 157

Vazdekis A., Sánchez-Blázquez P., Falcón-Barroso J., Cenarro A. J., Beasley M. A., Cardiel N., Gorgas J., Peletier R. F., 2010, MNRAS, 404, 1639

Vernet J. et al., 2011, A&A, 536, A105

Wambsganss J., 1998, Living Reviews in Relativity, 1, 12

Weijmans A.-M. et al., 2009, MNRAS, 398, 561

Weijmans A.-M., Krajnović D., van de Ven G., Oosterloo T. A., Morganti R., de Zeeuw P. T., 2008, MNRAS, 383, 1343

White S. D. M., Frenk C. S., 1991, ApJ, 379, 52

White S. D. M., Rees M. J., 1978, MNRAS, 183, 341

Williams M. J., Bureau M., Cappellari M., 2009, MNRAS, 400, 1665

Worthey G., 1992, in IAU Symposium, Vol. 149, The Stellar Populations of Galaxies, Barbuy B., Renzini A., eds., p. 507

—, 1994, ApJS, 95, 107

—, 1998, PASP, 110, 888

Wucknitz O., 2002, MNRAS, 332, 951

York D. G. et al., 2000, AJ, 120, 1579

Yoshii Y., Arimoto N., 1987, A&A, 188, 13

Zakharov A. F., 2006, ArXiv Astrophysics e-prints

Zaritsky D., Gonzalez A. H., Zabludoff A. I., 2006a, ApJ, 642, L37

—, 2006b, ApJ, 638, 725

Nederlandse Samenvatting

Melkwegstelsels zijn enorme systemen, bestaande uit sterren en gas, die de "bouwstenen" van ons universum vormen.
In dit proefschrift richten wij ons met name op de structuur en de verdeling van donkere en zichtbare materie in de binnengebieden van vroeg-type melkwegstelsels, de zwaarste melkwegstelsels in ons universum. Ons uiteindelijke doel is de bepaling van de helling van de Initiële Massa Functie (IMF) voor lichte sterren, middels directe waarnemingen van spectra van melkwegstelsels. De IMF is een empirische functie die in de astronomie gebruikt wordt om de verdeling van de initiële stermassa's voor een groep sterren die allen op hetzelfde moment geboren zijn, te beschrijven. Aangezien de eigenschappen en latere ontwikkeling van een ster nauw gerelateerd zijn aan haar initiële massa, vormt de IMF een onmisbaar hulpmiddel voor astronomen die grote groepen sterren willen bestuderen. De stellaire IMF is bijvoorbeeld de belangrijkste factor om de kleur en helderheid van de melkwegstelsels te berekenen.

Hoewel vaak ondergewaardeerd, is de IMF een hoeksteen van de moderne astrofysica en kosmologie, waardoor het detecteren van variaties in de IMF-vorm met de eigenschappen van melkwegstelsels diepe inzichten in stervormingsprocessen kan verschaffen. Een systematische verandering van de IMF met omgeving, metalliciteit, of kosmische 'terugkijk-tijd', zou erop kunnen wijzen dat alle stervorminggeschiedenissen, stellaire massa's en dichtheden die tot op heden afgeleid zijn uit waarnemingen en modellen, systematisch fout zijn. Bijgevolg zal dit ons begrip van de vormingsmechanismen en de chemische evolutie van sterrenstelsels in een kosmologisch verband sterk veranderen.

Voor de zoektocht naar een variabele IMF is het essentieel om de meest extreme omstandigheden, waar stervorming zeer uiteenlopend kan zijn, te onderzoeken. Dit is de motivering die ons leidde om ons tijdens het schrijven van dit proefschrift te concentreren op de zwaarste sterrenstelsels in het universum, waarvan de vorming volgens het zogenaamde ΛCDM paradigma nog steeds een grote uitdaging voor de moderne kosmologie is.

Historisch overzicht

Sterrenkunde is de oudste natuurwetenschap ter wereld. Sinds het begin van de beschaving hunkerde de mens altijd naar een goed begrip van de onderliggende orde van de wereld die hem omringt. Men voelde altijd een diepe fysiologische behoefte aan antwoorden op existentiële vragen als '*Hoe werd het universum gecreëerd?*', '*Waar is het universum van gemaakt?*', of '*Wat is de kosmische betekenis van het menselijk leven*'. Dit zette mensen aan om hun ogen naar de hemel te richten, en te zoeken naar " The Big Picture".

Het woord "astronomie" werd door de oude Grieken bedacht ($\alpha\sigma\tau\rho o\nu$, "astron-", and $\nu\acute{o}\mu o\varsigma$ "-nomie": "recht en orde van de sterren"). Zij waren de vaders van de oude kosmologie, die de eerste elegante theorieën en wiskundige formules ontwikkelden om de wonderen van de kosmos te beschrijven.

De Grieken waren ook degenen die de term Melkweg introduceerden. Zij gebruikten "kuklos" voor "melkachtige cirkel" voor de zwakke band van diffuus licht die zij in de onmetelijkheid van de nachtelijke hemel konden zien. Later doopten de Romeinen dit "Via Lactea", ("Via" voor Weg en "Lactea" voor Melk). Vele eeuwen later, in 1610, richtte Galileo Galilei voor het eerst de nieuw uitgevonden telescoop op de nachthemel, en besefte hij dat de Melkweg geen 'wazige' vloeistof was, maar slechts een verzameling van een groot aantal van sterren, te zwak om met het blote oog te onderscheiden.

Onder de invloed van de filosoof Plato waren de Grieken de eersten die een universum zonder goddelijke wezens poogden te beschrijven. Zij probeerden de bewegingen van de planeten door de combinatie van uniforme, perfecte cirkelvormige bewegingen te verklaren en te voorspellen. De Grieken wisten de afstand van de aarde naar de maan te schatten, en probeerden zelfs de grootte van het hele universum te berekenen. Zij geloofden dat het eindig, onveranderlijk en eeuwig was. Plato's leerling Aristoteles domineerde het denken op dit gebied. De *Aristotelische Kosmos* bestond uit weinig meer dan ons Zonnestelsel, met de aarde in het midden en de perfecte 'sfeer van de vaste sterren' aan de rand.

Het Aristotelische dogma dat beweert dat het universum slechts zo groot als ons Melkwegstelsel is, bleef gedurende vele eeuwen van kracht ('*Ipse Dixit*'), ondanks de komst van de telescoop en grote ontwikkelingen in positionele astronomie en stellaire astrofysica.

Slechts aan het einde van het "Grote Debat" tussen de astronomen Harlow Shapley en Heber Curtis op 26 April 1920, realiseerden astronomen zich dat de vele andere *"nebulae"*, wolkachtige objecten met spiraalvormige structuren die aan de nachtelijke hemel gezien werden, eigenlijk externe sterrenstelsels waren,

bestaande uit een enorm aantal sterren. In werkelijkheid ging de discussie in het "Grote Debat" over de grootte van het universum, en meer in het bijzonder, over de aard van spiraalnevels, en de vraag of deze systemen kleine delen van ons eigen Melkwegstelsel waren, of dat zij aparte systemen zo groot als de Melkweg waren. Shapley verdedigde deze eerste hypothese, met het argument dat als deze "nebulae" externe systemen zouden zijn, hun afstanden van de orde van honderd of meer lichtjaren zouden moeten zijn, een feit dat de meeste astronomen op dat moment volstrekt onaanvaardbaar achtten. Aan de andere kant kwam Curtis op voor het idee van de "Eiland Universa" (een term bedacht door de filosoof *Immanuel Kant*): hij geloofde dat de spiraalnevels extragalactisch waren en stelde daarom dat het universum veel groter dat de Melkweg moest zijn.

Het debat werd eindlijk beslecht door de bepaling van de afstand tot de *Andromedanevel* door Edwin Hubble. Deze ontdekking veranderde onze kijk op het universum: het was opeens een veel grotere plaats dan iedereen tot dan toe had gedacht.

De volgende revolutie kwam hier onmiddellijk na, toen astronomen ontdekten dat het universum niet statisch is, zoals iedereen toen geloofde, maar dat het uitdijt.

"Here is the letter that has destroyed my Universe."
Shapley, 1924

Melkwegstelsels: de bouwstenen van het universum

Hubble verdient erkenning voor het zetten van een van de eerste stappen op weg naar een coherente theorie van de evolutie van Melkwegstelsels: hij was een van de eersten die een morfologisch classificatieschema van sterrenstelsels publiceerde (Hubble 1926). Het Hubble-diagram, ook wel bekend als "Hubbles stemvork", classificeert sterrenstelsels op basis van het uiterlijk van nevels op fotografische beelden (zie Figuur 1). Dit schema, dat nog steeds gebruikt wordt, verdeelt melkwegstelsels in drie grote klassen: elliptische, lensvormige en spiraalstelsels. Deze groepen zijn vervolgens in verband met meer specifieke eigenschappen onderverdeeld, zoals de hoeveelheid afvlakking voor elliptische stelsels en de aard van de armen of de aanwezigheid van een *balk* voor spiralen. Een vierde klasse, gescheiden van de andere drie, omvat melkwegstelsels met een onregelmatige vorm. Elliptische en lensvormige melkwegstelsels vormen samen de klasse van "vroeg-type" stelsels, terwijl de spiraalstelsels en onregelmatige

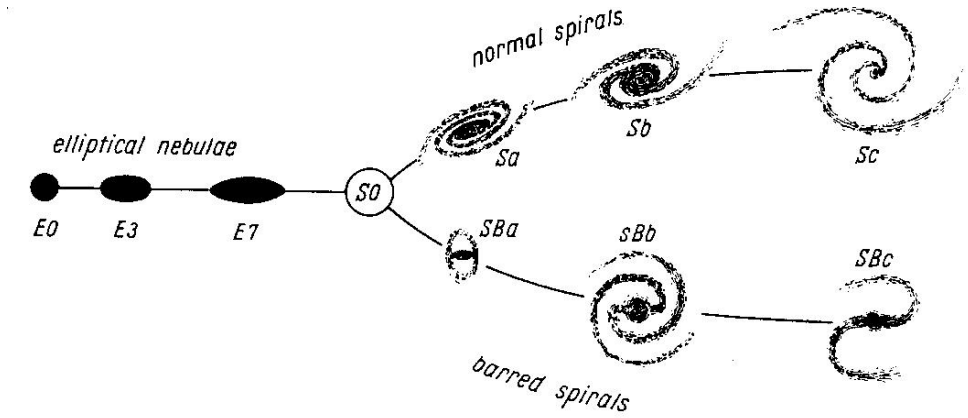

Figuur 1: Het oorspronkelijke classificatieschema van Hubble (*Uit: The Realm of the Nebulae, Hubble 1936*). Vanwege de vorm wordt het diagram ook wel de 'stemvork' genoemd. Aan de linkerkant van de vork vinden wij vroeg-type sterrenstelsels die in elliptische en lensvormige opgesplitst kunnen worden. Stelsels aan de rechterkant (spiralen) worden laat-type, of spiralen, genoemd. Elliptische stelsels worden verder onderverdeeld in de categoriën met nummers tussen 0 en 7, overeenkomstig met hun afvlakking. Lensvormige stelsels worden als S0 aangeduid en werden historisch geïnterpreteerd als een brug tussen elliptische en spiraalstelsels. Spiralen zijn in twee klassen onderverdeeld: normaal (S) en met balk (SB).

stelsels vaak worden aangeduid als "laat-type". Deze nomenclatuur is nog steeds in gebruik en is de bron van het wijdverspreide maar onjuist geachte geloof dat de Hubble-reeks een evolutionaire opeenvolging weerspiegelt van elliptische sterrenstelsels via lensvormige stelsels naar (balk)spiralen. Hubble was hier vanaf het begin duidelijk over en zei dat er geen evolutionaire interpretatie gesuggereerd werd en dat de naamgeving slechts betrekking had op de positie in het diagram.

De evolutie van melkwegstelsels is een heel gecompliceerd proces. Later bleek dat elliptische en spiraalmelkwegstelsels, naast het uiterlijk, ook zeer verschillende fysische eigenschappen hebben. Dit proefschrift richt zich op de vroeg-type stelsels, omdat over de vormingsgeschiedenis van deze stelsels in de hedendaagse extragalactische astrofysica druk gedebatteerd wordt. Deze systemen spelen echter een substantiële rol in het huidige kosmologische model, ΛCDM, daar zij meer dan de helft van de totale stellaire massa in het universum bevatten.

De hiërarchische vorming van structuur in het ΛCDM universum

De Λ-Koude Donkere Materie theorie (in het Engels Λ-*Cold Dark Matter*, ΛCDM) is een fundamentele theorie die veel waarnemingen van sterrenstelsels in het universum met succes kan verklaren. Volgens deze theorie wordt het universum gedomineerd door deeltjes die, behalve door middel van zwaartekracht, bijna geen interacties aangaan met andere materie. Daarom bestempelen we deze deeltjes als "donker". Volgens het huidige kosmologische model van sterrenstelselvorming, bekend als het "Hiërarchische Paradigma" , worden sterrenstelsels hiërarchisch gevormd. Volgens deze theorie vormen kleine structuren het eerst, waarna deze met elkaar samensmelten en zo grotere halo's van donkere materie vormen. De baryonische materie in deze halo's koelt af en vormt stellaire systemen die we nu waarnemen als sterrenstelsels. Op deze manier zijn de eerste sterrenstelsels gevormd.

De vorming en ontwikkeling van vroeg-type stelsels is binnen dit paradigma ook hiërarchisch, en botsingen, accretie en lokale stervorming spelen allemaal een belangrijke rol. Dit is echter niet genoeg om de zwaarste systemen die wij vandaag zien te produceren. Processen waarbij twee of meer sterrenstelsels fuseren (*mergers*), vormen het enige model waarmee de zware en grote elliptische stelsels die we zien in het universum kunnen worden verklaard. Deze mergers in het hiërarchische scenario duiden erop dat de zwaardere sterrenstelsels later dan de minder zware sterrenstelsels vormen; dit lijkt echter in schril contrast te staan met het feit dat de zeer zware vroeg-type stelsels al op hoge roodverschuiving (vroeg in het leven van het universum) klaar zijn met hun vorming.

Gedetailleerde kennis van de interne structuur en verdeling van de zichtbare en donkere materie in zware melkwegstelsels en een betrouwbare studie van de sterpopulaties van de zware ETGs is derhalve cruciaal voor een beter begrip van de vorming en evolutie van deze systemen en om de processen in de hiërarchische vormingsscenario volledig te begrijpen.

De totale massa van sterrenstelsels: Sterke zwaartekrachtlenzen

Zwaartekrachtlenzen zijn fenomenen die worden voorspeld door Einsteins Algemene Relativiteitstheorie: een zeer zwaar voorwerp (de zwaartekrachtlens) zoals een melkwegstelsel of een cluster van melkwegstelsels, dat zich tussen de waarnemer en een achtergrondobject bevindt, buigt lichtstralen van het achtergrondobject af. Dit effect hangt af van zowel de geometrie als de massa van de lens: de afbeelding van het object kan worden verschoven ten opzichte van de

positie waar de waarnemer het object zou zien zonder lens, het beeld kan worden misvormd, of, in het meest spectaculaire geval (sterke zwaartekrachtlenzen, zoals die in dit proefschrift) worden vervormd tot meerdere afbeeldingen, bogen of zelfs complete ringen, die bekend staan als Einsteinringen. Zwaartekrachtlenzen zijn een extreem krachtig en bruikbaar astrofysisch gereedschap. Met behulp van slechts de zwaartekracht bieden ze de mogelijkheid om de massa van een lens binnen een karakteristieke straal, de zogenaamde Einsteinstraal, te bepalen. Deze methode is onafhankelijk van het feit of deze massa bestaat uit zichtbare materie, donkere materie, of beide. De nadelen hiervan zijn dus ook dat er geen onderscheid gemaakt kan worden tussen deze twee vormen van materie en dat de ruimtelijke verdeling van de massa niet nauwkeurig kan worden bepaald.

De baryonische massa van sterrenstelsels: sterpopulaties en kinematica

Het licht van sterren is de belangrijkste bron van informatie over melkwegstelsels. Dit komt doordat dit licht van al het uitgezonden licht het gemakkelijkst waarneembaar is. Niet alle sterren zijn gelijk en niet alle sterren hebben dezelfde massa: sommige sterren zijn veel zwaarder dan de zon, maar de meeste sterren zijn lichter dan de zon. In zware sterren verloopt kernfusie van met name waterstof, het lichtste en meest voorkomende element in het heelal, bijzonder goed, terwijl in hele lichte sterren kernfusie zich heel langzaam voltrekt. Het is dan ook zo dat zware sterren vele malen korter leven dan lichte sterren: hoewel er meer brandstof aanwezig is, verbruikt de ster zoveel meer energie dat de brandstofvoorraad ook eerder opgebruikt is. Daarom bepaalt de initiële massa van de ster het latere evolutionaire pad.

De Initiële Massa Functie (IMF), het hoofdonderwerp van dit proefschrift, beschrijft de verdeling van stellaire massa's voor sterren die gelijktijdig en samen gevormd worden tijdens een stervormingsuitbarsting in een bepaald deel van een melkwegstelsel. Vanwege de hierbovengenoemde redenen is de IMF een onmisbaar bestanddeel voor de bepaling van de waarneembare eigenschappen van sterpopulaties in sterrenstelsels (dat wil zeggen, kleur, helderheid en lichtkracht, stervormingsgeschiedenis).

Helaas staan de meeste elliptische stelsels in het Heelal op een erg grote afstand van ons en is het daarom in het algemeen niet mogelijk om individuele sterren in deze stelsels te onderscheiden met bestaande telescopen. We kunnen echter wel het totale licht ('geïntegreerde licht') zien, dat door meerdere sterren samen in deze sterrenstelsels wordt uitgestraald. Er zijn modellen van

sterpopulaties ontwikkeld om dit geïntegreerde licht van sterrenstelsels te kunnen interpreteren.

De kleuren van de sterren kunnen aan hun leeftijd gekoppeld worden: blauwe kleuren geven een jonge stellaire bevolking aan, terwijl als sterrenstelsels roodgelig zijn, dit meestal betekent dat de sterren lang geleden gevormd zijn. Behalve uit waterstof en helium bestaan sterren uit "metalen". Dit is de astronomische benaming voor alle elementen die zwaarder dan helium zijn en slechts een kleine fractie van de massa in een ster vormen. Naast leeftijd zijn ook metalen belangrijk voor de uiteindelijke kleur van de ster: er geldt hier dat des te meer metalen er in de sterren zitten, des te roder de kleur van de ster is. Het is echter moeilijk om te onderscheiden of de rode kleur op een oude of op een metaalrijke sterpopulatie duidt. Vroeg-type sterrenstelsels zijn erg rood in kleuren, omdat hun stellaire populatie zowel oud als metaalrijk is.

Om de leeftijd en metalliciteit van sterren in een sterrenstelsel te bepalen wordt gebruik gemaakt van een techniek die spectroscopie wordt genoemd. Met spectroscopie wordt het licht van een stelsel tot een spectrum gesplitst.

Wanneer men goed naar een sterspectrum kijkt, dan blijkt dat er op tal van plaatsen (golflengtes) in het spectrum donkere lijntjes zitten. Deze plaatsen zijn donkerder omdat atomen in de atmosfeer van een ster het licht op deze specifieke golflengtes absorberen. Op andere plaatsen kan men meer lichtgevende lijntjes te zien, omdat atomen op die specifieke golflengtes licht uitstralen. Het eerste type spectrum wordt daarom een absorptielijnspectrum genoemd, terwijl het tweede type emissielijnspectrum heet. De positie van de absorptielijnen hangt af van het soort atomen in de steratmosfeer en van de snelheid van de ster. Verschillende absorptielijnen van verschillende elementen zijn meer of minder gevoelig voor een of meer van de parameters van de populatie sterren (leeftijd, metalliciteit, IMF). Als men dus een goed (astronomen zeggen: met een hoge signaal-ruisverhouding, S/N) spectrum van een sterrenstelsel weet te verkrijgen, kan met door de relatieve sterkte van verschillende lijnen (elementen) de leeftijd, metalliciteit en andere eigenschappen van de gemiddelde, geïntegreerde stellaire populatie berekenen.

Door in een waargenomen spectrum van een ster de posities van de lijnen te vergelijken met de lijnen in een referentiespectrum waarvan de snelheid bekend is, is het ook mogelijk om de snelheid van een ster te bepalen. Maar, zoals we al zeiden, wanneer we het spectrum van een melkwegstelsel waarnemen, zien we niet het licht van één enkele ster maar van vele miljoenen sterren tegelijk. Deze sterren hebben niet allemaal dezelfde snelheid: sommige sterren bewegen wat sneller en andere bewegen wat langzamer. In een melkwegstelselspectrum van gecombineerd sterlicht zijn de lijnen een stuk breder dan in een individueel

sterspectrum. Door nu de breedte van de lijnen in een melkwegstelsel te vergelijken met de breedte van de lijnen in een sterspectrum is het mogelijk om de verdeling van snelheden in een melkwegstelsel te bepalen.

Door de analyse van de lichtverdeling en de snelheids- en snelheidsdispersieprofielen (voortgebracht door respectievelijk de geordende en willekeurige beweging van de sterren) is het mogelijk om belangrijke informatie over de structuur van elliptische stelsels te verkrijgen. De snelheid waarmee de sterren moeten bewegen is gerelateerd aan de grootte van de gravitatiekracht, die alleen afhangt van de massa en de onderlinge afstanden tussen de sterren. Door het bestuderen van stersnelheden kunnen we dus leren hoe de lichtgevende massa verdeeld is in een melkwegstelsel. In het algemeen blijkt dat sterren in melkwegstelsels zowel systematische bewegingen, zoals rotatie om het centrum kunnen vertonen, als willekeurige bewegingen, waarbij ze kriskras langs elkaar vliegen. In het bijzondere geval van zware vroeg-type stelsels blijkt dat sterren in deze systemen worden gedomineerd door willekeurige beweging.

Dit proefschrift: De Initiële Massa Functie in zware vroeg-type sterrenstelsels

Alle bovengenoemde methodes om de massaverdeling te bestuderen in een stelsel (totale massa via zwaartekrachtlenzen en zichtbare massa via de sterpopulatie en kinematica van sterren) hebben echter beperkingen. Het grote voordeel van het afleiden van eigenschappen van elliptische stelsels met behulp van de combinatie van zwaartekrachtlenzen, dynamica en sterpopulatieanalyse is dat deze drie methodes elkaar erg goed aanvullen. Door het simultaan toepassen van deze drie methodes kunnen bepaalde problemen opgelost worden die zouden onstaan als de methodes apart worden gebruikt.

Dit is precies wat we hebben gedaan met de X-Shooter Lens Survey (XLENS). Een van de belangrijkste resultaten van het onderzoek in dit proefschrift is dat wij een nieuwe techniek ontwikkeld hebben die is gebaseerd op de combinatie van deze drie methoden en die ons in staat stelt om de Initiële Massa Functie (IMF) in zware elliptische stelsels berekenen. Met de combinatie van deze methoden kunnen we de interne structuur van de stelsels in groot detail bestuderen en demonstreert deze studie ondubbelzinnig hoe de zichtbare materie van de donkere materie kan worden gescheiden.

In dit proefschrift hebben wij de XLENS wetenschappelijke doelen gepresenteerd, en in het bijzonder richtten we ons op de bepaling van eigenschappen aan het lage-massa eind van de stellaire IMF, middels de vergelijking van melk-

wegstelselspectra met modellen van sterpopulaties. We hebben sterrenstelsels met verschillende snelheiddispersies geselecteerd om mogelijke verbanden tussen de IMF en de massa of de snelheidsdispersie van de sterrenstelsels te vinden. We hebben aangetoond dat de helling van de Initiële Massa Functie (IMF) niet universeel is maar steiler wordt naarmate de stellaire snelheidsdispersie van een sterrenstelsel toeneemt. Voor het eerst, hebben we ook een limiet voor lichtste massa in de stellaire IMF gebepaald: we hebben berekend wat de massa van de lichtste ster is die bijdraagt aan het licht van een melkwegstelsel.

Acknowledgments

So long, and thanks for all the fish.
"The Hitchhiker's Guide to the Galaxy", Douglas Adams

Who gets to determine when the old ends and the new begins?
It's not on the calendar, it's no a birthday, it's not a new year,
it's an event – big or small –, something that changes us,
ideally it gives us hope, a new way of living and looking at the world,
letting go of old habits, old memories.
What's important is that we never stop believing
we can have a new beginning, but it's also important to remember
amid all the crap are a few thinks really worth holding on to.

And here we are!
It is finally time to thank all those who have helped me, or just accompanied me, during this extraordinary, unique and unforgettable experience that was my PhD.

As tradition demands, but also very deservedly, the first words are dedicated to my irreplaceable supervisors. Dear Léon Koopmans and Scott Trager I would have never made it until this point, without your patience, perseverance and enthusiasm. When we started our project four years ago, I had no idea what scientific research meant. You have taught me to be critical, to check and recheck my calculations, to be *less Italian*, but above all, you have shown me how to stop and think before jumping to conclusions. Thanks to you, I grew up and matured. I am aware that I have a long and difficult way in front of me, and since I will soon leave the Netherlands where everything is a flat plain, it will be an uphill climb!, but now I feel ready (or almost) to face the brutal world of research with awareness and solid background ... and perhaps a semi-decent English too!
Not everyone knows that it was not Léon to hire me, but it was me to choose him as supervisor. I remember very well the first phone call when *I* interviewed *him*! I

was positively surprised by the conversational and informal tone of our phone call. I was extremely excited by the cool project and by him... I thought that, despite the great success in the field and the many years of experience, the person on the other side of the phone could not be so old! And then, I was even more surprised to know that another Big Professor, Scott Trager, would be pleased to participate in our project. Of course I was honoured.
When I finally arrived in Groningen... Can you imagine my surprise to discover that this Big Professor collected Simpsons's action figures?!
To conclude... and rephrasing a masterpiece (Spiniello et al. 2011)...
'As lensing, dynamics and stellar population, you are perfect when combined together in the super-visioning of a PhD student. The personalities of the two of you are complementary and they allow, once combined in a self-consistent way, the robust growth and independent development of any young researcher who will then be shipped to the outside scientific world.'

You have been and always will be my mentors.

Before starting with the long list of people that deserve my gratitude, I would like to thank Mr. Ubbo Emmius ... a Frisian researcher who I have not had the pleasure of meeting because he died about 350 years before my birth, but whose existence and academic achievements allowed me to spend four marvellous years at the Kapteyn Astronomical Institute. I am also grateful to the LKBF financial support, that gave me the possibility to travel all around the world.

I thank Prof. dr. M. Capaccioli, Dr. G. Covone and Dr. N.R. Napolitano, for the precious help during my Master Thesis project. I am very grateful to the reading committee, Prof. dr. R.L. Davies, Prof. dr. A. Helmi, and Prof. dr. K.H. Kuijken, for thoughtful comments that have improved the quality of this manuscript.

This thesis owes a lot to Charlie Conroy, whose simple stellar population models provided an indispensable ingredient to achieve the presented results. I would also like to kindly thank Tommaso Treu, Alessandro Sonnenfeld, Oliver Czoske, Chris Fassnacht, Sherry Suyu and Michele Cappellari for the many scientific interactions, very often resulted in good ideas and new projects.

Dear Kapteyners I would like to thank you all for sharing with me these four years of coffee-breaks, stimulating lunch-talks and colloquia, funny happy-hours, and for making of the Kapteyn Institute such a lively place.
I am grateful to the Kapteyn Computer Group for their help, and in particular I would like to thank Wim for being such a friendly person. I love that every time you meet me in the corridor you notice that I'm singing! You always ask me why, and I always reply 'why not? I am happy!'.

Hennie, Jackie, Gineke, Christa, Lucia, you are the most efficient and valid secretaries I have ever met, thank you for your precious help in dealing with money and bureaucracy.

Karina and Reynier thank you for the many conversations we had in the corridors of the institute about science, but also just about weather, food, people, Dutch, Italian, Napolitan, Spanish and Argentinian cultures. Bob, Salim, Mark, Renzo, Mariano, thank you for the several lunches in the name of gossip and funny stories about famous astronomers!

Stefy, Kyle, Mark, Alexandros and Wouter, you deserve a special thanks: it was not an easy task sharing the office with a noisy, crazy Neapolitan Girl, with her coffee-moka and her continuously talking!!! Wouter thanks for all the scientific (& non scientific) conversations we had in our office, luckily Alexandros always works with high-volume music! It is a pleasure to discuss and chat with you and I hope we will keep in touch and complete the very cool scientific project we started with Gergö, Scott and the students. Alexandros, thanks for trying to teach me how to roll a cigarette and for 'tolerating' my insatiable desire to gossip!

Simona, my scientific nemesis, we did not have the chance to spend a lot of time together in Groningen but I will never forget the warm welcome that you and John reserved me when I arrived.

Matteo, unfortunately we have never been Kapteyners at the same time, although the shadow of your presence is still vivid and bright here in Groningen. I own to your (and Oliver's) sublime work the starting idea of my project! Thanks! It was nice to team up with you against the 'elderly' to decide the color and style of the figures :P

To my current and former groups members, thanks a lot for the numerous scientific interactions we had during the last years. Gergö, thank you for the pleasant 'soft-singing' background music and our personal coffee-breaks, with real Neapolitan KIMBO espresso! Koshy, macha, thanks for being my brother, father, friend, and my personal 'Jiminy Cricket' ... just one more thing: Do not sit anymore on desks!!! Yanping, thank you for sharing with me the many problems, errors, inconsistencies and sometimes even insanities of the XSH pipeline ... as they say *misery loves company!* Gerjon, you have been my very first student! It has been a pleasure to share with you the little bit of experience I have acquired during my PhD research. I am really impressed by your skills and by your weird working-times ;) Despite IDL, I am sure you will graduate with a great final thesis!

Kyle & Shoko, thanks for the many many times you have corrected my English and kindly told me that I had just invented a new word that does not exist neither in English nor in American ... Shoko, I can assure you that my

improvements in English pronunciation are very *promising*!

A special *'Grazie'* goes to the former and current *'Italian-gang'* populating the Kapteyn in time and space. Above all to Giamba, my dear 'ghost-housemate', also known as *Gesù*, whose presence at home was highlighted only by the presence of his bicycle downstairs, but whose nice girlfriend's visits, Ada, made our flat pleasantly smelling of delicious chocolate muffins! Stefy I will not forget our conversation about doctors, blood-pressure, knees injuries, and health-problems. Grazie per i tuoi tanti consigli e per tutte le volte in cui io ero esaurita e disperata e tu hai saputo tirarmi sù di morale con un semplice sorriso o un dolce abbraccio! Lelli, my 'Ubbo Emmius-brother', we started together and are going to finish almost together! Grazie per aver condiviso questi ultimi difficili mesi e per avermi sopportata durante le mie innumerevoli crisi d'ansia!

I am grateful to the very first people I met in Groningen: Parisa and Alicia. Without you my first evening would have been in the name of melancholy and bad mood. Thank you for that unforgettable dinner!

My little son Pratyush, how could I have done without your crazy, wild parties, your deep and strange philosophy theories, and your stories about your "drunken-saturday nights"? Your mum is proud of you! Even if you hide it behind cigarettes and alcohol, you are an undisputed genius. Do not let life change you!

Mark-macha-(van) den Broccolo, despite your bad and questionable music tastes, you have been a great friend!!! I cannot imagine my PhD experience without you. Scusa se spesso ti ho usato come 'valvola di sfogo', pouring down on you all my 'napoletanitá' :-P ! Our exemplary language exchanges should be published in some major newspapers, we dienen naar de 'Nederlandse Taalunie' hen te sturen, altrimenti potremmo considerare l'opportunitá di recapitarli alla 'Accademia della Crusca' ... vabbuò, teniamocèl strètt strètt e zitt zitt nuje stí scemità!!! Insieme abbiamo saccheggiato uno studentato, pasticciato in cucina in un inimitabile stile oland-napoletano, fumato, bevuto liquori fatti in casa, ballato, parlato di scienza, spettegolato, imparato nuove lingue, giocato a basket, viaggiato e chiacchierato con sconosciuti in più di una nazione... GRAZIE!

Astrophysics is my main passion. But it is not the only one. Despite being only 160 cm tall, another big passion of my life is basketball. My stay in the Netherlands would have not been the same without my beloved basketball club: *De Groene Uilen*.

Als speler en coach heb ik drie jaar lang een actieve rol in de club gehad. Dankzij deze leuke mensen heb ik ook hier mijn favoriete sport kunnen beoefenen,

en bovenal heb ik Nederlands geleerd (min of meer :P) en veel nieuwe en waardevolle vrienden ontmoet. Heren 5, Dames 4, Dames 3, Dames 2, coach Erik, Kaj, Carlos, Jorien, Jacco, Lex, Henrieke, en Feikje, bedankt allemaal! Ik zal jullie niet vergeten. Een superspeciaal bedankje gaat uit naar mijn geliefde 'Relaxing things group': Marijn, mijn persoonlijke Nederlands docent, Sara, mijn tweede moeder een Reneé, mijn favoriete forward! Het is altijd supergezellig met jullie...LEKKETJES! Ik hoop dat we contact blijven houden, ook al wonen we niet meer in dezelfde stad!

Esimio dottor Gallo, grazie di esistere! Tutte le mattine, quando mi sveglio, ringrazio il cielo per il grande onore che mi hai concesso con la tua amicizia, per avermi permesso di cucinare per te tortillas, lasagne, e una quantità indescrivibile di *magere hamburgers*, di farti il caffè, di ricevere continuamente le tue costruttive critiche e i tuoi preziosi consigli su come trovare marito e sistemarmi. Ogni sera, prima di andare a nanna (sí, alle 21:00, quando i 'giovini' escono) dico una preghierina al Dio Gabriele perchè mi conceda un altro insostituibile giorno illuminato dalla sua presenza... ahahahah... Siamo seri per un minuto: Grazie davvero per esserci sempre stato durante questi quattro anni... specialmente per innaffiare le piante e lasciare 'ricordini' a casa mia! Sei una persona stupenda, un vero amico, anche se imbranato e *'principino'*! Grazie anche per avermi iniziato alle meraviglie di YouTube!

Caro vecchio Franz, coinquilino, grande amico e compagno di mercato!!! Grazie per le tante chiacchierate, per le serate fuori al balconcino e per le camomille o i thé nelle fredde e piovose sere d'inverno! Grazie perchè hai sopportato con pazienza la mia maniacale maniera di mettere a posto, e di ficcare il naso in affari e cose non mie! Grazie per la condivisione del frigo, di vegetali e frutta! Sei un ottimo coinquilino ed un amico insostituibile ... !

Andi, Franz, Giamba, Jovana, Melania & Gabriele (il quarto coinquilino sempre e per sempre!) thank you for making our 'Castle' such a pleasant and peaceful place to stay! Living together has not always been easy, but we had it all set and we did a great job!

Fabri & Timea, siete una bellissima coppia, vi auguro il meglio dalla vita e spero di vedervi prestissimo! Fabri, viste le tue continue selezioni e scremature, grazie per non avermi ancora cancellato dagli amici di Facebook :P

Piccola, chiassosa Alessandra, il tuo temperamento e la tua energia fanno di te una persona magica; e con il tuo potente vocione siciliano metti immensa allegria.

Questi quattro anni Groninghiani sono stati davvero intensi; ho cambiato notevolmente e drasticamente la mia vita, ciononostante, non ho assolutamente dimenticato i miei amici italiani, quelli con cui sono cresciuta e maturata, quelli con cui ho scoperto ed odiato la meccanica quantistica, quelli con cui mi sono ubriacata, ho giocato a basket.

Un fortissimo *Grazie* ai fisici ed astrofisici della Federico II e alla mitica SNAP e i suoi membri (giocatori e tifosi)! SNAPPI, siete la squadra di basket meno organizzata e piú entusiasta che io abbia mai allenato, nonchè stupendi amici.

Capitan Chicca sei mitica e ti voglio un gran bene! Grazie per avermi accompagnato a casa quando ero talmente ubriaca da voler aprire il portone con il dito e da vomitare davanti all'ascensore del mio pianerottolo...! A questo proposito... grazie per il vino di Pierino! Grazie a tutti i 'rionesi' e 'procangianesi' per le mitiche serate in 'Little Square Totò'!

Elisa, grazie per aver migliorato e reso felice il mio fratellino e per essere una grande amica, dolce e premurosa! Ti voglio bene!

Gisy, riusciremo mai a vivere nella stessa città noi due? Nonostante la distanza spazio-temporale, la nostra amicizia é speciale e sono sicura che durerà.

E dulcis in fundo ... a Roberta, la mia migliore amica, un semplice e diretto GRAZIE!. Roby, Berta, Melinda, Mola, non basterebbe una intera tesi di dottorato per listare tutte le pazzie, le gite, le mangiate, le citazioni divertenti, gli sbagli, gli sport, i pettegolezzi che abbiamo fatto insieme nel corso di questi dieci e piú anni di intensa amicizia. Eccoti una selezione di *eventi (e nomi) random* che non dimenticherò mai: in palestra spiando e 'classificando' Nero, Guanti e Blue...le telefonate a parlare di Frittatino...al cimitero per fotografare le tombe...i tuoi grossi errori con Cugino (e qui sorvolo!) e il Secchio (che odieremo sempre profondamente!), o i miei grossi errori col Cugino di cugino e Dolce...le avventure di Pallino & Family...il macellaio di Imma e il chitarrista che dovevi sposare...la banana splint...a formia coi nostri amici Rollo & Foca...a Groningen, sui giochi per bambini...i ricordi confusi e alcolici al Covo dei Briganti...Semola!

Chiara Spiniello

The Kapteyn has definitively been my second house in Groningen, and the Kapteyners have been my second family. However, I am extremely grateful to my first, real family and I believe they deserve a special place in my thesis as they occupy a special place in my heart too. This is the reason why I decided to conclude with few more pages of *Special acknowledgments*, dedicated to my unique marvellously noisy family.

Ringraziamenti

Le amicizie te le scegli... la famiglia no!

Ebbene, se anche ciò non fosse vero, io non avrei dubbi nel scegliere esattamente la pazza, chiassosa, scombinata ma meravigliosa e splendida famiglia che mi è capitata!!!

Sia dal lato materno (Fam. Pigliasco) che dal lato paterno (Fam. Spiniello), ho avuto l'immensa fortuna di crescere ed essere circondata da persone davvero speciali. A tutte queste persone devo molto; loro mi hanno insegnato il valore della famiglia, mi hanno sempre protetto ed aiutato in periodi difficili e hanno gioito insieme a me nei momenti felici. Il minimo che io possa fare é dedicare a tutti loro questo manoscritto, e riservargli le ultime pagine, *'scritte in una lingua a loro comprensibile'!*

Chi non ha mai avuto il piacere di conoscere i 'Pigliasco-allargati', non potrá mai apprezzarci. Siamo in assoluto la famiglia più unita e affiatata che io abbia mai visto, ma anche la più rumorosa e scombinata.
Avete visto il film 'Il mio grosso grasso matrimonio greco' ?
Ecco, i personaggi sono sicuramente inspirati a noi Pigliasco!
Nella famiglia Pigliasco, ognuno ha il suo ruolo... nel corso degli anni, io sono diventata quella comprensiva che ha la pazienza di sopportare tutte le zie (persino Stefania), quella a cui si chiedono i favori che nessun'altro ha voluto fare (specie tecnologici e linguistici), ma soprattutto la poeta.
Indi per cui, non posso esimermi da comporre i miei ringraziamenti in rima baciata.

I Pigliasco, che famiglia spettacolare,
ad uno ad uno li dovrei ringraziare...
generosi, disponibili e sempre sorridenti
sono perfetti come amici e come parenti!
Un solo difetto comune li contraddistingue
c'hanno tutti lunghe, lunghissime lingue!!!
Se per caso un segreto tu vuoi confidare,
certe persone ti conviene evitare:
in un batter d'occhio lo sapranno fino alle Seischelle,
se tu lo dici ad una a caso delle 'quattro sorelle' !
Stefania, impicciona, religiosa e viaggiatrice,
Nietta su FB la più accanita giocatrice,
Lucia preoccupata e sempre ansiosa,
e Paola, più rilassata e molto golosa.
I poveri fratelli, insieme coi mariti,
sono vittime e vanno di certo compatiti.
Nonostante le sorelle ci facciano penare,
sono anche sempre pronte ad aiutare.
Il grande dono di questo esteso, pazzo famiglione
é l'amore tramandato da generazione in generazione.
Nonna Tetta e Nonno Giggino sempre tanto ne hanno donato,
e a noi della nuova generazione ci é stato tramandato:
Cosí l'ufficiale LUCOSANIFRAPALUSTE si é ampliato
con il TORILUPAGIAPA si é accoppiato
e il PALASASIGICHINOSEANDGUIDA ha (pro-)creato.
Ma noi Pigliasco-allargati siamo come coniglietti
ci innamoriamo, NON ci sposiamo ma facciamo figlioletti!
Una nuova generazione felice, sfrenata, forte e vigorosa
sará il futuro di questa famiglia meravigliosamente rumorosa!

Cari cugini, nipoti e zii, siete troppi da ringraziare ad uno ad uno... sappiate solo che vi voglio bene e non cambierei nemmeno una virgola in nessuno di voi (vabbè magari qualche virgola sí! :P) Un GRAZIE speciale a quelli di voi che hanno affrontato un lungo viaggio, con le pazze limitazioni sui bagagli della Ryanair e il tempaccio olandese, per essere qui al mio fianco nel giorno del mio dottorato. Lo apprezzo infinitamente. Spero riusciremo a restare uniti e a tenere alto (o basso, vista l'altezza media di 150cm!) il nome della famiglia!

Gli Spiniello per fortuna sono leggermente meno pazzi e più ordinari, ma non per questo banali o noiosi.
Diciamo semplicemente che da questo lato della famiglia si parla uno alla volta, ci si capisce, si domanda e si risponde in maniera sensata e più ordinata, ma senza ombra di dubbio ci si diverte, l'armonia e la serenità non mancano mai, così come non mancano mai la tavola apparecchiata e le carte francesi. A tal proposito, ringrazio i membri di 'Villa Arzilla' per avermi iniziato al gioco del *Burraco*. Quante partite ho dovuto guardare, in religioso silenzio, prima di essere finalmente accettata al tavolo da gioco con gli adulti!
Zia Rosaria, grazie per essere la madrina più figa che ci sia! Grazie per le chiacchierate, reali o emailizzate, per i consigli sentimentali, le lezioni di vita e le tante, tante risate!!!
Zio Mario, grazie per la tua speciale pasta al forno !!!
Sergio Provolò e Fiorella Scimmietta, voi resterete sempre i miei cuginetti piccoli, anche se oramai uno sfiora i due metri e l'altra è quasi dottoressa. Sono molto orgogliosa di voi e sono contenta del bel rapporto che abbiamo.

Ritengo sia superfluo nominare tutti gli zii e i cugini ad uno ad uno, anche se sono sicura che esista almeno un motivo per essere grata ad ognuno di loro, ad esempio le feste di Natale o quelle di Pasqua che aspetto con ansia e sogno tutto l'anno! Ciò che sicuramente è vero è che siamo una famiglia unica e speciale. Sperò, anzi sono sicura, che rimarremo uniti e continueremo a divertirci insieme anche nelle generazioni future e che non lasceremo svanire l'amore la simpatia, l'allegria e la profonda amicizia sincera che nonna Teresa, nonna Lina, nonno Guido e zio Umberto ci hanno insegnato e tramandato.

Siamo ormai in dirittura di arrivo e, approcciandoci alle 200 pagine, ritengo sia finalmente ora di ringraziare le due persone che mi hanno dato la vita e a cui devo tutto. Mamma & Papá, anche noti ai più come Toto & Peppina o Raimondo & Sandra, GRAZIE!
Anche se spesso abbiamo forti 'divergenze di opinioni', se vi prendo in giro per l'inglese a dir poco maccheronico o per le troppe chiacchiere superflue, anche se critico molto, vi voglio un immenso bene. Vi rispetto e vi ammiro per la famiglia che avete costruito e in cui mi avete cresciuta. Vi invidio per come siete ancora innamorati, dopo tanti anni... anche se spesso preferirei meno smancerie in pubblico !!! La Mia Mamma, con la cocciutaggine tipica della *'Famiglia Pigliasco'*, sará vero che quando le chiedi come si chiama, moltro probabilmente ti risponde che ore sono e va a dire a tutti che le hai chiesto dove abiti ... ma è altrettanto vero che quando le dici che hai un problema, anche piccolo e stupido,

non trova pace fino a che non l'ha risolto per te. Mamma, con i tuoi bimbi, la TUA scuola, la preside, le colleghe, con il tuo Guiduccio, e Gianni-si-arrabbia, con la tua illogicissima logica, mi hai insegnato il valore della famiglia e mi ha trasmesso un amore incondizionato e irrazionale.
Il mio Papà orso aggressivo e agorafobico (o Pigliasco-fobico) da giovane, ed 'orsacchiotto di peluche', dolce e coccoloso da vecchietto! Grazie per aver compensato alla mancanza materna del 'gene matematico' nel mio DNA! Grazie per essere sempre stato al mio fianco, per avermi difeso e protetto, per aver creduto in me in ogni situazione ed in ogni momento. Nonostante in genere io odi le ostentazioni, mi rende felice sentire quanto sei orgoglioso di me quando 'ti vanti' con amici e parenti dei miei successi descrivendomi come la nuova Einstein!!!

Mamma, Papà, grazie anche per non esservi fermati nella procreazione pur avendo raggiunto la perfezione al primo colpo!
Guiduccio caro..quante ce ne siamo combinate a vicenda io e te! Quante volte avrei voluto strozzarti, annegarti, buttarti dal balcone, gettarti in mezzo ai leoni e le tigri... ho fantasticato e progettato modi di ucciderti e farla franca per anni! Eppure, oggi non ti cambierei con nessun altro e sono grata e felicissima del bel rapporto che abbiamo instaurato. Nonostante i presupposti e le aspettative non lasciavano ben sperare, sei diventato una persona stupenda: intelligente, determinato, e molto molto buono.

'Alti e bassi, abbiamo corso insieme gridando di gioia,
abbiamo scalato alte montagne, montagne russe,
siamo precipitati verso il basso, il buio profondo,
abbiamo poi guardato con occhi fieri, e dall'alto, il mondo.
Abbiamo viaggiato nel bene e nel male,
lontani nella stessa stanza,
e vicini più che mai a chilometri di distanza.
La vita passa, ma poche cose restano, pilastri fissi dell'esistenza.
Tu, fratello mio, sei uno di questi.
Non importa cosa ci riserverà il futuro
e quali situazioni ci troveremo ad affrontare:
so che comunque vada, adesso e sempre..
l'uno sull'aiuto e il rispetto dell'altra, potrà contare.'

Chiara Spiniello